
CBPF - CENTRO BRASILEIRO DE PESQUISAS FÍSICAS

# First-principle validation of Fourier's law on n-vector models and related applications of q-statistics

Henrique Santos Lima

Advisor: Constantino Tsallis

RIO DE JANEIRO
2024

# Aknowledgments

First and foremost, I extend my deepest gratitude to my family. To my mother, Elaine, and father, Afrânio, who instilled in me the values of hard work and perseverance, your faith in my abilities has been my guiding light, as well as my goal to honor you every day of my life. Without you, I would be nothing; I would not even exist. I could enumerate many reasons to love you, but it would certainly yield an entire book collection, not a simple acknowledgment in a Ph.D. thesis.

To my beloved wife, Barbara, who has been there with me for nearly a decade, always supporting me through my insecurities, fatigue, nervousness, and perseverance. This recognition is just a small token of my immense gratitude for your enduring love and support, as well as my appreciation for you being an excellent mother and wife.

To my daughter, Aurora, who is my hope, my everything, you inspire me to fight and conquer everything within my power to make you happy. You are the greatest example of pure and true love. You enter this acknowledgment as the most sincere gratitude that exists within me. I have no words to express everything I feel about having you in our life.

To my grandparents, Joel and Valdelice, who are the foundation of our family. The values of hard work and never giving up that were passed through my mother came from you. Your tireless fight to provide education to our entire family is truly admirable. To my aunt, Eliene, for being a great advisor and supporting me in the most difficult times. I would like to thank all my family, your encouragement has fueled my ambition.

Next, I would like to express my sincere appreciation to my advisor, C. Tsallis. Your guidance has been invaluable. Your wisdom and patience have not only shaped this work but also shaped me as a researcher and as a person. Your tireless battle for the truth, for questioning, which is the principle of the genuine science, is my greatest admiration for you .

To my colleagues, P. O. de Fabrittis, P. R. A. de Oliveira, M. M. A. Paixão, J. P. S. Melo, E. S. dos Santos, F. C. de Medeiros, among others, your camaraderie and discussions have enriched this journey immeasurably. I am also grateful to U. Tirnakli, D. Eroglu, F. D. Nobre, D. M. Abramov, and M. M. A. Paixão. Your contributions to this work have been highly significant.

I would like to acknowledge the financial support provided by Cnpq and FAPERJ as well as National Laboratory of Scientific Computation (LNCC) to give us the opportunity to use the SDumont supercomputer.

Finally, I would like to express my strong disregard for individuals who do not question scientific ideas, echoing the stance of Lord Kelvin (despite his eminence as a scientist). If the progress of science were left to such individuals, we would still be confined to the knowledge of the early 1900s, clinging to certain theories as dogma and inevitably failing

to comprehend certain physical phenomena.

"FIRST-PRINCIPLE VALIDATION OF FOURIER'S LAW ON N-VECTOR MODELS AND RELATED APPLICATIONS OF Q-STATISTICS"

**HENRIQUE SANTOS LIMA**

Tese de Doutorado em Física apresentada no Centro Brasileiro de Pesquisas Físicas do Ministério da Ciência Tecnologia e Inovação. Fazendo parte da banca examinadora os seguintes professores:

Constantino Tsallis - Orientador/CBPF

Hans J. Herrmann – UFC

José Soares de Andrade Júnior – UFC

Jürgen Fritz Stilck – UFF

Airton Deppman – USP

Rio de Janeiro, 25 de abril de 2024.

# Abstract

We numerically investigate the thermal conductivity of $n$-vector models with $n = 1, 2, 3$ using molecular dynamics simulations. For $n = 1$, our focus is on the $d = 1$ lattice of ferromagnetically coupled planar rotators in the inertial XY model, considering both local and coupling anisotropies. In the limit of extreme anisotropy, these models approach the Ising model.

For the classical inertial nearest-neighbor XY ferromagnet ($n = 2$) in dimensions $d = 1, 2, 3$, with $N = L^d$ representing the total number of lattice sites, we derive the thermal conductance expression,

$$\sigma(T, L)\, L^{\delta(d)} = A(d) e_{q(d)}^{-B(d)\,[L^{\gamma(d)}T]^{\eta(d)}}, \ (\text{with } e_q^z \equiv [1 + (1-q)z]^{1/(1-q)};\ e_1^z = e^z)\,. \qquad (1)$$

The parameters $A(d)$, $B(d)$, $q(d)$, $\eta(d)$, $\delta(d)$, and $\gamma(d)$ depend on the dimension $d$.

Our numerical results reveal consistent dependencies among $(q, \eta, \delta, \gamma)$ that comply with normal thermal conductivity (Fourier's law) in all dimensions. The one-dimensional classical inertial Heisenberg model ($n = 3$) also verifies Fourier's law, with the thermal conductivity becoming independent of lattice size as $L \to \infty$. We find that the thermal conductance $\sigma(L, T)$ for all models can be well-fitted by a function originated from the nonextensive statistical mechanics: $\sigma(L, T) = A(d) \exp_{q(d)}(-B(d)|x|^{\eta(d)})$. The scaling law, $\frac{\eta\gamma}{q-1} = 1$, guarantees the validity of Fourier's law in all dimensions.

On related topics with $q$-statistics, we study human electroencephalograms of typical human adults (EEG), very specifically their inter-occurrence times across an arbitrarily chosen threshold of the signal (observed, for instance, at the midparietal location in scalp). The distributions of these inter-occurrence times differ from those usually emerging within Boltzmann-Gibbs statistical mechanics. They are instead well approached within the $q$-statistical theory, based on non-additive entropies characterized by the index $q$. The present method points towards a suitable tool for quantitatively accessing brain complexity, thus potentially opening useful studies of the properties of both typical and altered brain physiology.

We also stimulate promising investigations about quantum chaos at the *edge of chaos*, a domain well-described by $q$-statistics. These ongoing investigations follow a comprehensive exploration of a specific quantum system exhibiting strong chaos in some regions, a scenario typically governed by Boltzmann-Gibbs statistics.



**Key Words:** Transport phenomena, Non-extensive statistical mechanics, Molecular dynamics, $n$-vector models, Human electroencephalograms, Quantum chaos.

# Resumo

Investiga-se numericamente a condutividade térmica dos modelos $n$ vetoriais com $n = 1, 2, 3$, utilizando simulações de dinâmica molecular. Para $n = 1$, foca-se na rede $d = 1$ de rotores planares ferromagneticamente acoplados no modelo XY inercial, considerando tanto anisotropias locais quanto de acoplamento. No limite de anisotropia extrema, esses modelos se aproximam do modelo de Ising. Para o modelo ferromagnético clássico inercial de primeiros vizinhos ($n = 2$) em dimensões $d = 1, 2, 3$, com $N = L^d$ representando o número total de sítios na rede, deriva-se a expressão da condutância térmica,

$$\sigma(T, L)\, L^{\delta(d)} = A(d)\, e_{q(d)}^{-B(d)\,[L^{\gamma(d)}T]^{\eta(d)}}, (\text{com } e_q^z \equiv [1 + (1-q)z]^{1/(1-q)};\ e_1^z = e^z). \quad (2)$$

Os parâmetros $A(d)$, $B(d)$, $q(d)$, $\eta(d)$, $\delta(d)$ e $\gamma(d)$ dependem da dimensão $d$. Tais resultados numéricos revelam dependências consistentes entre $(q, \eta, \delta, \gamma)$ que estão em conformidade com a condutividade térmica normal (Lei de Fourier) em todas as dimensões. No modelo clássico de Heisenberg inercial unidimensional ($n = 3$) também verifica-se a Lei de Fourier, com a condutividade térmica se tornando independente do tamanho da rede conforme $L \to \infty$. Descobriu-se que a condutância térmica $\sigma(L, T)$ para todos os modelos pode ser bem ajustada por uma função originada da mecânica estatística não extensiva: $\sigma(L, T) = A(d) \exp_{q(d)}(-B(d)|x|^{\eta(d)})$. A lei de escala, $\frac{\eta,\gamma}{q-1} = 1$, garante a validade da Lei de Fourier em todas as dimensões.

Em tópicos relacionados com a $q$-estatística, estudamos eletroencefalogramas (EEG) de adultos típicos, especificamente seus tempos de interocorrência através de um limiar arbitrariamente escolhido do sinal (observado, por exemplo, na localização midparietal no couro cabeludo). As distribuições desses tempos de interocorrência diferem daquelas que geralmente emergem dentro da mecânica estatística de Boltzmann-Gibbs. Elas são, em vez disso, bem descritas pela $q$-estatística, baseada em entropias não aditivas caracterizadas pelo índice $q$. O método atual aponta para uma ferramenta adequada para acessar quantitativamente a complexidade cerebral, abrindo caminho para estudos úteis das propriedades da fisiologia cerebral típica e alterada.

Também estimulamos investigações promissoras sobre o caos quântico na *fronteira do caos*, um domínio bem descrito pela $q$-estatística. Estas investigações em andamento seguem uma exploração abrangente de um sistema quântico específico que apresenta caos forte em algumas regiões, um cenário tipicamente governado pela estatística de Boltzmann-Gibbs.

**Palavras-Chave:** Fenômenos de transporte, Mecânica estatística não-extensiva, Dinâmica molecular, Modelos $n$-vetoriais, Eletroencefalogramas humanos, Caos quântico

# Contents

# Chapter 1

# Introduction

Transport properties naturally emerge in macroscopic systems which are not in equilibrium. For instance, if a system is in permanent contact with two or more reservoirs having different temperatures, electrical potentials, concentrations and mean velocities, transfer of heat and of similar quantities (charge, mass, momentum) spontaneously occur. These phenomena lead to linear relations between causal quantities (appropriate gradients, assumed to be asymptotically small) and their effects (corresponding transfers) yielding characteristic coefficients such as thermal conductivity, electrical conductivity, diffusivity and viscosity, appearing respectively in Fourier's, Ohm's, Fick's and viscosity Newton's laws.

We focus here on Fourier's law. In the absence of radiation and convection, this law [1] consists in a linear relation between heat flux $\mathbf{J}$ and the gradient of the temperature field $-\nabla T$ which causes this flux, thus yielding, at the stationary state, the well known relation $\mathbf{J} = -\kappa \nabla T$, which is the flow of energy per unit of $L^{d-1}$ per unit of time, being $\kappa > 0$ referred to as the *thermal conductivity* of the $d$-dimensional medium and $L$ its linear size.

This important transport property currently satisfies some rules, namely that $\kappa$ neither depends on the gradient of the temperature as long as it is small, nor on the system size as long as it is large [2]. This centennial law was usually used to deal with three-dimensional materials, because in the nineteenth century atoms and molecules were only theoretical particles, with no direct evidence of their existence. Nowadays, various low-dimensional systems have been experimentally [3, 4] and theoretically [5, 6, 7, 8, 9, 10, 11, 12, 13] investigated and some of them, even in one-dimension, obey that important relation [14, 15, 16]. In contrast, it has also been claimed that this law is violated in cases such as ballistic diffusion regime [17, 18], non-momentum conserving systems [19], and anomalous heat diffusion [20, 21, 22]. Let us also mention its possible experimental invalidity in carbon nanotubes [23].

Paradigmatic ferromagnets are in general described by a set of interacting spins in a crystalline $d$-dimensional lattice that contains $n$ spin vector components such that $|\mathbf{S}| = 1$. In the absence of external fields and inertial terms, the Hamiltonian of these systems can

be expressed in the following form:

$$\mathcal{H} = -J \sum_{\langle ij \rangle} \sum_{m=1}^{n} S_i^m S_j^m \;\; (J > 0;\; \sum_{m=1}^{n} (S_i^m)^2 = 1) \,, \tag{1.1}$$

where $\langle ij \rangle$ denotes first-neighboring spins, and $n = 1, 2, 3, \infty$ correspond respectively to the Ising, $XY$, Heisenberg and spherical models [24]. Their transport properties have been little investigated in the literature [25, 26, 27, 28, 29, 30]. In particular, the Ising model has no intrinsic dynamics, and is therefore unfeasible by molecular dynamical approaches. Extensions of Monte Carlo techniques exist [31], but these methods are not grounded on first-principles and no information about the evolution of the system can be provided. For instance, if the system is in a non-stationary state, the heat flux fluctuates and can be positive or negative. Within a molecular dynamics approach, all information is available at any instant of time. Knowledge about the Ising case (i.e., $n = 1$) might be important for the thermal control of spin excitations [32, 33] and skyrmion-hosting materials [34], among others.

In the case of a coupled XY nearest-neighbor-interacting rotator chain ($n = 2$), the temperature dependence of the thermal conductance was, in first approximation, well-fitted by a $q$-Gaussian distribution [29],

$$P_q(u) = P_0 \exp_q(-\beta u^2) \;, \tag{1.2}$$

defined in terms of the $q$-exponential function,

$$\exp_q(u) = [1 + (1-q)u]_+^{1/(1-q)} \;; \quad (\exp_1(u) = \exp(u)) \;\; , \tag{1.3}$$

where $P_0 \equiv P_q(0)$ and $[y]_+ = y$, for $y > 0$ (zero otherwise). The distribution in Eq. (1.2) is very common in the context of nonextensive statistical mechanics [35], since it appears from the extremization of the generalized entropy, known as $S_q$, characterized by a real index $q$ [36, 37],

$$S_q = k \sum_{i=1}^{W} p_i \left( \ln_q \frac{1}{p_i} \right) \;\; , \tag{1.4}$$

where we have introduced the $q$-logarithm definition,

$$\ln_q u = \frac{u^{1-q} - 1}{1-q} \;; \qquad (\ln_1 u = \ln u) \;\; . \tag{1.5}$$

Therefore, one recovers Boltzmann-Gibbs (BG) entropy,

$$S_{\rm BG} = -k \sum_{i=1}^{W} p_i \ln p_i \;, \tag{1.6}$$

as $\lim_{q\to 1} S_q = S_{\rm BG}$, whereas in the microcanonical ensemble, where all microstates present equal probability, $p_i = 1/W$, Eq. (1.4) becomes,

$$S_q = k \ln_q W \ . \tag{1.7}$$

Above, the $q$-exponential function in Eq. (1.3) appears precisely as the inverse function of the $q$-logarithm of Eq. (1.5), i.e., $\exp_q(\ln_q u) = \ln_q(\exp_q(u)) = u$.

Since the introduction of the entropy $S_q$ in Eq. (1.4), a large amount of works appeared in the literature defining generalized functions and distributions (see, e.g., Ref. [35]). Particularly, a recent study based on superstatistics, has found a stretched $q$-exponential probability distribution [38],

$$P_q(u) = P_0 \exp_q(-\beta|u|^\eta) \quad (0 < \eta \leq 1), \tag{1.8}$$

as well as its associated entropic form.

In this essay, we studied the classical inertial XY model for $d = 1, 2$ and 3 dimensional cases (Chapter 2), as well as classical inertial Ising and Heisenberg model in one-dimensional lattices, with linear size $L$, which allowed us to evaluate the validity of the Fourier's law. We consider the first and last ends in thermal contact with heat baths at temperatures $T_h$ and $T_l$ ($T_h > T_l$), respectively. All remaining rotators ($i = 2, \cdots, L-1$) interact by means of nearest-neighbor ferromagnetic couplings and evolve in time through molecular-dynamics numerical simulations. Furthermore, we better characterized the conductivity change for a more extended range of temperatures, resulting in the $q$-stretched exponential as in Eq. (1.8) instead of the $q$-Gaussian distribution as in Eq. (1.2). All results presented here are based in the most recent articles about this subject [39, 40, 41], and an ongoing research, focusing on a one-dimensional classical inertial generic-ranged $XY$-model, namely $\alpha - XY$ model [42].

In summary, in the first part of this thesis, we analyze the thermal conductance of classical inertial $n = 1, 2, 3$-vector models. Our numerical data validate Fourier's law and the thermal conductance is well-fitted by the functional form of Eq. (1.8). The present results suggest that this form should apply in general for the thermal conductance of nearest-neighbor-interacting systems of classical rotators.

In the second part of this thesis, we present related applications with $q$-statistics as in human electroencephalograms. The distribution of inter-occurrence times across an arbitrarily chosen threshold of the signal is well-fitted by a combination of a $q$-stretched exponential and a power law, clearly indicating that $q$-statistics provides a good description of typical human beings [43]. We also study humans with Attention-Deficit/Hyperactivity Disorder (ADHD), and we show that with this approach, we are able to classify and possibly assess human atypicalities [44].

Still in this part, we conduct an investigation which can be valuable at the edge of chaos, which is a transition between ordered and disordered systems. Within the de

Broglie-Bohm theory, we numerically study a generic two-dimensional anharmonic oscillator including cubic and quartic interactions in addition to a bilinear coupling term. Our analysis of the quantum velocity fields and trajectories reveals the emergence of dynamical vortices. In their vicinity, fingerprints of chaotic behavior such as unpredictability and sensitivity to initial conditions are detected. The simultaneous presence of the off-diagonal $-kxy$ and nonlinear terms leads to robust quantum chaos very analogous to its classical version [45]. This investigation suggests that, as the quantum chaos is very analogous to classical one, we can investigate instead of strong chaos regions, the weak chaos one [46, 47].

# Chapter 2

# A brief discussion about thermostatistics

## 2.1 The postulates of thermodynamics

In this section, we discuss the postulates of thermodynamics. We examine some postulates that needed adaptations, showing that such adaptations are truly dependent on the progress of novel theoretical investigations.

The four postulates of thermodynamics according to H. Callen [48] are statements about the property of a simple thermodynamic system. They are stated as follows:

> Postulate I. There exist **particular states** ( called **equilibrium states**) of **simple systems** that, macroscopically, are characterized completely by the internal energy $U$, the volume $V$, and the mole numbers $N_1, N_2, \ldots, N_r$, of the chemical components.

In the first postulate, it is emphasized that it holds for simple ones, and if equilibrium states for such systems exist, we are able to completely characterize them by internal energy $U$, volume $V$ and mole numbers $N$ for each chemical component. Such systems have only two types of work: mechanical and chemical. In a magnetic one, for instance, the 'magnetic work' must be taken into account, and in dielectric ones, the work due to the variation of the polarization vector cannot be neglected. Therefore, the first postulate is restricted to a particular class of thermodynamic systems, and additional considerations would be needed to encompass general ones.

> Postulate II. There exists a function ( called the entropy $S$) of the extensive parameters of any composite system, defined for all **equilibrium states** and having the following property: The values assumed by the extensive parameters in the absence of an internal constraint are those that maximize the entropy over the manifold of constrained **equilibrium states**.

In the second postulate, it is affirmed the existence of a function called entropy, which is very important in the realm of statistical physics (obviously also in thermodynamics).

This entropy has extensive parameters, such as $U$, $V$ and $N$. It also emphasizes the necessity to exist equilibrium states, which is a requirement for the maximization of entropy after the removal of internal constraints related with the equilibrium states. It is worth to emphasize that the maximization of entropy is only achieved when such system is large and closed or isolated.

> Postulate III. The entropy of a composite system is additive over the constituent subsystems. The entropy is continuous and differentiable and is a monotonically increasing function of the energy.

The postulate III is referring to a composite system, which might be defined as a set of simple systems, statistically independent, requiring the same description with energy, volume and number of moles for each simple system, which at equilibrium becomes a single system with the same intensive parameters, such as temperature $T$, pressure $P$, and chemical potentials $\mu_1, \mu_2 \ldots \mu_r$.

> Postulate IV. The entropy of any system vanishes in the state for which

$$\left(\frac{\partial U}{\partial S}\right)_{U,N_1,\ldots,N_r} = 0 \text{ (that is, at the zero of temperature)}. \tag{2.1}$$

The fourth postulate is equivalent to the third law of thermodynamics (Nernst postulate), in which $\lim_{T\to 0} S = 0$. The derivative in Eq. (2.1) is the temperature, so it is same that to say: *the entropy of any system vanishes at* $T = 0$. There are many examples of systems have a (positive) non-zero entropy at zero temperature, such as many quantum systems. It is a common misconception that the Nernst Postulate is responsible for the impossibility of reaching absolute zero. However, even in a world governed by classical statistical mechanics, absolute zero would remain unattainable. Therefore, a more accurate formulation would be $\lim_{T\to 0} S \geq 0$, which applies universally to all systems.

Furthermore, these concepts primarily focus on simple systems with short-range interactions. To summarize, Callen's postulates of thermodynamics are specifically applicable to simple systems rather than complex ones.

We highlight the four postulates, due to the requirements about extensivity and additivity. It is worth to notice that complex systems, with long-range interactions or not, are not included in these postulates, indicating that additivity and/or extensivity are not obligatory. We need to be aware that despite of some similarities, extensivity and additivity are not *two phases of the same coin*. In the R. H. Swendsen's book [49], it is written in page 121:

> The properties of additivity and extensivity are often confused. This is probably due to the fact that many textbooks restrict their discussion of thermodynamics to homogeneous systems, for which both properties are true.

**Additivity** is the more fundamental property. It is true **whenever the range of interactions between particles is small compared to the size of the system**. **Extensivity** is only true to the extent that the surface of the system and the interface with its container **can be neglected**.

So, it is possible that these properties may not hold in complex systems. In general, in complex system, additivity is broken, and particularly in systems with long-range interactions, the extensivity is also broken in standard approaches, such as in gravitational systems [50], magnetic nanoparticle ensembles [51], among others ([52, 53, 54, 55]).

### 2.1.1 Additivity and extensivity

A system with $N$ independent subsystems $A_i$ is additive if and only if its entropic form obeys the following relation

$$S(A_1 + A_2 + \cdots + A_N) = S(A_1) + S(A_2) + \cdots + S(A_N)\,. \tag{2.2}$$

Conversely, a system is extensive, if and only if

$$\lim_{N\to\infty} \frac{S(A)}{N} < \infty\,. \tag{2.3}$$

Another important property of entropy is its homogeneity. A function $f(x)$ is homogeneous of degree $n$ if and only if, for any $\lambda \in \mathbb{R}$, we have $f(\lambda x) = \lambda^n f(x)$. If entropy is both additive and homogeneous of degree 1 across all its constituents, then this entropy is extensive. However, the converse is not necessarily true. If an entropy is extensive, it does not guarantee that the entropy of the system is additive.

The importance of extensivity to thermodynamics is beyond mathematical formulations. According to Euler's theorem, a function $f(x_1, x_2, \ldots, x_N)$, homogeneous of degree $n$, can be related with its derivatives by the relation as follows:

$$nf(x_1, x_2, \ldots, x_N) = \sum_{i=1}^{N} x_i \frac{\partial f}{\partial x_i}\,, \tag{2.4}$$

so, for $n = 1$, the entropy preserves the structure of its differential form, resulting in $S = \frac{U}{T} + \frac{p}{T}V - \frac{\mu}{T}N$, and all feasible Legendre transformations can be done, which allows us to define the free energies, as $F \equiv U - TS$ (Helmholtz free energy) and $G \equiv F + PV$ (Gibbs free energy), as well as $H \equiv U + PV$ (enthalpy), among others.

### 2.1.2 Reformulated "mandatory" postulates

The reformulated versions of those postulates according to R. H. Swendsen [49], are given by:

**Postulate I: There exist equilibrium states of a macroscopic system that are characterized uniquely by a small number of extensive variables.**

**Postulate II: The values assumed by the extensive parameters of an isolated composite system in the absence of an internal constraint are those that maximize the entropy over the set of all constrained macroscopic states.**

**Postulate III: The entropy of a composite system is additive over the constituent subsystems.**

**Postulate IV: The entropy is a continuous and differentiable function of the extensive parameters.**

The author makes it clear that the third postulate is valid when the interactions are short-ranged, in some approximations (page 120),

> Most interactions between molecules are **short ranged**. If we **exclude gravitational interactions and electrical interactions involving unbalanced charges, the direct interaction between any two molecules is essentially negligible at distances of more than a few nanometers**. As discussed at the end of Chapter 7, this leads to an **approximate** separation of the integrals defining the entropy for the subsystems, so that the entropy of the composite system is just the sum of the entropies of the subsystems.

So, the basis of thermodynamics' postulates involve a specific type of system: a short-ranged one. Long-range interactions are overlooked in certain assumptions. Nevertheless, thermodynamics is a robust and well-established theory capable of describing all equilibrium properties of macroscopic systems. Grounded on empirical evidence, it offers a powerful framework for understanding a wide array of phenomena, from gas behavior to heat engine efficiency, and even black hole properties [56]. Therefore, while these postulates are important, they do not fully encompass the vast scope of thermodynamics.

## 2.2 The range of standard statistical physics

The Boltzmann entropy is defined in terms of the total number of microstates, $W$, such that $S = k_B \ln W$. The standard microcanonical ensemble theory is entirely based in this entropy. This entropy is additive, but it has some limitations even for simple ideal gases. These limitations are evident in Gibbs's paradox [57], which is only resolved by ad hoc introducing $N!$ in the denominator of the total number of the microstates, justified by quantum mechanics. This adjustment takes into account the effective indistinguishability

of the particles. To make it clearer, in complex systems, it is common to find the total number of microstates as a power law of the number of particles, namely $W_N \sim N^{\rho}$. When it happens, this entropy is no more extensive, by definition. To preserve the Legendre transformations in thermodynamics we need to consider another entropy that maintains such property [35].

The Shannon entropy, a generalization of Boltzmann entropy, is defined in terms of microstates' probabilities, $p_i$, such that $S = -k_B \sum_{i=1}^{W} p_i \ln p_i$. The Boltzmann entropy is recovered when $p_i = \frac{1}{W}$. After using the constraints $\sum_i^W p_i = 1$ and $\sum_{i=1}^W E_i p_i = U$ as Lagrange multipliers, we obtain the canonical distribution, which is given by $\rho_{eq} = \frac{e^{-\beta E_i}}{Z}$, where $E_i$ is the energy associated with the microstate $i$, $\beta \equiv 1/k_B T$ ($k_B$ is the Boltzmann constant), and $Z$ is the canonical partition function $Z \equiv \sum_i e^{-\beta E_i}$. This distribution has a wide variety of applications in standard statistical physics. However, it also has some limitations. In Gibbs's book [58], on page 35, it is written,

> In treating of the canonical distribution, we shall always suppose the multiple integral in equation (92) to have a finite value, as otherwise the coefficient of probability vanishes, and the law of distribution becomes illusory. This will exclude certain cases, but not such apparently, as will affect the value of our results with respect to their bearing on thermodynamics. It will exclude, for instance, cases in which the system or parts of it can be distributed in unlimited space [...]. It also excludes many cases in which the energy can decrease without limit, as when the system contains **material points which attract one another inversely as the squares of their distances**. [...]. For the purposes of a general discussion, it is sufficient to call attention to the assumption implicitly involved in the formula (92).

Not only J. W. Gibbs, but A. Einstein [59], E. Fermi [60], E. Majorana [61], C. E. Shannon [62], L. Tisza [63], among others [64, 65, 66, 67, 68, 69], were well aware of some problems regarding additivity and nonextensivity in long-range systems. In these systems, the inequivalence between ensembles, mainly the correspondence from microcanonical to canonical results is an object of study even nowadays ([52, 53]).

In the subsequent introductory chapter, we will discuss various families of nonextensive entropies, their properties, and provide details on their concavity and possible thermodynamic descriptions. These entropies generalize Boltzmann-Gibbs entropy in specific limits.

# Chapter 3

# Exploring the neighborhood of $q$-exponentials

This chapter is based on the article *with the same name*, published in Entropy in 2020 [37].

Nonadditive entropies have been used as a basis to explain a diversity of phenomena, from astrophysics to the oscillatory behavior of El Niño [70, 71, 72], from DNA to financial markets [73, 74] from high-energy physics of collisions to granular matter and cold atoms [75, 76, 77], among many others. It turns out that wide classes of complex systems can be satisfactorily handled within a generalization of Boltzmann–Gibbs (BG) statistical mechanics based on the nonadditive entropy

$$S_q \equiv k\frac{1-\sum_{i=1}^{W} p_i^q}{q-1} = k\sum_{i=1}^{W} p_i \ln_q \frac{1}{p_i} \quad (q \in \mathbb{R};\, S_1 = S_{BG} \equiv -k\sum_{i=1}^{W} p_i \ln p_i;\, \sum_{i=1}^{W} p_i = 1)\,, \tag{3.1}$$

where $W$ is the total number of microstates and $k$ is a conventional positive constant (usually $k = k_B$ in physics, and $k = 1$ in computational sciences), the $q$-logarithmic function being defined as $\ln_q z \equiv \frac{z^{1-q}-1}{1-q}$ ($\ln_1 z = \ln z$). This theory is currently referred to as nonextensive statistical mechanics, or $q$-statistics for short [36, 78, 79, 35]. The optimization of $S_q$ with simple constraints yields

$$p_i = \frac{e_q^{-\beta_q E_i}}{\sum_{j=1}^{W} e_q^{-\beta_q E_j}}\,, \tag{3.2}$$

where $\{E_i\}$ are the energy eigenvalues, and the $q$-exponential function (inverse of the $q$-logarithmic function) is defined as follows:

$$e_q^x \equiv [1+(1-q)x]_+^{\frac{1}{1-q}} \quad (q \in \mathbb{R};\, e_1^x = e^x)\,, \tag{3.3}$$

where $[z]_+ = z$ if $z > 0$ and zero if $z \leq 0$; notice that this definition implies that, for $q < 1$,

there is a cutoff at $x_{cutoff} = -1/(1-q) < 0$, for $x > 0$ and $x_{cutoff} = 1/(1-q) > 0$ for $x < 0$ [36]. In the limit $q \to 1$, Equation (3.2) recovers the celebrated BG weight.

The aim of the present introductory chapter is to discuss in detail some departures from a pure $q$-exponential function which frequently emerge in real situations. Such variations are used in the statistics of nucleotides in full genomes [73], the re-association of folded proteins [80], standard map for intermediate values of the control parameter [81], to mention but a few. We focus on crossover statistics (Section 3.1), linear combinations of $q$-exponential functions (Section 3.2), linear combinations of $q$-entropies (Section 3.3), and some two-indices entropies, namely $S_{q,\delta}$ [56], $S^{BR}_{q,q'}$ [82] and $S_{q,q'}$ [83] (Section 3.4).

## 3.1 Multiple Crossover Statistics

Crossover statistics is often useful whenever the phenomenon which is focused on exhibits a $q$-exponential behavior within a range of the relevant variables, and then makes a crossover to another $q$-exponential function with a different index $q$. Although rare, it can, in principle, happen that several crossovers successively occur one after the other. We will refer to it as *multiple crossover statistics*.

Illustrations of such crossovers can be found in [80, 84, 85, 86, 87, 88].

Let us consider the following ordinary differential equation:

$$\frac{dy}{dx} = -a y^q \quad (y(0) = 1;\, a \in \mathbb{R})\,. \tag{3.4}$$

Its solution is given by

$$y(x) = e_q^{-a\,x}\,. \tag{3.5}$$

Multiple crossovers emerge from the following nonlinear ordinary differential equation:

$$\frac{dy}{dx} = -\sum_{k=1}^{M} a_k\, y^{q_k} \quad (q_1 < q_2 < \cdots < q_M)\,, \tag{3.6}$$

with $y(0) = 1$, and $0 \le a_1 \le a_2 \le \cdots \le a_M$, where the right-hand term is constituted by a linear combination of nonlinear terms. Consequently

$$x = \int_y^1 \frac{dz}{\sum_{k=1}^{M} a_k\, z^{q_k}}\,. \tag{3.7}$$

We know that Equation (3.7) has analytical solutions for $M = 1$ and $M = 2$. For $M > 2$, we need to solve this equation numerically.

Particularly for crossover between two curves ($M = 2$) with $q_1$ and $q_2$, we have:

$$\frac{dy}{dx} = -a_1 y^{q_1} - a_2 y^{q_2} = -\mu_{q_1} y^{q_1} - (\lambda_{q_2} - \mu_{q_1}) y^{q_2} \quad (y(0) = 1)\,, \tag{3.8}$$

where we have identified $(a_1, a_2) \equiv (\mu_{q_1}, \lambda_{q_2} - \mu_{q_1})$ in order to facilitate the connection with the notation used in [80]. Let us incidentally mention that this equation enabled the study of the anomalous behavior of folded proteins.

To solve Equation (3.8), we use Equation (3.7), which yields

$$x = \frac{1}{\mu_{q_1}} \left\{ \frac{y^{1-q_1} - 1}{q_1 - 1} - \frac{\left(\frac{\lambda_{q_2}}{\mu_{q_1}}\right) - 1}{1 + q_2 - 2q_1} \right. \\ \times \left[ H\left(1; q_2 - 2q_1, q_2 - q_1, \left(\frac{\lambda_{q_2}}{\mu_{q_1}}\right) - 1\right) \right. \\ \left. \left. - H\left(y; q_2 - 2q_1, q_2 - q_1, \left(\frac{\lambda_{q_2}}{\mu_{q_1}}\right) - 1\right) \right] \right\} \tag{3.9}$$

with

$$H(y; a, b, c) = y^{1+a}\, {}_2F_1\left(\frac{1+a}{b}, 1; \frac{1+a+b}{c}; -y^b c\right) , \tag{3.10}$$

where ${}_2F_1$ is a hypergeometric function.

For the particular case $q_1 = 1$, we obtain

$$y = \frac{1}{\left[1 - \frac{\lambda_{q_2}}{\mu_1} + \frac{\lambda_{q_2}}{\mu_1}\, e^{(q_2 - 1)\,\mu_1 x}\right]^{\frac{1}{q_2 - 1}}} . \tag{3.11}$$

It is certainly worth mentioning that its $q_2 = 2$ instance yields $y = \left[1 - \frac{\lambda_2}{\mu_1} + \frac{\lambda_2}{\mu_1}\, e^{\mu_1 x}\right]^{-1}$, whose $\lambda_2/\mu_1 >> 1$ asymptotic behavior becomes $y \propto 1/[e^{\mu_1 x} - 1]$. It is precisely through this ordinary-differential path that Planck found, in his historical 19 October 1900 paper, the thermostatistical factor which eventually led to his celebrated law for the black-body radiation with the ultimate identification $\mu_1 x \to h\nu/k_B T$ [89, 90].

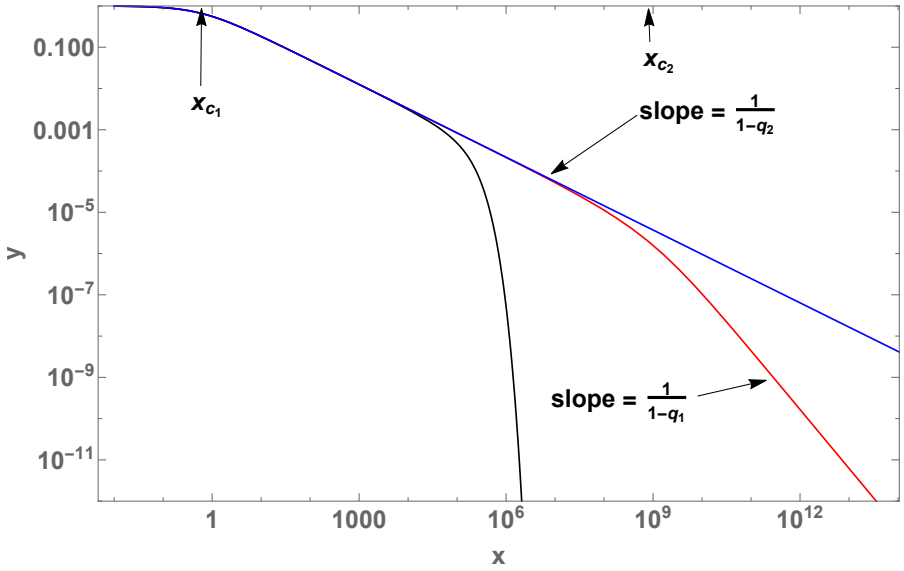


Figure 3.1: $y(x)$ (log-log plot). For the case $M = 1$ with $(q, a) = (2.7, 1)$ (blue curve) and, for the case $M = 2$, the crossover between two curves, namely with $q_1 = 1$ (black curve) and $q_1 = 1.7$ (red curve) respectively, both with $(q_2, \lambda_{q_2}, \mu_{q_1}) = (2.7, 1, 1 \times 10^{-5})$. For the red curve, we have the crossover characteristic values $(x_{c_1}, x_{c_2}) = (0.588, 8.407 \times 10^8)$, which indicate the passage from one regime to another.

For the case $M = 3$, we have

$$\frac{dy}{dx} = -a_1 y^{q_1} - a_3 y^{q_2} - a_3 y^{q_3} \tag{3.12}$$

whose analytical solution is intractable. Therefore, we use numerical methods to solve it. In contrast, the characteristic values $(x_{c_1}, x_{c_2}, x_{c_3})$ where changes of behavior of the curve occur are analytically accessible. Those values are obtained through the following considerations. For the characteristic value $x_{c_1}$, we have

$$y(x_{c_1}) \sim [(q_3 - 1)a_3 x_{c_1}]^{-\frac{1}{q_3 - 1}} \sim 1\,. \tag{3.13}$$

Consequently

$$x_{c_1} = \frac{1}{[(q_3 - 1)a_3]}\,. \tag{3.14}$$

For $x_{c_2}$ we have

$$y(x_{c_2}) \sim [(q_2 - 1)a_2 x_{c_2}]^{-\frac{1}{q_2 - 1}} \sim [(q_3 - 1)a_3 x_{c_2}]^{-\frac{1}{q_3 - 1}}\,, \tag{3.15}$$

hence

$$x_{c_2} = \frac{[(q_3 - 1)a_3]^{\frac{q_2 - 1}{q_3 - q_2}}}{[(q_2 - 1)a_2]^{\frac{q_3 - 1}{q_3 - q_2}}}\,. \tag{3.16}$$

Similarly, we have

$$x_{c_3} = \frac{[(q_2 - 1)a_2]^{\frac{q_1 - 1}{q_2 - q_1}}}{[(q_1 - 1)a_1]^{\frac{q_2 - 1}{q_2 - q_1}}}\,. \tag{3.17}$$

Therefore, for the $M = 3$ particular case whose parameter values are $a_1 = 5 \times 10^{-11}$, $a_2 = 1 \times 10^{-4}$ and $a_3 = 1$, with $q_1 = 1.2$, $q_2 = 1.7$ and $q_3 = 2.7$ , we have $x_{c_1} \approx 0.59$, $x_{c_2} \approx 1.68 \times 10^7$ and $x_{c_3} \approx 5.47 \times 10^{13}$, as shown in Figure 3.2 a,b. It is similarly possible to study multiple crossovers for the case $M > 3$.

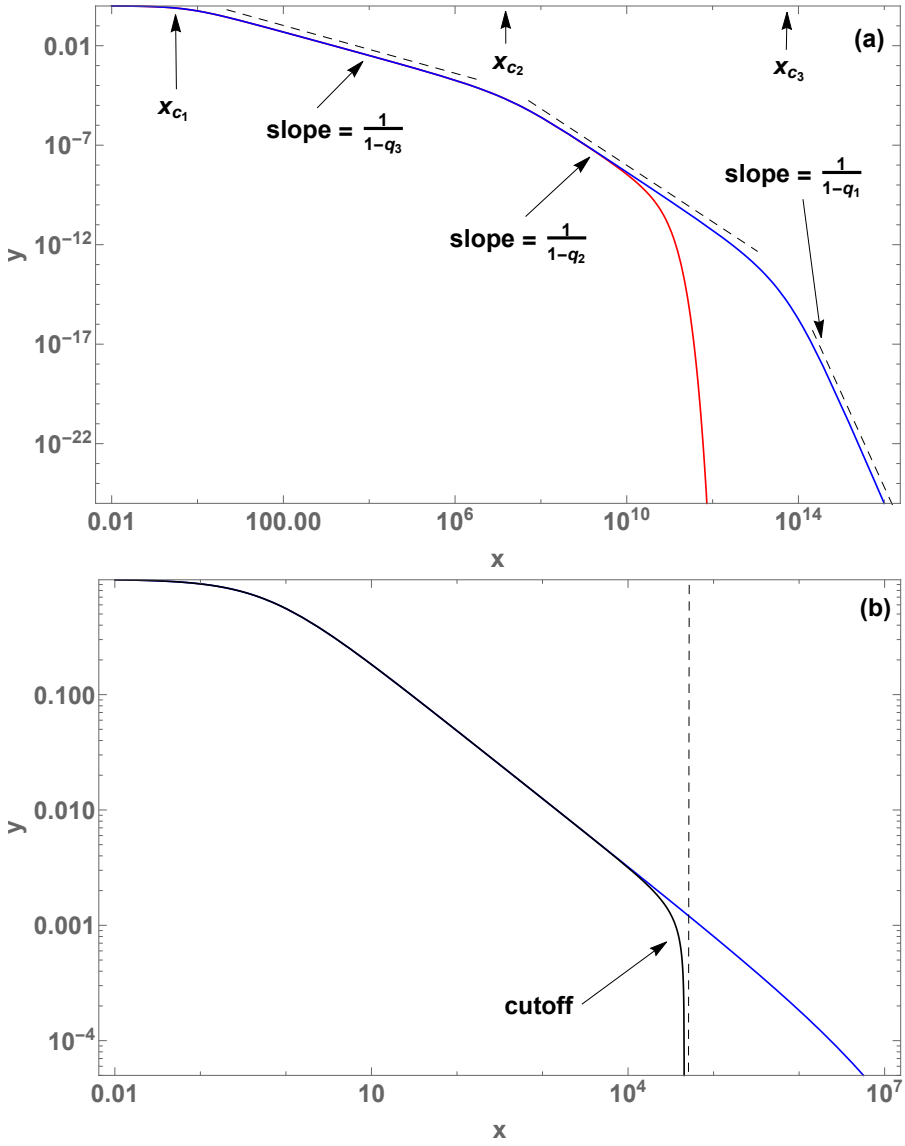


Figure 3.2: Crossovers in $y(x)$ for $M = 3$ (log-log plots) (**a**) between two curves with $(q_1, q_2) = (1, 1.7)$ (red curve), $(q_1, q_2) = (1.2, 1.7)$ (blue curve) respectively, both with $(q_3, a_1, a_2, a_3) = (2.7{,}5 \times 10^{-11}{,}1 \times 10^{-4}{,}1)$, and (**b**) a change was done on the blue curve, with $q_1 = -1$ (black curve); the cutoff occurs at $x_{cutoff} \approx 4.48 \times 10^4$.

## 3.2 Linear Combination of Normalized $q$-Exponentials

For a linear combination of normalized $q$-exponentials, we consider a probability distribution function $P = P(x)$ , $x \in X \subset \mathbb{R}^+$ such that:

$$P(x) = \sum_{k=1}^{M} b_k \, p_k(x) = \sum_{k=1}^{M} b_k \, \frac{e_{q_k}^{-\beta_{q_k} x}}{Z_{q_k}} \quad (q_1 \leq q_2 \leq \cdots \leq q_M < 2;\, \beta_{q_k} > 0\,, \forall\, k)\,, \tag{3.18}$$

with $\sum_{k=1}^{M} b_k = 1 \quad (b_k \geq 0)$, $\{Z_{q_k}\}$ being normalization factors (the upper limit $q < 2$ emerges in order to $\{Z_{q_k}\}$ being finite). Those quantities are determined by imposing,

for all $k \in \{1, ..., M\}$,

$$\int_0^{\infty} dx\, p_k(x) = 1 \;\; if \;\; q_k \geq 1\,, \tag{3.19}$$

$$\int_0^{\frac{1}{\beta_{q_k}(1-q_k)}} dx\, p_k(x) = 1 \;\; if \;\; q_k < 1\,. \tag{3.20}$$

It follows

$$Z_{q_k} = \frac{1}{\beta_{q_k}(2-q_k)}\,, \;\forall\, q_k < 2\,. \tag{3.21}$$

Let us focus on two specific particular cases, namely $M = 2$ with $q_1 = q_2 \equiv q$, and $M = 3$ with $q_1 = q_2 = q_3 \equiv q$; $\beta_{q_1} \equiv \beta_1$, $\beta_{q_2} \equiv \beta_2$, $\beta_{q_3} \equiv \beta_3$, and $Z_{q_k} \equiv Z_k$. It follows that

$$p(x) = b_1 \frac{e_q^{-\beta_1 x}}{Z_1} + b_2 \frac{e_q^{-\beta_2 x}}{Z_2} \tag{3.22}$$

with $b_2 = 1 - b_1$, $1/Z_1 = \beta_1(2-q)$, and $1/Z_2 = \beta_2(2-q)$, and

$$p(x) = b_1 \frac{e_q^{-\beta_1 x}}{Z_1} + b_2 \frac{e_q^{-\beta_2 x}}{Z_2} + b_3 \frac{e_q^{-\beta_3 x}}{Z_3} \tag{3.23}$$

with $b_3 = 1 - b_1 - b_2$, $1/Z_1 = \beta_1(2-q)$, $1/Z_2 = \beta_2(2-q)$ and $1/Z_3 = \beta_3(2-q)$. See Figures 3.3 and 3.4.

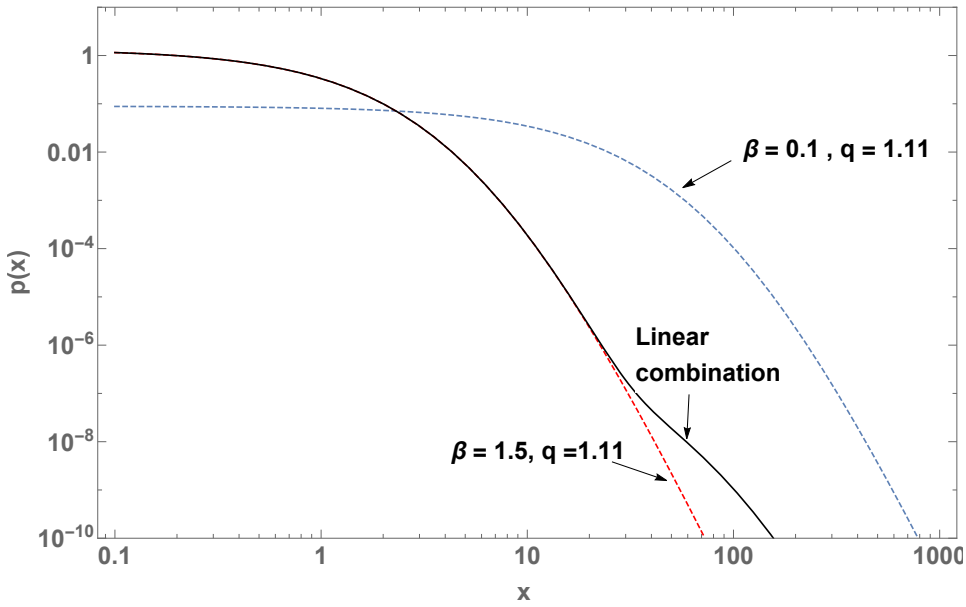


Figure 3.3: $p(x)$ (log-log plot) of three curves (case $M = 2$) with parameters $q = 1.11$ and $\beta = 0.1$ (blue dashed curve), $\beta = 1.5$ (red dashed curve), and their linear combination (black curve) with $b_1 = 1 \times 10^{-5}$ and $b_2 = 1 - b_1$.

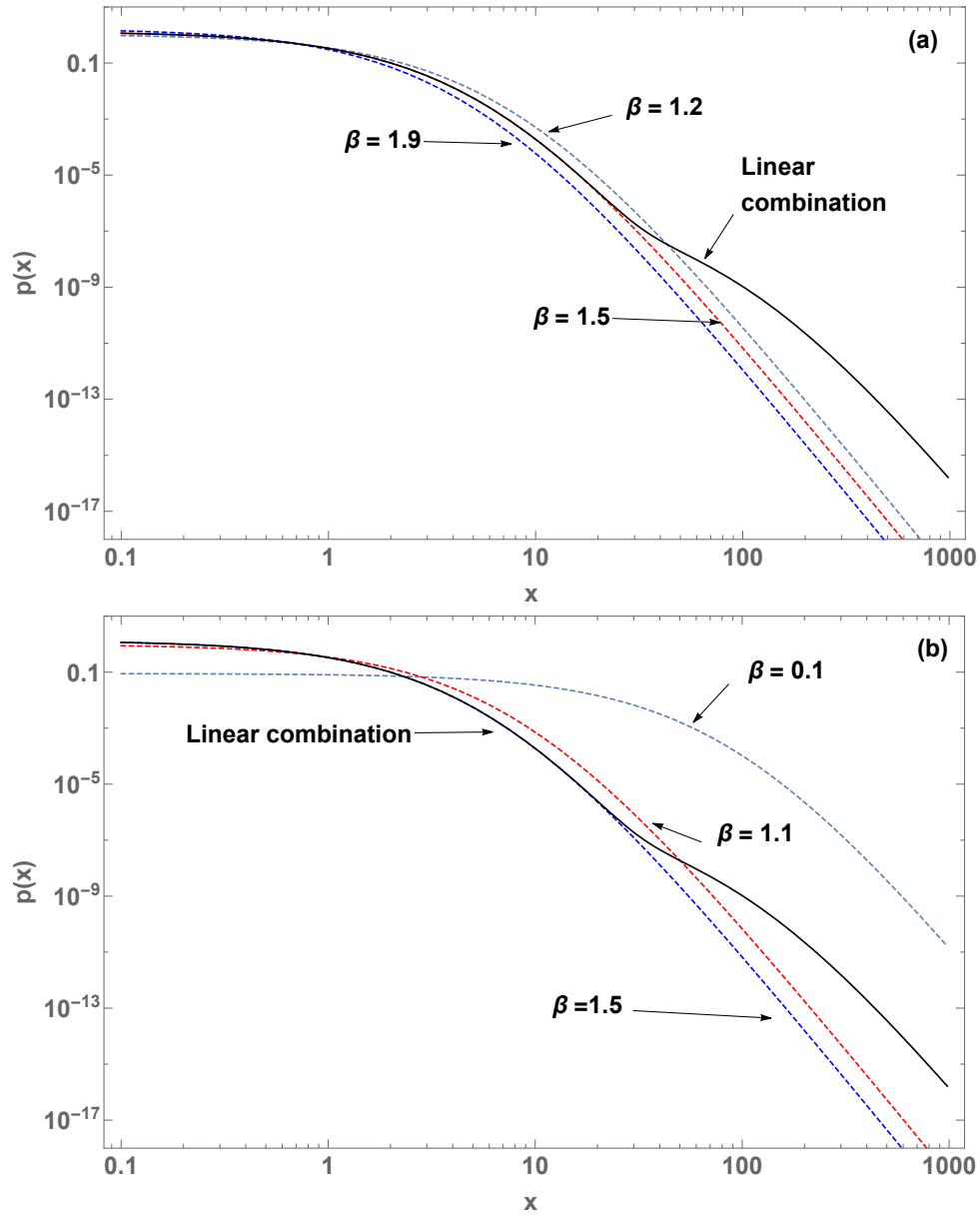


Figure 3.4: $p(x)$ (log-log plots) of four curves with parameters $q = 1.11$, $\beta = 1.9$ (blue dashed curve), $\beta = 1.5$ (red dashed curve), $\beta = 1.2$ (gray dashed curve), and their linear combination (black curve). (**a**) Four curves with $\beta = 1.5$ (blue dashed curve), $\beta = 1.1$ (red dashed curve), $\beta = 0.1$ (gray dashed curve) and their linear combination (black curve). (**b**) With $b_1 = 1 \times 10^{-5}$, $b_2 = 1 \times 10^{-3}$ and $b_3 = 1 - b_1 - b_2$, both with $q = 1.11$ (case $M = 3$) .

In Figure 3.4 ($M = 3$), we fix the value $q_k = 1.11$ for $k = 1, 2, 3$. Another illustration of the linear combination consists of fixing the value $\beta_{q_k} = \beta$ for $k = 1, 2, 3$ and using three different values for $q_k$. In the case illustrated in Figure 3.5, the linear combination remains close to the curve corresponding to $(q, \beta) = (1.2, 0.1)$.

$$p(x) = b_1 \frac{e_{q_1}^{-\beta x}}{Z_{q_1}} + b_2 \frac{e_{q_2}^{-\beta x}}{Z_{q_2}} + b_3 \frac{e_{q_3}^{-\beta x}}{Z_{q_3}} \tag{3.24}$$

with $b_3 = 1 - b_1 - b_2$, $1/Z_{q_1} = \beta(2 - q_1)$, $1/Z_{q_2} = \beta(2 - q_2)$ and $1/Z_{q_3} = \beta(2 - q_3)$.

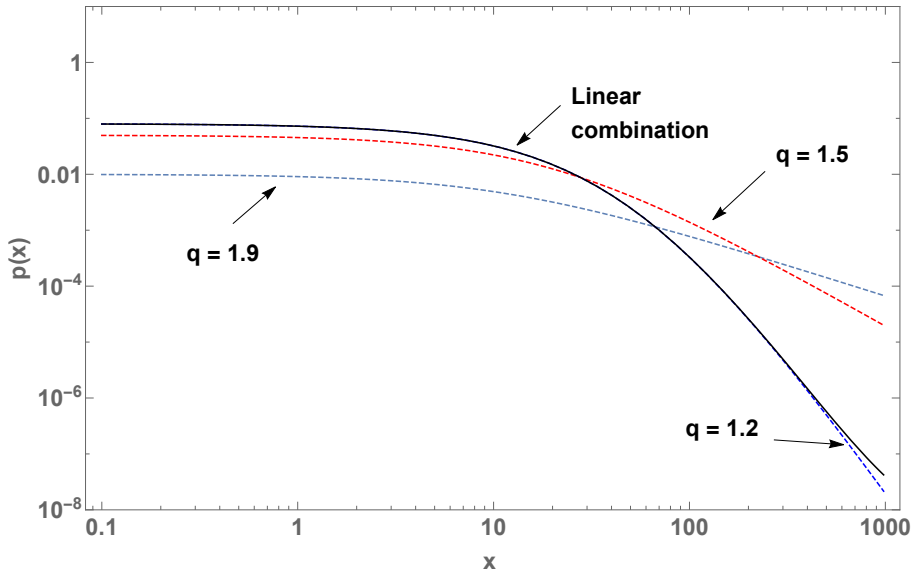


Figure 3.5: $p(x)$ (log-log plot) of four curves (case $M = 3$) with parameters $\beta = 0.1$, $q = 1.2$ (blue dashed curve), $q = 1.5$ (red dashed curve), $q = 1.9$ (gray dashed curve), and their linear combination (black curve) with $b_1 = 1 \times 10^{-5}$, $b_2 = 1 \times 10^{-3}$ and $b_3 = 1 - b_1 - b_2$.

Linear combinations of this kind (either of $q$-exponentials, or of $q$-Gaussians) have been fruitfully used in [73, 81, 91, 92].

## 3.3 Linear Combination of $q$-Entropies

A linear combination of $q$-entropies can be written as follows:

$$S(\{p_i\}) = \sum_{k=1}^{M} c_k \, S_{q_k}(\{p_i\}) \quad (q_1 < q_2 < \cdots < q_M) \quad (c_k \geq 0) \, . \tag{3.25}$$

This expression is generically not normalized. If we happen to prefer normalization for some specific reason, it is enough to divide Equation (3.25) by $\sum_{k=1}^{M} c_k$.

With the constraints $\sum_i p_i - 1 = 0$ and $\sum_i p_i E_i - U = 0$, where $U$ is the internal energy of the system and $\{E_i\}$ are the energy eigenvalues, we define the functional $f(\alpha_1, \alpha_2, \{p_i\})$ as follows:

$$f(\alpha_1, \alpha_2, \{p_i\}) \equiv \sum_{k=1}^{M} c_k \, S_{q_k}(\{p_i\}) + \alpha_1 \left(1 - \sum_i p_i\right) + \alpha_2 \left(U - \sum_i p_i E_i\right) \, . \tag{3.26}$$

Then, through extremization, we obtain

$$\frac{\partial}{\partial p_j} f = 0 = \sum_k c_k \left\{ \ln_{q_k} \frac{1}{p_j} - \left(\frac{1}{p_j}\right)^{1-q_k} \right\} - \alpha_1 - \alpha_2 E_j \tag{3.27}$$

hence

$$E(p_j) = -\frac{\alpha_1}{\alpha_2} + \frac{1}{\alpha_2}\sum_k c_k \left\{ \ln_{q_k} \frac{1}{p_j} - \left(\frac{1}{p_j}\right)^{1-q_k} \right\}. \tag{3.28}$$

We introduce convenient new variables, namely

$$\alpha_1 \equiv -\alpha_2 \mu, \;\; \alpha_2 \equiv \beta\,. \tag{3.29}$$

This enables us to express $X_j \equiv \beta(E_j - \mu)$ as an explicit function of $p_j$, namely

$$X_j = \sum_k c_k \left\{ \ln_{q_k} \frac{1}{p_j} - \left(\frac{1}{p_j}\right)^{1-q_k} \right\}. \tag{3.30}$$

The cutoff condition, whenever present, is given by $\lim_{p_j \to 0} X(p_j, q_1, q_2, \ldots, q_M) \equiv X_c(q_1, q_2, \ldots, q_M)$. For instance, for $M = 3$, we have (see Fig. 3.6)

$$X_c(q_1, q_2, q_3) = \frac{c_1}{q_1 - 1} + \frac{c_2}{q_2 - 1} + \frac{c_3}{q_3 - 1}, \;\; (1 < q_1 \leq q_2 \leq q_3). \tag{3.31}$$

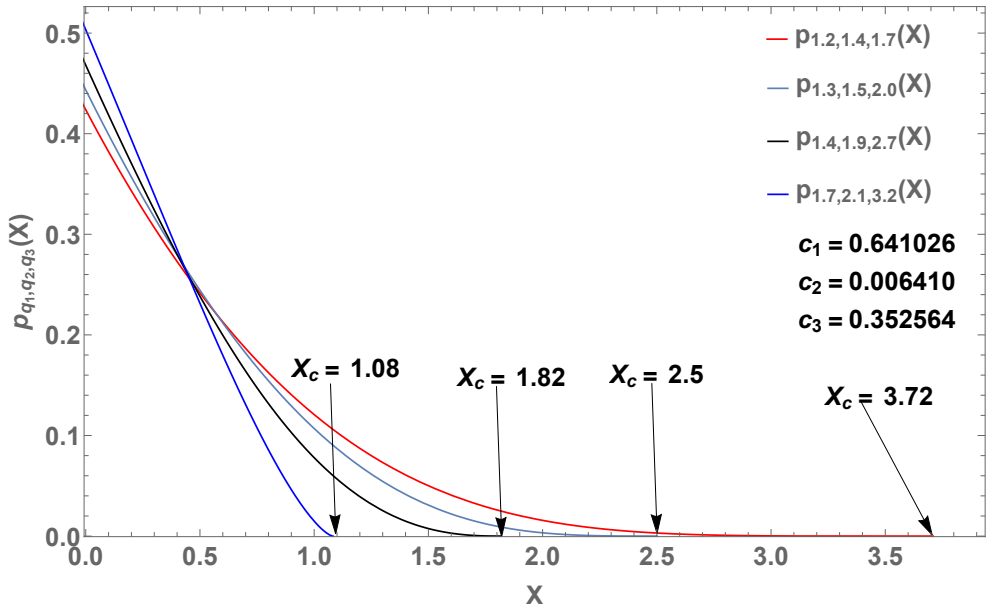


Figure 3.6: Four probability distributions $p_{q_1,q_2,q_3}(X)$ ($M$=3) based on Equation (3.30) with $(c_1, c_2, c_3) = (0.641026, 0.006410, 0.352564)$. From (3.31), we respectively obtain the cutoff values $X_c = 1.08$ for $(q_1, q_2, q_3) = (1.7, 2.1, 3.2)$ (blue curve), 1.82 for $(q_1, q_2, q_3) = (1.4, 1.9, 2.7)$ (black curve), 2.50 for $(q_1, q_2, q_3) = (1.3, 1.5, 2.0)$ (gray curve) and $X_c = 3.72$ for $(q_1, q_2, q_3) = (1.2, 1.4, 1.7)$.

The $M = 2$ particular case of (3.25) has been focused on in [91]:

$$S(\{p_i\}) = c_1 S_{BG}(\{p_i\}) + c_2 S_q(\{p_i\}) \tag{3.32}$$

where one of the entropies is the BG entropy (i.e., $q_1 = 1$), and the other one $S_q(\{p_i\})$ corresponds to $q_2 \equiv q \neq 1$. Then, we have (see Fig. 3.7)

$$p_j = \left\{ aW\left( A_q e^{-(q-1)X_j} \right) \right\}^{\frac{1}{q-1}} \tag{3.33}$$

where $W(z)$ is the Lambert function, implicitly defined by $We^W = z$ (see, for instance, [93]), $A_q \equiv \frac{1}{a} e^{-(q-1)\left(1-\frac{c_2}{c_1(q-1)}\right)}$, $\alpha_1 \equiv -\mu\alpha_2$, $\beta \equiv \frac{\alpha_2}{c_1}$ and $X_j \equiv \beta(E_j - \mu)$ (this definition of $\beta$ differs from that in Equation (3.29)), with $a \equiv \frac{c_1}{c_2 q} = \frac{c_1}{(1-c_1)q}$. $A_q$ is determined via the normalization of the probabilities $\{p_j\}$, i.e.,

$$\sum_j p_j = \sum_j \left\{ aW\left( A_q e^{-(q-1)X_j} \right) \right\}^{\frac{1}{q-1}} = 1. \tag{3.34}$$

In other words, $A_q$ implicitly depends on $(q, c_1)$. Whenever appropriate, we may go to the continuum limit. If it is allowed to consider $X \geq 0$, we have

$$\int_0^\infty \left\{ aW\left( A_q e^{-(q-1)X} \right) \right\}^{\frac{1}{q-1}} dX = 1\,, \tag{3.35}$$

hence

$$q a^{-\frac{1}{q-1}} = W(A_q)^{\frac{1}{q-1}} \left[ q + W(A_q) \right]\,. \tag{3.36}$$

This expression determines $a$ as an explicit function of $(q, A_q)$.

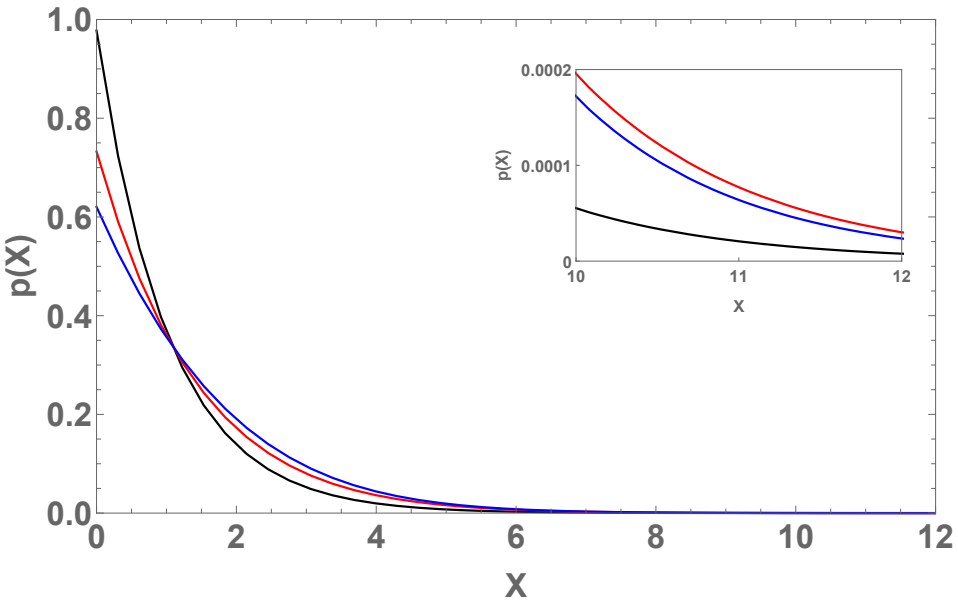


Figure 3.7: Three probability distributions $p(X)$ based on Equation (3.33) with $c_1 = 0.3$ and $q = 1.01$ hence $A_q = 0.0238786$ (black curve), $q = 1.2$ hence $A_q = 0.6798077$ (red curve), and $q = 1.5$ hence $A_q = 2.3025270$ (blue curve).

It is known that, in nonextensive statistical mechanics [94], the constraints under which the entropy is optimized might be chosen with escort distributions, namely, $\sum_i p_i - 1 = 0$ and $\frac{\sum_i p_i^q E_i}{\sum_i p_i^q} - U_q = 0$. We then have

$$\tilde{f}(\alpha_1, \alpha_2, \{p_i\}) \equiv c_1 S_{BG}(\{p_i\}) + c_2 S_q(\{p_i\}) + \alpha_1 \left(1 - \sum_i p_i\right) + \alpha_2 \left[U_q - \frac{\sum_i p_i^q E_i}{\sum_i p_i^q}\right] \quad (3.37)$$

hence

$$p_j = \left\{ a e_q^{(q-1)} W\Big(B_q \, e_q^{-(q-1)X_j}\Big)\right\}^{\frac{1}{q-1}} , \quad (3.38)$$

where $X_j \equiv \beta'(E_j - \mu)$ with $\beta'$ defined as

$$\beta' \equiv \frac{\beta}{\sum_j p_j^q + (1-q)\beta U_q} \quad (3.39)$$

with $\beta \equiv \frac{\alpha_2}{c_1}$. Clearly, $B_q$ is determined by

$$\sum_j p_j = \sum_k \left\{ a \, e_q^{(q-1)} W\Big(B_q e_q^{-(q-1)X_j}\Big)\right\}^{\frac{1}{q-1}} = 1 \, . \quad (3.40)$$

Let us remind at this point that extremizing $S_q$ with standard constraints is equivalent to extremizing $S_{2-q}$ with escort constraints. The equivalence implies in doing the transformation $q \to 2 - q$ [94, 95].

Let us address now the concavity/convexity of $S\{p_i\}$. We illustrate with the linear combination of two ($M = 2$) $q$-entropies with $q_1$ and $q_2$, assuming $p_1 \equiv p_2 \equiv \cdots \equiv p_{(W-1)} \equiv p$ and $p_W = 1 - (W-1)p$. In other words, we consider

$$\begin{aligned} S_{q_1,q_2}(p) = c_1 \left[(W-1)p \ln_{q_1}\left(\frac{1}{p}\right) + (1-(W-1)p)\ln_{q_1}\left(\frac{1}{1-(W-1)p}\right)\right] + \\ c_2 \left[(W-1)p \ln_{q_2}\left(\frac{1}{p}\right) + (1-(W-1)p)\ln_{q_2}\left(\frac{1}{1-(W-1)p}\right)\right] . \end{aligned} \quad (3.41)$$

The study of concavity of (3.41) can be done in the $(q_1, q_2)$ space, taking also into consideration the regions of non admissibility in which the entropy is neither concave nor convex.

We clearly note that when $W = 3$ (see Figure 3.8b), the black region is reduced compared to the $W = 2$ case (Figure 3.8a). This result tends to suggest that the black region tends to disappear at $W \to \infty$, while the pink (convex) region predominates.

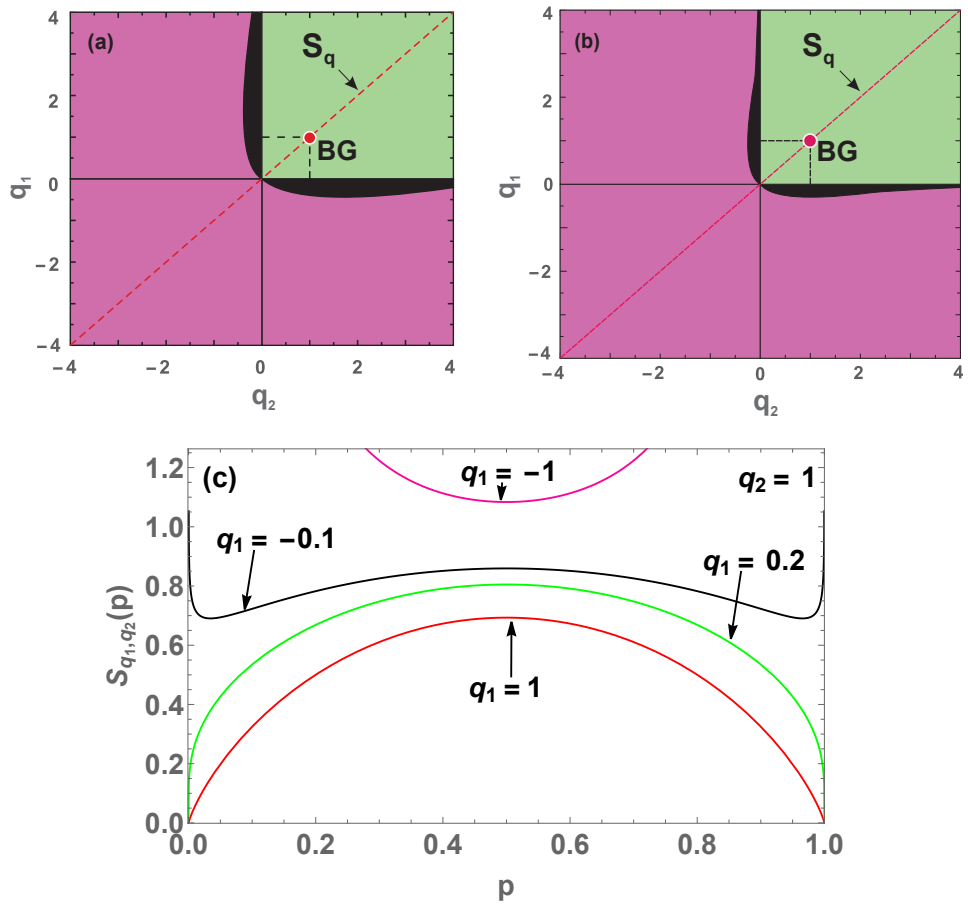


Figure 3.8: Concavity/convexity mapping for (3.41) with $(c_1, c_2) = (0.48, 0.52)$, $W = 2$ (**a**) and $W = 3$ (**b**). The green (pink) region represents all points whose entropy (3.41) is concave (convex). The black region represents all points whose entropy is neither concave nor convex, having two local minima points and a local maximum in between (a global maximum point at $p = 0.5$ and divergences at $p = 0$ and $p = 1$). On the red point is localized the Boltzmann–Gibbs entropy and over the red dashed line cutting the origin, we have all the $S_q$ entropies. On the concave (convex) region we have $S_q$, $q > 0$ ($q < 0$). (**c**) Four ($W = 2$) entropies with $q_2 = 1$, and $q_1 = 1$ (blue curve), $q_1 = 0.2$ (green curve), $q_1 = -0.1$ (black curve) and $q_1 = -1$ (pink curve).

## 3.4 Other Departures—Two-Indices Entropies

We focus here on other type of departures from pure $q$-exponentials, originated now from two-indices nonadditive entropies which recover $S_q$ as particular instances.

### 3.4.1 $S_{q,\delta}$

From [56], we have

$$S_{q,\delta} \equiv \sum_{i=1}^{W} p_i \left[\ln_q \frac{1}{p_i}\right]^{\delta} \quad (q \in \mathbb{R};\ \delta > 0)\,. \tag{3.42}$$

We verify that $S_{q,1} = S_q$. Extremization of $S_{q,\delta}$ under usual constraints yields

$$E(p_j) = -\frac{\alpha_1}{\alpha_2} + \frac{1}{\alpha_2}\left\{\left[\ln_q \frac{1}{p_j}\right]^{\delta} - \delta\left(\frac{1}{p_j}\right)^{1-q}\left[\ln_q \frac{1}{p_j}\right]^{\delta-1}\right\}. \tag{3.43}$$

Through (3.29), we have

$$X_j = \left\{\left[\ln_q \frac{1}{p_j}\right]^{\delta} - \delta\left(\frac{1}{p_j}\right)^{1-q}\left[\ln_q \frac{1}{p_j}\right]^{\delta-1}\right\}. \tag{3.44}$$

Taking into account the transformation $q \to 2 - q$ mentioned below Equation (3.40), the cutoff occurs for $q > 1$, and $X_c(q, \delta)$ is given by (see Fig. 3.9)

$$X_c(q, \delta) = (q-1)^{-\delta} \quad (q > 1). \tag{3.45}$$

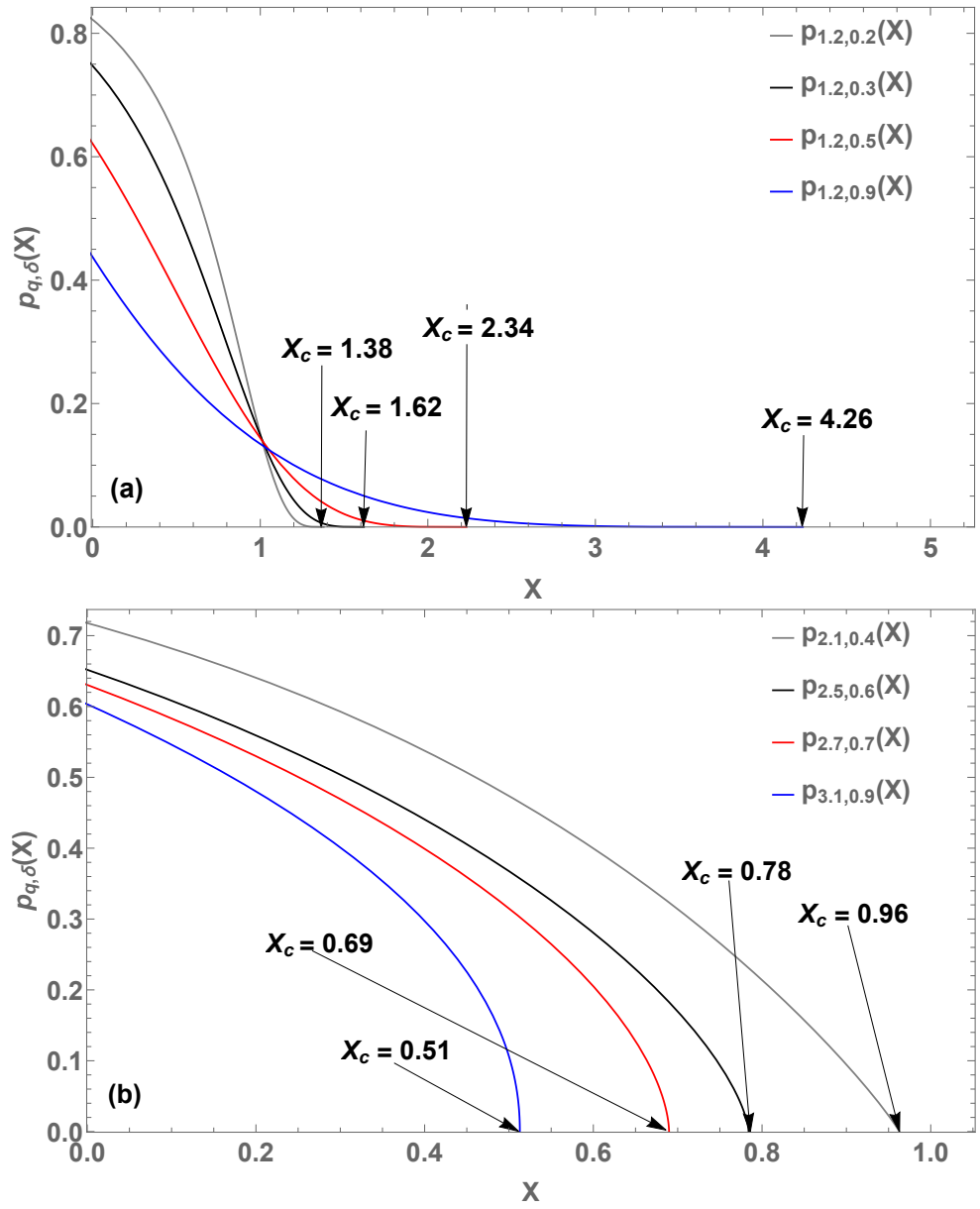


Figure 3.9: Illustrative probability distributions $p_{q,\delta}(X)$. (**a**) $q = 1.2$ and $\delta = 0.2$ hence, through (3.45), $X_c = 1.38$ (gray curve); $\delta = 0.3$, hence $X_c = 1.62$ (black curve); $\delta = 0.5$ hence $X_c = 2.34$ (red curve) and finally, $\delta = 0.9$ hence $X_c = 4.26$ (blue curve); (**b**) $(q, \delta) = (3.1, 0.9)$ hence $X_c = 0.51$ (blue curve); $(q, \delta) = (2.7, 0.7)$ hence $X_c = 0.69$ (red curve); $(q, \delta) = (2.5, 0.6)$ hence $X_c = 0.78$ (black curve); and $(q, \delta) = (2.1, 0.4)$ hence $X_c = 0.96$ (gray curve).

We verify that $p_{q,\delta}(X)$ is single-valued for $q \geq \delta$ and multi-valued otherwise.

Let us now consider the case $p_1 \equiv p_2 \equiv \cdots \equiv p_{(W-1)} \equiv p$ and $p_W = 1 - (W-1)p$ hence

$$S_{q,\delta}(p) = (W-1)p \left[\ln_q \left(\frac{1}{p}\right)\right]^\delta + (1-(W-1)p) \left[\ln_q \left(\frac{1}{1-(W-1)p}\right)\right]^\delta , \qquad (3.46)$$

where $p \in \left[0, \frac{1}{W-1}\right]$. This expression will help us to study the concavity/convexity of the

entropy for increasing values of $W$. See Figures 3.10 and 3.11.

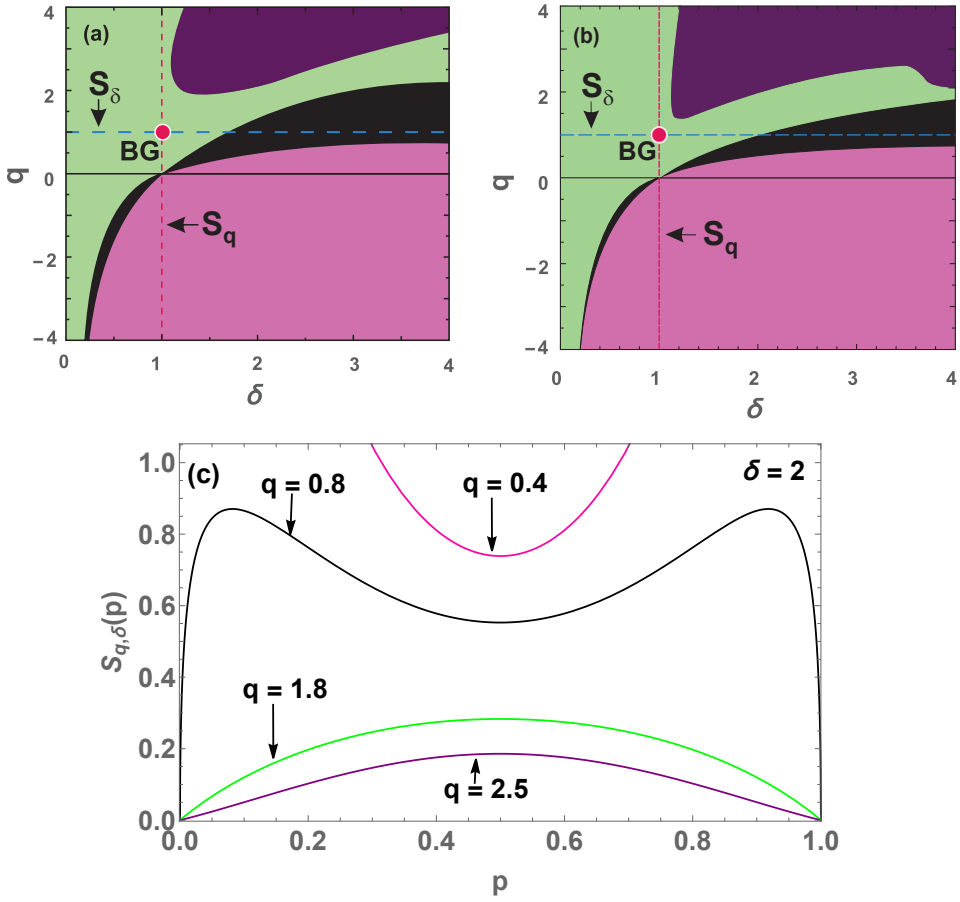


Figure 3.10: Concavity/convexity regions for $S_{q,\delta}$ (3.46) (**a**) $W = 2$. (**b**) $W = 3$. The green (pink) region represents all points whose entropy (3.41) is concave (convex). The black region represents all points whose entropy is neither concave nor convex, having two local maxima ( inflexion) points and another local minimum (maximum) in between. The points of transition at $\delta = 2$ are: $q_c = 1/2$ (both $W = 2$ and $W = 3$) (pink $\leftrightarrow$ black); $q_c = 4/3$ ($W = 2$) and $q_c \sim 0.98$ ($W = 3$) (black $\leftrightarrow$ green) and $q_c = 2$ (both cases) (black $\leftrightarrow$ purple). At $q = 1$, we have the transition from non concave to concave at $\delta_c = 1 + \ln 2$ ($W = 2$) and for $W = 3$, we have $\delta_c < 1 + \ln 3$. The blue dashed horizontal line represents $S_\delta$, while the red dashed vertical line represents all $S_q$ entropies, and the red point is the BG entropy. (**c**) Four cases ($W = 2$) for $\delta = 2$ with the respective colors: $q = 0.4$ and $q = 1.8$ (convex and concave regions respectively); $q = 0.8$ (black region) and $q = 2.5$ (purple region) (non concave and non convex regions).

The black region is clearly reduced for $W = 3$ (see Figure 3.10b), but the purple region at, for example, $\delta = 3.8$ and $q = 2.15$, invades the concave region. It is not excluded that the purple region gradually expands with $W$ in such way that it approaches the black region.

We noticed that an inadvertence occurred in [56]. Indeed, it was therein indicated that, for all entropies $S_\delta$, it would be $\delta_c(W) = 1 + \ln W$, but this is not exactly so in some cases. As we verify in what follows, we always have $\delta_c \in (\ln W, 1 + \ln W]$. Therefore,

the formula in [56] constitutes an upper bound of $\delta_c$.

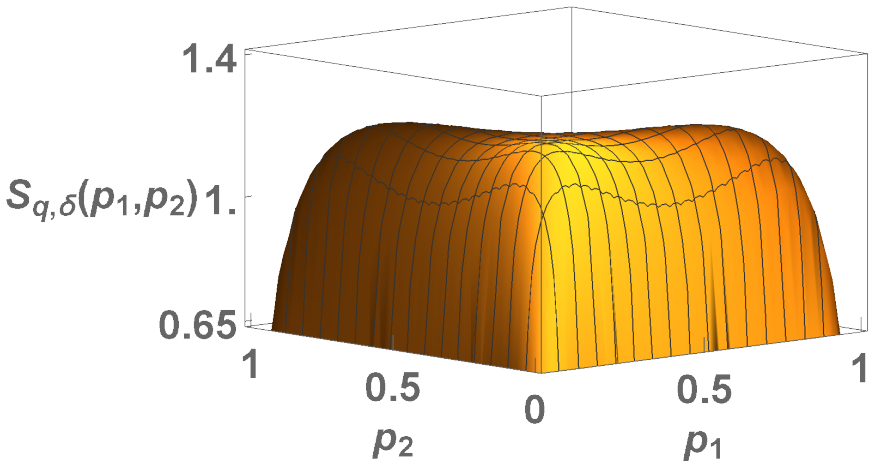


Figure 3.11: Plot for $S_{q,\delta}$ with $W = 3$, $q = 1$ and $\delta = 1 + \ln 3$. We clearly observe that $\delta_c = 1 + \ln W$ is not valid here, because in this value, the entropy is not concave, much less the values close to this.

The probability is limited by $p \geq \frac{1}{W-1}$. Numerically, we analyze the plot $1/\ln W \times \delta_c - \ln W$. If it was $\delta_c = 1 + \ln W$ for all entropies $S_\delta$, we should obtain $\delta_c - \ln W = 1$ for all values of $W$, which is not the case.

The interpretation of $\delta_c$ is given by the transition green $\leftrightarrow$ black; no transition black $\leftrightarrow$ pink appears to exist.

We notice in Figures 3.10, 3.12, and 3.13 that the divergence of $\delta_c$ in the limit $W \to \infty$ means that $S_\delta$ is concave in the thermodynamic limit for any positive $\delta$.

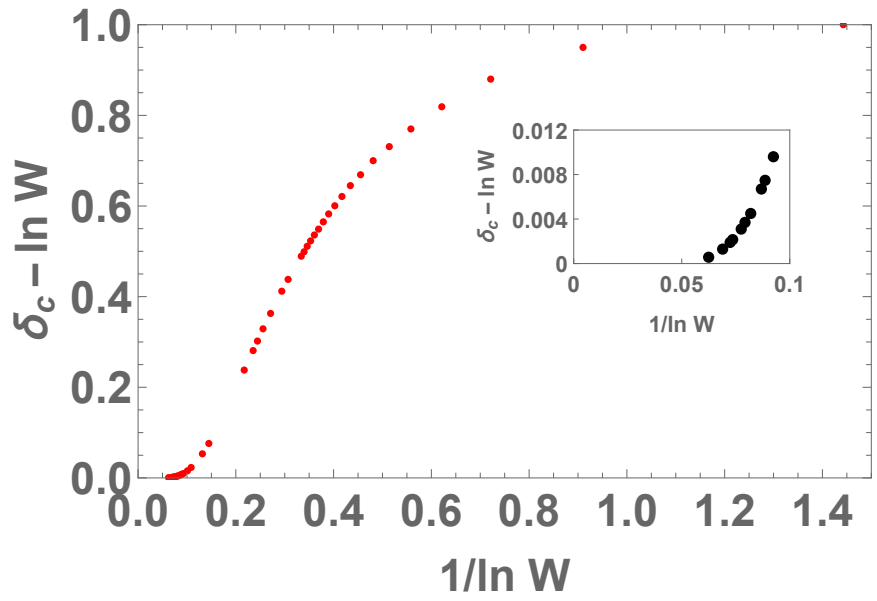


Figure 3.12: Plot for $1/\ln W \times \delta_c - \ln W$ with $W_{max} = 9 \times 10^6$. Here, $\delta_c \in (\ln W, 1 + \ln W]$. In the inset, we indicate the behavior of that function closer to origin.

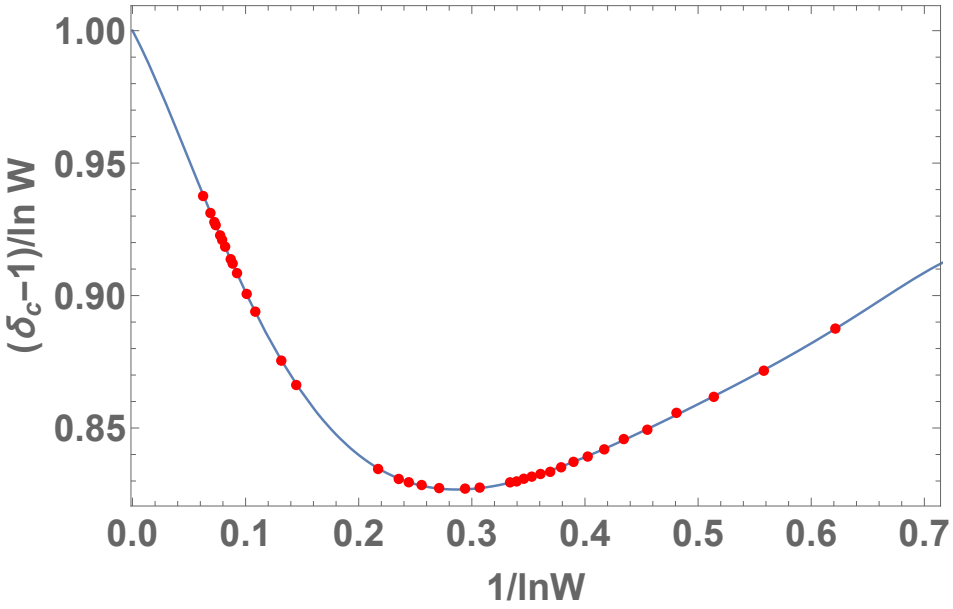


Figure 3.13: Plot for $1/\ln W \times (\delta_c - 1)/\ln W$ with $W_{max} = 9 \times 10^6$. The regression by excluding the $W = 2$ and $W = 3$ points yields an 8th degree polynomial of $x \equiv 1/\ln W$, namely $f(x) \approx 1 - 0.794252x - 6.20252x^2 + 60.9556x^3 - 223.39x^4 + 466.1x^5 - 588.297x^6 + 420.626x^7 - 130.677x^8$. It means that, when $W \to \infty$ we have $x \to 0$, thus $\lim_{x\to 0} f(x) = 1$, therefore $\delta_c \sim 1 + \ln W$ which diverges at infinity .

### 3.4.2 Borges–Roditi Entropy $S^{BR}_{q,q'}$

Borges and Roditi [82] extended the entropy $S_q$ as follows:

$$S^{BR}_{q,q'} = \frac{\sum_{i=1}^{W} p_i^q - \sum_{i=1}^{W} p_i^{q'}}{q' - q}\,, \quad ((q, q') \in \mathbb{R}^2)\,, \tag{3.47}$$

with $S^{BR}_{q,1} = S^{BR}_{1,q} = S_q$, where $BR$ stands for Borges–Roditi; notice that $S^{BR}_{q,q'} = S^{BR}_{q',q}$ .

Extremization with usual constraints, and using (3.29), we have:

$$X_j = \frac{1}{q' - q}\left(q p_j^{q-1} - q' p_j^{q'-1}\right). \tag{3.48}$$

For $q, q' < 1$, $p$ monotonically decreases to zero when $X$ increases to infinity. For $q, q' > 1$, $p$ is multivalued, hence physically inadmissible. For $q < 1$, $q' > 1$ (hence, for $q > 1, q' < 1$ ), $p$ is single-valued and exhibits a cutoff at $X_c$. See Figure 3.14 for typical examples.

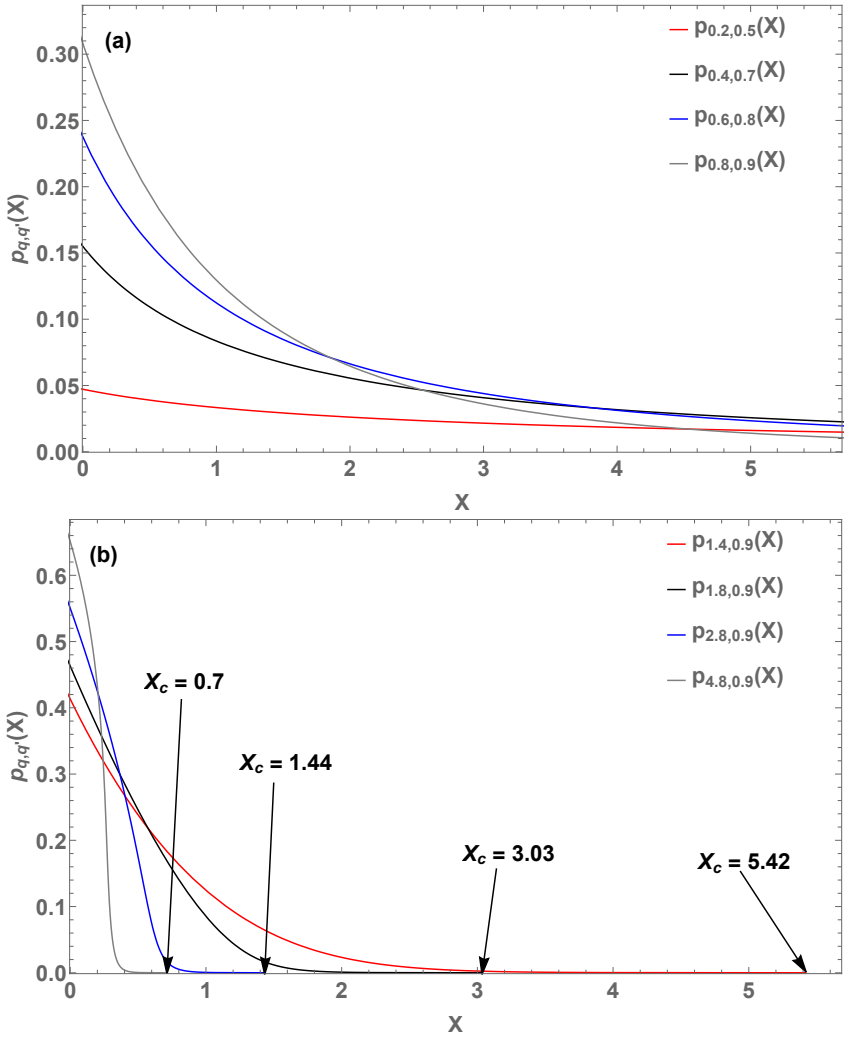


Figure 3.14: Eight illustrative Borges–Roditi probability distributions. (**a**) $(q, q') = (0.2, 0.5)$ (red curve); $(q, q') = (0.4, 0.7)$ (black curve); $(q, q') = (0.6, 0.8)$ (blue curve), and $(q, q') = (0.8, 0.9)$ (gray curve). (**b**) $(q, q', X_c) = (1.4, 0.9, 5.42)$ (red curve), $(q, q', X_c) = (1.8, 0.9, 3.03)$ (black curve), $(q, q', X_c) = (2.8, 0.9, 1.44)$ (blue curve), and $(q, q', X_c) = (4.8, 0.9, 0.7)$ (gray curve).

Let us focus now on the concavity of $S_{q,q'}^{BR}$. By considering the same case that led to Equation (3.46), we obtain here

$$S_{q,q'}(p) = \frac{1}{q'-q}\left[(W-1)p^q + (1-(W-1)p)^q - (W-1)p^{q'} - (1-(W-1)p)^{q'}\right]. \tag{3.49}$$

The purple region undergoes a slight change whether we compare the Figures 3.15a ($W = 2$) and Figures 3.15b ($W = 3$), although it appears that the rectangular purple region at $W = 3$ does not increase for $W > 3$. Indeed, if it did that, it would affect the BG and $S_q$ entropies whose convexity/concavity are known. With respect to the black region, the fact of that region shrinks from $W = 2$ to $W = 3$ suggests that it possibly disappears in $W \to \infty$.

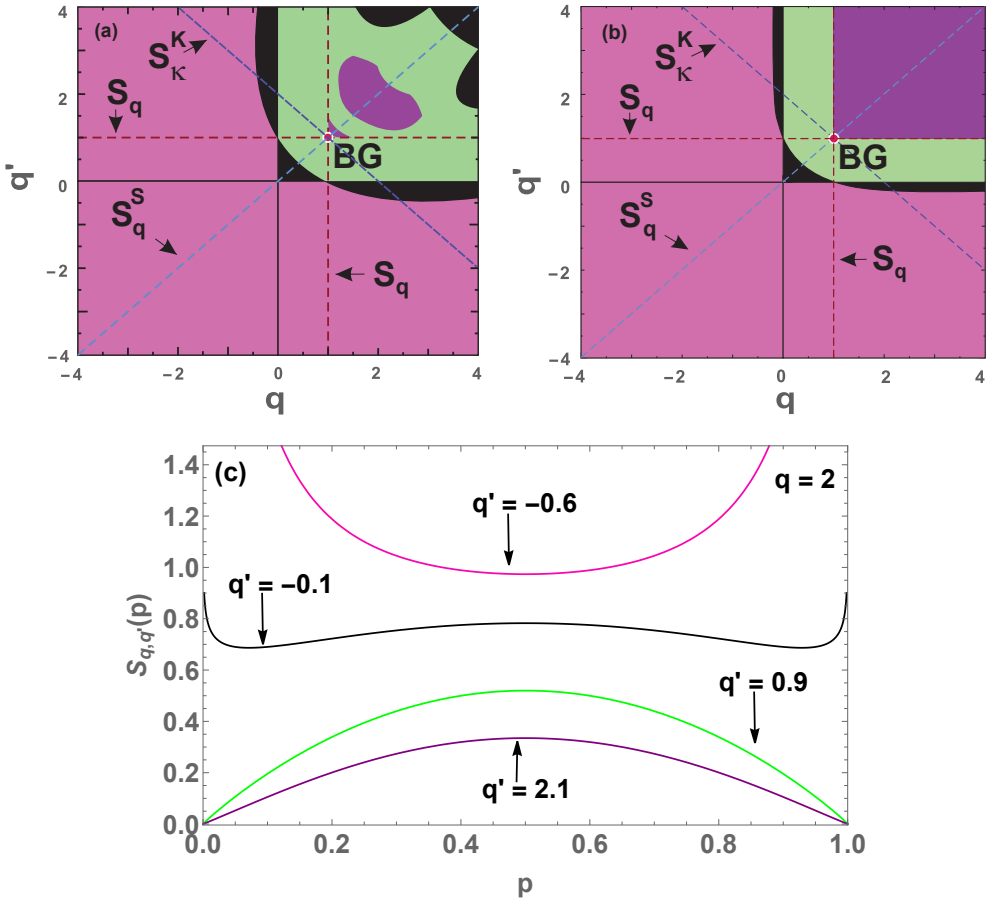


Figure 3.15: Concavity/convexity for $S^{BR}_{q,q'}$ (3.49) with (**a**) $W = 2$ and (**b**) $W = 3$. The green (pink) region represents all points whose entropy (3.49) is concave (convex). The black (purple) region represents all points whose entropy is neither concave nor convex, having two local maxima (inflexion) points and another local minimum (maximum) in between. The red dashed vertical lines represent all $S_q$ entropies and the red point is the BG entropy, while the light (dark) blue lines represents all Shafee $S^S_q$ (Kaniadakis $S^K_\kappa$) entropies [96, 97]. (**c**) Four illustrative cases ($W = 2$) with $q = 2$ and its respective colors: $q' = -0.6$ and $q' = 0.9$ (pink and green regions respectively ); $q = -0.1$ (black region) and $q = 2.1$ (purple region).

$S_{q,q'}$

On the basis of some algebraic properties, $S_q$ has been generalized in [83, 98, 99]:

$$S_{q,q'} = \sum_{i=1}^{W} p_i \ln_{q,q'} \frac{1}{p_i} \tag{3.50}$$

with

$$\ln_{q,q'} z \equiv \frac{1}{1-q'}\left[\exp\left(\frac{1-q'}{1-q}(z^{1-q}-1)\right)-1\right]. \tag{3.51}$$

We verify that $\ln_{q,1} = \ln_{1,q} = \ln_q$, hence $S_{q,1} = S_{1,q} = S_q$. with $S_{q,1} = S_{1,q} = S_q$. Clearly, we can reformulate (3.51) in terms of $\ln_q$ such that

$$\ln_{q,q'} z = \frac{1}{1-q'}\left[\exp\Big((1-q')\ln_q z\Big) - 1\right]. \tag{3.52}$$

The reformulated version of the extremized entropy $S_{q,q'}$ is written as

$$X_j = \exp\left((1-q')\ln_q \frac{1}{p_j}\right)\left[\frac{1}{1-q'} - \left(\frac{1}{p_j}\right)^{1-q}\right] - \frac{1}{1-q'} \tag{3.53}$$

The cutoff equation $X_c(q, q')$ is given by

$$X_c(q, q') = \frac{1}{1-q'}\left[e^{-\frac{1-q'}{1-q}} - 1\right],\ q > 1. \tag{3.54}$$

For $q > 1$ and $0 < q' < 1$, $p$ is single-valued and exhibits a cutoff at $X_c$ (see Fig. 3.16). For $q, q' < 1$, $p$ is multi-valued, hence, it is inadequate for physical purposes. For $0 < q < 1$ and $q' > 1$, $p$ exhibits clearly a cutoff.

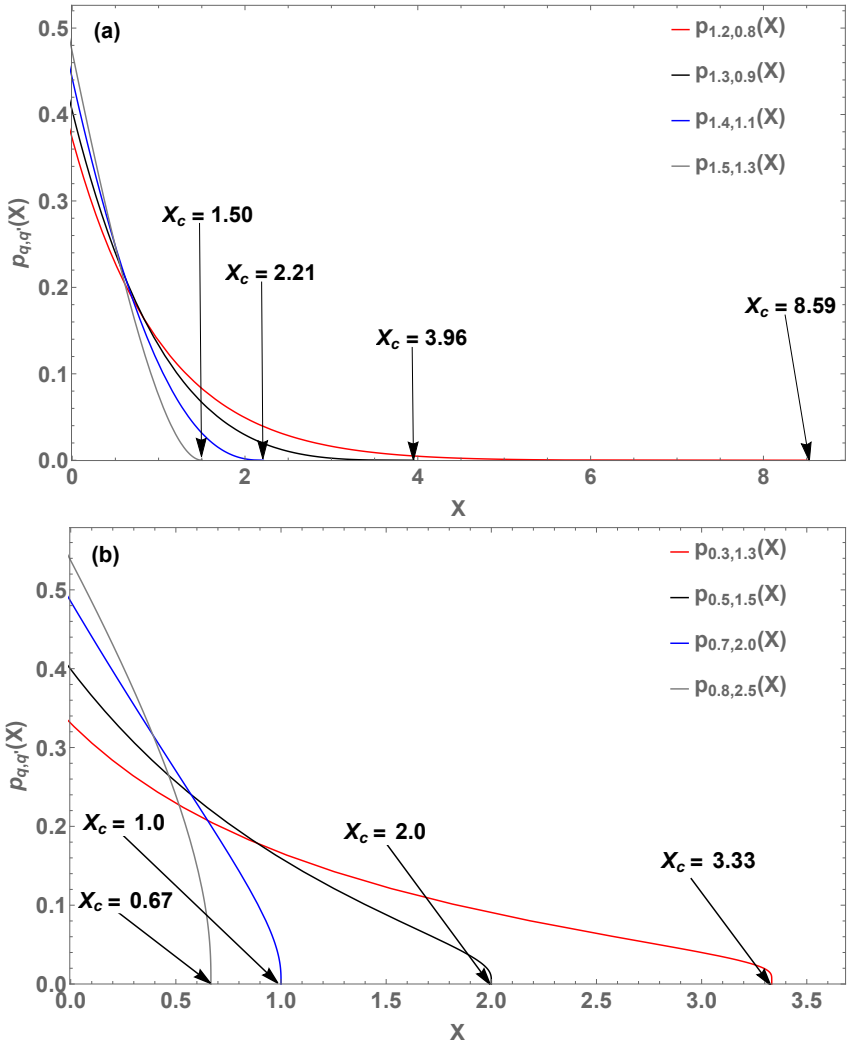


Figure 3.16: Eight illustrative probability distributions $p_{q,q'}(X)$. (**a**) $(q, q', X_c) = (1.5, 1.3, 1.5)$ (gray curve), $(q, q', X_c) = (1.4, 1.1, 2.21)$ (blue curve), $(q, q', X_c) = (1.3, 0.9, 3.96)$ (black curve), and $(q, q', X_c) = (1.2, 0.8, 8.59)$ (red curve). (**b**) $(q, q', X_c) = (0.8, 2.5, 0.67)$ (gray curve), $(q, q', X_c) = (0.7, 2.0, 1.0)$ (blue curve), $(q, q', X_c) = (0.5, 1.5, 2.06)$ (black curve), and $(q, q', X_c) = (0.3, 1.3, 3.33)$ (red curve).

Analogously to (3.46), we write the Equation (3.50) as

$$S_{q,q'}(p) = (W-1)p \ln_{q,q'}\left(\frac{1}{p}\right) + (1-(W-1)p)\ln_{q,q'}\left(\frac{1}{1-(W-1)p}\right). \tag{3.55}$$

In Figures 3.17a,b, we observe that the purple region appears to remain the same for all $W \geq 2$. In contrast, the black region for $W = 3$ is slightly smaller than that for $W = 2$, which suggests that, in $W \to \infty$, such a region might disappear. We checked for large values of $W$, and this scenario is confirmed. This happens in two different ways: the black region close to the BG point gradually disappears, being replaced by the pink (convex) region, and the black region in the negative part of $q'$ also disappears, being replaced by the green (concave) region.

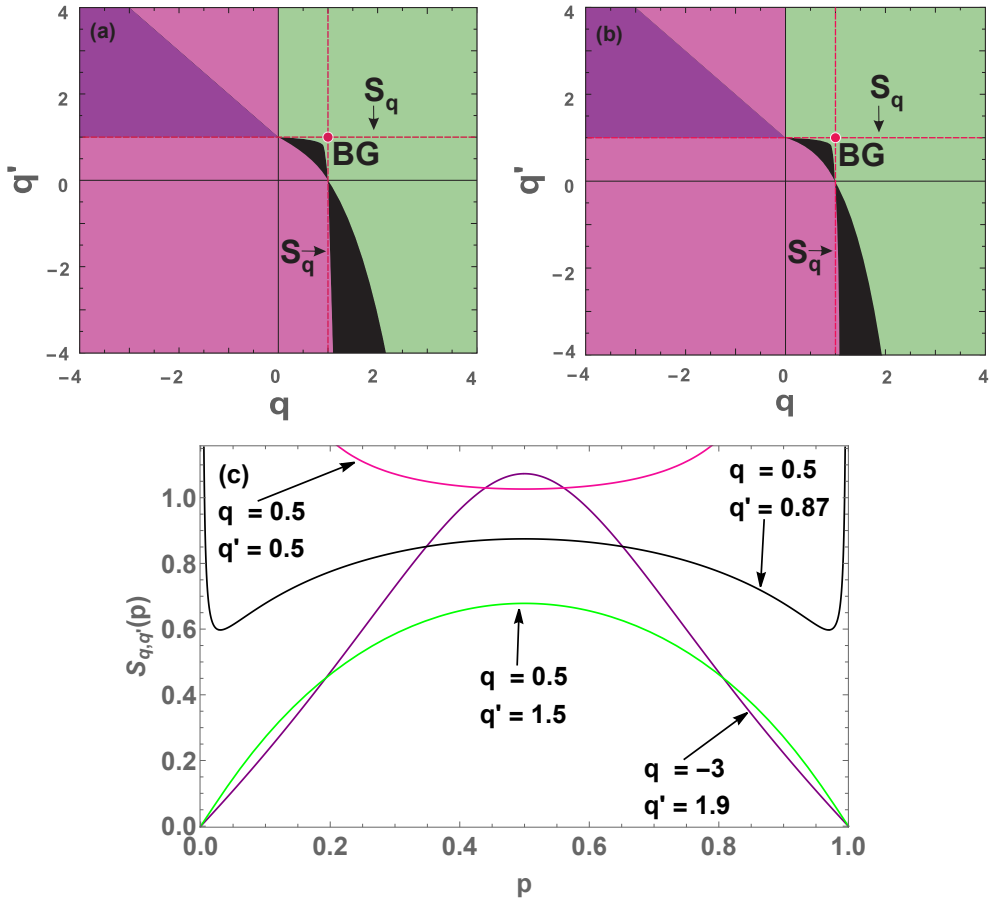


Figure 3.17: Concavity/convexity for $S_{q,q'}$ (3.55) with (**a**) $W = 2$ and (**b**) $W = 3$. The green (pink) region represents all points whose entropy (3.55) is concave (convex). The black (purple) region represents all points whose entropy is neither concave nor convex, having two local maxima (inflexion) points and another local minimum (maximum) in between. The red dashed vertical line represents all $S_q$ entropies and the red point is the BG entropy. (**c**) Four cases ($W = 2$) with the respective colors: with $q = 0.5$, $q' = 0.5$ and $q' = 1.5$ (pink and green regions) and $q' = 0.87$ (black region), and $(q', q) = (1.9, -3)$ (purple region).

In summary, we have explored here various mathematical properties related to extensions of $q$-exponentials and $q$-entropies, including some double-index nonadditive entropies.

In the case of crossover statistics (Equation (3.7)), there are multiple changes in the slopes of the corresponding log-log plots. The values of the abscissa at which the relevant quantities make crossovers between two successive regimes are characterized by $x_c$, analytically calculated in all cases, as illustrated in Figures 3.1 and 3.2.

When we consider linear combinations of normalized $q$-exponentials, we may focus on the influence of the $q_k$'s and of the $\beta_k$'s in Equation (3.18). For a single value of $\beta_k$ and various values for the $q_k$'s, the result might be close to one of the $q$-exponentials, whereas if we adopt a single value of $q_k$ and various values for the $\beta_k$'s, the outcome might be sensibly different from all the $q$-exponentials, as illustrated in Figures 3.3–3.5.

With respect to the linear combination of $q$-entropies, it is generically impossible to

have the probability distribution $p_j$ in Equation (3.30) as an explicit function of $X_j$. Notice, however, that we do have $X_j$ as an explicit function of $p_j$. This is in contrast with the case where we have linear combinations of the normalized $q$-exponentials. The final results for these two types of linear combinations clearly differ, as first shown in [91]. Let us emphasize that, consistently, the operations of linearly combining and entropic extremization do not commute.

In addition to that, for the linear combination of two nonadditive entropies (case $M = 2$), as well as for the three double-index nonadditive entropies (namely, $S_{q,\delta}$, $S^{BR}_{q,q'}$ and $S_{q,q'}$), we have studied their convexity/concavity in the indices-space. The results depend naturally on the total number of states ($W$). The limit $W \to \infty$ is particularly interesting, since it corresponds to the thermodynamical limit. We verify that, in the case of a linear combination of two $q$-entropies ($M = 2$), the concave region remains one and the same for all values of $W$. Indeed, the value of $W$ only affects the size of the convex region, as illustrated in Figure 3.8. It seems plausible that, in the $W \to \infty$ limit, the only possibilities which remain are either concave or convex. In what concerns $S_{q,\delta}$, $S^{BR}_{q,q'}$ and $S_{q,q'}$, regions in the indices-space exist, for a given value of $W$, where the entropy is concave, or convex, or none of them, as illustrated in Figures 3.10, 3.15, and 3.17. For all these three entropies, the region which is neither concave nor convex does not disappear even for $W \to \infty$. In particular, we have studied in detail the case of $S_\delta$ ($q = 1$ and $\delta > 0$), and have obtained that convexity never emerges, $\forall\delta$, $\forall W$. A critical value $\delta_c(W)$ exists such that $S_\delta$ is concave for $\delta < \delta_c(W)$ and neither concave nor convex for $\delta > \delta_c(W)$; moreover, in the $W \to \infty$ limit, we verify that $\delta_c(W) \sim \ln W$. The results displayed in the present paper could hopefully guide the use of entropies differing from $S_q$ for large classes of natural, artificial and social complex systems.

# First-principle validation of Fourier's law on n-vector models

# Chapter 4

# Aspects of nonequilibrium statistical mechanics

## 4.1 Discussion about the connection between stationary state and equilibrium state

A system that is out of equilibrium, in some cases, tends to achieve an equilibrium state after long periods of time. However, not all systems out of equilibrium reach this particular state. There are systems that are always in nonequilibrium, and all variables that describe these systems depend on time at any instant. There are also systems where all variables do not depend on time after a long transient period, and this remains true throughout their evolution. This state is called a stationary state and is primarily known as a situation in which the probability density does not depend on time, having no relation to the principle of maximum entropy. Conversely, some stationary states are identified as regions where the entropy reaches its maximum. In such cases, the system is sufficiently large, and there is no net macroscopic flow of matter and energy within this system (isolated ). When it occurs, the equilibrium state is identical to the stationary one[1]. According to D. Ruelle [100]:

> (a') Equilibrium states are operationally definable. The state of an **isolated** system tends to an equilibrium state as time tends to $+\infty$("approach to equilibrium").
>
> (b') An equilibrium state of a system consists of one or more macroscopically homogeneous regions (called phases).

[1]It does not mean that Boltzmann-Gibbs statistics is the correct one. For standard statistics to hold, it is necessary that all points of the system visit all accessible regions in phase space over a long period of time. In other words, the system must be ergodic in the mean. However, some authors claim that a weak form of ergodicity is sufficient, called $\epsilon$-ergodicity [101].

(c') Equilibrium states can be described by thermodynamics, in particular they can be parameterized by a finite number of thermodynamic parameters which determine all thermodynamic functions.

From those starting points, we investigate some mathematical constructions of nonequilibrium statistical mechanics and their relations with equilibrium.

### 4.1.1 Description of the dynamics of a classical system

In classical mechanics, the Hamiltonian of a conservative system in Cartesian coordinates may be written as

$$\mathcal{H} = \sum_{i=1}^{d} \frac{p_i^2}{2m_i} + \frac{1}{2} \sum_{\substack{i,j \\ i \neq j}} V(|\mathbf{q}_i - \mathbf{q}_j|) \tag{4.1}$$

where $m_i, \mathbf{p}_i, \mathbf{q}_i$ are the mass, momentum, and coordinate of the particle $i$, respectively. The right-hand side of the Hamiltonian represents the potential. By the Hamilton's equation, namely $\dot{\mathbf{q}}_i = \frac{\partial \mathcal{H}}{\partial \mathbf{p}_i}$ and $\dot{\mathbf{p}}_i = -\frac{\partial \mathcal{H}}{\partial \mathbf{q}_i}$, we have

$$\begin{aligned} \dot{\mathbf{q}}_i &= \frac{\mathbf{p}_i}{m} \\ \dot{\mathbf{p}}_i &= -\nabla_i V(\mathbf{q}_1, \mathbf{q}_2, \ldots, \mathbf{q}_N)\,. \end{aligned} \tag{4.2}$$

At any instant of time, we obtain the position and momentum of each particle $i$, by Eqs. (4.2). The system evolves in time and preserves the volume of the phase space, starting from the previous assumption that the system is *conservative*. The probability density of such system evolves in such way that

$$\frac{\partial \rho}{\partial t} = -i\mathcal{L}\rho \tag{4.3}$$

where $i\mathcal{L}\,. = \{\mathcal{H}, .\}$.The Eq. (4.3) represents the mathematical formulation of the Liouville's theorem, which states that the volume of the phase space is conserved during its evolution. No probability density is known *a priori*. For instance, in linear response theory, we start from Liouville equation to derive the average of certain function $O(t)$ under some perturbation in the Hamiltonian $-X(t)A$ as follows:

$$\delta \langle O(t) \rangle = \int_{-\infty}^{t} d\tau\, X(\tau) \chi_{OA}(\tau - t) \tag{4.4}$$

$$\chi(t)_{AO} = \theta(t) \langle \{O(t), A\} \rangle_{eq}\ , \tag{4.5}$$

where $\theta(t)$ is the Heaviside function[2]. Now, by considering $\rho_{eq} = \frac{e^{-\beta \mathcal{H}}}{Z}$ the Boltzmann

[2]It is introduced by causality. It is also a good manner to easily obtain its Fourier-Laplace transform.

weight, we obtain

$$\chi(t)_{AO} = \theta(t)\beta \left\langle O(t), \dot{A} \right\rangle_{eq} . \tag{4.6}$$

which is an elegant description of the response function, although certain assumptions were made to derive this expression. The issue with Eq.(4.6) pertains to the assumption of equilibrium. However, this expression cannot be applied indiscriminately. Using this expression in systems that are not in equilibrium can yield incorrect results. A common approach to simplify such averages is by substituting the "equilibrium response" function with a response function in a stationary state, defined as

$$\chi(t)_{AO} = \theta(t) \left\langle \{O(t), A\} \right\rangle_{st} , \tag{4.7}$$

where the subscript "st" denotes the stationary state.

The standard statistical mechanics plays an important role in describing the thermal properties of a system towards equilibrium. It is an awesome theory that simplifies almost all dynamics of a system and is capable of obtaining static response functions, such as magnetic susceptibility and thermal susceptibility, by solving the partition function of the problem. However, this theory must be used only when the stationary state is equivalent to the equilibrium state, and long-ranged interactions are negligible. For this reason, we need to take care with some assumptions and also verify if certain hypotheses are consistent with the true dynamics of the system. On the derivation of such formulas, assuming Boltzmann weight, R. Kubo et al.[102] wrote (page 151)

> Since we are interested in **near-equilibrium** states driven by external forces, we may assume that the external perturbation started to work in the infinite past, i.e., $t_0 \to -\infty$, when the system was in **equilibrium** at a certain temperature.[...]

So, it is evident that it is assumed that the probability distribution *a priori* as a canonical distribution, and the system is towards equilibrium. Also referring to equilibrium distributions, some criticism is taken about that. For instance, A. Einstein [59] argues in favor of the dynamics when he wrote

> Usually W is set equal to the number of ways (complexions) in which a state, which is incompletely defined in the sense of a **molecular theory** (i.e., coarse grained), can be realized. To compute W one needs a complete theory (something like a complete **molecular-mechanical theory**) of the system. For that reason it appears to be doubtful whether Boltzmann's principle alone, i.e., without a **complete molecular-mechanical theory** (Elementary theory) has any real meaning. The equation $S = k \log W + const.$ appears [therefore],

without an **Elementary theory**—or whatsoever one wants to call it—devoid of any meaning from a phenomenological point of view.

From first principles, it is important to consider that the dynamics of a system dictate the probabilities of its states. When an external perturbation is turned on, the distribution of probabilities may no longer be an equilibrium distribution at the initial time, but rather a more general one [36, 103].

From now on, we will provide some examples of formalisms from first-principles in which the stationary probability distribution corresponds to an equilibrium one.

### 4.1.2 Langevin dynamics

For a single particle randomly moving in a one-dimensional medium, the Langevin equation is defined as

$$m\dot{v} = -\gamma m v + f(x) + \sqrt{2A}\,\eta(t) \tag{4.8}$$

where $\gamma, v, f(x)$ and $\eta$ are the friction coefficient, velocity , deterministic force, and $\sqrt{2A}\,\eta$ the random force of the particle, respectively. $\eta$ is particularly chosen as a Gaussian white noise with zero mean value and $\langle \eta(t)\eta(t')\rangle = \delta(t-t')$. The force, in principle, depend only on the spatial coordinate $x$. In phase space coordinates, we have

$$\begin{aligned} \dot{x} &= \frac{p}{m} \\ \dot{p} &= -\gamma p + f(x) + \sqrt{2A}\,\eta\,. \end{aligned} \tag{4.9}$$

By considering $f(x) = 0$ and $p(0) = 0$, we obtain

$$\overline{p^2(t)} = \frac{A}{\gamma}\left(1 - e^{-2\gamma\, t}\right)\,. \tag{4.10}$$

Taking the average $\left\langle p^2 \right\rangle \equiv \lim_{t\to\infty} \overline{p^2(t)}$ in Eq. (4.10), and by considering the equipartition theorem, $\left\langle \frac{p^2}{2m} \right\rangle = \frac{1}{2} k_B T$, it yields $A = m\gamma k_B T$ [3].

#### From Langevin to Klein-Kramers and Fokker-Planck equations

From the Langevin equation it is possible to derive the partial equation which describes the probability distribution on phase space $\rho(x, p, t)$ which is given by

$$\frac{\partial \rho}{\partial t} = -\frac{p}{m}\frac{\partial \rho}{\partial x} - \frac{\partial[(f - \gamma p)\rho]}{\partial p} + m\gamma k_B T \frac{\partial^2 \rho}{\partial p^2}\,. \tag{4.11}$$

[3]The constant $A$ has unit of momentum squared over time. Indeed, $\sqrt{2A}\,\eta$ has no unit of force, but it preserves the units after the integration procedure. The integration is carried out by assuming $d\eta = \sqrt{dt}\,\mathcal{N}(0,1)$, where $\mathcal{N}(0,1)$ is a Gaussian white noise with zero mean and unit variance, so $\sqrt{2A}\,d\eta$ has units of momentum.

It is called Klein-Kramers equation.

Considering $m \ll 1$, we have

$$\dot{x} = \frac{f(x)}{\gamma m} + \sqrt{\frac{2k_B T}{m\gamma}}\eta(t)\,, \tag{4.12}$$

and the associated partial differential equation for $\rho(x,t)$, is given by:

$$\frac{\partial \rho}{\partial t} = -\frac{1}{\gamma m}\frac{\partial (f\rho)}{\partial x} + \frac{k_B T}{\gamma m}\frac{\partial^2 \rho}{\partial x^2}\,, \tag{4.13}$$

where $\frac{k_B T}{m\gamma}$ corresponds to the diffusion coefficient[4]. This equation is called Fokker-Planck equation[5].

**Connection with Boltzmann-Gibbs distribution**

In the stationary state, we have for a conservative force, with confined potential, the following result for the stationary distribution $\rho_{st}(x)$ for the Fokker-Planck equation:

$$\rho_{st}(x) \propto e^{-V(x)/k_B T}\,, \tag{4.14}$$

and surprisingly, for the Klein-Kramers equation, we have

$$\rho_{st}(x,p) \propto e^{-H(x,p)/k_B T}\,. \tag{4.15}$$

It means that the stationary state distribution of those particular systems are, indeed, Boltzmann weights[6].

We should be careful with that, because nonconfined potentials lead us to undesirable results, which does not coincide with the Boltzmann weight. Also there are some problems in which the diffusion coefficient really depends on the probability distribution, such that $D = D(\rho)$. In the particular case where $D(\rho) \equiv D_0 \rho^{1-q}$, the stationary distribution $\rho$ is given by a generalized distribution, namely $q$-exponential distribution (See the introductory Chapter 2 for details).

[4]Some authors define the diffusion coefficient as $\frac{k_B T}{\gamma}$, but they also assume $\gamma \to m\gamma$. The diffusion coefficient, usually named as $D$, must be units of length squared over time, which means that all definitions are correct. Out of mere curiosity, the diffusion coefficient can be obtained by a relation with the second cumulant of position, namely $D = \lim_{t\to\infty} \frac{1}{2}\frac{\overline{x(t)^2} - \left(\overline{x(t)}\right)^2}{t}$ .

[5]The derivation of the Klein-Kramers and Fokker-Planck equations are quite simple and can be found in Ref. [104].

[6]This specific condition, where the flux vanishes at the boundaries is often called reflective boundary condition.

## 4.2 Transport phenomena and some linear relations

### 4.2.1 Transport of mass

In transport of mass, the flux of concentration of some homogeneous substance is given by

$$J_N = -D\nabla n \tag{4.16}$$

where $D$ is the diffusion coefficient, and $n = \frac{m_s}{V}$, which is the concentration of certain amount of substance with mass $m_s$ in a solution volume $V$. It is the *Fick's first law* [105]. The Eq. (4.16) relates the gradient of concentration of the amount of substance to its flux of concentration. In other words, the gradient of concentration generates a flux of particles of the solute in the opposite direction, indicating that the diffusion occurs from the high to the low concentration of the material. In general, considering an ideal diffusion, the concentration rate obeys a continuity equation given as follows

$$\frac{\partial n}{\partial t} + \nabla \cdot \mathbf{J}_N = 0\,, \tag{4.17}$$

then, substituting Eq. (4.17) into Eq. (4.16), we obtain

$$\frac{\partial n}{\partial t} = D\nabla^2 n\,, \tag{4.18}$$

which is a diffusion equation for the concentration of a given solute. It is the *Fick's second law* and Eq. (4.18) is also known as diffusion equation. An interesting fact about this equation concerning to its application not only in fluids, but in solids and gases [106, 107].

### 4.2.2 Transport of momentum

Restricting to the realm of fluid mechanics, the simplest continuity for a given fluid may be written as

$$\frac{\partial \rho}{\partial t} + \nabla \cdot (\rho \mathbf{v}) = 0\,, \tag{4.19}$$

where $\rho$ is the fluid density and $\mathbf{v}$ is the fluid velocity field[7]. It is worth to notice that the flux here has no linear relation with the gradient of some field. However, when the velocity field is conservative, the flux of particles can be written as

$$\mathbf{J}_N = \rho\nabla\phi \tag{4.20}$$

where $\phi$ is the velocity potential. In Eq. (4.20), there are no assumptions about low and high potentials, and there are no implications regarding a second law as in Fick's

[7]If the fluid is incompressible, that is, the density is constant regardless of the changes in pressure it undergoes, then, from the continuity equation, we have $\nabla \cdot \mathbf{v} = 0$.

second law. It is also worth emphasizing that, despite the fact that density has a similar relation with mass and volume of a system to concentration, concentration is restricted to a certain substance in another, while density is related to the system as a whole. In summary, for fluids, a linear relation with some gradient is achieved only for conservative velocity fields, which is a very particular case and it is hard to find in nature due to the complex interactions and forces in a fluid. In fluid dynamics, the assumption of conservative velocity fields is only a theoretical construction for idealized situations. In other words, almost all fluids must be investigated assuming non-conservative velocities.

The key factor in fluid mechanics refers to the effects of stress applied to a fluid. The transport of momentum is intrinsically linked to *some property*, as it is the mechanism through which *some concept* emerges and operates within a fluid. This *concept* determines the efficiency of momentum transfer within the fluid, thereby influencing the fluid's resistance to flow gradients. According to Newton's law of viscosity [108], the stress applied to fluid layers is proportional to the velocity gradient. Hence, this crucial relationship can be expressed as

$$\tau_{\alpha\beta} = \mu \frac{\partial v_\alpha}{\partial x_\beta}\,, \tag{4.21}$$

which $\tau_{\alpha\beta}$ are components of the shear stress tensor (in units of force per unit area). For this relation there is no continuity equation. The *concept* and *property* which we are referring, namely $\mu$ is called viscosity[8]. In principle, we need to find the solution for the velocity field and then, find the shear stress, but the equation which describes a incompressible fluid, namely Navier-Stokes equations [109], is extremely hard to solve and almost in all cases, needs to be solved numerically. The Newton's law for viscosity exhibits a linear relation between a stress tensor and the velocity field, but it remains linear only for viscosities not dependent on the same velocity field. When this relation is maintained, the fluid which obeys this relation is called Newtonian, otherwise, it is called non-Newtonian fluid. Examples of Newtonian fluids are: water, mineral oil, and milk and for non-Newtonian fluids, we have animal blood, ketchup, toothpaste, and so forth. There are subtypes of Newtonian and non-Newtonian, but it is out of the scope of this thesis.

### 4.2.3 Transport of heat

In transport of heat, a difference of temperature between two different reservoirs generates a heat flux, which is the rate of energy per unit area (energy per time per unit area). The heat transfer occurs from the hot to cold reservoir, thus, this empirical law can be given by

$$\mathbf{J} = -\kappa \nabla T \tag{4.22}$$

[8]Just for clarification, in anisotropic fluids, the viscosity is not a constant, but a tensor of rank 4, thus yielding the following relation for the shear stress tensor: $\tau_{\alpha\beta} = \mu_{\alpha\beta\gamma\delta}\frac{\partial v_\gamma}{\partial x_\delta}$.

where $\kappa$ is the thermal conductivity, which is related with the amount of heat that certain system conduct. The minus sign in Eq. (4.22) arises from the second law of thermodynamics, more specifically, from the Clausius statement, which says that *heat can never pass from a colder to a warmer body without some other change, connected therewith, occurring at the same time.* The Eq. (4.22) is known as Fourier's law of conduction [1]. The continuity equation for ideal heat conduction is given by

$$\frac{\partial u}{\partial t} + \nabla \cdot \mathbf{J} = 0 \tag{4.23}$$

where $u$ is the energy of the system per unit volume, considering a three-dimensional system. It is worth be mentioned that in one and two-dimensional systems, the flux is not defined with the same units of the three-dimensional case. The problem is only the definition of area. The area here is the transversal section of the volume where the flux trespass. In one and two-dimensional systems, the area is the unit of the atoms (area as unit) and transversal length. Therefore, the heat flux is energy per unit time per unit $[Length]^{d-1}$ for a $d$-dimensional system.

Let us notice that Eq. (4.22) holds linear if and only if the thermal conductivity depends on intensive variables, as temperature and pressure. When it happens, we say that the Fourier's law is obeyed, and such system presents normal heat conduction. Otherwise, the system presents anomalous heat conduction. For instance, when the thermal conductivity depends on thermal gradient.

### 4.2.4 Transport of charges

The flux of charges taking account magnetic effects is given by

$$\mathbf{J}_q = \sigma(\mathbf{E} + \mathbf{v} \times \mathbf{B})\,. \tag{4.24}$$

In the absence of magnetic field, Eq. (4.25) becomes

$$\mathbf{J}_q = \sigma \mathbf{E}\,. \tag{4.25}$$

By using Maxwell equations $\nabla \cdot \mathbf{E} = \rho/\epsilon$ and $\nabla \times \mathbf{E} = \mu \mathbf{J}_q + \epsilon\mu \frac{\partial \mathbf{E}}{\partial t}$[9], we have

$$\frac{\partial \rho}{\partial t} + \nabla \cdot \mathbf{J}_q = 0\,, \tag{4.26}$$

which is the continuity equation for the Ohm's law [110]. Assuming that the electrical field is conservative, we have

$$\mathbf{J} = -\sigma \nabla \phi \tag{4.27}$$

[9]Here, we are assuming linear dielectric and magnetic materials, or, at least, materials subject to weak fields.

where $\phi$ is the electrical potential. This equation is similar in structure with the other constitutive relations and even more similar to the linear relations which have a continuity equation, such as Fick's law and Fourier's law.

In the next chapter, we will focus on discussing the connection between micro and macro heat flux. Our aim is to derive the thermal conductivity of classical inertial $n$-vector models.

# Chapter 5

# Classical inertial $n$-vector models

## 5.1 Non-inertial form

The Hamiltonian of an arbitrary, isotropic $n$-model with $n$ components of spin $S$, namely $\mathbf{S}_\ell$, is defined as

$$\mathcal{H} = -\mathcal{J}\sum_{\langle \ell\ell' \rangle} \mathbf{S}_\ell \cdot \mathbf{S}_{\ell'} = -\mathcal{J}\sum_{\langle \ell\ell' \rangle}\sum_{m=1}^{n} S_\ell^m S_{\ell'}^m;\ |\mathbf{S}_\ell|^2 = S^2\,, \tag{5.1}$$

where $\ell$ and $\langle \ell\ell' \rangle$ represent the points and the nearest-neighboring spins in a $d$-dimensional lattice. We define the distance between neighboring spins as unit, without loss of generality. The exchange coupling $\mathcal{J}$ determines whether a system exhibits ferromagnetic ($\mathcal{J} > 0$) or antiferromagnetic behavior ($\mathcal{J} < 0$). In all definitions from now on, we will set normalized spins, in such way that, $\mathbf{S}_\ell \to \dfrac{\mathbf{S}_\ell}{S}$, thus resulting in spins with unit norm ( $|\mathbf{S}_\ell|^2 = 1$ ).

Another way to represent this model is as follows,

$$\mathcal{H} = \frac{\mathcal{J}}{2d}\sum_{\langle \ell\ell' \rangle}[1 - \mathbf{S}_\ell \cdot \mathbf{S}_{\ell'}]\,, \tag{5.2}$$

and it is valid for all $n$-vector models. The difference between Eqs. (5.1) and (5.2) concerns about the zero-point energy. We are assuming $d$-dimensional lattices with volume $[0, L_1] \times [0, L_2] \cdots \times [0, L_d]$ with $L_1 = L_2 = \cdots = L_d$, and those that the angles between the lattice vectors are 90 degrees, for simplicity . For instance, let us consider all spins aligned in the $z$-direction, so, the total energy is $-2\mathcal{J}Nd$ in the first definition, and zero in the second one. It justifies the use of $2d$ neighbors for each unit cell. For instance, linear, square and cubic lattices have $2, 4, 6$ neighbors, respectively[1].

Let us emphasize that both Eqs. (5.1) and (5.2) are not inertial because the kinetic energy is naturally zero.

[1] In an arbitrary lattice, we define $z$ as the number of neighbors in which the total energy is $-\mathcal{J}Nz$.

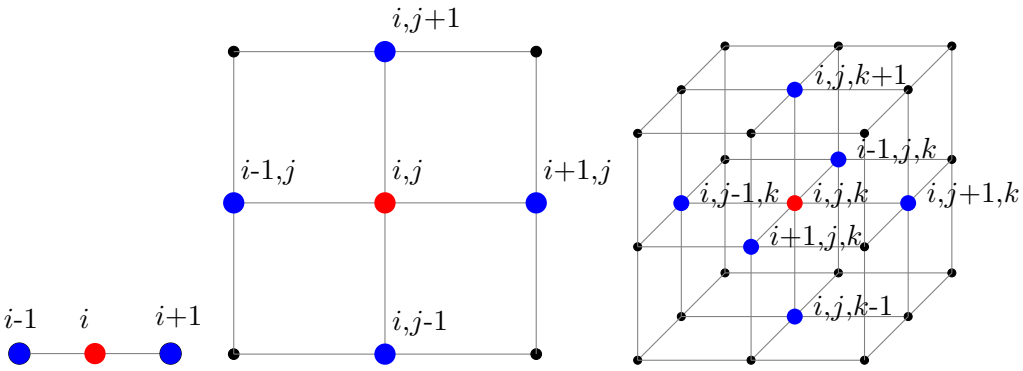


Figure 5.1: (Left) Nearest neighbors for a one-dimensional lattice. (Center) Nearest neighbors for a square lattice. (Right) Nearest neighbors for a cubic lattice. The neighbors are represented in color blue.

In quantum mechanics, an Hermitian operator evolves in time as follows

$$\frac{d}{dt}O = \frac{1}{i\hbar}[\mathcal{H}, O]\,, \tag{5.3}$$

where $[.,.]$ denotes the commutator between two operators. The commutation relations between spins operators are

$$[S^{\alpha}_{\ell}, S^{\beta}_{\ell'}] = i\hbar\epsilon_{\alpha\beta\gamma}S^{\gamma}_{\ell'}\delta_{\ell\ell'}\,, \tag{5.4}$$

therefore, the evolution of spins is given by

$$\dot{\mathbf{S}}_{\ell} = \mathbf{S}_{\ell} \times \sum_{\langle \ell' \rangle} \mathbf{S}_{\ell'} = -\mathbf{S}_{\ell} \times \frac{\partial \mathcal{H}}{\partial \mathbf{S}_{\ell}}\,, \tag{5.5}$$

where $\langle \ell' \rangle$ denotes only the summation over the nearest-neighbors. In a classical version, we have $[.,.]/i\hbar \to \{.,.\}$, in which $\{.,.\}$ is the Poisson bracket. The Eq. (5.5) remains valid replacing operators with spin coordinates, since the relation (5.4) in its classical version is $\epsilon_{\alpha\beta\gamma}S^{\gamma}_{\ell'}\delta_{\ell\ell'}$ in the left-hand side, differing by a factor $i\hbar$ [111].

We notice that Eq. (5.5) is only consistent for $n = 2$ and $n = 3$ vector models, due to the cross product not being well-defined for higher dimensions. Another problem is that for $n = 2$, the cross product results in a vector in $z$-direction which does not exist in the $XY$-model, in other words, the time evolution of the spins are zero in $x$ and $y$ components. Summarizing, only $n = 3$ has non-trivial equations of motion, which is the Heisenberg model. To avoid these problems, an inertial term must be added to allow the spins to evolve in time. This inertial term is simply the sum of the kinetic energy of all particles in the lattice.

## 5.2 Inertial form

To add a total kinetic energy in those systems we need to include a summation over the kinetic energy of all rotors, namely $\frac{\mathbf{p}_\ell^2}{2I_\ell}$ where $\mathbf{p}_\ell$ and $I_\ell$ denote the angular momentum[2] and the moment of inertia of a rotor in the lattice point $\ell$. Considering rotors with the same moment of inertia ($I_\ell = I\,\forall\ell$), we have the inertial $XY$-model defined as

$$\mathcal{H} = \sum_{\ell=1}^{L^d} \frac{\mathbf{p}_\ell^2}{2I} + \frac{\mathcal{J}}{2d} \sum_{\langle \ell,\ell' \rangle} \left[1 - \mathbf{S}_\ell \cdot \mathbf{S}_{\ell'}\right]. \tag{5.6}$$

The equations of motion can be derived by Euler's equations for rigid bodies[112], yielding

$$\begin{aligned} \dot{\mathbf{S}}_\ell &= \boldsymbol{\omega}_\ell \times \mathbf{S}_\ell = \frac{\mathbf{p}_\ell}{I} \times \mathbf{S}_\ell \\ I\dot{\boldsymbol{\omega}}_\ell &= \dot{\mathbf{p}}_\ell = \mathcal{J}\mathbf{S}_\ell \times \sum_{\langle \ell' \rangle} \mathbf{S}_{\ell'} \end{aligned} \tag{5.7}$$

It is worth emphasizing that that these equations can also be obtained using noncanonical Hamiltonian equations, wherein

$$\begin{aligned} \dot{\mathbf{S}}_\ell &= -\mathbf{S}_\ell \times \frac{\partial \mathcal{H}}{\partial \mathbf{p}_\ell} \\ \dot{\mathbf{p}}_\ell &= -\mathbf{S}_\ell \times \frac{\partial \mathcal{H}}{\partial \mathbf{S}_\ell}. \end{aligned} \tag{5.8}$$

The relations in Eq. (5.8) enable us to straightforwardly derive the equations of motion from more complex Hamiltonians.

### 5.2.1 Classical inertial $n$-vector models in canonical coordinates

**$XY$ model**

The classical Hamiltonian in canonical coordinates for $n = 2$ is obtained through polar coordinates using $S_\ell^x = \cos\theta_\ell$ and $S_\ell^y = \sin\theta_\ell$, thus yielding

$$\mathcal{H} = \sum_{\ell=1}^{L^d} \frac{\mathbf{p}_\ell^2}{2I} + \frac{\mathcal{J}}{2d} \sum_{\langle \ell,\ell' \rangle} \left[1 - \cos(\theta_\ell - \theta_{\ell'})\right], \tag{5.9}$$

where $\mathbf{p}_\ell = p_\ell \hat{\mathbf{z}}$ assuming the constraint $\mathbf{p}_\ell \cdot \mathbf{S}_\ell = 0$, therefore, it leads us to the following equations of motion:

$$\begin{aligned} \dot{\theta}_\ell &= \frac{p_\ell}{I} \\ \dot{p}_\ell &= -\mathcal{J} \sum_{\langle \ell' \rangle} \sin(\theta_\ell - \theta_{\ell'}). \end{aligned} \tag{5.10}$$

[2] We avoid the notation $\mathbf{L}$ for angular momentum, because we use $L$ for the linear lattice size.

Let us notice that the advantage of using Eqs. (5.10) lies in the number of equations to integrate. For instance, when using Eqs. (5.10), we deal with $2L^d$ first-order ordinary differential equations, whereas Eqs. (5.8) lead us to $4L^d$ equations, taking into account the components of both the spin and angular momentum vectors.

**Heisenberg model**

For the Heisenberg model, we use spherical coordinates by replacing

$$\mathbf{S}_\ell = (\sin\theta_\ell \cos\phi_\ell, \sin\theta_\ell \sin\phi_\ell, \cos\theta_\ell)\,, \tag{5.11}$$

resulting in the following Hamiltonian:

$$\mathcal{H} = \sum_\ell \frac{p_{\theta_\ell}^2}{2I} + \frac{p_{\phi_\ell}^2}{2I\sin^2\theta_\ell} + \frac{\mathcal{J}}{2d}\sum_{\langle \ell\ell'\rangle}\left[1 - \cos\left(\phi_\ell - \phi_{\ell'}\right)\sin\theta_\ell \sin\theta_{\ell'} - \cos\theta_\ell\cos\theta_{\ell'}\right]\,. \tag{5.12}$$

From Eqs. (5.12), the equations of motion are

$$\begin{aligned}
\dot{\theta}_\ell &= \frac{p_{\theta_\ell}}{I} \\
\dot{\phi}_\ell &= \frac{p_{\phi_\ell}}{I\sin^2\theta_\ell} \\
\dot{p_{\theta_\ell}} &= -\mathcal{J}\sum_{\langle \ell'\rangle}\left[\sin\theta_\ell\cos\theta_{\ell'} - \cos\left(\phi_\ell - \phi_{\ell'}\right)\cos\theta_\ell\sin\theta_{\ell'}\right] \\
\dot{p_{\phi_\ell}} &= -\mathcal{J}\sum_{\langle \ell'\rangle}\sin\left(\phi_\ell - \phi_{\ell'}\right)\sin\theta_\ell\sin\theta_{\ell'}\,.
\end{aligned} \tag{5.13}$$

We notice that the second Eqs. in (5.13) have singularities at $\theta_\ell = n\pi$, $\forall n \in \mathbb{Z}$, therefore, these equations can not be integrated in this way. To avoid such problem, we need to integrate Eqs. (5.8) leading us to $6L^d$ first-order ordinary differential equations.

## 5.3 Anisotropic $n$-vector models

### 5.3.1 Anisotropic exchange interactions

This model is used to study phase transitions and critical phenomena in anisotropic magnetic systems. The anisotropy, introduced by having different values of $\mathcal{J}^m$ for different $m$, can lead to interesting and complex behavior. For example, it can break the symmetry of the system and lead to the formation of different phases [113].

$$\mathcal{H} = -\sum_{\langle \ell\ell'\rangle}\sum_{m=1}^{n}\mathcal{J}^m S_\ell^m S_{\ell'}^m;\ |\mathbf{S}_\ell|^2 = 1 \tag{5.14}$$

Particularly, for $n = 3$ and $\mathcal{J}^x = \mathcal{J}^y \neq \mathcal{J}^z$ it is called Heisenberg $XXZ$ model, where the symmetry is broken due to the anisotropic exchange coupling $\mathcal{J}^z$. When $\mathcal{J}^x \neq \mathcal{J}^y \neq \mathcal{J}^z$

it is called $XYZ$ model. Notice that, in this case, when $\mathcal{J}^m = \mathcal{J}$, $m = x, y, z$, we recover the standard isotropic Heisenberg model (or Heisenberg XXX model). Despite the nomenclatures, all these models correspond to particular cases of the anisotropic Heisenberg models.

The equations of motion are quite simple, and are given as follows by

$$\dot{\mathbf{S}}_\ell = \mathbf{p}_\ell \times \mathbf{S}_\ell \,, \tag{5.15}$$

and

$$\mathbf{p}_\ell = \mathbf{S}_\ell \times \sum_{\langle \ell' \rangle} (\mathcal{J}^x S^x_{\ell'}, \mathcal{J}^y S^y_{\ell'}, \mathcal{J}^z S^z_{\ell'}) \,. \tag{5.16}$$

The Eq. (5.15) is the same for all models with only the kinetic energy momentum-dependent. Therefore, we focus only on the equations of motion for the angular momentum.

### 5.3.2 Standard interaction with a external magnetic field

A simple example of an anisotropic interaction is when a external magnetic field $\mathbf{h}_\ell$ is turned on and interacts with all points of the lattice, with magnetic moment $\mu$, yielding

$$\mathcal{H}_M = -\mu \sum_\ell \mathbf{h}_\ell \cdot \mathbf{S}_\ell \,. \tag{5.17}$$

As a simplification, we can consider a field $\mathbf{h}$ uniformly interacting with all spins in the lattice, thus resulting in

$$\mathcal{H}_M = -\mu \mathbf{h} \cdot \sum_\ell \mathbf{S}_\ell \,. \tag{5.18}$$

In real experiments we bias the field in a single directions, for instance, the $z$-direction, as follows

$$\mathcal{H}_M = -\mu \, h^z \sum_\ell S^z_\ell \tag{5.19}$$

When we apply a strong magnetic field in a certain direction to the lattice, all spins tend to align in its direction because it is energetically favorable. However, when the field is weak, thermal fluctuations can disrupt this alignment, causing the spins to orient in random directions, as observed in a paramagnet. The field must be sufficiently high to align the spins, since as the temperature increases, thermal fluctuations become even more pronounced.

The equations of motion for the general case of the classical inertial magnetic field interaction are given by Eq. (5.15) and

$$\dot{\mathbf{p}}^M_\ell = \mathbf{S}_\ell \times \mu \, \mathbf{h}_\ell \,. \tag{5.20}$$

It is the most common anisotropy and is easily found in almost all books of thermostatistics [114].

### 5.3.3 Uniaxial anisotropy

The Hamiltonian of the uniaxial anisotropic interaction is given by

$$\mathcal{H}_u = D \sum_{\ell} (\mathbf{S}_\ell \cdot \hat{\mathbf{n}}_\ell)^2 \,, \tag{5.21}$$

where $D$ is the uniaxial anisotropy constant, which determines the strength of the anisotropy, and $n_\ell$ is the unit vector along the direction of the *easy axis* at site $\ell$. The term $(S_\ell \cdot n_\ell)^2$ represents the square of the projection of the spin onto the easy axis. This term is minimized when the spin is aligned with the easy axis, which is the preferred direction of the spin due to the anisotropy.

In this model, the anisotropy tends to align all spins along their respective easy axes. The specific form of the anisotropy can vary depending on the physical system under consideration [115]. For example, in some systems, the easy axis might be the same for all spins, while in others, it might vary from spin to spin. The given Hamiltonian can describe both situations.

The equations of motion for the classical inertial uniaxial interaction are given by Eq. (5.15) and

$$\dot{\mathbf{p}}^u_\ell = -2D(\mathbf{S}_\ell \cdot \hat{\mathbf{n}}_\ell)\hat{\mathbf{n}}_\ell \,. \tag{5.22}$$

This interaction will be taken account in Chapter 8 with the aim to achieve the Ising model.

### 5.3.4 Dzyaloshinskii-Moriya interaction

The Dzyaloshinskii-Moriya interaction (DMI), also known as antisymmetric exchange, is a contribution to the total magnetic exchange interaction between two neighboring magnetic spins. It is a term in the Hamiltonian and can be written as

$$\mathcal{H}_{DM} = \sum_{\ell\ell'} \mathbf{D}_{\ell\ell'} \cdot (\mathbf{S}_\ell \times \mathbf{S}_{\ell'}) \,, \tag{5.23}$$

where $\mathbf{D}_{\ell\ell'}$ is an axial vector describing an antisymmetric magnetic exchange between spins located at sites $\ell$ and $\ell'$. In magnetically ordered systems, DMI favors a spin canting of otherwise parallel or antiparallel aligned magnetic moments and thus, is a source of weak ferromagnetic behavior in an antiferromagnet. It is fundamental to the production of magnetic skyrmions and explains the magnetoelectric effects in a class of materials termed multiferroics [116, 117, 118].

The functional form of the DMI can be obtained through a second-order perturbative analysis of the spin-orbit coupling interaction, between ions. The magnitude and direction of the Dzyaloshinskii-Moriya vector are dictated by the symmetries of neighboring ions.

The DMI is crucial in understanding various spin-related phenomena and is particularly relevant in the study of two-dimensional magnets. The equations of motion for the classical inertial DM interaction, assuming that the DM vector does not depend on the orbital angular momentum, are given by Eq. (5.15) and

$$\dot{\mathbf{p}}_\ell^{DM} = -\sum_{\ell'} \left[\mathbf{D}_{\ell\ell'}(\mathbf{S}_\ell \cdot \mathbf{S}_{\ell'}) - (\mathbf{D}_{\ell\ell'} \cdot \mathbf{S}_\ell)\mathbf{S}_{\ell'}\right] . \tag{5.24}$$

Despite the name, $\mathbf{D}_{\ell\ell'}$ was previously described as a vector which the magnitude and direction are dictated by the symmetries of neighboring ions, thus, the antisymmetry is not an mandatory condition for this vector. Assuming a uniform DM vector, namely $\mathbf{D}$, we obtain a simplified version of this interaction, which is more convenient for simulations and analytical purposes in quantum mechanics. More simplifications can be made, as long as they are appropriate and lead us to consistent results in the realm of physics. In this situation $\mathbf{D}_{\ell\ell'} = \mathbf{D}$, therefore, we have

$$\dot{\mathbf{p}}_\ell^{DM} = -\sum_{\ell'} \left[\mathbf{D}(\mathbf{S}_\ell \cdot \mathbf{S}_{\ell'}) - (\mathbf{D} \cdot \mathbf{S}_\ell)\mathbf{S}_{\ell'}\right] , \tag{5.25}$$

which is more simple to solve analytically[3].

In this section we show some possible interactions which might be valuable in the study of anisotropic $n$-vector models. It also encourages future investigations of the dynamics of such systems. In the next section we will detail $n$-vector models with generic-range interactions, which plays an important role in the study of magnetic systems with strong and weak spin correlations.

## 5.4 $n$-vector models with generic-range interactions

The Hamiltonian of $n$-vector models with generic-range interactions [119, 120] is given by

$$\mathcal{H} = \sum_\ell \frac{\mathbf{p}_\ell^2}{2I} + \frac{\mathcal{J}}{2\tilde{N}} \sum_{\substack{\ell,\ell' \\ \ell' \neq \ell}} \frac{1 - \mathbf{S}_\ell \cdot \mathbf{S}_{\ell'}}{r_{\ell\ell'}^\alpha} , \tag{5.26}$$

where $r_{\ell\ell'} \equiv |\ell - \ell'|$ denotes the distance between the rotators in a $d$-dimensional lattice. The factor $\tilde{N}$ becomes the system extensive, and it is defined as follows

$$\tilde{N} = \sum_{\substack{\ell,\ell' \\ \ell' \neq \ell}} r_{\ell\ell'}^{-\alpha}/N . \tag{5.27}$$

[3]For instance, see Ref. [118]

It is worth emphasizing that in the limit $\alpha \to \infty$, we recover the standard $n$-vector models with nearest-neighbors, while for $\alpha = 0$, it recovers the mean-field model [121].

The definition in Eq. (5.26) originates from considering spins that interacts in a generic way, such that the exchange coupling is no more a constant $\mathcal{J}$, but a matrix with elements $\mathcal{J}_{\ell\ell'}$. In this way, we assume a nontrivial interaction between the sites $\ell$ and $\ell'$, where $\mathcal{J}_{\ell\ell'} \equiv \frac{\mathcal{J}}{\tilde{N} r^{\alpha}_{\ell\ell'}}$. Now, in certain limits, it behaves as a system with very long, long and short-range interactions, specifically at $0 < \alpha/d < 1$, $1 < \alpha/d < \infty$, and $\alpha = \infty$, respectively.

The generic-range $n$-vector models for $n = 1, 2$ and 3 are called $\alpha$-Ising, $\alpha$-$XY$, and $\alpha$-Heisenberg models, respectively. The equations of motion are easily obtained by the substitution $\mathcal{J}\sum_{\langle\ell'\rangle}\mathbf{S}_{\ell'} \to \frac{\mathcal{J}}{\tilde{N}}\sum_{\ell'\,\ell'\neq\ell}\frac{\mathbf{S}_{\ell'}}{r^{\alpha}_{\ell\ell'}}$, thus yielding

$$\begin{aligned} \dot{\mathbf{S}}_{\ell} &= \frac{\mathbf{p}_{\ell}}{I} \times \mathbf{S}_{\ell} \\ \dot{\mathbf{p}}_{\ell} &= \mathbf{S}_{\ell} \times \frac{\mathcal{J}}{\tilde{N}} \sum_{\substack{\ell' \\ \ell'\neq\ell}} \frac{\mathbf{S}_{\ell'}}{r^{\alpha}_{\ell\ell'}} \,. \end{aligned} \tag{5.28}$$

The Eq. (5.28) dictates the evolution of the classical inertial $n$-vector model for $n = 2$ and $n = 3$ [122], and its structure reveals that a generic description of interactions is not easy to solve analytically. Now, we will describe a more restricted approach to deal with the $n = 2$ version.

### 5.4.1 $\alpha$-$XY$ model

Particularly, for $n = 2$, we can also define the spins in polar coordinates as in the standard $XY$ model, giving the Hamiltonian

$$\mathcal{H} = \sum_{\ell=1}^{L^d} \frac{\mathbf{p}_{\ell}^2}{2I} + \frac{\mathcal{J}}{2\tilde{N}} \sum_{\substack{\ell\ell' \\ \ell'\neq\ell}} \frac{[1 - \cos(\theta_{\ell} - \theta_{\ell'})]}{r^{\alpha}_{\ell\ell'}} \,, \tag{5.29}$$

which yields the following equations of motion

$$\begin{aligned} \dot{\theta}_{\ell} &= \frac{p_{\ell}}{I} \\ \dot{p}_{\ell} &= -\frac{\mathcal{J}}{\tilde{N}} \sum_{\substack{\ell' \\ \ell'\neq\ell}} \frac{\sin(\theta_{\ell} - \theta_{\ell'})}{r^{\alpha}_{\ell\ell'}} \,. \end{aligned} \tag{5.30}$$

As mentioned before, the $\alpha$-Heisenberg model remains with the same problems when we try to use spherical coordinates, so, in this model, we must evolve Eqs. (5.28) in time in order to obtain the noncanonical coordinates $(\mathbf{S}_{\ell}(t), \mathbf{p}_{\ell}(t))$.

Let us notice that even in canonical coordinates and in a one-dimensional systems at low spin excitations, the equations of motion are not trivial, due to the evolution of $p_{\ell}$ resulting in a generic range system of coupled harmonic oscillators.

## 5.5 Langevin baths in classical inertial $n$-vector models

The equations for motion for $n$-vector models with Langevin heat baths can be written as follows:

$$\begin{aligned}\dot{\mathbf{S}}_\ell &= \frac{\mathbf{p}_\ell}{I} \times \mathbf{S}_\ell \\ \dot{\mathbf{p}}_\ell &= \mathcal{J}\mathbf{S}_\ell \times \sum_{\langle \ell' \rangle} \mathbf{S}_{\ell'} + (\boldsymbol{\eta}_h - \gamma_h \mathbf{p}_\ell)\,\delta_{\ell h} + (\boldsymbol{\eta}_l - \gamma_l \mathbf{p}_\ell)\,\delta_{\ell l}\end{aligned} \tag{5.31}$$

where $h$ and $l$ denote the rotators in the hot and cold reservoirs in a Langevin heat bath, respectively. The noise vectors $\boldsymbol{\eta}_{h/l}$, for instance, for the Heisenberg model have three components each one. Conversely, for the $XY$ model, the noises are applied along the $z$-direction. In other words, the noises must be in the same direction than the angular momenta. The constant $\gamma_{h/l}$ are the damping coefficients. Still about noises, we assume that all components of $\boldsymbol{\eta}_{h/l}$ are Gaussian white noises, which means that

$$\begin{aligned}\langle \eta^\alpha_{h/l}(t)\eta^\beta_{h/l}(t)\rangle &= 2Ik_BT_{h/l}\gamma_{h/l}\delta(t-t')\delta_{\alpha\beta},\ \ \alpha,\beta = x,y,z \\ \langle \eta^\alpha_{h/l}(t)\rangle &= 0,\ \ \alpha = x,y,z\end{aligned} \tag{5.32}$$

The equations (5.31) represent Langevin equations only at the ends. The region without baths is called the *bulk*.

There are other types of thermostats that we could use in our simulations, such as the Andersen, Berendsen, Nosé-Hoover, and Bussi-Dnadio-Parrinello thermostats [123, 124, 125, 126, 127]. However, the aim of our approach is not concerned with rescaling velocities or obtaining the exact canonical distribution. In the next chapters, we will demonstrate the importance of Eqs. (5.31) in nonequilibrium molecular dynamics. This approach is entirely based on first principles.

## 5.6 Lagrangian heat flux of $n$-vector models

To connect a microscopic system, out of equilibrium, with the heat flux, it is necessary to understand how the continuity equation behaves when the total energy of certain system evolves in time. The continuity equation for an ideal thermal conductor [4] is given by

$$\frac{\partial e}{\partial t} + \nabla \cdot \mathbf{J} = 0\,. \tag{5.33}$$

Let us transform Eq. (5.33) in its integral form, first integrating both sides in a volume $V$, so

$$\int_V \frac{\partial e}{\partial t} dv + \int_V \nabla \cdot \mathbf{J} dv = 0\,. \tag{5.34}$$

[4] We call ideal thermal conductor, a system whose thermal convection and radiation can be neglected.

The first part in Eq. (5.34) yields $\frac{dE}{dt}$ and the second one, yields $\oint_A \mathbf{J} \cdot d\mathbf{a}$. Particularly, for a discrete system, the surface integral results in

$$\oint_A \mathbf{J} \cdot d\mathbf{a} = \sum_{\ell} (\mathbf{J}_\ell - \mathbf{J}_{\ell'}) \cdot \hat{\mathbf{n}}_{\ell'} \Delta a \tag{5.35}$$

where $(\mathbf{J}_\ell - \mathbf{J}_{\ell'}) \cdot \hat{\mathbf{n}}_{\ell'}$ represents the difference of flow projected in the normal direction of the surface of the lattice, and $\Delta a$ is a small element of the surface. To clarify this notation, let us consider a $d$-dimensional lattice with coordinates $\ell = (\ell_1, \ell_2, \ldots, \ell_d)$. If $\ell' = (\ell_1 + \delta\ell_1, \ell_2, \ldots, \ell_d)$, where $\delta\ell_1$ represents a displacement on the lattice, the normal vector is represented by $\hat{\mathbf{n}}_{\ell'} = (1, 0, \ldots, 0)$. For $\ell' = (\ell_1, \ell_2 + \delta\ell_2, \ldots, \ell_d)$ the normal vector is $\hat{\mathbf{n}}_{\ell'} = (0, 1, \ldots, 0)$, and so forth. In particular, for one-dimensional flow, the notation is simplified because, $\hat{\mathbf{n}}_{\ell'} = \hat{\mathbf{x}}$ for all neighboring lattice sites.

$$\frac{1}{\Delta a}\frac{dE}{dt} + \sum_{\ell} (\mathbf{J}_\ell - \mathbf{J}_{\ell'}) \cdot \hat{\mathbf{n}}_{\ell'} = 0\,. \tag{5.36}$$

Let us notice that, the first part of Eq. (5.36) has the same units as the heat flux (energy per unit of time per unit of area), and the second one represents the difference between the flow with positions $\ell$ and $\ell'$. In this way, the heat flux for each element of the system can be obtained by

$$\frac{1}{\Delta a}\frac{dE_\ell}{dt} + (\mathbf{J}_\ell - \mathbf{J}_{\ell'}) \cdot \hat{\mathbf{n}}_{\ell'} = 0\,. \tag{5.37}$$

The flux $\mathbf{J}_\ell$ is often called Lagrangian heat flux [128] and it is completely determined by the microscopic behavior of a system. The connection with the macroscopic heat flux is given by the average $\langle J_\ell^\alpha \rangle \equiv J^\alpha$ for $\alpha = x, y, z$, taking into account both time and space variables.

Considering an isotropic medium, the thermal conductivity can be obtained by

$$k = \frac{|\mathbf{J}|}{|\nabla T|}\,, \tag{5.38}$$

where the thermal gradient is directly obtained by the solution of heat equation [5].

Let us emphasize that for anisotropic media the expression Eq. (5.38) breaks down due to the tensor behavior of the thermal conductivity, thus, it might be not accessible directly, but using another approach, namely Green-Kubo relation, although it presents some limitations [129].The most applicable situation is when the heat flux flows in $x$-direction. It results in a simple expression given by

$$k = \frac{JL}{\Delta T}\,, \tag{5.39}$$

[5]For an ideal heat conduction, which is the focus of this thesis, the heat equation is given by $\frac{\partial T}{\partial t} = a\frac{\partial^2 T}{\partial t^2}$, where $a$ is called thermal diffusivity.

with $\Delta T = T_h - T_l$ being the difference of temperatures between the hot and cold reservoir,

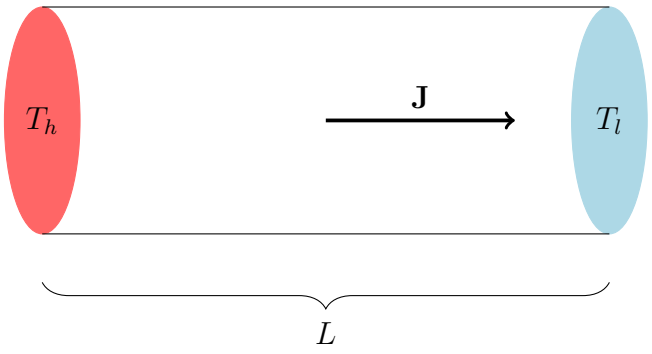


Figure 5.2: Illustration of the flow in $x$-direction in a cylinder. The hot reservoir (red color) is represented by the temperature $T_h$ while the cold reservoir is represented by the temperature $T_l$. The heat flux $\mathbf{J} = J\hat{\mathbf{x}}$ is transferred from hot to cold reservoirs. In this particular case, $L$ coincides with the height of the cylinder.

and $L$ represents the linear size through which the flow passes. We focus on these systems when the flux is one-dimensional, even though the system can exist in any dimensional space. For instance, $n$-vector models can describe magnetic systems on a d-dimensional lattice, where heat transport may occur only in the x-direction. In this scenario, the dimension of the lattice is $d$, while the dimension of the flow is one. In some circumstances, the flux in other directions is so negligible that it can be ignored. For instance, when we apply periodic boundary conditions along the regions outside of the heat baths.

### 5.6.1 One-dimensional Lagrangian heat flux of the $n$-vector models in noncanonical coordinates

All $\alpha$ components of the heat flux may be written as

$$J_\ell^\alpha = \frac{1}{2L^{d-1}} \sum_{\substack{\langle \ell'_\alpha \rangle \\ \ell'_\alpha > \ell_\alpha}} \left( \mathbf{S}_\ell \cdot \dot{\mathbf{S}}_{\ell'} - \mathbf{S}_{\ell'} \cdot \dot{\mathbf{S}}_\ell \right) . \tag{5.40}$$

Here, we set moment of inertia and exchange coupling as unitary in Eq. (5.6) (or define the heat flux in units of $\mathcal{J}/I$), for simplification purposes . For a heat flux only in $x$-direction, we have

$$J_\ell = \frac{1}{2} \sum_{\substack{\langle \ell'_x \rangle \\ \ell'_x > \ell_x}} \left( \mathbf{S}_\ell \cdot \dot{\mathbf{S}}_{\ell'} - \mathbf{S}_{\ell'} \cdot \dot{\mathbf{S}}_\ell \right) . \tag{5.41}$$

where $\ell'_x$ is the $x$ component of the nearest-neighbors in a $d$-dimensional lattice. The sum in Eq. (5.41) is considered only in the nearest-neighbors which are greater than the lattice

point in the same direction. To illustrate the definition, let us consider a two and three-dimensional lattice with one-dimensional flow. In the first case the sum in $x$-direction is at $(i+1, j)$, while in the second case, the neighbors are at $(i+1, j, k)$. Only the first coordinate of the lattice points change. In all cases, there is only one neighbor. The simplest case is when the lattice is a chain ($d = 1$) and the flux is one-dimensional. The Lagrangian heat flux is then, given by

$$J_i = \frac{1}{2}\left(\mathbf{S}_i \cdot \mathbf{S}_{i+1} - \mathbf{S}_{i+1} \cdot \dot{\mathbf{S}}_i\right) . \tag{5.42}$$

The derivation of Eq. (5.42) will be shown in Chapter 10, when we discuss about the Heisenberg chain. Notice that, when $n = 2$, by using polar coordinates for the spins $\mathbf{S}_i = (\cos\theta_i, \sin\theta_i)$, we obtain

$$J_i = \frac{1}{2}(p_i + p_{i+1}) \sin(\theta_i - \theta_{i+1}) . \tag{5.43}$$

Let us clarify that Eq. (5.43) can be directly obtained with the aid of Eqs. (5.9), (5.30), and (5.37). This is the expression for heat flux of the one-dimensional $XY$ model in a one-dimensional flow. In the case of the Heisenberg chain, we can use the general expression with noncanonical coordinates, Eq. (5.42).

## 5.7 Green-Kubo versus direct formalism

The Green-Kubo formula [130, 131] for heat flux is a useful tool for obtaining the thermal conductivity of a system which achieves the equilibrium state. This approach also gives a straightforward information about the thermal conductivity tensor. The relation for each component of the thermal conductivity is given by

$$k_{\alpha\beta} = \frac{1}{TV}\int_0^\infty dt\, \langle J_\ell^\alpha(0) J_\ell^\beta(t)\rangle_{eq} \tag{5.44}$$

and for an isotropic medium and one-dimensional heat flux, we have

$$k = \frac{1}{k_B T^2 V}\int_0^\infty dt\, \langle J_\ell(0) J_\ell(t)\rangle_{eq} \tag{5.45}$$

where $V$ is the volume, $T$ is the temperature , $k_B$ is the Boltzmann constant, and $\langle J_i(0) J_j(t)\rangle_{eq}$ represents the heat flux correlation function assuming Boltzmann weigths when the perturbation is turned on. In contrast with Green-Kubo relation, the direct method has some limitation regarding to the off-diagonal terms of the thermal conductivity tensor, however, the Green-Kubo formula assumes the equilibrium hypothesis[6], thus

[6]The hypothesis is that for a long-time in the past (from $-\infty$ to $t$) the time-dependent distribution reaches the equilibrium state, and the correspondent phase space distribution is assumed to be a canonical one.

define the probability *a priori*. As previously discussed in Chapter 4, not all systems achieve the stationary state, and even if it does, not all stationary states are equivalent to the equilibrium one.

Referring to the Green-Kubo formula for heat conduction, it is valid for large systems. However, these formulas may not accurately describe thermal conductivity in small systems or systems with finite size effects. Furthermore, there can be nonlinear corrections to Fourier's law, which are not captured by the Green-Kubo formula. The standard Green-Kubo formula may not be valid for systems with long-range or nonstationary correlations, necessitating a generalized version of the Green-Kubo formula for such systems. Additionally, the Green-Kubo formula assumes that the system is in equilibrium at the initial time when the external field is turned on, which may not always be the case in real-world systems. These limitations need to be taken into account when applying the Green-Kubo formula to practical problems in heat conduction and other linear transport phenomena.

In contrast, the assumption of equilibrium has no implication in the direct formalism, since it is a natural nonequilibrium method and can be suitable for a wide variety of systems being also consistent with small ones. Another important remark about the direct method concerning about the derivation of the thermal conductivity from heat equation, given by $\frac{\partial T}{\partial t} = \nabla \cdot (k \nabla T)$, which for one-dimensional heat transfer, we have

$$\frac{\partial T}{\partial t} = \frac{\partial}{\partial x}\left(k \frac{\partial T}{\partial x}\right) . \tag{5.46}$$

Even with nonlinear contributions to the thermal conductivity, the thermal conductivity can be obtained by Eq. (5.39), although the Fourier's law is naturally broken ($\kappa$ can be dependent on the thermal gradient and so forth). Therefore, we are able to simulate systems with anomalous heat conduction without resorting to unphysical considerations, such as assuming equilibrium in a system that is in a permanent nonequilibrium state.

In the next chapters, we will show some results applying the direct method to classical inertial $n$-vector models.

# Chapter 6

# XY model in $d = 1, 2, 3$ dimensions

*PRIMARY causes are unknown to us; but are subject to simple and constant laws, which may be discovered by observation, the study of them being the object of natural philosophy.*
*Heat, like gravity, penetrates every substance of the universe, its rays occupy all parts of space. The object of our work is to set forth the mathematical laws which this element obeys. The theory of heat will hereafter form one of the most important branches of general physics.*
J. Fourier, 1822, Théorie Analytique de la Chaleur (English translation).

This chapter is based on the recent article *First-principle validation of Fourier's law in d = 1, 2, 3 classical systems*, published in Physica D: Nonlinear Phenomena [39].

In this chapter we numerically study the thermal transport in the classical inertial nearest-neighbor XY ferromagnet in $d = 1, 2, 3$, the total number of sites being given by $N = L^d$, where $L$ is the linear size of the system.

## 6.1 Model

The Hamiltonian of the $d$-dimensional inertial ferromagnetic XY model is given by

$$\mathcal{H} = \frac{1}{2}\sum_{\ell=1}^{L^d} p_\ell^2 + \frac{1}{2}\sum_{\langle \ell,\ell' \rangle} \left[1 - \cos(\theta_\ell - \theta_{\ell'})\right], \tag{6.1}$$

where $\langle \ell, \ell' \rangle$ denotes nearest-neighboring rotors in the $d$-dimensional lattice [29, 27, 28]. Because we assume that the particles have the same mass and the same moment of inertia, we have considered unit momenta of inertia and unit first-neighbor coupling constant

without loss of generality, and $(p_\ell, \theta_\ell)$ are conjugate canonical pairs. We use periodic boundary conditions along $(d-1)$ directions, and leaving open for 1-dimensional ends. One of the ends being at a low temperature heat bath $T_l$ and the other one at high temperature $T_h$ (see Fig. 6.1 for the illustration for $d = 1$ and 2).

The equation of motion for the one-dimensional model is given as,

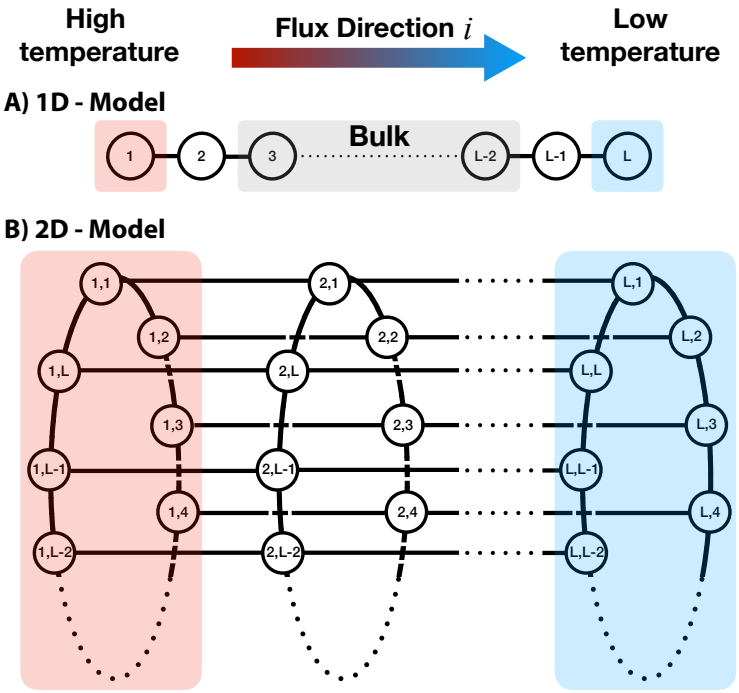


Figure 6.1: The lattice structure of the present A) $d = 1$ model ($L$ sites) and B) $d = 2$ model ($L^2$ sites). Red shaded areas represent hot heat bath, $T_h$, and blue areas are cold heat bath, $T_l$. The heat flux direction is from the hot heat bath to the cold one. To sensitively compute the heat flux and conductance, the bulk selected from the 3rd component to $L-2$ one in the flux direction to avoid direct random noise from the heat baths. The bulk is illustrated for 1D-model in A), which is straightforwardly generalized for dimensions $d$=2 and 3.

$$
\begin{aligned}
\dot{\theta}_i &= p_i \ \ (i = 1, \ldots, L) \\
\dot{p}_1 &= -\gamma_h p_1 + F_1 + \sqrt{2\gamma_h T_h}\eta_h(t) \\
\dot{p}_i &= F_i \ \ (i = 2, \ldots, L-1) \\
\dot{p}_L &= -\gamma_l p_L + F_L + \sqrt{2\gamma_l T_l}\eta_l(t)\,,
\end{aligned}
\tag{6.2}
$$

the force components being given by

$$
\begin{aligned}
F_1 &= -\sin(\theta_1 - \theta_2) - \sin(\theta_1) \\
F_i &= -\sin(\theta_i - \theta_{i+1}) - \sin(\theta_i - \theta_{i-1}) \\
F_L &= -\sin(\theta_L) - \sin(\theta_L - \theta_{L-1}),
\end{aligned}
\tag{6.3}
$$

where $i = 2, \ldots, L-1$, the friction coefficients are chosen $\gamma_l = \gamma_h = 1$ (for numerical convenience), and $\eta_l$ and $\eta_h$ represents the Gaussian white noise with zero mean value and unit variance. Note that, in a relativistic context, these equations must be modified.

### 6.1.1 Equations of motion for $d > 1$ Lattices

#### 2-Dimensional Lattice

The equations of motion for $d = 2$ are written as follows

$$\begin{aligned}
\dot{\theta}_{i,j} &= p_{i,j} \;\; ((i,j) = 1, \ldots, L) \\
\dot{p}_{1,j} &= -\gamma_h p_{1,j} + F_{1,j} + \sqrt{2\gamma_h T_h}\eta_{j,h}(t) \\
\dot{p}_{i,j} &= F_{i,j} \;\; (i = 2, \ldots, L-1) \\
\dot{p}_{L,j} &= -\gamma_l p_{L,j} + F_{L,j} + \sqrt{2\gamma_l T_l}\eta_{j,l}(t)\,,
\end{aligned} \tag{6.4}$$

the force components being given by

$$\begin{aligned}
F_{1,j} = &-\sin(\theta_{1,j} - \theta_{2,j}) - \sin(\theta_{1,j}) \\
&- \sin(\theta_{1,j} - \theta_{1,j+1}) - \sin(\theta_{1,j} - \theta_{1,j-1}) \\
F_{i,j} = &-\sin(\theta_{i,j} - \theta_{i+1,j}) - \sin(\theta_{i,j} - \theta_{i-1,j}) \\
&- \sin(\theta_{i,j} - \theta_{i,j+1}) - \sin(\theta_{i,j} - \theta_{i,j-1}) \\
F_{L,j} = &-\sin(\theta_{L,j}) - \sin(\theta_{L,j} - \theta_{L-1,j}) \\
&- \sin(\theta_{L,j} - \theta_{L,j+1}) - \sin(\theta_{L,j} - \theta_{L,j-1})
\end{aligned} \tag{6.5}$$

where $\theta_{i,1} = \theta_{i,L+1}$ and $\theta_{i,0} = \theta_{i,L}$. The friction coefficients $\gamma_l$ and $\gamma_h$ have been chosen $\gamma_l = \gamma_h = 1$, and all components of the vectors $\eta_{j,l}$ and $\eta_{j,h}$ are random Gaussian distributions with zero mean value and unit variance.

#### 3-Dimensional Lattice

For $d = 3$, we have similarly :

$$\begin{aligned}
\dot{\theta}_{i,j,k} &= p_{i,j,k} \;\; ((i,j,k) = 1, \ldots, L) \\
\dot{p}_{1,j,k} &= -\gamma_h p_{1,j,k} + F_{1,j,k} + \sqrt{2\gamma_h T_h}\eta_{j,k,h}(t) \\
\dot{p}_{i,j,k} &= F_{i,j,k} \;\; (i = 2, \ldots, L-1) \\
\dot{p}_{L,j,k} &= -\gamma_l p_{L,j,k} + F_{L,j,k} + \sqrt{2\gamma_l T_l}\eta_{j,k,l}(t)\,,
\end{aligned} \tag{6.6}$$

the force components being given by

$$
\begin{aligned}
F_{1,j,k} &= -\sin(\theta_{1,j,k} - \theta_{2,j,k}) - \sin(\theta_{1,j,k}) \\
&\quad - \sin(\theta_{1,j,k} - \theta_{1,j+1,k}) - \sin(\theta_{1,j,k} - \theta_{1,j-1,k}) \\
&\quad - \sin(\theta_{1,j,k} - \theta_{1,j,k+1}) - \sin(\theta_{1,j,k} - \theta_{1,j,k-1}) \\
F_{i,j,k} &= -\sin(\theta_{i,j,k} - \theta_{i+1,j,k}) - \sin(\theta_{i,j,k} - \theta_{i-1,j,k}) \\
&\quad - \sin(\theta_{i,j,k} - \theta_{i,j+1,k}) - \sin(\theta_{i,j,k} - \theta_{i,j-1,k}) \\
&\quad - \sin(\theta_{i,j,k} - \theta_{i,j,k+1}) - \sin(\theta_{i,j,k} - \theta_{i,j,k-1}) \\
F_{L,j,k} &= -\sin(\theta_{L,j,k}) - \sin(\theta_{L,j,k} - \theta_{L-1,j,k}) \\
&\quad - \sin(\theta_{L,j,k} - \theta_{L,j+1,k}) - \sin(\theta_{L,j,k} - \theta_{L,j-1,k}) \\
&\quad - \sin(\theta_{L,j,k} - \theta_{L,j,k+1}) - \sin(\theta_{L,j,k} - \theta_{L,j,k-1})
\end{aligned}
\tag{6.7}
$$

where $\theta_{i,1,k} = \theta_{i,L+1,k}, \theta_{i,0,k} = \theta_{i,L,k}, \theta_{i,j,1} = \theta_{i,j,L+1}$ and $\theta_{i,j,0} = \theta_{i,j,L}$. The friction coefficients $\gamma_l$ and $\gamma_h$ have been chosen $\gamma_l = \gamma_h = 1$, and all components of the matrices $\eta_{j,k,l}$ and $\eta_{j,k,h}$ are random Gaussian distributions with zero mean value and unit variance.

This approach can be extended for $d > 3$, where the lattice points are $\ell = (i_1, i_2, \ldots, i_d)$. The boundary conditions are quite complicated. For instance, for $d = 4$, we have $\theta_{i,1,k,m} = \theta_{i,L+1,k,m}$, $\theta_{i,0,k,m} = \theta_{i,L,k,m}$, $\theta_{i,j,1,m} = \theta_{i,j,L+1,m}$, $\theta_{i,j,0,m} = \theta_{i,j,L,m}$, $\theta_{i,j,k,1} = \theta_{i,j,k,L+1}$ and $\theta_{i,j,k,0} = \theta_{i,j,k,L}$. The equations of motion also must be modified, assuming for coordinates for each point of the lattice. The noise increases its rank to 4.

## 6.2 Methods

The dynamical evolution was conducted using the Velocity-Verlet algorithm [132, 133] with step size $dt = 0.01$; after discarding a transient time, the average of the heat flux is computed for $4 \times 10^8$ time steps and 80 randomly initialized realizations. The transient time is carefully selected for different system sizes by considering the development of the conductivity curve for varying temperature values. The system is assumed to be stationary when the conductivity curve reaches a steady state. For simplicity, we set $T_h = T(1 + \Delta)$ and $T_l = T(1 - \Delta)$ with $\Delta = 0.125$, where $T$ is the average temperature . The macroscopic conductivity $\kappa$ is given by

$$\kappa = \frac{J}{(T_h - T_l)/L} = \frac{J}{2\Delta T/L} \tag{6.8}$$

where $J = \langle J_l \rangle_{bulk}$ is the time and space average of heat flux along the bulk of the lattice in the stationary state, which connects the microscopic level (the equations of motion) with the macroscopic one (the average of the heat flux and thermal conductivity) via the continuity equation. The bulk is defined as the entire system excluding the sides in high and low temperature heat baths and their first neighbors to avoid the direct effect of stochastic dynamics on the flux calculation (see Fig. 6.1). Therefore, the possible minimum system length for any lattice topology $L^d$ is $L = 5$ to compute the flow as desired. Furthermore, to reduce the direct effect of noise on the flux, one can ignore more than two nearest neighbors to the heat baths from the calculation for large systems. The time derivative of the Hamiltonian Eq. 6.1 can be written as

$$\frac{d\mathcal{H}}{dt} = -\frac{1}{2}\sum_{\ell=1}^{L^d}(J_\ell - J_{\ell'}) \tag{6.9}$$

where $J_\ell = (p_\ell + p_{\ell'})\sin(\theta_\ell - \theta_{\ell'})$ is the Lagrangian flux [128], $\ell \in \{1, \cdots, L^d\}$ is a unique label for each site and $\ell'$ is the nearest-neighbor of site-$\ell$ towards to hot reservoir. Therefore, $J_\ell$ is defined as the energy transfer per unit time, per transverse $(d-1)$-dimensional "area" $L^{d-1}$. Note that the calculation of $J_\ell$ is independent of the lattice dimension $d$ since the flow direction is always in one direction from the high temperature end to the cold one. The statement for the flux direction is straightforward for $d = 1$; however, the model for $d > 1$ has periodic boundary conditions for interacting sides on $(d-1)$ dimensions. Then the flux is defined only through the axis where the boundaries are ended with the heat baths in any lattice dimension $d \in \mathbb{Z}^+$. The macroscopic conductivity $\kappa$ only depends on the specific material and its temperature. This is essentially the content of Fourier's 1822 law, where only the macroscopic phenomenon was considered [1].

The (dimensionless) conductivity $\kappa$ and the (dimensionless) "conductance" $\sigma$ are, by definition, related through

$$\kappa \equiv \sigma L^d \,. \tag{6.10}$$

As we shall later on verify, this specific definition of $\sigma$ [29] does not depend, for $d = 1$, on $L$ in the $T \to 0$ limit (see Fig. 2).

The asymptotic power-law relation between $T$ and $\sigma$ (or $\kappa$) was numerically explored for the one-dimensional first-neighbor planar-rotator model [27]. Furthermore, a collapse of the power-law distributions was discovered through the following $q$-Gaussian [29]

$$\sigma(T, L) = \sigma(0, L)\, e_q^{-B_q (L^{1/3} T)^2}\,, \tag{6.11}$$

where, for $d = 1$, $\sigma(0, L)$ is independent from $L$, and $(q, B_q) \simeq (1.55, 0.40)$, the $q$-exponential function being defined as $e_q^z \equiv [1 + (1-q)z]^{1/(1-q)}$ ($e_1^z = e^z$). The $q$-Gaussian form (6.11) was proposed in [29] because, under appropriate simple constraints, it extremizes the nonadditive entropy

$$\begin{aligned} S_q &\equiv k\, \frac{1 - \sum_i p_i^q}{q-1} = k \sum_i p_i \ln_q \frac{1}{p_i} \\ &= -k \sum_i p_i^q \ln_q p_i = -k \sum_i p_i \ln_{2-q} p_i \end{aligned} \tag{6.12}$$

where $k$ is a positive constant such that for $q = 1$, $k = k_B$ ($k_B$ is the Boltzmann constant), and $\ln_q z \equiv \frac{z^{1-q}-1}{1-q}$ ($\ln_1 z = \ln z$) [36, 35, 134]. We straightforwardly verify that $S_1 = S_{BG} \equiv -k \sum_i p_i \ln p_i$, where BG stands for Boltzmann-Gibbs. We also verify that, for two statistically independent systems $X$ and $Y$ (i.e., $p_{ij}^{X+Y} = p_i^X p_j^Y$),

$$\frac{S_q(X+Y)}{k} = \frac{S_q(X)}{k} + \frac{S_q(Y)}{k} + (1-q)\frac{S_q(X)}{k}\frac{S_q(Y)}{k}\,. \tag{6.13}$$

This property exhibits the nonadditivity of the entropic functional $S_q$ for $q \neq 1$. For $q = 1$ we recover the well known BG additivity $S_{BG}(X+Y) = S_{BG}(X) + S_{BG}(Y)$, which follows Penrose's definition of entropic additivity [135].

## 6.3 Results

We revisit here the $d = 1$ results of [29] by exploring higher values of $T$. It turns out that, while the $q$-Gaussian Ansatz was good enough for the conductivity $\sigma$ at the relatively low temperatures considered in [29], the present numerics at a wider range of $T$ require a more general Ansatz, namely the stretched $q$-exponential

$$y(x) = e_q^{-B|x|^\eta} \tag{6.14}$$

with $q \geq 1$, $\eta > 0$ and $B > 0$. The $q$-Gaussian form Eq. (6.11) is recovered as the $\eta = 2$ particular limit of this more general form. The form Eq. (6.14) introduces one more parameter, namely $\eta$, which fits our numerical data very satisfactorily. Note that we used

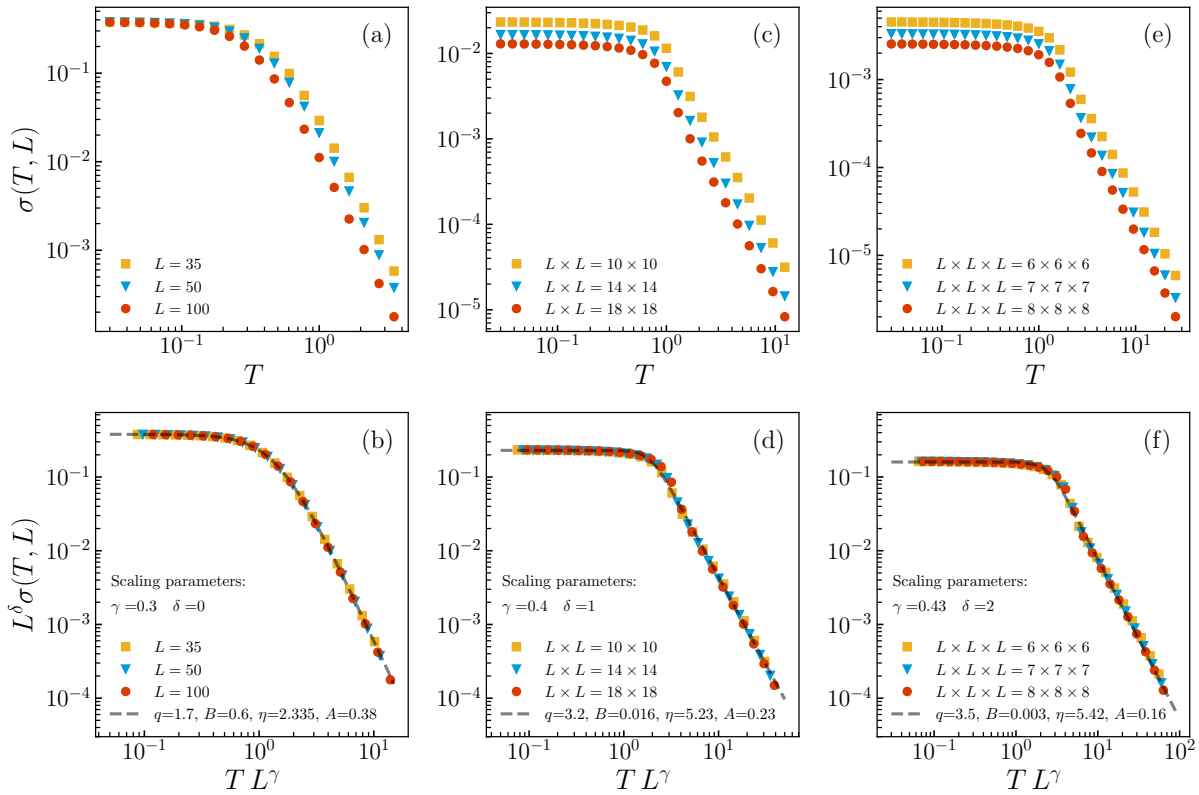


Figure 6.2: Thermal conductance as a function of temperature for $d$-dimensional lattice structures ($d = 1, 2$ and 3). *Top:* Conductance $\sigma$ plotted for (a) dimension $d = 1$ for sizes $L = 35, 50$ and 100, (c) $d = 2$ with $L \times L = 10 \times 10, 14 \times 14$ and $18 \times 18$ and (e) $d = 3$ with $L \times L \times L = 6 \times 6 \times 6, 7 \times 7 \times 7$ and $8 \times 8 \times 8$. *Bottom:* Collapse of $\sigma$ values for all available system sizes in dimensions (b) $d = 1$, (d) $d = 2$ and (f) $d = 3$ using the relations for temperature $T \to TL^{\gamma}$ and $\sigma \to \sigma L^{\delta}$, scaling parameters, $\delta$ and $\gamma$, are given on the associated sub-figures. Collapsed $\sigma$ values are accurately fitted with $\sigma(T, L) = A(1-(1-q)B(TL^{\gamma})^{\eta})^{1/(1-q)}$ using the optimal parameters in the legend for the fitting curves (dashed gray lines). The number of time steps used for all $d$ case is $4 \times 10^8$ and an average is taken over 80 experiments. The number of transients thrown away for the system to attain the stationary state is at least $2.6 \times 10^{11}$ for $d = 1$, $8.0 \times 10^{10}$ for $d = 2$ and $5.6 \times 10^{10}$ for $d = 3$.

the standard least squares method to find the best-fitting curve for our numerical data. By so doing, we follow the successful Ansatz proposed in [136] for neutron experiments with standard spin glasses. This is specifically shown in what follows here below.

All our results for $d = 1, 2$ and 3 collapse in the following universal form:

$$\sigma(T, L)\, L^{\delta(d)} = A(d)\, e_{q(d)}^{-B(d)[T\, L^{\gamma(d)}]^{\eta(d)}} , \tag{6.15}$$

where $(A, B, q, \eta, \gamma, \delta)$ are fitting parameters (Fig. 6.2). Let us emphasize here that Fourier's law corresponds to the $L \to \infty$ limit [1] of this equation, hence, both $\sigma$ and

[1] Out of mere clarification, the asymptotic limit of a $q$-exponential is given by the relation $e_q^{-x} \sim x^{-1/(q-1)}$, then, for a $q$-stretched exponetial as in Eq. (6.15), it follows that $e_q^{-bx^{\eta}} \sim x^{-\eta/(q-1)}$.

$\kappa$ decay with power laws, namely $\sigma \sim 1/L^{\rho_\sigma}$ and $\kappa \sim 1/L^{\rho_\kappa}$, where $\rho_\sigma \equiv \delta + \gamma\frac{\eta}{q-1}$ and $\rho_\kappa \equiv \rho_\sigma - d$ as exhibited in Fig. 6.3. The validation of Fourier's law is confirmed if $\rho_\kappa = 0$ or, equivalently, $\rho_\sigma = d$, making the thermal conductivity independent of the lattice size.

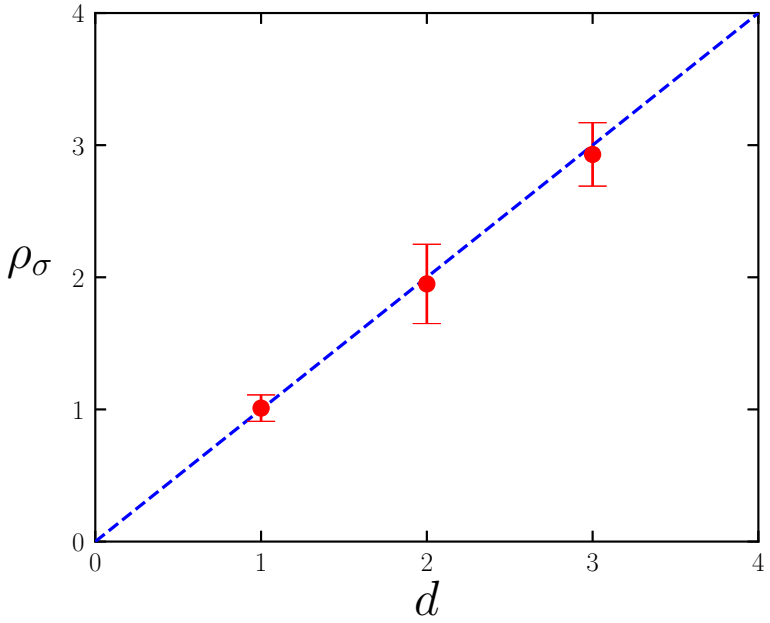


Figure 6.3: $\sigma \propto 1/L^{\rho_\sigma(d)}$ $(L \to \infty)$ and $\kappa = \sigma L^d \propto L^{d-\rho_\sigma(d)}$. The dots correspond to the present numerical results. The dashed line indicates the validity of Fourier's law, i.e., $\lim_{L\to\infty} \kappa(T, L)$ is a finite $T$-dependent quantity. These results strongly suggest that $\rho_\sigma = d$, hence $\rho_\kappa = 0$, for all values of $d$, possibly including noninteger values as well.

In this chapter, we numerically demonstrate that the heat conduction in $XY$-model for all dimensions exhibits no abnormality. For $d = 1, 2, 3$, the thermal conductivity follows a power law behavior, $\kappa_{XY} \sim T^{-\rho_d}$ with $\rho_d = \eta_d/(q_d - 1)$, where $(\rho_1, \rho_2, \rho_3) \approx (3.33, 2.38, 2.17)$ showing a decrease as the dimension increases. The $q$-stretched exponential, a typical function in $q$-statistics, has been proven useful in the study of transport phenomena, particularly, in heat conduction. Furthermore, such approach provides a closed formula to all feasible regimes, facilitating the analysis of the thermodynamic limit.

Does it hold for $n = 1$ vector model? We will see in Chapter 7, numerical evidence of normal heat conduction in the Ising chain.

# Chapter 7

# Ising chain

*The new theories explained in our work are united for ever to the mathematical sciences, and rest like them on invariable foundations; all the elements which they at present possess they will preserve, and will continually acquire greater extent. Instruments will be perfected and experiments multiplied. The analysis which we have formed will be deduced from more general, that is to say, more simple and more fertile methods common to many classes of phenomena.*
J. Fourier, 1822, Théorie Analytique de la Chaleur (English translation).

This chapter is based on the recent article *Ising chain: Thermal conductivity and first-principle validation of Fourier's law*, published in Physica A: Statistical Mechanics and its Applications [40].

In the present study we approach, for a linear chain, the Ising limit via two different types of extremely anisotropic $XY$ models, namely through the addition of a local term in the Hamiltonian (preliminary discussed in [137]), or by allowing the $XY$ interaction to be anisotropic.

## 7.1 Models and methods

Let us first focus on the local possibility. We assume that the Hamiltonian of the inertial $XY$ model includes a local energy being proportional to a self-interaction between spins in the $x$-direction. This Hamiltonian can then be written as follows

$$\mathcal{H}_{XY}^{l} = \sum_{i=1}^{L} \frac{p_i^2}{2} + \frac{1}{2} \sum_{\langle i,j \rangle} \Big[ 1 - \cos(\theta_i - \theta_j) \Big] + \epsilon_l \sum_{i=1}^{L} \sin^2 \theta_i \,, \tag{7.1}$$

where $\epsilon_l \in [0, \infty)$ is a coupling constant associated with this local energy. This model is similar to Blume-Capel one [138, 139], but with $n = 2$ instead of $n = 1$. For increasing

$\epsilon_l$, the third term in the Hamiltonian dominates, thus exhibiting properties that are characteristic of the $n = 1$ class of the Hamiltonian Eq. (5.2). The limit $\epsilon_l \to \infty$ corresponds to a complete crossover from the $XY$ model to the Ising one.

We consider the Hamiltonian described by Eq. (7.1), adding Langevin heat baths acting only on the first and the last particles of the chain with temperatures $T_h$ and $T_l$ ($T_h \geq T_l$) respectively. The corresponding equations of motion are given by

$$\begin{aligned} \dot{\theta}_i &= p_i \ \text{ for } i = 1, \ldots, L \\ \dot{p}_1 &= -\gamma_h p_1 + F_1 + \eta_h(t) \\ \dot{p}_i &= F_i \ \text{ for } i = 2, \ldots, L-1 \\ \dot{p}_L &= -\gamma_l p_L + F_L + \eta_l(t) \end{aligned} \tag{7.2}$$

where the force components are

$$F_i = -\epsilon_l \sin(2\theta_i) - \sum_{\langle j \rangle} \sin(\theta_i - \theta_j)\,, \tag{7.3}$$

where, for each $i$, $\langle j \rangle$ means that we are summing over nearest-neighbor pairs; $\eta_{h/l}$ are Gaussian white noises with correlations

$$\begin{aligned} \langle \eta_{h/l}(t)\eta_{h/l}(t') \rangle &= 2\gamma_{h/l} T_{h/l} \delta(t - t') \\ \langle \eta_h(t)\eta_l(t') \rangle &= 0\,. \end{aligned} \tag{7.4}$$

The heat flux is derived via continuity equation; the Lagrangian heat flux $J_i$ [128] is given by

$$J_i = \frac{1}{2}(p_i + p_{i+1}) \sin(\theta_i - \theta_{i+1})\,. \tag{7.5}$$

Let us emphasize that Eq. (7.5) has the same form $\forall \epsilon_l$, i.e. that of the Lagrangian heat flux of the $XY$ model itself [39]. Despite of the fact that the local term does not contribute to the structure of the heat flux, the evolution of the canonical coordinates is quite different for different values of $\epsilon_l$. Indeed, the presence of the local force [Eq. (7.3)] enters into the average $J \equiv \langle J_i \rangle_{bulk}$, which is then affected by $\epsilon_l$. This average $\langle J_i \rangle_{bulk}$ is considered only for the particles within the bulk, excluding the ends that are naturally affected by the random forces. The thermal conductance $\sigma$ of the chain is defined as follows

$$\sigma \equiv \frac{\kappa}{L} = \frac{J}{T_h - T_l}. \tag{7.6}$$

This definition is obtained through the one-dimensional heat equation $\frac{\partial T}{\partial t} \propto \frac{\partial^2 T}{\partial x^2}$. In the steady state, $\frac{\partial T_{st}}{\partial t} = 0$, where $T_{st} = T_{st}(x)$ is the steady-state temperature field. By imposing the boundary conditions $T_{st}(0) = T_h$ and $T_{st}(L) = T_l$ we have the solution

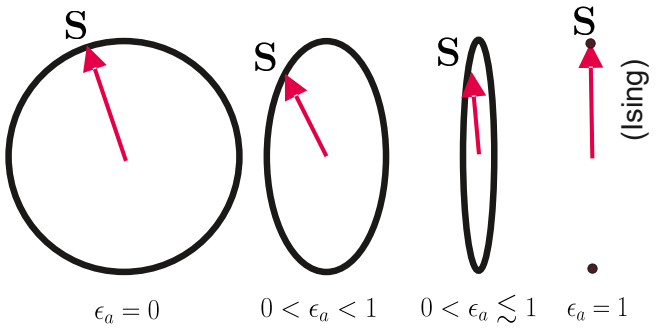


Figure 7.1: Schematic representation of the anisotropic $XY$ coupling.

$T_{st}(x) = \frac{T_l - T_h}{L} x + T_h$, hence the heat flux is given by

$$J = \kappa \frac{T_h - T_l}{L} = \sigma (T_h - T_l)\,, \tag{7.7}$$

consistently with Eq. (7.6).

Let us focus now on the second possibility, namely the anisotropically coupled $XY$-model with $L$ interacting spins $\mathbf{S}_i$. The corresponding Hamiltonian is given by

$$\mathcal{H}^a_{XY} = \sum_{i=1}^{L} \frac{p_i^2}{2} - \mathcal{J}_x \sum_{\langle i,j \rangle} S_i^x S_j^x - \mathcal{J}_y \sum_{\langle i,j \rangle} S_i^y S_i^y \,. \tag{7.8}$$

We define $\mathcal{J}_x \equiv \mathcal{J}(1+\epsilon_a)/2$ and $\mathcal{J}_y \equiv \mathcal{J}(1-\epsilon_a)/2$ with $|\epsilon_a| \leq 1$ and $\mathcal{J} > 0$ . This Hamiltonian can be rewritten in polar coordinates as follows:

$$\mathcal{H}^a_{XY} = \sum_{i}^{L} \frac{p_i^2}{2} + \frac{1}{2} \sum_{\langle i,j \rangle} [1 + \epsilon_a - \cos(\theta_i - \theta_j) - \epsilon_a \cos(\theta_i + \theta_j)] \tag{7.9}$$

Without loss of generality, we set moment of inertia and exchange interaction $\mathcal{J}$ equal to unity. Notice that $\theta_i = 0\ , \forall i$, leads to zero potential energy, for all $\epsilon_a$. Notice also that $\epsilon_a = \pm 1$ correspond to the Ising model along the $y$ and $x$ axes respectively, whereas $\epsilon_a = 0$ recovers the standard isotropic $XY$-model (see Fig. 7.1). The equations of motion are the same as in Eq. (7.2), the forces being now written as follows:

$$F_i = -\sum_{\langle j \rangle} \Big[ \sin(\theta_i - \theta_j) + \epsilon_a \sin(\theta_i + \theta_j) \Big] \,. \tag{7.10}$$

The heat flux of the anisotropically coupled $XY$ model is given by

$$\begin{aligned} J_i = & \frac{p_i + p_{i+1}}{2} \sin(\theta_i - \theta_{i+1}) \\ & + \epsilon_a \frac{p_i - p_{i+1}}{2} \sin(\theta_i + \theta_{i+1}) \,. \end{aligned} \tag{7.11}$$

For both models, we implement the equations of motion with Velocity Verlet algorithm [132, 133]. In our simulation, we set the step size $dt = 0.01$, $\gamma_h = \gamma_l = 1.0$, and the

temperatures $T_{h/l} = T(1 \pm \Delta)$, with $\Delta \equiv 0.125$ arbitrarily chosen as a small value taking account that $T = (T_h + T_l)/2$. The coordinates and momenta are initially set to zero; the sum of the $L$ momenta is only approximately conserved since this is a canonical molecular-dynamical approach.

We directly compute the averages from Eqs. (7.5) and (7.11), assuming a transient time equal to $10^{10}$, which ensures the arrival to the stationary state; we then average the heat flux along 200 equally spaced intervals of $4 \times 10^8$ time-steps. After that, Eq. (7.6) is used for 23 different values for the temperature $T$, with $\epsilon_l$ and $\epsilon_a$ ranging from 0 to 0.7 by steps of 0.1.

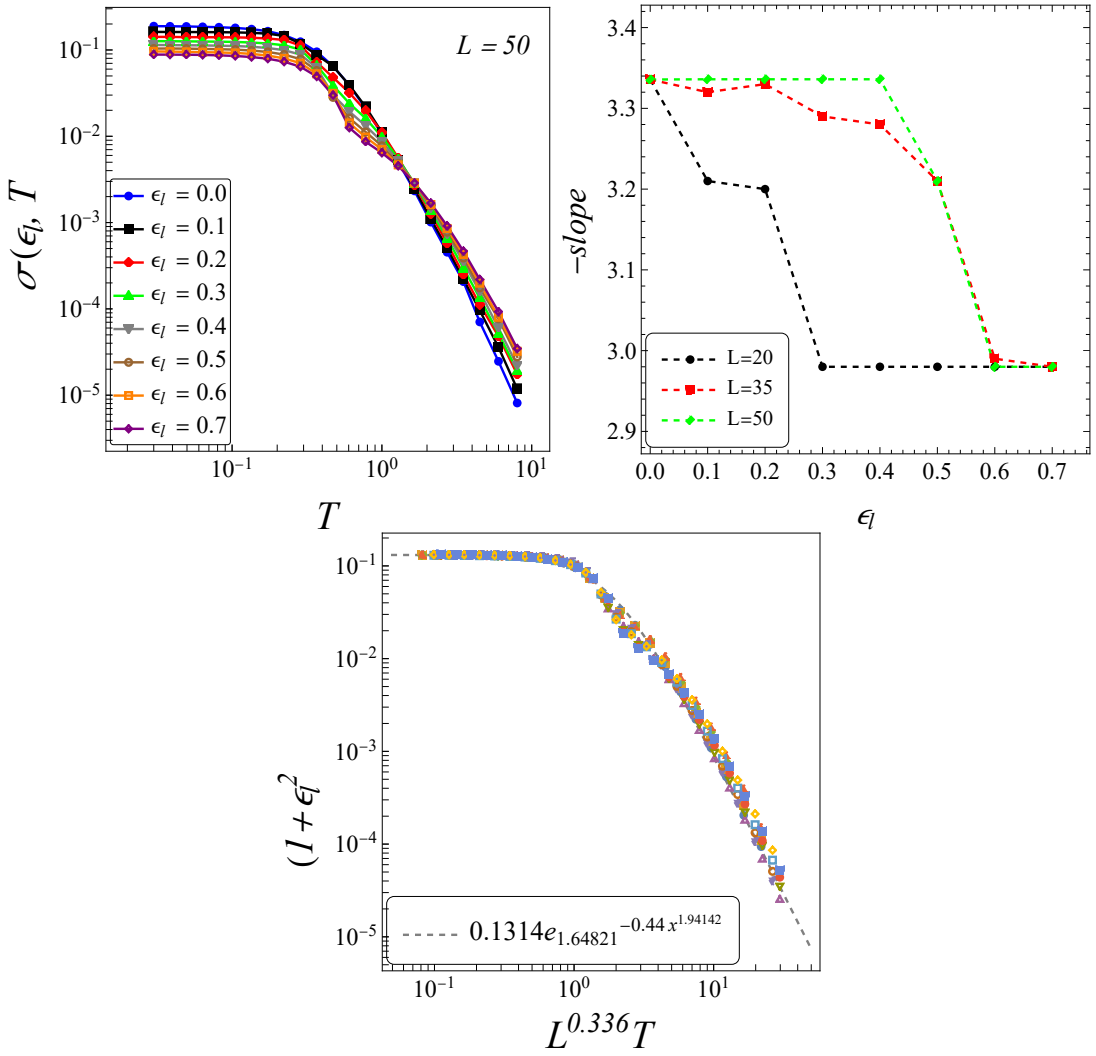


Figure 7.2: *Left:* Thermal conductance of the first anisotropic model as a function of temperature for one-dimensional lattice structure and the local coupling constant for $L = 50$. *Center:* Plot of -slope versus $\epsilon_l$ for $L = 20, 35, 50$. All the curves approach the same saturation value $slope_l \simeq -3.0$. *Right:* Collapse with a stretched $q$-exponential form, from $\epsilon_l = 0.4$ to $\epsilon_l = 0.7$ with $L = 20, 35, 50$. The values of the minimum ($T_{min}$) and maximum ($T_{max}$) temperatures are 0.03 and 8.0 respectively.

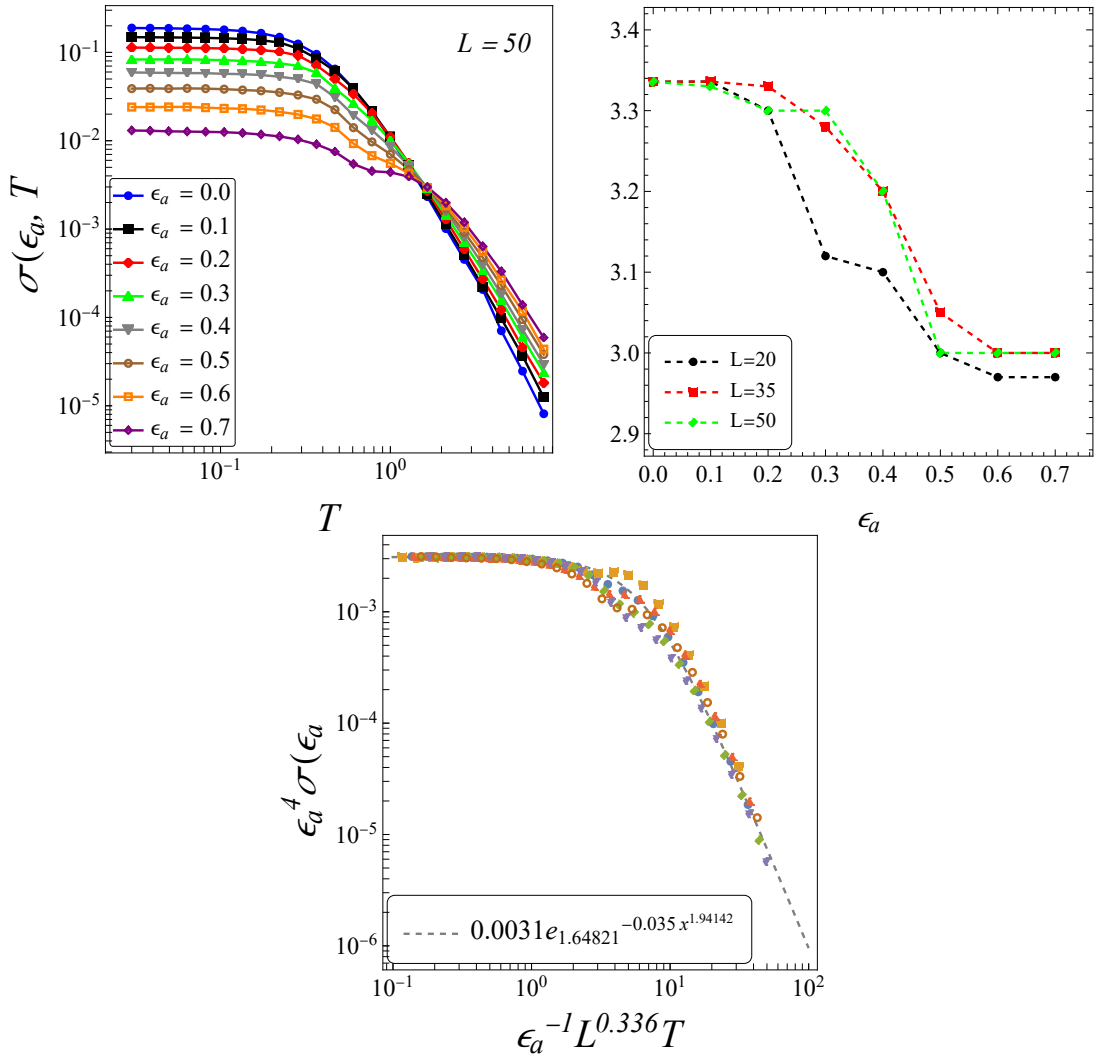


Figure 7.3: *Left:* Thermal conductance of the second anisotropic model as a function of temperature for one-dimensional lattice structure and the local coupling constant for $L = 50$. *Center:* Plot of -slope versus $\epsilon_a$ for $L = 20, 35, 50$. All the curves approach the same saturation value $slope_a \simeq -3.0$. *Right:* Collapse with a stretched $q$-exponential form, for $\epsilon_a = 0.6$ and $\epsilon_a = 0.7$ with $L = 20, 35, 50$. The values of the minimum ($T_{min}$) and maximum ($T_{max}$) temperatures are 0.03 and 8.0 respectively.

## 7.2 Results

We observe in Figs. 7.2 and 7.3 that, at low temperatures, the thermal conductance $\sigma$ decreases for increasing anisotropic parameters $\epsilon_l$ and $\epsilon_a$: $\sigma$ decreases for the first model (Fig. 7.2) slower than for the second one (Fig. 7.3). For the first model, for instance, the decrease is related to the fact that, at small oscillations ($\theta_i \simeq 0$), an additional force $-2\epsilon_l\theta_i$ emerges which reduces the mean heat flux, hence the thermal conductance. A similar effect is present in the second model with regard to $\epsilon_a$.

At intermediate temperatures a crossover becomes preliminary evident. This is due to the fact that the rotators are now at excited states, and therefore start being angularly constrained because of the anisotropy, as depicted in Fig. 7.1. We can see in Fig. 7.2

that, after that intermediate regime, the absolute value of the slope reduces more and more until it saturates, making the cases $\epsilon_l = 0.5, 0.6, 0.7$ to virtually coincide. The Ising regime neatly emerges in the $\epsilon_l > 1/2$ region.

We can collapse all thermal conductances of both models, except in the crossover region, with a stretched $q$-exponential Ansatz (see [136, 39]), defined as

$$y(x) = e_q^{-Bx^\eta} \quad (x \geq 0, q \geq 1, \eta > 0, B > 0)\,, \tag{7.12}$$

where $e_q^z \equiv [1+(1-q)z]^{\frac{1}{1-q}}$ ($e_1^z = e^z$). Consistently with this Ansatz, we verify that, in the thermodynamic limit ($L \gg 1$), $\sigma(\epsilon_l, T) \propto \sigma(\epsilon_a, T) \propto T^{-\frac{\eta}{q-1}}$, where $(\eta, q) \approx (1.94, 1.65)$ thus yielding the slope $\eta/(q-1) \approx 3.0$. This value is already shown in Figs. 7.2 (center) and 7.3 (center). Another important observation is that $\kappa = \sigma L$ does not depend on the system size $L$. This is a simple consequence from the fact that, at fixed temperatures, we have $\sigma \sim L^{-\gamma\frac{\eta}{q-1}}$, with $\gamma = 0.336$, hence $\sigma \propto L^{-1}$, thus validating, through both anisotropic models, the Fourier's law in the Ising limit.

Let us emphasize that, in the isotropic $XY$ model, $\sigma_{XY} \sim T^{-3.34}$ [39] while, in the Ising limit, we have $\sigma_{Ising} \sim T^{-3.0}$. The parameters $(q, \eta, \gamma)$ of the XY and Ising models are sensibly different. However, when all those parameters are combined together, a remarkable numerical result is obtained, namely that the thermal conductivity $\kappa$ becomes asymptotically independent of the lattice size, thus obeying Fourier's law. It should be noted that $\frac{\eta\gamma}{q-1} \approx 1$ for both the Ising and $XY$ linear chains. It is in fact plausible to expect that, for the $n$-vector models, $\frac{\eta\gamma}{q-1} \approx 1$ for all values of $n$ .

Therefore, in response to the question posed in Chapter 6, it is indeed confirmed that the Ising chain exhibits normal heat conduction, with $\kappa_{Ising} \sim T^{-3}$, and it does not depend on lattice size. We will now pose another question: Does it also hold for $n = 3$ vector models? In Chapter 8, we will present numerical evidence supporting the conclusion that there is no abnormality in heat conduction for the Heisenberg chain, and therefore for $n = 1, 2, 3$ vector models as well.

# Chapter 8

# Heisenberg chain

*THE effects of heat are subject to constant laws which cannot be discovered without the aid of mathematical analysis. The object of the theory which we are about to explain is to demonstrate these laws; it reduces all physical researches on the propagation of heat, to problems of the integral calculus whose elements are given by experiment. No subject has more extensive relations with the progress of industry and the natural sciences; for the action of heat is always present, it penetrates all bodies and spaces, it influences the processes of the arts, and occurs in all the phenomena of the universe.*

J. Fourier, 1822, Théorie Analytique de la Chaleur (English translation).

This chapter is based on the recent article *First-Principle Validation of Fourier's Law: One-Dimensional Classical Inertial Heisenberg Model*, published in Entropy [41].

In the present work, we analyze the thermal transport in a one-dimensional classical inertial Heisenberg model of linear size $L$, considering the first and last particles in thermal contact with heat baths at temperatures $T_h$ and $T_l$ ($T_h > T_l$), respectively.

## 8.1 Model and Methods

The one-dimensional classical inertial Heisenberg model, for a system of $L$-interacting rotators, is defined by the Hamiltonian,

$$\mathcal{H} = \frac{1}{2}\sum_{i=1}^{L} \boldsymbol{p}_i^2 + \frac{1}{2}\sum_{\langle ij \rangle} \left(1 - \mathbf{S}_i \cdot \mathbf{S}_j\right) , \tag{8.1}$$

where $\boldsymbol{p}_i \equiv (p_{ix}, p_{iy}, p_{iz})$ and $\mathbf{S}_i \equiv (S_{ix}, S_{iy}, S_{iz})$ represent, respectively, continuously varying angular momenta and spin variables at each site of the linear chain, whereas $\sum_{\langle ij \rangle}$ denote summations over pairs of nearest-neighbor spins; herein, we set, without loss of

generality, $k_{\rm B}$, moments of inertia, and ferromagnetic couplings, all equal to the unit. Moreover, spins present the unit norm, $\mathbf{S}_i^2 = 1$, and at each site, angular momentum $\boldsymbol{p}_i$ must be perpendicular to $\mathbf{S}_i$, yielding $\boldsymbol{p}_i \cdot \mathbf{S}_i = 0$; these two constraints are imposed at the initial state and should be preserved throughout the whole time evolution.

One should notice that, in contrast to a system of coupled classical XY rotators, where canonical conjugate polar coordinates are commonly used [39], in the Heisenberg case, one often chooses Cartesian coordinates [140, 122, 141]. The reason for this is essentially technical, since in terms of spherical coordinates (more precisely, $\theta, \phi$, and their canonical conjugates $p_\theta, p_\phi$), a troublesome term $(1/\sin^2\theta)$ appears in the corresponding equations of motion, leading to numerical difficulties [142, 143]. However, some of the analytical results to be derived next recover those of the classical inertial XY model for $\mathbf{S}_i = (\sin\theta_i, \cos\theta_i, 0)$ and $\boldsymbol{p}_i = p_i\hat{\mathbf{z}}$.

It is important to mention that previous research on the thermal conductivity has been carried out for a classical one-dimensional Heisenberg spin model, by using Monte Carlo and Langevin numerical simulations [25], as well as for a classical one-dimensional spin-phonon system, through linear-response theory and the Green–Kubo formula [144]. These investigations did not take into account the kinetic contribution in Equation (8.1), so that in order to obtain the thermal conductivity they assumed the validity of Fourier's law. The main advantage of the introduction of the kinetic term in Equation (8.1) concerns the possibility of deriving equations of motion, making it feasible to follow the time evolution of the system through molecular-dynamics simulations, by a numerical integration of such equations. This technique allows one to validate Fourier's law, as well as obtain its thermal conductivity directly.

In order to carry out this procedure, we consider an open chain of rotators with the first and last particles in thermal contact with heat baths at higher and lower temperatures, $T_h$ and $T_l$ ($T_h > T_l$), respectively (cf. Figure 10.1), whereas all remaining rotators ($i = 2, \cdots, L-1$) follow their usual equations of motion (see, e.g., Refs. [140, 122, 141]). In this way, one has for sites $i = 2, \ldots, L-1$,

$$\begin{aligned} \dot{\mathbf{S}}_i &= \boldsymbol{p}_i \times \mathbf{S}_i \ , \\ \dot{\boldsymbol{p}}_i &= \mathbf{S}_i \times (\mathbf{S}_{i+1} + \mathbf{S}_{i-1}) \ , \end{aligned} \tag{8.2}$$

whereas the rotators at extremities follow standard Langevin dynamics,

$$\begin{aligned} \dot{\boldsymbol{p}}_1 &= -\gamma_h \boldsymbol{p}_1 + \mathbf{S}_1 \times \mathbf{S}_2 + \boldsymbol{\eta}_h \ , \\ \dot{\boldsymbol{p}}_L &= -\gamma_l \boldsymbol{p}_L + \mathbf{S}_L \times \mathbf{S}_{L-1} + \boldsymbol{\eta}_l \ . \end{aligned} \tag{8.3}$$

Above, $\gamma_h$ and $\gamma_l$ represent friction coefficients, whereas $\boldsymbol{\eta}_h$ and $\boldsymbol{\eta}_l$ denote independent three-dimensional vectors, $\boldsymbol{\eta}_h \equiv (\eta_{hx}, \eta_{hy}, \eta_{hz})$, $\boldsymbol{\eta}_l \equiv (\eta_{lx}, \eta_{ly}, \eta_{lz})$, where each Cartesian component stands for a Gaussian white noise with zero mean and correlated in time,

$$
\begin{aligned}
&\langle \eta_{h\mu}(t) \rangle = \langle \eta_{l\mu}(t) \rangle = 0 \ , \\
&\langle \eta_{h\mu}(t) \eta_{l\nu}(t') \rangle = \langle \eta_{h\mu}(t') \eta_{l\nu}(t) \rangle = 0 \ , \\
&\langle \eta_{h\mu}(t) \eta_{h\nu}(t') \rangle = 2\delta_{\mu\nu}\gamma_h T_h \delta(t-t') \ , \\
&\langle \eta_{l\mu}(t) \eta_{l\nu}(t') \rangle = 2\delta_{\mu\nu}\gamma_l T_l \delta(t-t') \ ,
\end{aligned}
\tag{8.4}
$$

with the indexes $\mu$ and $\nu$ denoting Cartesian components; from now on, we will set the friction coefficients $\gamma_h$ and $\gamma_l$ equal to the unit. One should mention that different types of thermostats have been used to investigate transport properties in systems out of equilibrium (see, e.g., Ref. [145] for an application of Nosé–Hoover thermostats to a system of interacting planar rotators); however, for the present Heisenberg chain, we found it more convenient to use standard Langevin thermostats, as defined above.

The condition of a constant norm for the spin variables yields

$$
\frac{dS_i}{dt} = \frac{d\left(\mathbf{S}_i \cdot \mathbf{S}_i\right)^{1/2}}{dt} = 0 \quad \Rightarrow \quad \mathbf{S}_i \cdot \dot{\mathbf{S}}_i = 0 \ , \tag{8.5}
$$

which should be used together with $\boldsymbol{\ell}_i \cdot \mathbf{S}_i = 0$ in order to eliminate $\ddot{\boldsymbol{\ell}}_i$ and calculate $\ddot{\mathbf{S}}_i$ from Equations (8.2) and (8.3). For rotators at sites $i = 2, \cdots, L-1$, one has

$$
\ddot{\mathbf{S}}_i = \left(\mathbf{S}_{i+1} + \mathbf{S}_{i-1}\right) - \left[\mathbf{S}_i \cdot \left(\mathbf{S}_{i+1} + \mathbf{S}_{i-1}\right) + \dot{\mathbf{S}}_i^2\right] \mathbf{S}_i \ , \tag{8.6}
$$

whereas, for those at extremities,

$$
\begin{aligned}
\ddot{\mathbf{S}}_1 &= -\dot{\mathbf{S}}_1 + \mathbf{S}_2 - \left[\mathbf{S}_1 \cdot \mathbf{S}_2 + \dot{\mathbf{S}}_1^2\right] \mathbf{S}_1 + \mathbf{S}_1 \times \boldsymbol{\eta}_h \ , \\
\ddot{\mathbf{S}}_L &= -\dot{\mathbf{S}}_L + \mathbf{S}_{L-1} - \left[\mathbf{S}_L \cdot \mathbf{S}_{L-1} + \dot{\mathbf{S}}_L^2\right] \mathbf{S}_L + \mathbf{S}_L \times \boldsymbol{\eta}_l \ .
\end{aligned}
\tag{8.7}
$$

For the system illustrated in Figure 8.1, we will consider the temperatures of the heat baths differing by $2\varepsilon$, with $\varepsilon$ representing a positive dimensionless parameter; moreover, the temperature parameter $T = (T_h + T_l)/2$ will vary in a certain range of positive values. Equations (8.6) and (8.7) are transformed into first-order differential equations (e.g., by defining a new variable $\mathbf{V}_i \equiv \dot{\mathbf{S}}_i$) to be solved numerically through the velocity Verlet method [132, 133], with a time step $dt = 0.005$, for different lattice sizes $L$ . The rotators at the bulk (i$= 2, \cdots, L-1$) follow a continuity equation,

$$
\frac{dE_i}{dt} = -(J_i - J_{i-1}) \ , \tag{8.8}
$$

where

$$
E_i = \frac{1}{2}\boldsymbol{p}_i^2 + \frac{1}{2}\sum_{j=i\pm1}\left(1 - \mathbf{S}_i \cdot \mathbf{S}_j\right) \ , \tag{8.9}
$$

so the stationary state is attained for $(dE_i/dt) = 0$, i.e., $J_i = J_{i-1}$. The derivation is simple, since from Equation (8.5) and $\mathbf{p}_i \cdot \mathbf{S}_i = 0$, we have $\dot{\mathbf{S}}_i^2 = \mathbf{p}_i^2$, hence,

$$\frac{d}{dt}E_i = \dot{\mathbf{S}}_i \cdot \ddot{\mathbf{S}}_i - \frac{1}{2}\left[\dot{\mathbf{S}}_i \cdot (\mathbf{S}_{i+1} + \mathbf{S}_{i-1}) + \mathbf{S}_i \cdot \left(\dot{\mathbf{S}}_{i+1} + \dot{\mathbf{S}}_{i-1}\right)\right] . \tag{8.10}$$

This equation, together with Equation (8.6), yields

$$\frac{d}{dt}E_i = \frac{1}{2}\left[\dot{\mathbf{S}}_i \cdot (\mathbf{S}_{i+1} + \mathbf{S}_{i-1}) - \mathbf{S}_i \cdot \left(\dot{\mathbf{S}}_{i+1} + \dot{\mathbf{S}}_{i-1}\right)\right] = 0 \tag{8.11}$$

at the stationary state. Data are obtained at stationary states, which, as usual, take longer to reach for increasing lattice sizes. For numerical reasons, to decrease fluctuations in the bulk due to the noise, we compute an average heat flux by discarding a certain number of particles $k$ near the extremities (typically $k \simeq 0.15L$). In this way, we define an average heat flux as

$$J \equiv \frac{1}{L-2k}\sum_{i=k+1}^{L-k}\langle J_i\rangle \ , \tag{8.12}$$

$$J_i = \frac{1}{2}\left(\mathbf{S}_i \cdot \dot{\mathbf{S}}_{i+1} - \mathbf{S}_{i+1} \cdot \dot{\mathbf{S}}_i\right) \ , \tag{8.13}$$

whereas $\langle..\rangle$ denotes time and sample averages, which will be described next.

Let us emphasize that for $\mathbf{S}_i = (\sin\theta_i, \cos\theta_i, 0)$ and $\boldsymbol{p}_i = p_i\hat{\mathbf{z}}$, one recovers the expression for the heat flux of the classical inertial XY model, i.e., $J_i = \frac{1}{2}(p_i + p_{i+1})\sin(\theta_i - \theta_{i+1})$ [39, 128], showing the appropriateness of the Cartesian-coordinate approach used herein for the classical inertial Heisenberg model.

Let us now describe the time evolution procedure; for a time step $dt = 0.005$, each unit of time corresponds to 200 integrations of the equations of motion. We considered a transient of $5 \times 10^7$ time units to compute the averages $\langle J_i\rangle$ in Equation (8.12), and checked that this transient time was sufficient to fulfill the condition $J_i = J_{i-1}$ (within, at least, a three-decimal digits accuracy), for all values of $L$ analyzed. After that, simulations were carried out for an additional interval of $2 \times 10^8$ time units (leading to a total time of $2.5 \times 10^8$ for each simulation). The interval $2 \times 10^8$ was divided into 80 equally spaced windows of $2.5 \times 10^6$ time units, so that time averages were taken inside each window; then an additional sample average was taken over these 80 time windows, leading to the averages $\langle J_i\rangle$.

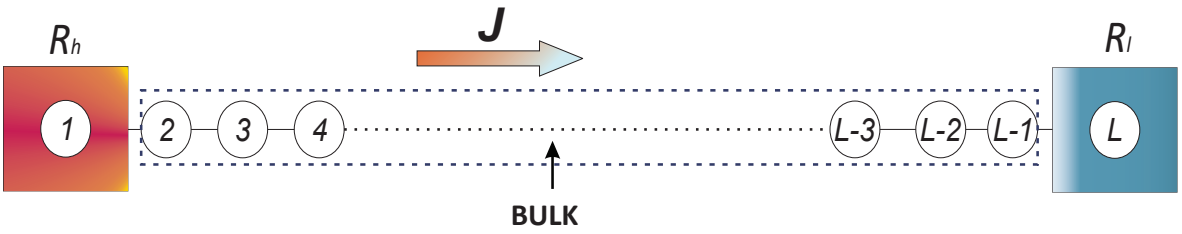


Figure 8.1: Illustration of the system defined in Equation (8.1), where the rotators at extremities of the chain are subjected to heat baths at different temperatures. The hot ($R_h$) and cold ($R_l$) reservoirs are at temperatures $T_h = T(1+\varepsilon)$ and $T_l = T(1-\varepsilon)$, respectively, leading to an average heat flux $\mathbf{J} = J\mathbf{x}$ throughout the bulk (see text). The rotators at sites $i = 2, \ldots, L-1$ interact with their respective nearest neighbors.

Using the results of Equation (8.12), one may calculate the thermal conductivity and consequently, the thermal conductance by the relation,

$$\sigma = \frac{J}{T_h - T_l} = \frac{J}{2T\varepsilon} \equiv \frac{\kappa}{L} \; . \tag{8.14}$$

In the next section, we present the results of both quantities, obtained from the numerical procedure described above.

## 8.2 Results

We simulate the system of Figure 8.1 for different lattice sizes, namely, $L = 50, 70, 100$, 140, considering the heat-bath temperatures differing by $2\varepsilon$, with $\varepsilon = 0.125$. The temperature parameter $T = (T_h + T_l)/2$ varied in the interval $0 < T \leq 3.5$, capturing both low- and high-temperature regimes. The values of $L$ ($L \geq 50$) were chosen adequately to guarantee that the thermal conductivity $\kappa$ did not present any dependence on the size $L$ in the high-temperature regime, as expected.

In Figure 8.2, we present numerical data for the thermal conductivity Figure 2a and thermal conductance Figure 2b versus temperature (log–log representations) and different sizes $L$. The similar qualitative behaviors of the data displayed in both properties of Figure 10.2, for different values of $L$, evidence that the sizes considered in the present analysis ($L \geq 50$) are sufficiently large, in the sense that finite-size effects do not play a relevant role. In Figure 10.2a, we exhibit $\kappa(L,T)$ (the dependence of the thermal conductivity on the size $L$, used herein, will become clear below), showing a crossover between two distinct regimes (for $T \simeq 0.3$), as described next. (i) A low-temperature regime, where $\kappa$ depends on the size $L$, decreasing smoothly for increasing temperatures ($L$ fixed). The plots of Figure 10.2a show that, in the limit $T \to 0$, an extrapolated value, $\kappa(L,0) \equiv \lim_{T\to 0} \kappa(L,T)$, increases with $L$. Such a low-temperature increase with $L$ has been observed in other one-dimensional models (see, e.g., Refs. [145, 27, 29, 39]) and is reminiscent of the behavior expected for a chain of coupled classical harmonic oscillators. This anomaly is

attributed to the classical approach used herein, indicating that for low temperatures, a quantum–mechanical procedure should be applied. (ii) A high-temperature regime, where $\kappa$ essentially does not depend on $L$ (in the limit $L \to \infty$), as expected from Fourier's law. Moreover, in this regime, one notices that $\kappa$ decreases with the temperature as it generally occurs with liquids and solids. For increasing temperature, the thermal conductivity of most liquids usually decreases as the liquid expands and the molecules move apart; in the case of solids, due to lattice distortions, higher temperatures make it more difficult for electrons to flow, leading to a reduction in their thermal conductivity. The results of Figure 10.2a indicate that the thermal conductivity becomes independent of the lattice size in the limit $L \to \infty$, scaling with the temperature as $\kappa(T) \sim T^{-2.25}$ at high temperatures. Therefore, the system becomes a thermal insulator at high temperatures, approaching this state according to $\kappa(T) \sim T^{-2.25}$. Despite the simplicity of the one-dimensional classical inertial Heisenberg model of Figure 10.1, the present results are very close to experimental verifications in some antiferromagnetic electrical insulators, such as the Heisenberg chain cuprates $Sr_2CuO_3$ and $SrCuO_2$, for which the thermal conductivity is well-fitted by a $1/T^2$ law at high temperatures [146]. We should note that the one-dimensional Heisenberg model with nearest-neighbor ferromagnetic interactions, defined by the Hamiltonian of Equation (8.1), does not present an equilibrium phase transition, being characterized by a paramagnetic state for all temperatures $T > 0$. In this case, one may perform the following transformations in the Hamiltonian of Equation (8.1), leaving it unaltered: $1/2 \to -1/2$ (which incorporates the coupling constant), as well as $\mathbf{S}_j \to -\mathbf{S}_j$, keeping $\mathbf{S}_i$ unchanged. Consequently, the Hamiltonian of Equation (8.1) applies to antiferromagnetic systems at high temperatures, as well.

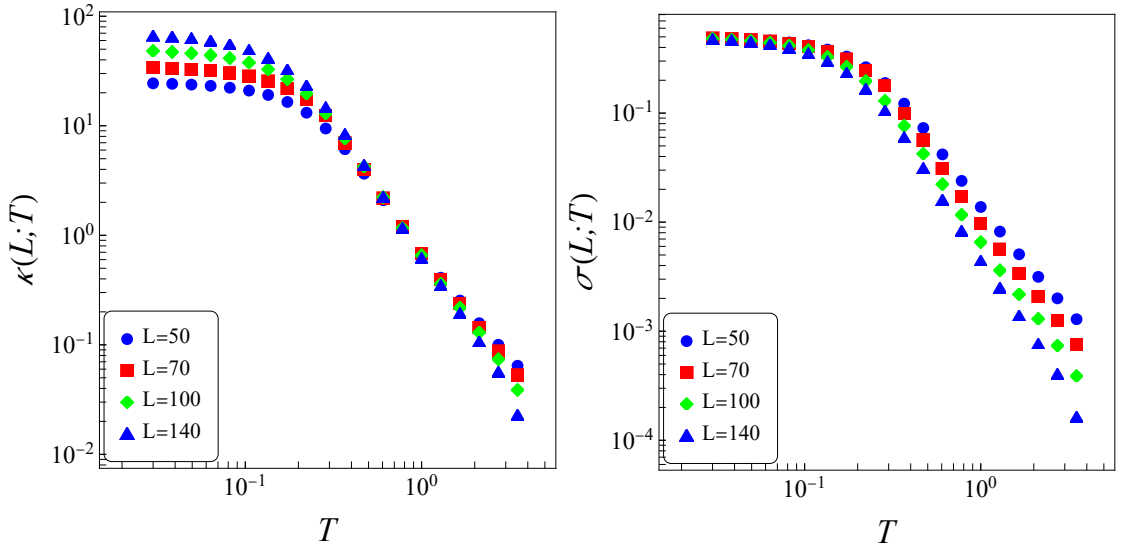


Figure 8.2: Numerical data for the thermal conductivity [panel (**a**)] and thermal conductance [panel (**b**)] are represented versus temperature (log–log plots) for different sizes ($L = 50, 70, 100, 140$) of the one-dimensional classical inertial Heisenberg model. One notices a crossover between the low- and high-temperature regimes for $T \simeq 0.3$. As expected, higher temperatures amplify the effects of the multiplicative noise, which is proportional to the square root of the corresponding temperatures $(T_h, T_l)$, currently leading to larger fluctuations in numerical data, as shown in panel (**a**). All quantities shown are dimensionless.

The same data of Figure 10.2a are exhibited in Figure 10.2b where we plot the thermal conductance $\sigma(L,T) = \kappa(L,T)/L$ versus temperature, characterized by the two distinct temperature regimes described above. The low-temperature regime shows that the zero-temperature extrapolated value $\kappa(L,0)$ scales as $\kappa(L,0) \sim L$, leading to $\sigma(L,0) \equiv \lim_{T\to 0} \kappa(L,T)/L \simeq 0.5$. Such low-temperature results are in full agreement with those obtained in previous simulations of coupled classical XY rotators [145, 27, 29, 39]. On the other hand, in the high-temperature regime, the thermal conductance presents a dependence on $L$, as expected.

In Figure 8.3, we exhibit the thermal-conductance data of Figure 8.2b in conveniently chosen variables, yielding a data collapse for all values of $L$ considered. The full line essentially represents the form of Equation (1.8), so that one writes

$$\sigma(L,T) = A \exp_q(-Bx^\eta) \ , \tag{8.15}$$

where $x = L^{0.475}T$, $q = 2.28 \pm 0.04$, $\eta = 2.88 \pm 0.04$, $A = 0.492 \pm 0.002$, and $B = 0.33 \pm 0.04$. Notice that this value of $\eta$ lies outside the range of what is commonly known as "stretched" [cf. Equation (1.8)], so that the form above should be considered rather as a "shrinked" $q$-exponential.

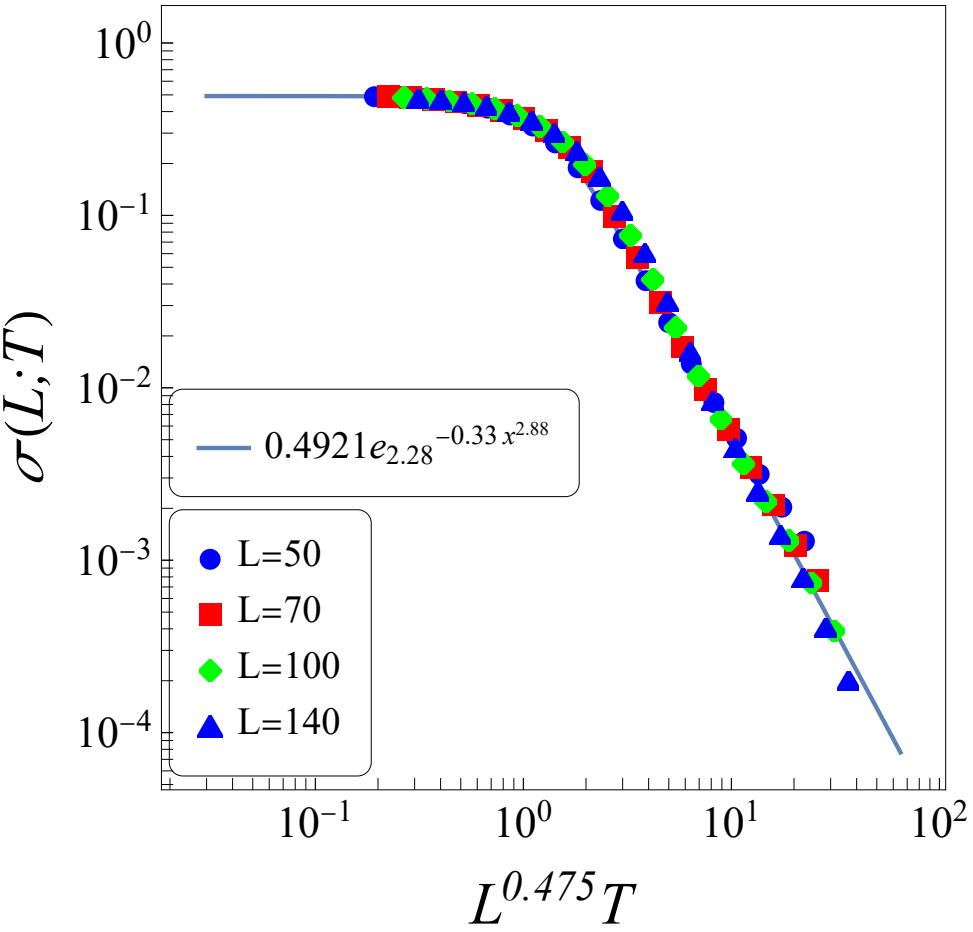


Figure 8.3: The plots for the thermal conductance of Figure 8.2b are shown in a log–log representation, for a conveniently chosen abscissa ($x = L^{0.475}T$), leading to a collapse of data for all values of $L$ considered. The fitting (full line) is given by the function of Equation (8.15).

It should be mentioned that, in the case of coupled nearest-neighbor-interacting classical XY rotators on $d$-dimensional lattices ($d = 1, 2, 3$) [39], the thermal conductance was also fitted by the form of Equation (8.15), with values of $\eta(d) > 2$. In particular, in the one-dimensional case, such a fitting was attained for $x = L^{0.3}T$, $q = 1.7$, and $\eta = 2.335$, showing that these numbers present a dependence on the number of spin components ($n = 2$, for XY spins and $n = 3$, for Heisenberg spins), as well as on the lattice dimension $d$. It is important to mention that the generalized forms in Equations (1.8) and (8.15) have been used in the literature for an appropriate description of a wide variety of physical phenomena, like velocity measurements in a turbulent Couette–Taylor flow [147], relaxation curves of RKKY spin glasses, such as CuMn and AuFe [136], cumulative distribution for the magnitude of earthquakes [148], and more recently, for the thermal conductance of a system of interacting XY rotators [39]. Moreover, its associated entropic form has been studied in detail in Ref. [38].

By defining the abscissa variable of Figure 8.3 in the general form $x = L^{\gamma(n,d)}T$, and using the $q$-exponential definition of Equation (1.3), the slope of the high-temperature

| $\frac{\eta\gamma}{q-1}$ | $d=1$ (linear chain) | $d=2$ (square lattice) | $d=3$ (simple cubic lattice) |
|---|---|---|---|
| $n=1$ (Ising ferromagnet) | 1.0063±0.015 $q=1.65\pm0.025$, $\eta=1.94\pm0.13$, $\gamma=0.336\pm0.003$ | — | — |
| $n=2$ ($XY$ ferromagnet) | 1.0007±0.005 $q=1.7\pm0.01$, $\eta=2.335\pm0.0125$, $\gamma=0.3\pm0.015$ | 0.95±0.22 $q=3.2\pm0.36$, $\eta=5.23\pm0.65$, $\gamma=0.4\pm0.06$ | 0.93±0.18 $q=3.5\pm0.34$, $\eta=5.42\pm0.65$, $\gamma=0.43\pm0.01$ |
| $n=3$ (Heisenberg ferromagnet) | 1.069± 0.083 $q=2.28\pm0.04$, $\eta=2.88\pm0.04$, $\gamma=0.475\pm0.0085$ | — | — |

Table 8.1: Values of the ratio $\eta\gamma/(q-1)$ (highlighted in blue color) analyzed up to the moment: $n=1$ ($d=1$) [40], $n=2$ (dimensions $d=1,2,3$) [39], together with the present results for $n=3$ ($d=1$). In all cases studied, the limit of Eq. (8.17) is numerically approached.

part of the thermal-conductance data scales with $L$, as

$$\sigma \sim L^{-[\eta(n,d)\gamma(n,d)]/[q(n,d)-1]} \ , \tag{8.16}$$

where we introduce the dependence $(n,d)$ on all indices. Since the thermal conductivity ($\kappa = L\sigma$) should not depend on the size $L$ (in the limit $L\to\infty$), Fourier's law becomes valid for

$$\frac{\eta(n,d)\gamma(n,d)}{q(n,d)-1} = 1 \ . \tag{8.17}$$

The data of Figure 8.3 lead to $[\eta(3,1)\gamma(3,1)]/[q(3,1)-1] = 1.069\pm0.083$, whereas those for XY rotators on $d$-dimensional lattices yield $1.0007, 0.95$, and $0.93$, for $d=1,2$, and 3, respectively [39], indicating the validation of Fourier's law for systems of coupled nearest-neighbor-interacting classical $n$-vector rotators, through the thermal conductance form of Equation (8.15).

Recently, similar analyses were carried out for an XY Hamiltonian with anisotropies, in such a way to approach the Ising model in particular limits [40]. All the results for the quantity in Equation (8.17), computed up to the moment, are summarized in Table 8.1, where one notices that finite-size effects play an important role in increasing dimensions, as expected.

In summary, we demonstrated that (i) for the classical one-dimensional inertial ferromagnetic Heisenberg model, the (macroscopic) Fourier-law is validated from (microscopic) first principles, i.e., the temperature-dependent thermal conductivity is, in the high-temperature regime, finite and independent of the system size (the low-temperature regime is to be handled within a quantum grounding, which is out of the goal of the present paper); (ii) For all temperatures and sizes, the thermal conductivity appears to be consistent with $q$-statistics since it can be neatly collapsed within a shrunken $q$-exponential form; (iii) within this shrunken $q$-exponential form, a single universal condition, namely $\frac{\eta(n,d)\gamma(n,d)}{q(n,d)-1} = 1$, validates the Fourier law for the $n$-vector models for $n=1,2,3$, which constitutes a numerical indication that this centennial macroscopic law is possibly valid for all values of $(n,d)$, where $n\to\infty$ and $n\to0$ correspond to the spherical model and 'self-avoiding walk', respectively. It is not our present aim to review the rich existing literature on the validity of the Fourier law within diverse classical and quantum approaches,

but we rather restrict our focus to analytical and numerical first-principle approaches of classical systems that are similar to the present one.

# Chapter 9

# $\alpha$-$XY$ chain

This chapter is based on a ongoing research entitled *Fourier's law breakdown for the planar-rotator chain with generic-range coupling*, which will be available in a preprint version soon [42].

The purpose of the present work is to numerically study how this behavior is generalized in the presence of generically-ranged interactions $1/r_{ij}^{\alpha}$ ($\alpha \geq 0$) in the same type of inertial XY model [119, 120]. The $\alpha \to \infty$ limit recovers the above-mentioned nearest-neighborhood case and, in the $\alpha = 0$ limit, we recover the mean field model [121]. The influence of arbitrary $\alpha$ in this peculiar heat transport phenomenon was approached in [28], where the existence of a special value of $\alpha$ was detected, such that above it the Fourier's law is satisfied at high temperatures, whereas it is violated in all cases below that special value.

For clarity, let us anticipate at this stage our present main conclusion, namely that the results can, in all cases, be collapsed in the following universal form: $L^{\delta_\alpha}\sigma(T, L; \alpha) = A_\alpha e_{q_\alpha}^{-B_\alpha (L^{\gamma_\alpha} T)^{\eta_\alpha}}$, where $(\gamma_\alpha, \delta_\alpha, A_\alpha, B_\alpha)$ are $\alpha$-dependent non-negative coefficients and $q_\alpha$ is the index of the $q$-stretched exponential. We also investigate the threshold where, from that, the Fourier's law holds.

## 9.1 Model

Let us focus now on the details of the model, the numerical method, and the set of results. The Hamiltonian of the classical inertial one-dimensional $\alpha - XY$ is given by

$$\mathcal{H} = \sum_{i=1}^{L} \frac{p_i^2}{2} + \frac{\varepsilon}{2\tilde{L}} \sum_{\substack{j=1 \\ j \neq i}}^{L} \sum_{i=1}^{L} \frac{1 - \cos(\theta_i - \theta_j)}{r_{ij}^{\alpha}}\,, \tag{9.1}$$

where $p_i$ and $\theta_i$ are the angular momenta and coordinates (respectively), and

$$\tilde{L} \equiv \frac{1}{L} \sum_{\substack{i,j \\ j \neq i}} r_{ij}^{-\alpha} \,, \tag{9.2}$$

with $r_{ij} \equiv |i-j|$. We set the moment of inertia of the rotators as a unit, without loss of generality. The factor $\tilde{L}$ is introduced to make the Hamiltonian extensive (following the current notation in the literature) [119]. For $\alpha = 0$ we have $\tilde{L} = L - 1 \sim L$, and for $\alpha \to \infty$ we have $\tilde{L} = 2$. For the $d$-dimensional case, we change $\tilde{L} \to \tilde{N}$, where $N$ is no longer the linear lattice size. In the general case, for $\alpha = 0$ we have $\tilde{N} = N - 1 \sim N$, and for $\alpha \to \infty$ we have $\tilde{N} = 2d$, where $d$ is the dimension of the system (in the present case, $d = 1$). The general expression of $\tilde{N}$ is given by a relation proportional to

$$\ln_{\alpha/d} N \equiv \frac{N^{1-\alpha/d} - 1}{1 - \alpha/d} \,, \tag{9.3}$$

which for $0 \leq \alpha/d < 1$ this factor behaves as $\tilde{N} \sim N^{1-\alpha/d}$, for $\alpha/d = 1$ it presents a logarithmic divergence as $\tilde{N} \sim \ln N$. For $\alpha/d > 1$, this factor goes to a finite value, at the thermodynamic limit. So, there is a critical value, $\alpha_c/d = 1$, which, below this specific value, the system is very long-ranged, and above that, the system changes to other types of interaction.

Let us clarify that for $0 \leq \alpha/d < 1$, the system is very long-ranged, while for $1 < \alpha/d < \infty$ the system is long-ranged. The particular case of nearest-neighbors is the only one that is consistent with the definition of short-range interaction. The main explanation is because only for $\alpha/d \to \infty$ we can guarantee that all momenta of its distribution are finite, and beyond that, for all cases in which $\alpha/d < \infty$, the power law behavior of the interactions can not be neglected. From now on, let us use the notation for the one-dimensional system where only the linear lattice size is important, namely $L$, hence, $\tilde{L}$.

The equations of motion of the Hamiltonian described by Eq. (9.1), adding a Langevin heat bath whose only the first and the last particles are coupled in the heat bath with temperatures $T_h$ and $T_l$ ($T_h > T_l$), respectively, are given by:

$$\begin{aligned}
\dot{\theta}_i &= p_i \;\text{ for } i = 1, \ldots, L \\
\dot{p}_1 &= -\gamma_h p_1 + F_1 + \sqrt{2\gamma_h T_h}\eta_h(t) \\
\dot{p}_i &= F_i \;\text{ for } i = 2, \ldots, L-1 \\
\dot{p}_L &= -\gamma_l p_L + F_L + \sqrt{2\gamma_l T_l}\,\eta_l(t)
\end{aligned} \tag{9.4}$$

where we set the Boltzmann constant as a unit. The generalized force components (torque components) are:

$$F_i \equiv -\frac{\varepsilon}{\tilde{L}} \sum_{j \neq i} \frac{\sin(\theta_i - \theta_j)}{r_{ij}^{\alpha}} \tag{9.5}$$

and $\eta_{h/l}$ are Gaussian white noises with correlations:

$$\begin{aligned} \langle \eta_{h/l}(t)\eta_{h/h}(t')\rangle &= \delta(t-t') \\ \langle \eta_h(t)\eta_l(t')\rangle &= 0 \end{aligned} \tag{9.6}$$

For the measurements of the thermal conductance, we need to define the macroscopic heat flux along the lattice, namely $\mathcal{J}$, through the flux defined by the continuity equation for each particle $\frac{d}{dt}\mathcal{H}_i = -\sum_{j\neq i} J_{ij}$ as in [28], in such way that:

$$J_{ij} \equiv \frac{\varepsilon}{2\tilde{L}}(p_i + p_j)\frac{\sin(\theta_i - \theta_j)}{r_{ij}^{\alpha}} \tag{9.7}$$

After it, the average of $J_{ij}$ is defined as the flux on the right side of the lattice $\mathcal{J}_i$ in the following way:

$$\mathcal{J}_i \equiv \left\langle \sum_{j>i} J_{ij} \right\rangle . \tag{9.8}$$

We can define the flux on the left side of the lattice, but in the stationary state, both are equal in terms of absolute value. Finally, the heat flux $J$ is written as the average over the bulk particles, namely $J \equiv \langle \mathcal{J}_i \rangle_{\text{bulk}}$. Thus, the thermal conductance can be defined as:

$$\sigma = \frac{J}{T_h - T_l} = \frac{J}{2\Delta T} \equiv \frac{\kappa}{L}. \tag{9.9}$$

## 9.2 Methods and discussion

The preferable numerical method to solve the equations of motion is the Velocity Verlet algorithm [132], due to certain circumstances (as in the small step size) it preserves the energy conservation. In our simulation, we set the step size $dt = 0.01$, $\gamma_h = \gamma_l = 1.0$, $\varepsilon = 2$, and the temperatures $T_{h/l} = T(1 \pm \Delta)$, with $\Delta \equiv 0.125$ in such way that $T = (T_h + T_l)/2$. The coordinates and momenta are initially set to zero. We simulate from $t = 0$ to the maximum time $t_{max} = 1.65 \times 10^9$ ($1.65 \times 10^{10}$ in the $L = 20$ cases). We average the heat flux in a range of $20 - 40$ experiments, considering $4 \times 10^8$ time steps for each one ($8 \times 10^9 - 1.6 \times 10^{10}$ in total).

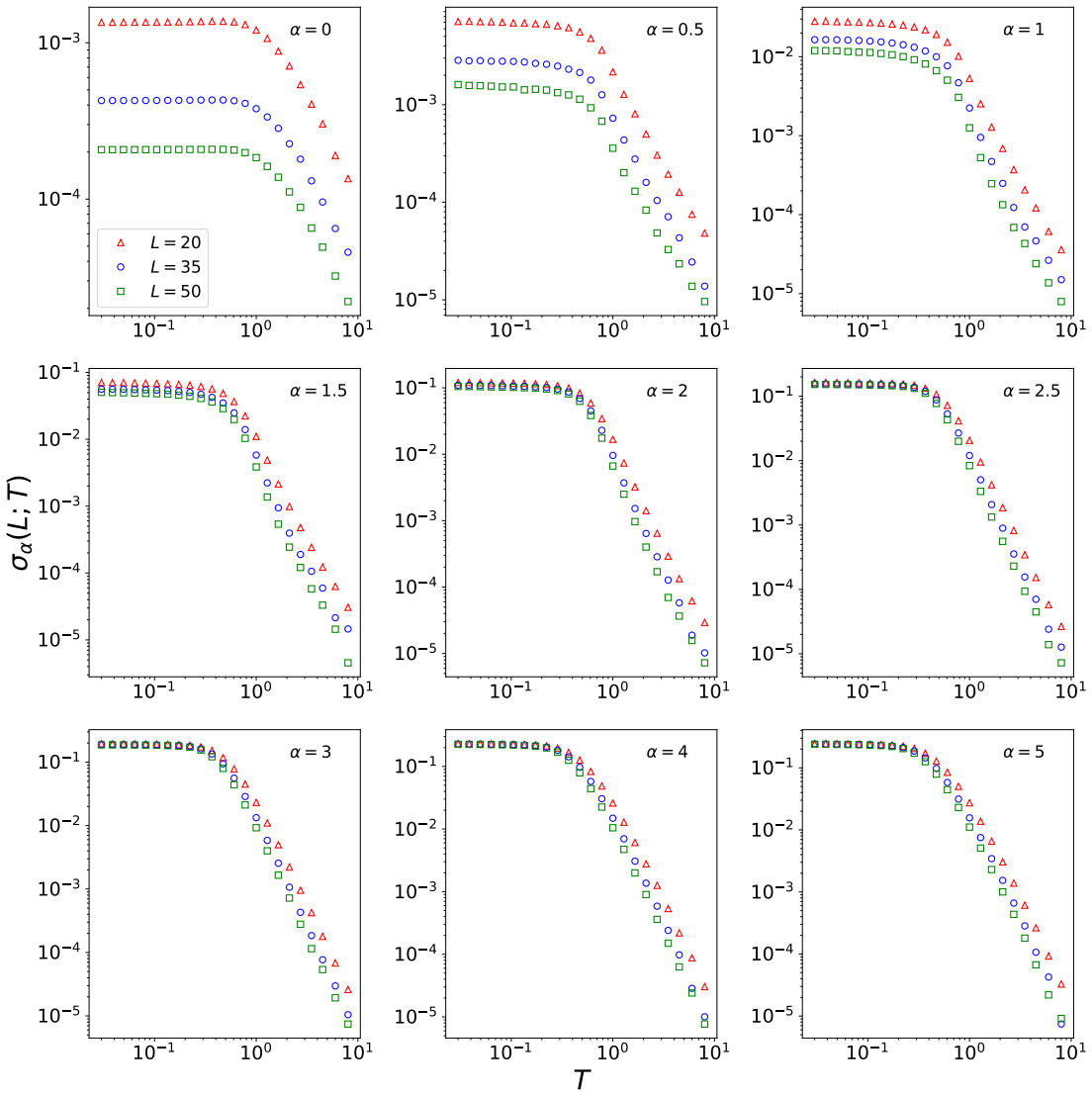


Figure 9.1: The plot of thermal conductance versus $T$ for $\alpha = 0, 0.5, 1, 1.5, 2, 3, 4, 5$ in log-log scale, for $L = 20$ (red), $L = 35$ (blue), and $L = 50$ (green).

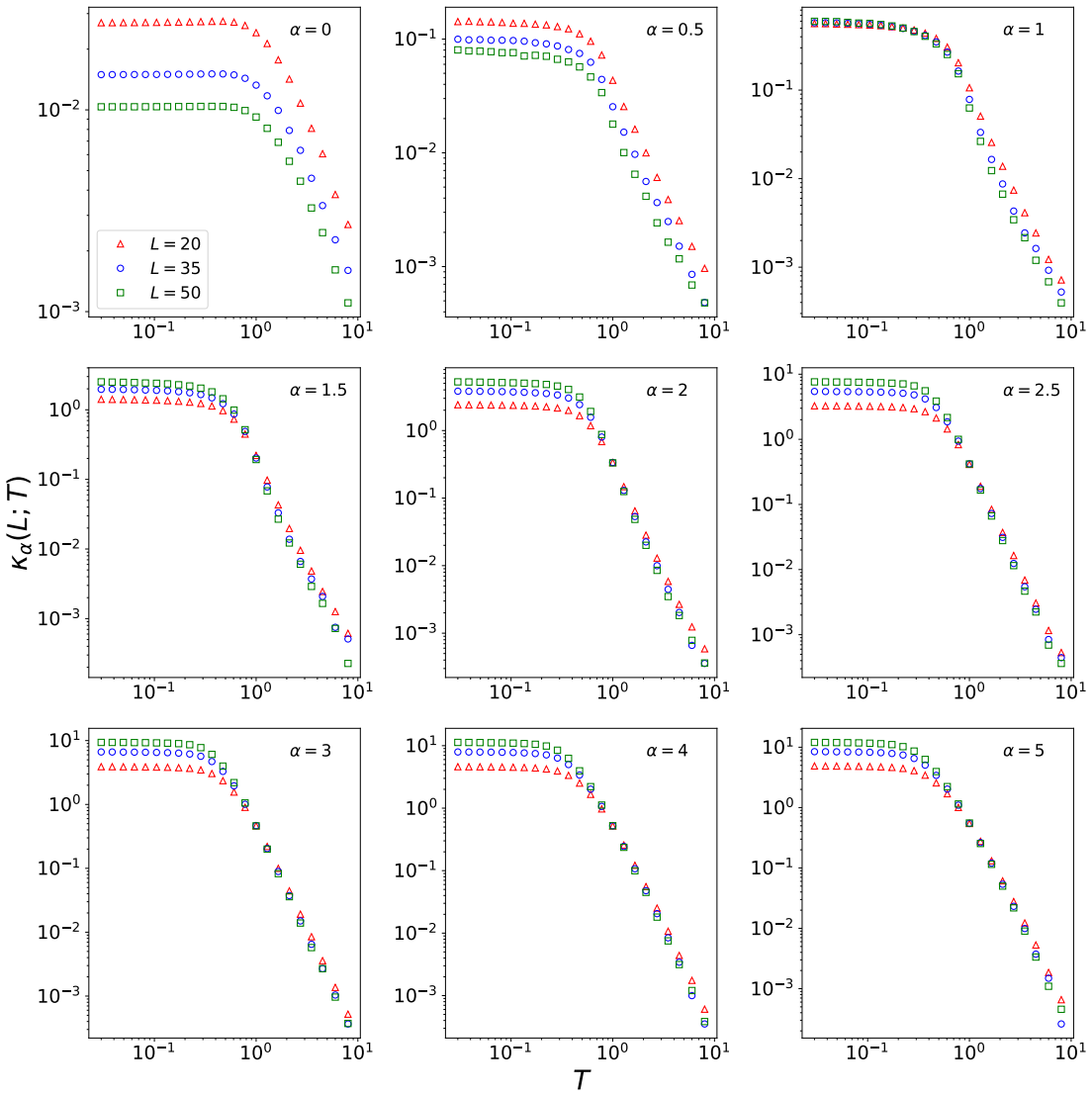


Figure 9.2: The plot of thermal conductivity versus $T$ for $\alpha = 0, 0.5, 1, 1.5, 2, 3, 4, 5$ in log-log scale, for $L = 20$ (red), $L = 35$ (blue), and $L = 50$ (green).

The general expression of the thermal conductance is finally obtained as

$$\sigma_\alpha(T; L) = L^{-\delta_\alpha} A_\alpha e_{q_\alpha}^{-B_\alpha (L^{\gamma_\alpha} T)^{\eta_\alpha}} \tag{9.10}$$

where $A_\alpha$, $B_\alpha$, $\delta_\alpha$, and $\gamma_\alpha$ are non-negative parameters, $\eta_\alpha > 2$, and $q_\alpha > 1$. In the $L^{\gamma_\alpha} T \to \infty$ limit, this expression leads to

$$\begin{aligned} \sigma_\alpha(T; L) &\sim A_\alpha L^{-\delta_\alpha} [B_\alpha (L^{\gamma_\alpha} T)^{\eta_\alpha}]^{1/(1-q_\alpha)} \\ &\propto L^{-\left[\delta_\alpha + \frac{\gamma_\alpha \eta_\alpha}{q_\alpha - 1}\right]} T^{-\frac{\eta_\alpha}{q_\alpha - 1}} \end{aligned} \tag{9.11}$$

We can see in Fig. 9.1 that for $\alpha = 0$ the thermal conductance varies substantially with the lattice size and it decreases as $\alpha$ increases. For instance, for $\alpha \geq 2$ the low-temperature

regime of the thermal conductance appears to be independent of the lattice size, indicating that the thermal conductivity is ballistic in this regime. The threshold $\alpha = 1$ seems to be almost uniformly dependent on the lattice size for all regimes. However, the logarithmic divergence in this case makes the high-temperature regime exhibit an inflection close to $T = 1$. The Fig. 9.2 highlight this phenomenon. The divergence effect also disturbs their neighbors as we notice in the cases $\alpha = 0.5$ and $\alpha = 1.5$.

For $0 \leq \alpha < 2$, the high-temperature regime is dependent on the lattice size, while out of this interval, the converse is noticed. Mainly for $\alpha = 2$, the thermal conductivity diminishes this dependence substantially, as well as the inflection point almost disappears. The case $\alpha = \infty$ was previously studied in Ref. [39] and it exhibits similar behavior as in $\alpha \geq 2$ cases.

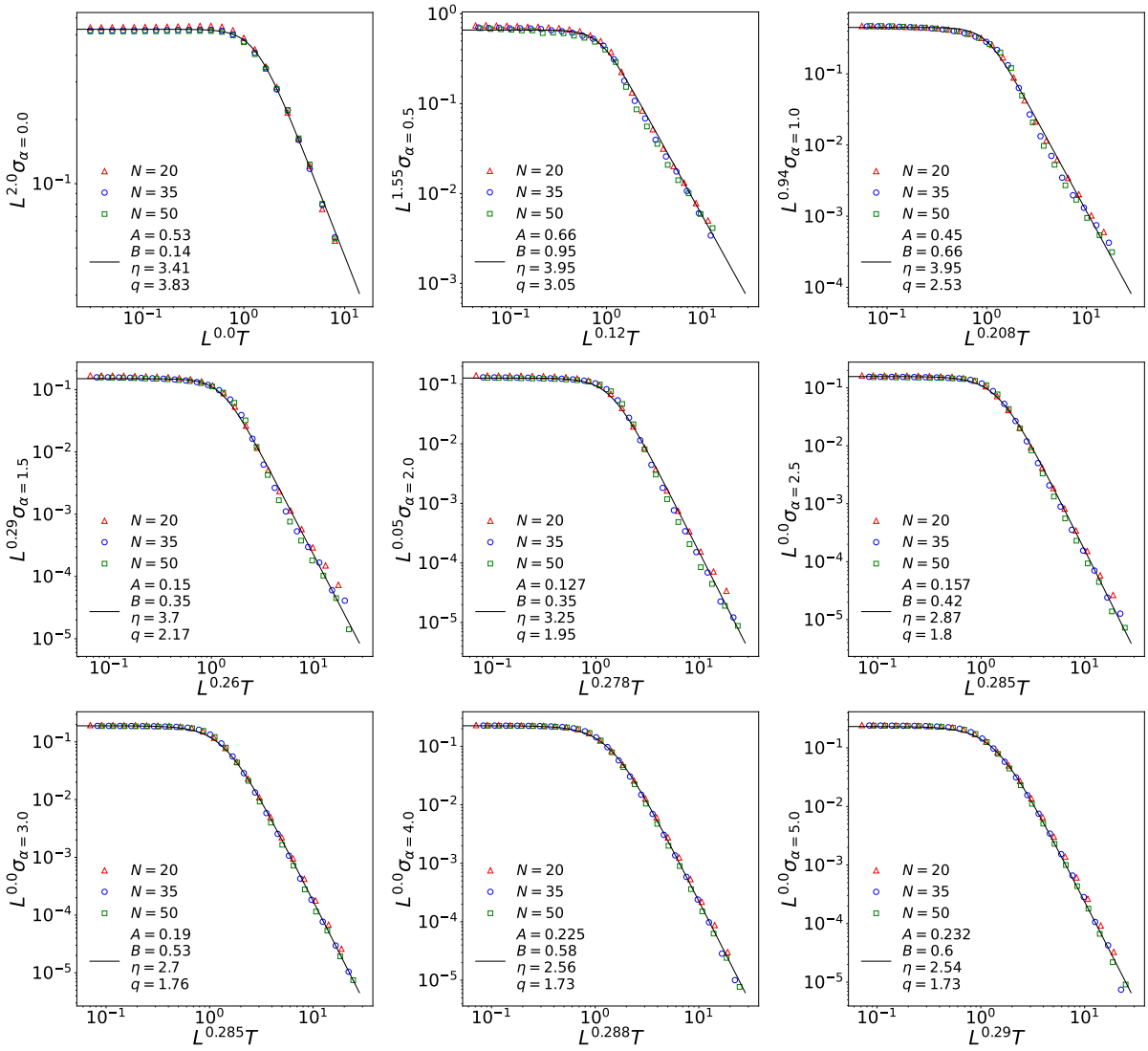


Figure 9.3: The plot of rescaled thermal conductance versus $L^{\gamma}T$ for $\alpha = 0, 0.5, 1, 1.5, 2, 3, 4, 5$ in log-log scale, for $L = 20$ (red), $L = 35$ (blue), and $L = 50$ (green). The black solid curve is a function as in Eq. (9.10).

In Fig. 9.3, we notice that the scaled thermal conductance, $L^{\delta_\alpha}\sigma_\alpha$ appears to behave

as constant at the low-temperature regime, therefore, at this limit, $\sigma_\alpha \sim L^{-\delta_\alpha}$. As $\alpha$ increases, the $\delta_\alpha$ values decrease rapidly, and for $\alpha \geq 2$ it almost vanishes. For $\alpha > 2$, this parameter starts to be zero.

For the high-temperature regime at the thermodynamic limit, the thermal conductance starts to exhibit a different scaling, as in Eq. (9.11). The particular cases $\alpha = 2, 2.5, 3, 4, 5$ exhibit a scaling $\delta_\alpha + \gamma_\alpha \eta_\alpha/(q_\alpha - 1) \sim 1$, in other words, $\sigma_\alpha \equiv \kappa_\alpha/L \sim L^{-1}$, indicating that $\kappa_\alpha \sim L^0$. The large-temperature asymptotic exponent of $\sigma_\alpha$ is the same of $\kappa_\alpha$, which yields $\sigma_\alpha \sim L^{-\eta_\alpha/(q_\alpha - 1)} \sim \kappa_\alpha$ .

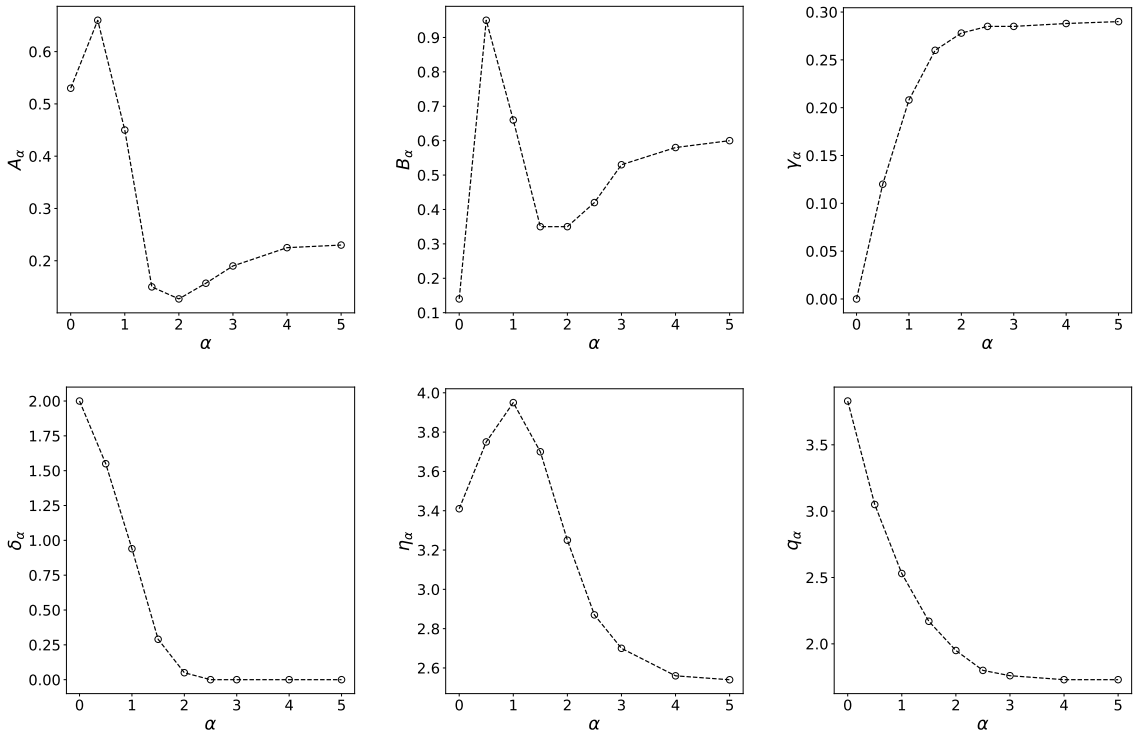


Figure 9.4: Plot of the six parameters, $(A, B, \gamma, \delta, \eta, q)$ versus $\alpha$. The polygonal solid lines are a guide to the eye.

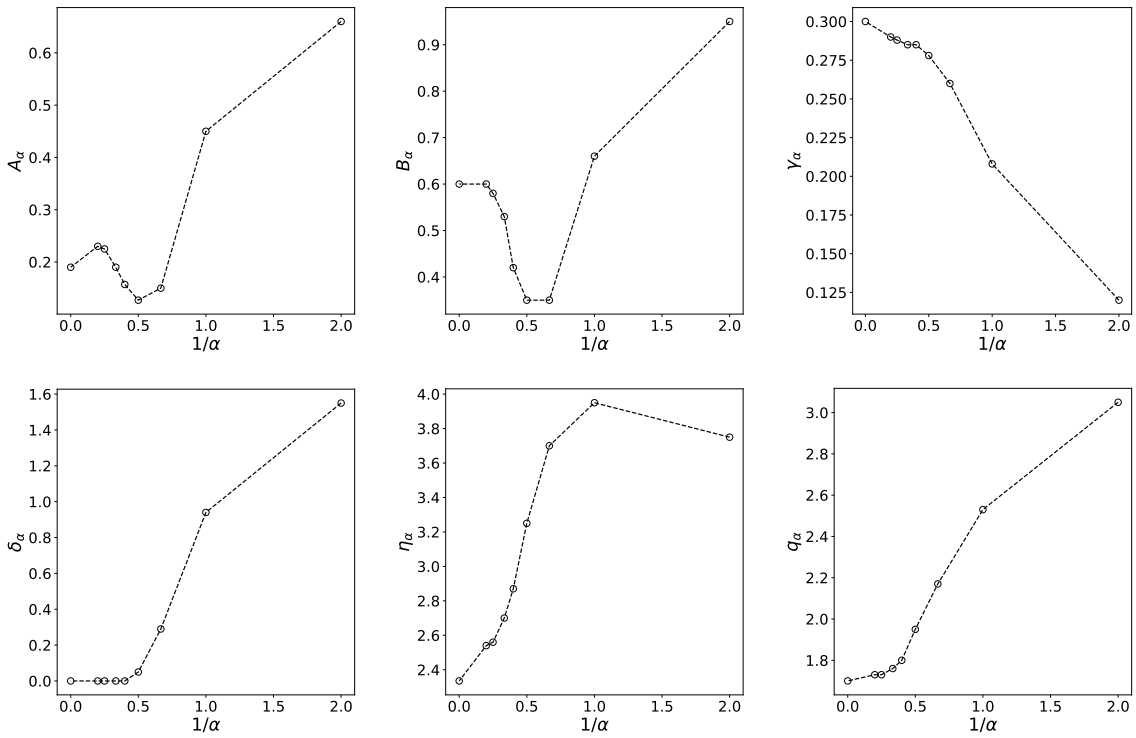


Figure 9.5: Same data as in Fig. 9.4 versus $1/\alpha$.

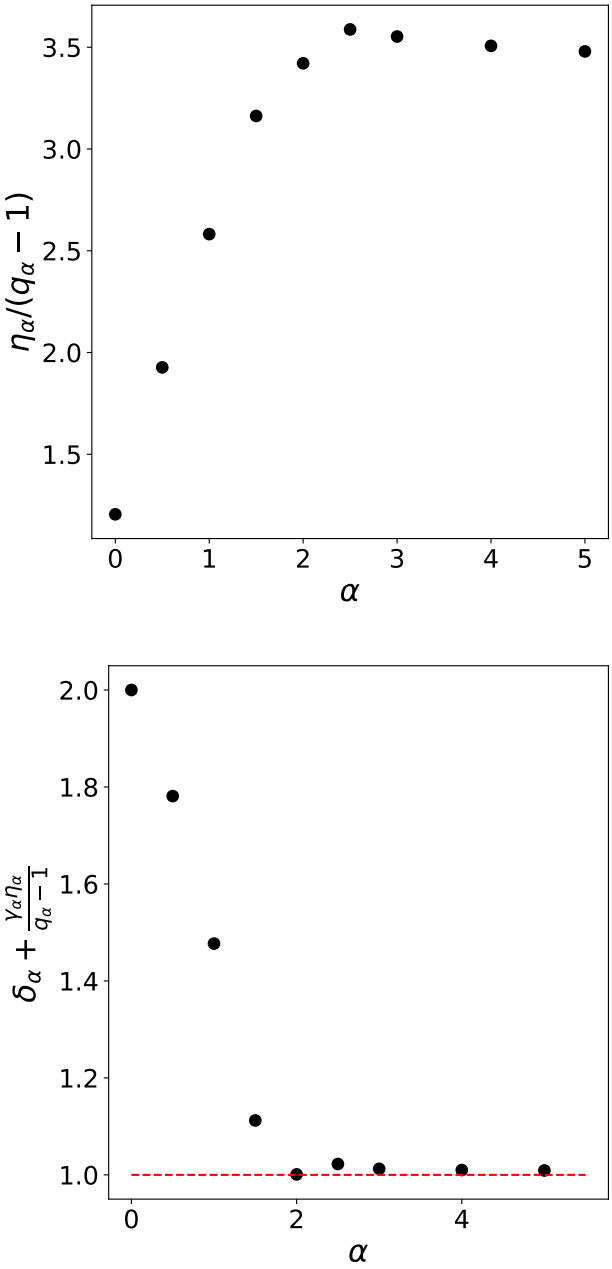


Figure 9.6: The $\alpha$-dependence of the exponent of the large-temperature asymptotic behavior of $\sigma_\alpha \equiv \kappa/L \propto T^{-\eta_\alpha/(q_\alpha-1)}$ (*top*), and the exponent of the large-$L$ asymptotic behavior, $\sigma_\alpha \propto L^{-[\delta_\alpha+\gamma_\alpha\eta_\alpha/(q_\alpha-1)]}$ (*bottom*). The requirement $\delta_\alpha+\gamma_\alpha\eta_\alpha/(q_\alpha-1)=1$ (red line) for the Fourier's law validity is numerically satisfied for $\alpha \geq 2$ and violated for $0 \leq \alpha < 2$.

Let us discuss the values of the parameters of Eq. (9.10). As we see in Fig. 9.4, the parameter $A_\alpha$ has a peak close to the critical value $\alpha_c = 1$, while it decreases until a minimum close to $\alpha = 1.5$ and $\alpha = 2$, and it finally becomes well-behaved after $\alpha = 2$. The same occurs for $B_\alpha$. Conversely, $\gamma_\alpha, \delta_\alpha, q_\alpha$ are monotonic functions of $\alpha$. The parameter $\eta_\alpha$ exactly exhibits a peak at $\alpha_c$ and decreases after that. A curious fact is that $\delta_\alpha$ goes to zero as $\alpha > 2$. This analysis, however, does not allow us to note the point at $\alpha = \infty$.

For this reason, let us consider the results in Fig. 9.5, which shows the parameters versus $1/\alpha$. The cases $A_\alpha \times 1/\alpha$ and $B_\alpha \times 1/\alpha$ present a peculiar behavior around $\alpha_c$, while $\eta_\alpha$ presents a similar behavior exact at $\alpha_c = 1$. In this particular analysis, however, $\gamma_\alpha, \delta_\alpha, q_\alpha$ exhibit atypical behavior around the neighbors of $\alpha_c$.

An interesting fact about the range $0 \leq \alpha < 1$ is that, the thermal conductance scales like $L^{2-\alpha}$ ($\delta_\alpha = 2 - \alpha,\ for\ \alpha < \alpha_c$). It can be justified by the derivation of the heat flux using the energy of each rotor, which scales like energy per length, then, using the property that $\mathcal{H} = \tilde{\mathcal{H}}/\tilde{L}$, where the renormalization is made by assuming a scale $t \to \sqrt{\tilde{L}}t$, we have a flux dependent on $L\tilde{L}$. Without loss of generality, we can use that

$$L\tilde{L} \sim \int_1^\infty dr\, \frac{r}{r^\alpha} = \frac{L^{2-\alpha} - 1}{2 - \alpha} \tag{9.12}$$

where we assume that $L \sim \int_1^L dx$, in the thermodynamic limit ($L - 1 \sim L$). Therefore, the new critical value for this one-dimensional system is $\alpha_c = 2$. It is verified in Fig. 9.6. This value is physically and mathematically quite different from the critical value for the interactions, $\alpha_c$. From the physical perspective, this is related to the regime in which Fourier's law starts to be valid, while the previous critical value of $\alpha_c = 1$ is related to the regime, up to that, where the model starts to be long-ranged or short-ranged. Below $\alpha_c = 1$, the model is considered very long-range. The critical value of $\alpha_c^* = 2$ can be explained in the following way: for $\alpha < \alpha_c^*$ the thermal conductivity becomes dependent on the lattice size in a non-trivial manner, such that the lattice size exponent is non-zero. In the $\alpha > \alpha_c^*$ regime, the thermal conductivity becomes independent of the lattice size. Also about the exponents, still in the regime of very long-range interactions, the absolute value of the lattice size exponent can be obtained as $\delta_\alpha + \gamma_\alpha \frac{\eta_\alpha}{q_\alpha - 1} = \frac{2-\alpha}{2}$. It can be obtained by the renormalized heat flux assuming straightforward a scale $1/\sqrt{L\tilde{L}} \sim L^{-\frac{2-\alpha}{2}}$. It corroborates with the values of the exponents, for instance, for $\alpha = 0, 0.5, 1$, we obtain numerically the absolute values of the exponents as $\delta_\alpha + \gamma_\alpha \frac{\eta_\alpha}{q_\alpha - 1} \sim 1, 0.78, 0.48$ against $1, 0.75, 0.5$.

We can see in Fig. 9.6 that Fourier's law is broken in the range of $0 \leq \alpha < 2$ while for $\alpha \geq 2$ the thermal conductivity no more is lattice size dependent. The exponent of the temperature increases from $\alpha = 0$ to $\alpha = 2$ and saturates for $\alpha > 2$. However, the exponent of the lattice size decreases from $\alpha = 0$ to $\alpha = 2$ and saturates for $\alpha \leq 2$. It indicates that the requirement $\delta_\alpha + \gamma_\alpha \frac{\eta_\alpha}{q_\alpha - 1} = 1$ starts to be satisfied at this limit. For $\alpha > \alpha_c^*$, at the thermodynamic limit, the expression $(L^{2-\alpha} - 1)/(2 - \alpha) \sim 1/(\alpha - 2)$, then, $\delta_\alpha = 0$, as the scaling for the thermal conductivity at high-temperature regime, which yields something as $\frac{1}{\sqrt{L\tilde{L}}} \sim \sqrt{\alpha - 2}$.

As previously mentioned, the low-temperature regime of the thermal conductivity, for $\alpha > 2$ is proportional to the linear size $L$. It also can be explained with the aid of Eq. (9.12). Let us notice that, at these values of $\alpha$, Eq. (9.12) becomes $L\tilde{L} \sim (\alpha - 2)^{-1}$,

thus yielding $\kappa_{\alpha>2}/L \propto (\alpha - 2)$, therefore $\kappa \propto L$. The very-long ranged regime at low temperature behaves as $\kappa_{0\leq\alpha<1} \propto L^{-(1-\alpha)}$ which is the well-known asymptotic behavior of $1/\tilde{L}$. Although it is an interesting fact, the low-temperature regime is only completely understood by a quantum mechanical approach. However, it is worth highlighting that there are real systems with large spins, that can be modeled quasi-classically, for instance, single-molecule magnets (SMMs) [149].

Let us emphasize that, the approach used to obtain the scale of the thermal conductance at high temperatures and the scale for the thermal conductance can be extrapolated for the $d$-dimensional $\alpha - XY$ model at the regime of very long-range interactions. For instance, we know that the three-dimensional heat flux $\mathcal{J}$ is naturally scaled by $L^{d-1}$ because the heat flux is the energy rate per unit area. Here, we are assuming a heat flux only in one direction. Therefore, the thermal conductance scales as $d+1-\alpha$, because $N = L^d$. Similarly, the scale of the thermal conductivity can be predicted as $d(1 - \alpha/(d + 1))$, based on the possible behavior of the mean field model ($\alpha = 0$). Although the scale of the thermal conductivity coincides with the square root of $L\tilde{L}$, it leads to non-integer values of the scale of the thermal conductivity for this particular case. So, we assume that the $1/2$ in the denominator of this scale is because the denominator for a $d$-dimensional lattice is simply $d + 1$. It can be justified by the integration of $N\tilde{N}$, which is equivalent to an effective $d+1$ dimensional system, $\int dr r^{d-1} r/r^{\alpha}$. We also integrate over the $d$ components of the momenta (the high-temperature limit can be viewed as a noninteracting system with a small perturbation [150], so, the contribution of the scale without the factor $L^{d-1}$ is $L^{d(1-\alpha/(d+1))}$, which yields the expected result. For instance, the thermal conductivities of the mean-field model, at low temperatures, behave as $L^{-2}, L^{-3}$ for two and three-dimensional systems, respectively. The high-temperature thermal conductivities of the same model behave as $L^{-2}, L^{-3}$, in agreement with the one-dimensional system, which has the same exponent at low and high temperatures. All exponents recover the limit $L^0$ when $\alpha = \alpha_c^* = d + 1$. So, when Fourier's law starts to hold, it is expected that the $d$-dimensional $\alpha - XY$ model possibly obeys these scales. The physical interpretation of the extra dimension in the scaling can be possibly related to circular waves. The $\alpha - XY$ model is a set of planar rotators that oscillates, but can not be interpreted as particles slowly carrying heat. The circular motion of the spins, makes the system propagate heat throughout the bulk, and, at very long-range regimes, it occurs in a large part of the system, in contrast with the system at $\alpha > 1$, where the interaction becomes weak. For the short-range case ($\alpha = \infty$), it ceases, staying only close to the neighbors.

## 9.3 Final remarks

In summary, Fourier's law is a remarkable relation between the heat flux and the thermal gradient. Although it is well-verified in a wide class of models, including ferromagnet-

ically coupled spin models, we can establish a limit for its validity. When $0 \leq \alpha < 2$, we show that this law is no longer obeyed, while for $\alpha \geq 2$, we ensure its validity. Particularly for the mean field model, such a system is a perfect thermal insulator, which means that, in the thermodynamic limit, the thermal conductivity rapidly vanishes. However, for $\alpha \geq 2$ the lattice size exponent of the thermal conductivity is zero, indicating that the system is not dependent on the lattice size at high temperatures. The thermal conductance scale of the very long-ranged models can be obtained as a power law of the lattice size, whose exponent is $\delta_\alpha = 2 - \alpha$. The high-temperature exponent for the thermal conductivity allows us to write the relation $\frac{\delta_\alpha}{2} + \gamma_\alpha \frac{\eta_\alpha}{q_\alpha - 1} = 0$, which is also applicable for the very long-ranged cases. The relations obtained here can be extrapolated to higher dimensions. For instance, the validity of Fourier's law for two and three-dimensional generic-ranged systems is possibly $\alpha_c^* = 3$ and $\alpha_c^* = 4$ ($\alpha_c^* = d + 1$ for a $d$-dimensional system), respectively. The extrapolation allows us to obtain the general $\delta_\alpha$ for a $d$-dimensional system in the very long-range regime, namely $\delta_\alpha = d + 1 - \alpha$, as well as the exponent of the thermal conductivity for the high-temperature regime ($\sim d(1 - \alpha/(d + 1))$), which is consistent with the simplest case, $\alpha = 0$.

The scaled thermal conductance was well-fitted by a $q$-stretched exponential, a typical function of $q$-statistics, and it was proved useful in the context of magnon heat transport [39, 40, 41]. Here and in the previous works referring to $n$-vector models, we were capable of obtaining closed expressions for the thermal conductance, and hence, the asymptotic limit of the thermal conductivity, then, verifying that classical inertial $n$-vector models present normal heat conduction. From a future perspective, we can numerically verify the regime of the validity of Fourier's law for the $d = 2, 3$ classical inertial $\alpha - XY$ models, as well as the possible agreement with our extrapolations.

# Related applications of q-statistics

# Chapter 10

# Neural complexity through a nonextensive statistical-mechanical approach of human electroencephalograms

*The brain is the organ of destiny. It holds within its humming mechanism secrets that will determine the future of the human race.*
Wilder G. Penfield, The second career: with other essays and addresses,1963.

This chapter is entirely based on the recent article with the same name of this chapter, published in Scientific Reports in 2023 [43].

## Introduction

The brain is widely recognized as a complex system since it is composed by billions of cells (neurons) which express individual behaviors and, at same time, they build a fully interconnected network with emergent, self-organized collective behaviors [151]. Thus, traditional reductionist scientific methodology from mechanistic rationality appears to fail for deeply understanding the brain and its associated mind inside a multidimensional environment [152]. On one hand, a humanity's great unresolved problem is to establish a suitable mental medicine, from epistemology [153] to the biomedical perspective. The problem begins in differentiating normality from typicality, illness from neurodiversity. And, upon this basis, to establish a taxonomy about mental typology for a more realistic nosography. On the other hand, several studies have explored brain complexity through entropic measures within the electroencephalogram (EEG), and found relationships between brain complexity and different mind conditions [154]. However, this issue yet is incipient. One way of accessing brain complexity is through the electroencephalogram

(EEG) signal [155], which is the electrical result of millions of neurons under each of the leads (electrodes) over time. The EEG is the simplest, least invasive and universally used form of functional recording of the human brain dynamics.

The pioneering works of Boltzmann [156] and Gibbs [157] (BG) established a magnificent theory which is structurally associated with the BG entropic functional

$$S_{BG} = -k \sum_{i=1}^{W} p_i \ln p_i \;\; (\sum_{i=1}^{W} p_i = 1)\,, \tag{10.1}$$

and consistent expressions for continuous or quantum variables; $k$ is a conventional positive constant (in physics, $k$ is chosen to be the Boltzmann constant $k_B$; in information theory and computational sciences, $k = 1$ is frequently adopted).

In the simple case of equal probabilities, this functional becomes $S_{BG} = k \ln W$. Eq. (10.1) is generically *additive* [135]. Indeed, if $A$ and $B$ are two probabilistically independent systems (i.e., $p_{ij}^{A+B} = p_i^A p_j^B$), we straightforwardly verify that $S_{BG}(A+B) = S_{BG}(A) + S_{BG}(B)$. The celebrated entropic functional (10.1) is consistent with thermodynamics for all systems whose $N$ elements are either independent or weakly interacting in the sense that only basically local (in space/time) correlations are involved. For example, if we have equal probabilities and the system is such that the number of accessible microscopic configurations is given by $W(N) \propto \mu^N$ ($\mu > 1$; $N \to \infty$), then $S_{BG}(N)$ is *extensive* (i.e., proportional to the number of elements) as required by thermodynamics. Indeed $S_{BG}(N) = k \ln W(N) \sim k(\ln \mu) N$.

However, complex systems are typically composed of many elements which essentially are non-locally correlated, building an intricate network of interdependencies from where collective states can emerge [158]. BG statistical mechanics appears to be generically inadequate for such systems because this theory assumes (quasi) independent components with short-range (stochastic or deterministic) interactions.

Indeed, if the correlations are nonlocal in space/time, $S_{BG}$ may become thermodynamically inadmissible. Such is the case of equal probabilities with say $W(N) \propto N^\nu$ ($\nu > 0$; $N \to \infty$): it immediately follows $S_{BG}(N) \propto \ln N$, which violates thermodynamical extensivity [158]. To satisfactorily approach cases such as this one, it was proposed in 1988 [36] to build a more general statistical mechanics based on the *nonadditive* entropic functional

$$S_q \equiv k \frac{1 - \sum_{i=1}^{W} p_i^q}{q-1} = k \sum_{i=1}^{W} p_i \ln_q \frac{1}{p_i} = -k \sum_{i=1}^{W} p_i^q \ln_q p_i = -k \sum_{i=1}^{W} p_i \ln_{2-q} p_i \;\; (q \in \mathbb{R}; S_1 = S_{BG})\,, \tag{10.2}$$

with the $q$-logarithmic function $\ln_q z \equiv \frac{z^{1-q}-1}{1-q}$ ($\ln_1 z = \ln z$), its inverse being the $q$-exponential $e_q^z \equiv [1 + (1-q)z]_+^{1/(1-q)}$; ($e_1^z = e^z$; $[z]_+ = z$ if $z > 0$ and vanishes otherwise); for $q < 0$, it is necessary to exclude from the sum the terms with vanishing $p_i$. We easily

verify that equal probabilities yield $S_q = k \ln_q W$. Also, we generically have the following functional nonadditivity

$$\frac{S_q(A+B)}{k} = \frac{S_q(A)}{k} + \frac{S_q(B)}{k} + (1-q)\frac{S_q(A)}{k}\frac{S_q(B)}{k} \,. \tag{10.3}$$

Consequently, in the $(1-q)/k \to 0$ limit, we recover the $S_{BG}$ additivity. For the anomalous class of systems mentioned above, namely if $W(N) \propto N^{\nu}$, we obtain, $\forall \nu$, the *extensive* entropy $S_{1-1/\nu}(N) = k \ln_{1-1/\nu} W(N) \propto N$, as required by the Legendre structure of thermodynamics [134, 78]. Finally, the optimization of $S_q$ under simple constraints yields $q$-exponential distributions for the (quasi)stationary states, instead of the usual BG exponentials.

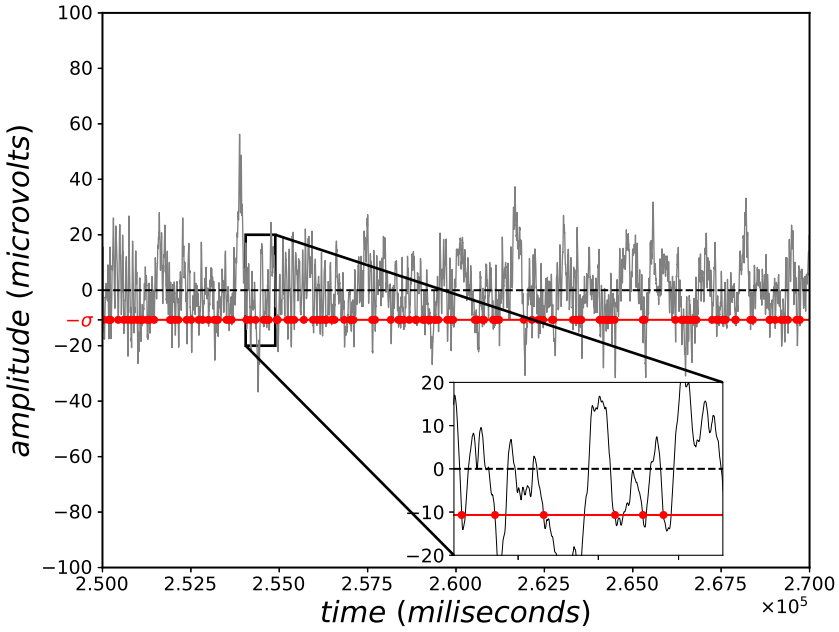


Figure 10.1: Segment of ongoing EEG from one subject (B006), recorded on the mid-parietal ($P_z$) location of the head. Red dots: time values when ddp (signal amplitude) crosses downwards the bottom threshold (1.0 standard deviation; red line). EEG sampling rate was 1000 Hz.

Since EEG is a massive electrical phenomenon, its amplitude is correlated with the cell synchronization. The regularity of time intervals between amplitude peaks that overcomes a typical threshold (in this case, one standard deviation), would reflect the system's complexity. If synchronization would be a stochastic and uncorrelated phenomenon, the distribution of inter-peak distances could possibly be estimated within the BG frame. But EEG is a highly non-equilibrium phenomenon, and it requires more general approaches. Independently of the nature of regularities, this phenomenon exhibits the complex nature of the system. It cannot be excluded that, in the realm of $q$-statistics where $q$ is a scalar measure of complexity, a possibly satisfactory description could be attained.

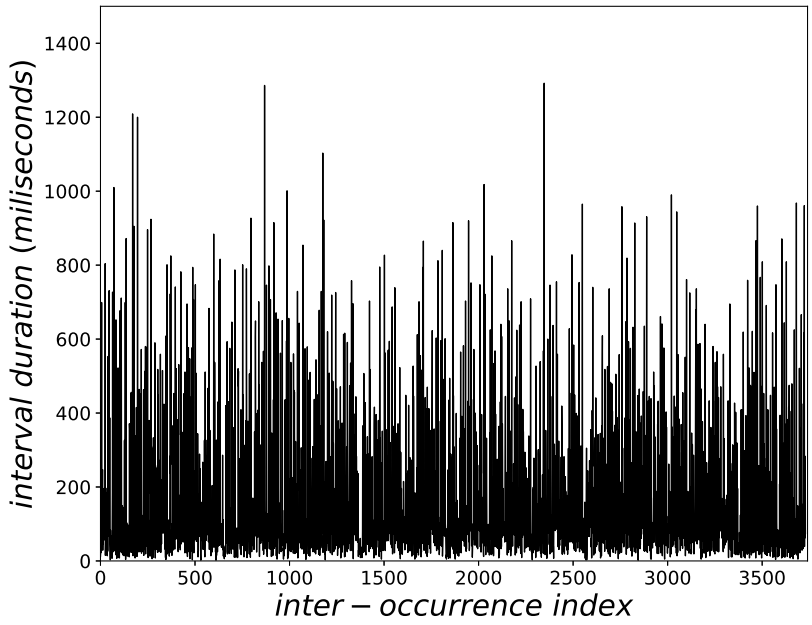


Figure 10.2: Sequence of inter-event time intervals from EEG signal, as detected in FIG. 10.1.

## Motivation, methodology and results

The above nonadditive entropies, as well as the nonextensive statistical mechanics grounded on them, have been already used to characterize various aspects of complexity. Various data obtained from EEG, magnetoencephalograms (MEG), electrocardiograms (ECG), and others, have been analyzed in connection to $q$-statistics [159, 160, 161, 162]. However, the discussion frequently focuses on qualitative ingredients. Our aim here is to demonstrate that nonextensive statistical mechanics is applicable to the brain as a complex system, thus providing specific values for the relevant parameters. Thus, we are analyzing human EEG's in a specific manner herein described which eventually provides a small number of real numbers (such as $q$) having the potential of satisfactorily characterizing different regions of the brain, different functional neuro-states, nosologically different classes of human phenomenologies.

We analized the EEG signal of ten typical adult humans from a match-to-sample task experiment with neutral affective interference for access working memory and attention, such in Yang and Zhen's study [163]. This work was approved by our ethical board for human research, under CAAE 50137721.4.0000.5269. Each EEG signal has 5-10 minutes length recorded with open eyes at 1000Hz sampling rate, through 20 channels disposed at 10-20 montage with eyes open. The high, low and band-pass filters were respectively 0.5, 150Hz and 60Hz. We did not apply any other filter to minimize signal manipulation.

We accessed signal recorded at the midparietal ($P_z$) site (see figure 3), where classical cognitive event-related potentials, as P300 [164], manifest during attention tasks. A

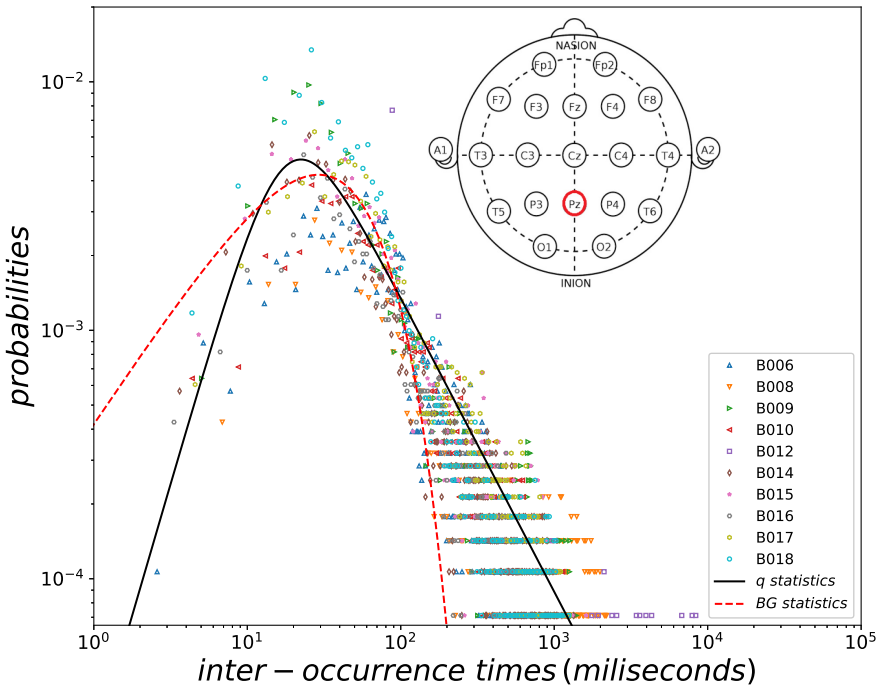


Figure 10.3: Probability distributions of EEG inter-occurrence times (500 equal logarithmic bins) and fittings with statistical models. Superimposed signal recorded on the $P_z$ location of ten subjects performing a work memory task. Amplitude threshold = 1.0 standard deviation. Fitting within Boltzmann-Gibbs statistical mechanics for non-complex systems (i.e., $q = 1$, dashed red curve). Fitting within nonextensive statistical mechanics for complex systems (i.e., $q \neq 1$, black continuous curve). See Methodology for details.

threshold was set at -1.0 standard deviation from $P_z$ signal average (figure 10.1, from subject B006). Taking negative voltages we are minimizing the effect of blink artifacts, which are positive waves, amplier in frontal places.

Each event is the numerical position $i$ of signal vector (1 second = 1000 positions) where the amplitude crossed the threshold downwards. The inter-event distances $i_n - i_{n-1}$ (where n = 1,...,N) were calculated (figure 10.2, from B006). The logarithm distribution of inter-event distances (with 500 distance classes) of all ten EEG signals at $P_z$ were superimposed, and the fitting was performed to the following $q$-statistical function (figure 10.3):

$$y_q = a_q \, x^{c_q} / [1 + (q-1)\beta_q \, x^{\eta_q}]^{\frac{1}{q-1}} \, , \tag{10.4}$$

where $(a_q, \beta_q, c_q, \eta_q, q) = (2.1 \times 10^{-5}, 2.0 \times 10^{-5}, 2.12, 2.96, 1.89)$ for the best fitting. And, for comparison, we also included the classical statistical BG function (where $q = 1$), as follows:

$$y_{BG} = a_{BG} \, x^{c_{BG}} \, e^{-\beta_{BG} \, x^{\eta_{BG}}} \, . \tag{10.5}$$

where $(a_{BG}, \beta_{BG}, c_{BG}, \eta_{BG}, q_{BG}) = (4.3 \times 10^{-4}, 0.023, 0.94, 0.93, 1)$ for the best fitting.

The fitting was performed using three different methods: dog leg trust region [165], trust region reflective [166] and crow search [167] algorithms, all available in Scipy library.

The constant $a$ is determined by imposing normalization, i.e., $\int_0^\infty dx\, y(x) = 1$. Consequently,

$$a_q^{-1} = \int_0^\infty dx\, \frac{x^{c_q}}{[1+(q-1)\beta_q x^{\eta_q}]^{\frac{1}{q-1}}} = (\beta_q(q-1))^{-\frac{c_q+1}{\eta_q}} \frac{\Gamma(\frac{1+c_q}{\eta_q})\Gamma(\frac{1}{q-1} - \frac{1+c_q}{\eta_q})}{\eta_q \Gamma(\frac{1}{q-1})} \tag{10.6}$$

for $q > 1$ and $\frac{1}{q-1} - \frac{1+c_q}{\eta_q} > 0$. In the $q \to 1$ limit, we obtain

$$a_{BG}^{-1} = \frac{\beta_{BG}^{-\frac{c_{BG}+1}{\eta_{BG}}} \Gamma\left(\frac{c_{BG}+1}{\eta_{BG}}\right)}{\eta_{BG}}. \tag{10.7}$$

It is observed that EEGs at $P_z$ position from all subjects express very similar distributions of distances. The EEG regularity was modelled by the $q$-statistics function instead BG one (figure 10.3).

# Discussion

Consistently with the use of $S_q$ entropy in numerous articles as a measure of complexity in neural systems, we believe that we bring here the demonstration of the applicability of non-extensive statistical mechanics on the collective behavior of a neural system through the regularities of EEG. This preliminary study exhibits as a proof of concept that $q$-statistics easily can quantitatively reveal some aspects of brain complexity through the $q$ parameter. Future research needs to be carried out to determine whether this measure will be sensitive enough to discriminate the complexity of different regions or different states of the brain, as well as aspects of inter-individual diversity (among them, brain diseases or even mental disorders). Consistently, we have verified here that brain phenomenology is not properly described within BG statistics (i.e., $q$=1). This is by no means surprising since BG statistics generically disregards inter-component long-range correlations and their collective behavior, which is well known in neural systems [151]. In contrast, $q$-statistics has been empirically shown to be a useful generalization of BGSM [78, 168, 77, 73, 76, 169]. In addition to other quite informative complexity measures and related methodologies applied to neurosciences [170, 171, 172, 173, 174], $q$-statistics hopefully also is useful in the present case. Here, it was applied through a quite simple methodology, using a functional model involving stretched $q$-exponentials which satisfactorily fit the empirical distributions of scalar inter-event intervals (see figure 3) . Many of these complex systems present $c_q \neq 0$, from basic chemical reactions through quantum tunneling [175] to financial market behavior [176], COVID-19 spreading [177], commercial air traffic networks [178] We are led to believe that we are dealing with universality classes of complexity, thus revealing, in what concerns information processing and energy dynamics, far more integrative networks than one might a priori expect from neural structures

[179].

By generalizing the BG theory, $q$-statistics shows that it could be a suitable and promising path to explore brain complexity. Our expectancy is that the $q$ parameter can be sensitive to different brain/mental states, to brain/mind development, and to neural diversity, perhaps clarifying the boundaries between the normal and the ill brain, including extreme cases such as Alzheimer, Pick, and Parkinson diseases. Consistently, a key outcome of emergence of self-organized new states in complex systems is an adaptive behavior facing environmental constraints [151]. Indeed, the concept of disease has also been related to reduced adaptive capabilities, and to the alteration of complexity [154, 180]. Along the lines of the seminal philosophical work of G. Canguilhem [153], normality should be related to the ability to create new rules (i.e., adaptation) instead of living by the same old norms. We intend to further explore, in the future, the neural diversity through the most remarkable paradigm of complexity.

# Chapter 11

# Identifying Attention-Deficit/Hyperactivity Disorder through complexity analysis of the electroencephalogram

> The brain has not explained the mind fully.
> Wilder G. Penfield, "Mystery of the Mind: A Critical Study of Consciousness and the Human Brain", p.88, Princeton University

This chapter is based on a recent finished research, with the same name of the chapter, which will be available in a preprint version soon [44] .

## Introduction

Complexity is a property of many systems in the Universe related to integration among system's components by long-range correlations in a multiscale organization. As a result, these systems are non-reducible in their constituents, capable of transitioning between different states or configurations [78, 151].

The lifeforms are dissipative systems that manifest endothermic long-term stability due to their capacity for self-organization since they are complex, controlling the entropy through allostatic mechanisms, which keep and regulate homeostasis in the face of environmental stressors [181, 182]. Therefore, pathological states, typically non-adaptive, would likely result in a decrease in the organism's complexity [183, 180, 184]. In recent decades, several studies have systematically identified alterations in the brain complexity of individuals with mental disorders. [185, 186, 154]. However, the meaning of those changes in complexity remains elusive. Indeed, some of those studies have indicated higher complexity in patients as compared to typical subjects.

Many procedures based on different theoretical paradigms have been developed to quantify complexity in the human brain activity, mainly based on classical methods such as approximate entropy or Lempel–Ziv complexity, using indices of predictability and regularity of time series from the electroencephalogram (EEG) [154]. In 1988, a generalization of the standard Boltzmann-Gibbs statistical mechanics (BGSM) — non-extensive statistical mechanics (NESM), known as $q$-statistics — was introduced [36]. The NESM functions satisfactorily describe the behavior of wide classes of natural, social, and artificial systems [78]. Recently, we have demonstrated the applicability of $q$-statistics to describe brain complexity by analyzing the temporal regularity of the EEG signal [43], fitting a $q$-exponential function upon the empirical distribution of the probabilities $y$ related to the occurrence of the events $x$ (in this case, events are time distances between EEG amplitudes that passes down a threshold), as follows:

$$y_q = a_q \, x^{c_q} / [1 + (q-1) b_q \, x^{h_q}]^{\frac{1}{q-1}} \tag{11.1}$$

which is equal to Eq. (10.4), where $a_q$ is the normalization constant, and $(b_q, c_q, h_q)$ are positive parameters. The parameter $c_q$ denotes the slope of the left tail, while the index $q$ and the parameter $h_q$ have a straightforward relation with the slope of the right tail in the $q$-stretched exponential function. Thus, $q$ departs further from unity as the range of the spatial-temporal correlations increases; in the limit of short-range correlations, we return to the original BG exponential ($q = 1$), which corresponds to strong chaos. In turn, the index $c_q$ characterizes the number of degrees of freedom. Physically, this parameter is related to the degeneracies of the physical states [114]. Some other complex systems are modeled by similar $q$-exponential functions with a power-law function, $(x_q^c)$, such as the financial market [176], air traffic [178], or COVID-19 spreading [177].

To study brain complexity and its relation to mind disorders, we believe that $q$-statistics can be an effective and consistent approach due to its wide applicability in describing the complexity of a wide range of systems and its simplicity in implementation.

Here, we have evaluated the neural complexity in the EEG of typical boys and those with diagnostics of attention-deficit/hyperactivity disorder (ADHD) by $q$-statistics. Although ADHD is a condition with relatively recognized biological bases, accurate biomarkers for precise diagnosis and understanding of its mechanisms remain undefined [187]. Some previous studies about NC were discordant as to whether the EEG complexity of ADHD was greater or lesser than that of typical peers [154]. However, some findings have shown that in ADHD children, NC is higher than their peers and ADHD adults [188]. Here, we have described neural complexity from the EEG of the same ADHD and typical subjects that we had previously studied using other psychophysiological methods. We observed marked differences of event-related potentials [189] and EEG topography [190]

between the groups, as well as high accuracy with respect to DSM diagnostics criteria by multivariate analysis [191].

By analyzing EEG complexity through $q$-statistics, we aim to show relevant differences between the typical and ADHD boys. Let us anticipate that $q$-statistics will effectively cluster the subjects based on the $q$ and $c$ parameters, which are uncorrelated quantities.

# Methods

## Subjects and procedures

We examined 19 typical and 19 ADHD boys, aged from 11 to 13 years, performing the Posner's Attention Network Test (ANT). The EEG's of the subjects were recorded using a Nihon Kohden NK1200 EEG System at 20 scalp points according to the International 10/20 System, with linked biauricular reference (A1+A2) at a sampling rate of 1000 Hz. The visual task required high cognitive effort during testing Posner's alertness, spatial orientation, and executive dimensions of sustained attention. The test lasted 20 minutes. For details, see Kratz et al. [192] and Abramov et al. [189]. Before the ANT task began, a short segment of EEG lasting about 5 minutes was collected (pretask), with open and closed eyes.

Two physicians evaluated the subjects independently of each other in order to reduce the bias associated with interpretation subjectivity. The classification of subjects regarding ADHD was based on the DSM-IV-TR criteria (at least six symptoms of inattention or hyperactivity/impulsivity were to be satisfied). The children had to also present mental/behavioral dysfunctionality in at least two environments (e.g., school and home). The criteria for inattention and hyperactivity/impulsivity symptoms were assessed through direct questioning of the parents regarding their child's characteristics, with responses recorded as "yes" or "no" for each criterion. A score between 0 and 18 was computed based on these responses. Boys with neurological or psychiatric comorbidities were excluded from the study. IQ was assessed using a reduced version of the Wechsler Intelligence Scale for Children (WISC) test, with the Vocabulary and Block Design subtests [193].

All subjects and their parents gave us written informed consent to participate in this study, which was performed following all international and local ethical rules after being approved by our independent ethical board (CEP-IFF), registered under CAAE 08340212.5.0000.5269 (2013).

## Data Analysis

The EEG signal was filtered using a convolution approach with a vector of size $t$ ( 1 bin = 1 milisecond) defined by:

$$V = exp(-x^2)/2 \tag{11.2}$$

where $x$ is ranging from $-\sqrt{2}$ to $+\sqrt{2}$ with size $t$. For low-pass filtering, $t = 10$ ms (100Hz). And for high pass filtering, the output from convolution of $V$ with $t = 2000$ms (0.5Hz) was subtracted from the original signal. Baseline slow oscillations as well the muscle artifacts were suitably minimized. For 60Hz suppression (a very deterministic artifact from power net), we adopted band-pass filtering using a Fast Fourier Transform approach. No other signal handling was done.

The negative part of the signal was used to perform the regularity analysis, where blink artifacts had little effect on the signal after filtering. We truncated the amplitudes smaller than -200 $\mu$V (with higher absolute value) because no brain sources physiologically generate larger ones in the EEG. From the remaining negative part of the signal, we calculate the standard deviation and every amplitude that passes down the threshold of -1.0 std. dev. was considered as a time event (see [43] for more detailed explanation). The histogram of these intervals was computed within 1000 classes from each of the 20 EEG channels. The classes were nearly 2 ms long, but EEG signals with several large amplitude artifacts (truncated at -200 microvolts) presented slightly higher thresholds, which resulted in distributions with larger time bins. These distributions of frequencies were normalized to probability distributions, the integral thus being equal to unity.

The analysis of the normalized frequencies of the inter-occurrence times leads to a fitting by the function currently emerging in nonextensive statistical mechanics, given by (11.1). The parameters of the function were empirically determined by fitting using the least squares method. However, convergence is carried out by estimation, given computational limitations that make it impossible to execute all loops within the appropriate slopes. For greater precision of the parameters c and q through a second fitting, we analytically determined the parameters b and h through the respective linear functions obtained from the correlation of these two parameters with q, originating from a first fitting (see Fig. 11.2). We bind the distributions of all channels of each subject for best convergence.

The probability distribution must obey the normalization condition, i.e., the integral $\int_0^\infty x^{c-h/(q-1)}\,dx$ can not diverge. This implies $(c+1)(q-1)/h < 1$. Our results satisfy this condition as shown in Fig. 11.3.

After fitting, individual values of $c$ and $q$ in each condition and group (as well averaged ones) were plotted on a $(q \times c)$ space to observe sample dispersion and possibly clustering. The Mann-Whitney U-Test inferred differences between groups and conditions. Correlations between parameters and other variables (DSM scores, I.Q. etc) were explored using the Pearson or Spearman Tests.

# Results

Since we had previously ascertained that typical human EEG distributions satisfy $c > 1$ in function (11.1) (at least for mid-parietal channel) [43], we adopted $c \leq 1$ at least in one channel of any condition as an exclusion criterion for the subject. So, the distributions that we regarded were those exhibiting left and right tails, representing observations from both typical and ADHD subjects. The dataset with such distributions corresponded to 15 typical and 15 ADHD boys.

Table 11.1: Relevant and confounding variables
(*) SD = standard deviation; (**) in hours/week (***) Income per month in Brazilian minimum wages

| Variable | Typical(mean) | Typical(SD*) | ADHD(mean) | ADHD(SD) |
|---|---|---|---|---|
| AGE | 11.33 | 0.90 | 11.80 | 0.94 |
| HOURS OF SLEEP (last night) | 7.33 | 2.26 | 7.67 | 1.80 |
| VIDEOGAME** | 3.47 | 1.25 | 3.20 | 1.61 |
| INTERNET** | 3.40 | 1.30 | 3.33 | 1.68 |
| YEARS OF STUDY | 6.07 | 1.22 | 6.33 | 1.29 |
| CURRENT SCHOOL GRADE | 5.93 | 1.28 | 5.53 | 1.77 |
| FAMILIAR INCOME*** | 8.43 | 6.84 | 5.90 | 8,83 |
| DSM-IN | 2.40 | 1.50 | 7.20 | 1.37 |
| DSM-IMP+HIP | 2.87 | 1.51 | 4.20 | 2.62 |
| DSM-TOTAL | 5.27 | 2.40 | 11.40 | 2.75 |
| IQ | 111.13 | 12.73 | 99.40 | 12.39 |
| c (task) | 1.80 | 0.01 | 2.00 | 0.00 |
| q (task) | 1.96 | 0.00 | 2.10 | 0.02 |
| c (pretask) | 1.68 | 0.01 | 1.90 | 0.01 |
| q (pretask) | 1.94 | 0.08 | 2.00 | 0.02 |

The distributions of frequencies reveal a $q$-stretched exponential profile, observing all subjects for each group and condition taken together in the same distribution (global distributions, with n(ADHD) = 15, n(typical) = 15, Fig. 11.1). The refined aspect of the distributions of task condition is due to the larger number of inter-event intervals computed in longer EEG vectors.

Each global distribution was fitted with the function (11.1). The empirical values found for the task and pretask parameters, were $q(\text{ADHD}) = 2.19$, $q(\text{typical}) = 2.34(2.35)$, $c(\text{ADHD}) = 1.89$, and $c(\text{typical}) = 1.71$. The correlations among the four parameters can be seen in Fig. 11.2: $c$ shows no significant correlation with the other ones. In parallel, $b$ and $h$ show strong correlation with $q$ ($r > 0.80$, Pearson Test). The respective linear functions were extracted to analytically set $b$ and $h$ for each group and condition (see methods). Subsequently, $q$ and $c$ were individually estimated by fitting the empirical distribution of each subject with the function (11.1).

There were no statistical differences between groups concerning confounding variables (age, time using videogame or internet, education, familiar incomes, and hours of sleep at night before the test), indicating no artifact of this kind influencing the results, and consequently that the two groups were paired (see Table 11.1). The I.Q.(estimated by WISC test) was slightly higher in typical boys than in ADHD ones, which was already

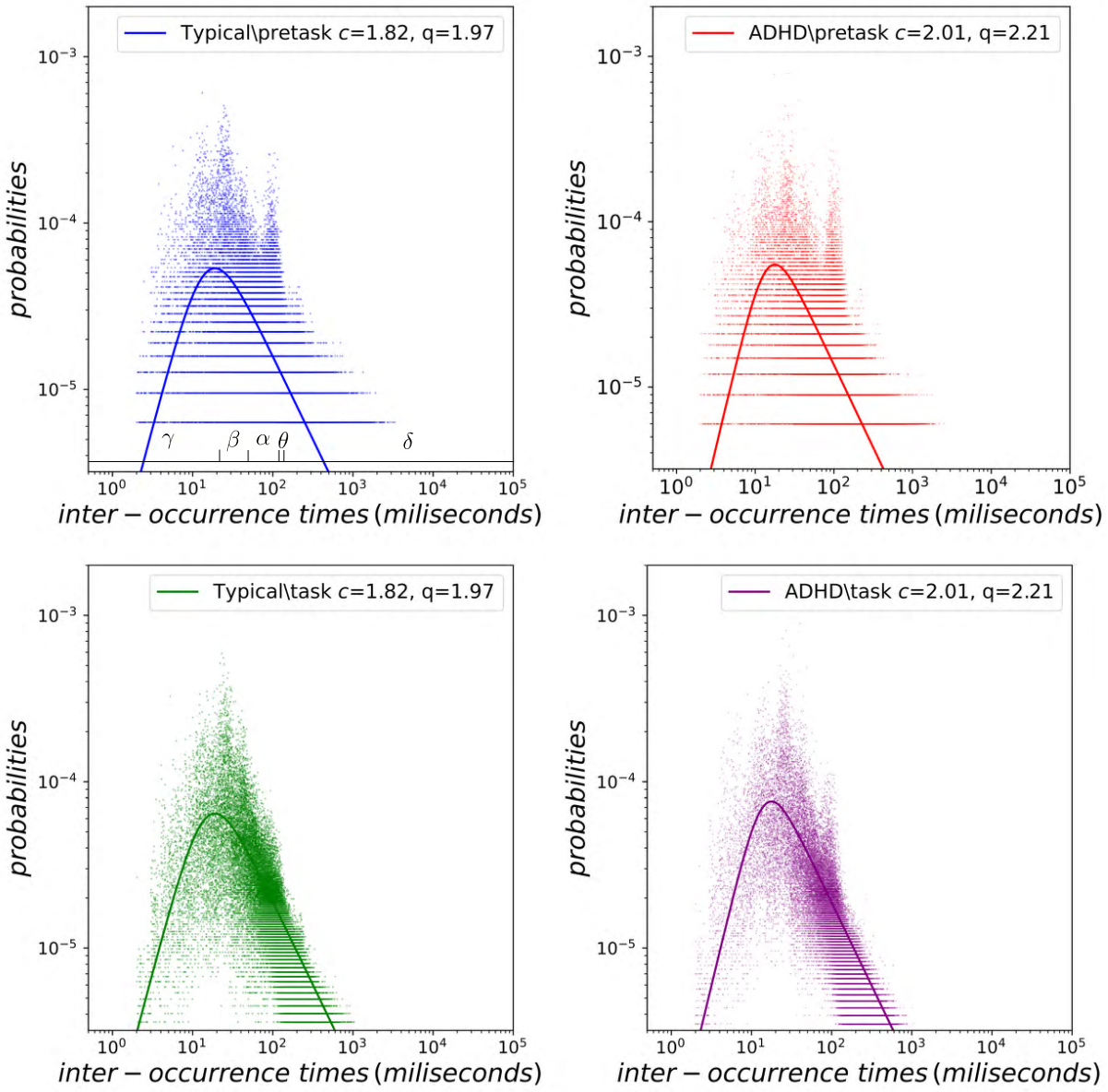


Figure 11.1: Probabilities versus inter-occurrence time events for all datasets and their corresponding fittings. (Top left) Typical\pretask,(top right) ADHD\pretask (bottom left) Typical\task, and (bottom right) ADHD\task. The Greek letters in Typical\pretask represent the following frequencies $\gamma$ (frequencies greater than 32 Hz), $\beta$ (between 13 and 31 Hz), $\alpha$ (between 8 and 12 Hz), $\theta$ (between 4 and 7 Hz), and $\delta$ (smaller than 4Hz), respectively. Notice that the data dispersion corresponding to pretask EEGs is larger than that corresponding to the task EEGs, possibly due to the time duration of the EEGs.

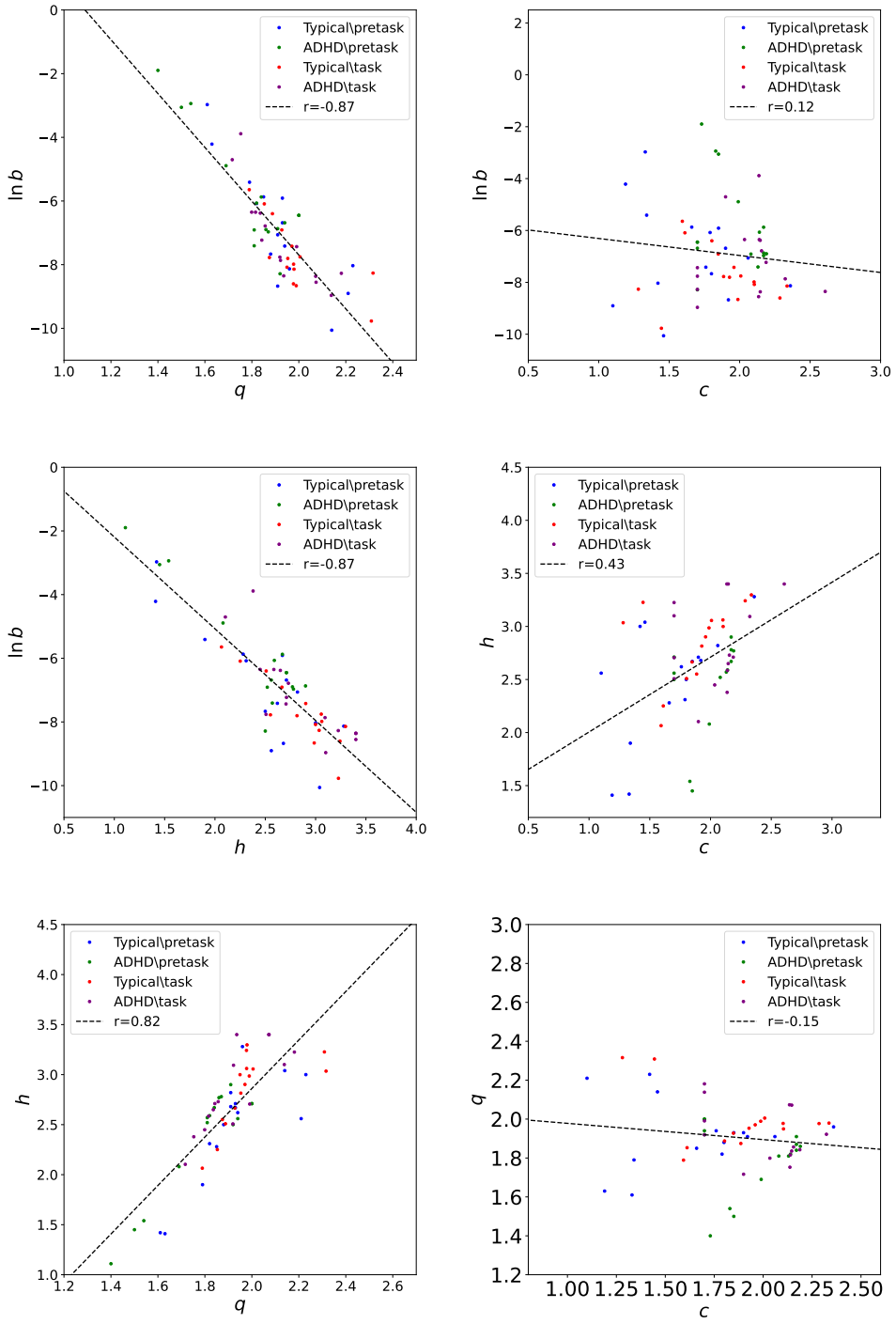


Figure 11.2: (Top left) $\ln b \times q$, (top right) $\ln b \times c$, (middle left) $\ln b \times h$, (middle right) $h \times c$, (bottom left) $h \times q$, and (bottom right) $q \times c$. The r(Pearson) of the dashed straight lines in the same order are -0.87, 0.12, -0.87, 0.43, 0.82, and -0.15. The blue, green, red, and purple points represent typical\pretask, ADHD\pretask, typical\task, and ADHD\task, respectively.

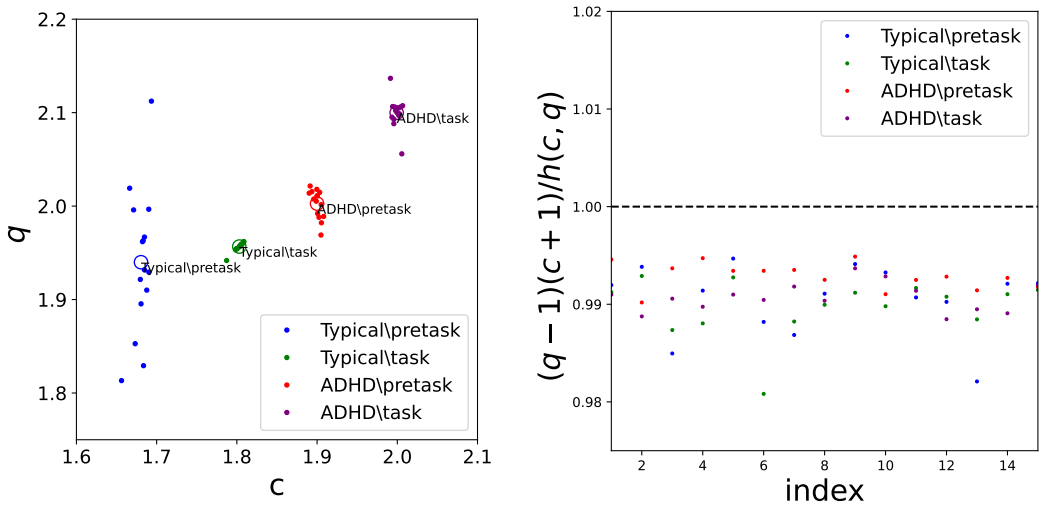


Figure 11.3: (Left) Linear plot of $q$ versus $c$. The empty circles refer to the mean values of $q$ and $c$ for all cases. (Right) The plot of the condition of normalization of the probability distribution, where $h(q)$ is given by an independent analysis of the four types of electroencephalograms (Typical and ADHD in pretask and task, respectively).

pointed out before [194, 195, 196]. However, all subjects of both groups fell within the range of statistically normal I.Q.

Unlike the DSM-IV scores for inattention, those for hyperactivity/impulsivity were not different between groups, prevailing the inattentive subtype in the ADHD group (see Table 11.1).

The averaged parameters $c$ and $q$ from samples were statistically lower for typical subjects compared to ADHD pairs (all $p < 0.01$, see Table 11.1), with very low standard deviations. Comparing conditions, only $q$ in ADHD differed between Task and pretask (p = 0.0004, Mann-Whitney U test, see means and std. deviations, Table 11.1). Fig. 11.3 shows the space $(c \times q)$, where all individual values form well-defined clusters relative to each group and condition. We observed 100 % accuracy in differentiating typical ADHD in the "task" condition since there was no overlapping regarding the values of $(c \times q)$ from these different groups. From all distributions taken together, the global values for $q$ and $c$ differed from averaged ones from individual fittings.

There is no monotonic correlation between $c$ and $q$ and DSM scores for Inattention (Fig. 11.4), nor for total scores (result not shown). However, well-defined clusters are observed in scatter plots for both $c$ and $q$(task), which appears to roughly coincide with the DSM cutoff for inattention (i.e., six criteria satisfied).

# Discussion

The traditional analytical-reductionist approach for studying the relationship between the human brain and mind usually comes down to correlating mental processes with

the dynamics of neural networks. However, this approach cannot be considered fully adequate, since it does not take into account the complexity of the phenomena that are being compared.

The science of complexity is gaining space every day for studying the cerebral basis of the mind and its disorders [188]. The informativeness in complex systems is non-addictive and non-extensive [78] due to the system's inviolable completeness: the whole is larger than the sum of its parts. Studying the molecular receptor or neuronal cell activity mechanisms, outside their intricate network of correlations, might not be the most appropriate way to understand brain dynamics related to mental processes. The possibility of using quantitative assessment of NC as a kind of more integral indicator of cerebral functioning seems promising in overcoming the above methodological difficulties in comparing the brain and mind and bringing the solution of these problems to a more adequate level.

Here, we have shown that the $q$ parameter, a complexity measure from NESM, seems to accurately discriminate ADHD young boys from their typical pairs. Corroborating other studies [154, 188], which used alternative procedures to infer brain complexity, here the NESM has shown that NC from EEG of ADHD subjects is higher than that of the typical ones. Let us emphasize that the present approach, based on NESM [36, 78], enables us to describe the system in terms of complexity using a very simple function involving basic parameters, such as $q$ and $c$. A hard problem in studying different mental disorders is the reliability of available diagnostic classifications and tools: The DSM (Diagnostic and Statistical Manual of Mental Disorders) is a qualitative/quantitative classifier of mind properties (phenomena, symptoms, and features) to a taxonomy of clusters (diagnostics), designed by expert's perceptions about human diversity [197, 198]. And at least for ADHD, the experts' taxonomy seems to correspond to biological reality. Previously, we had shown high accuracy (nearly 80 percent) among DSM-IV criteria for ADHD and multivariate analysis of the same subjects [191]. Now we have accessed complexity by $q$-statistics, and we observed satisfactory accuracy of $q$ and $c$ parameters to classify the subjects as ADHD or typical. We are concomitantly showing that (1) the DSM seems to adequately identify and describe ADHD and (2) possibly we can objectively identify ADHD by measuring objective and relevant properties of the brain, such as NC. However, the design of definitive and universal models for putative brain mechanisms appears to be elusive due to their extremely complex nature. We did not find other studies within which such a high accuracy of agreement between complexity measures and ADHD diagnostics would be achieved [199, 200, 201, 202].

Although we have shown that $q$-statistic can describe NC, it would still be premature to interpret the clinical meaning of the difference in $q$ values found between ADHD and typical subjects. To explain the observed higher complexity in ADHD, we need further studies that we are currently running. In physics, this parameter is related to complexity

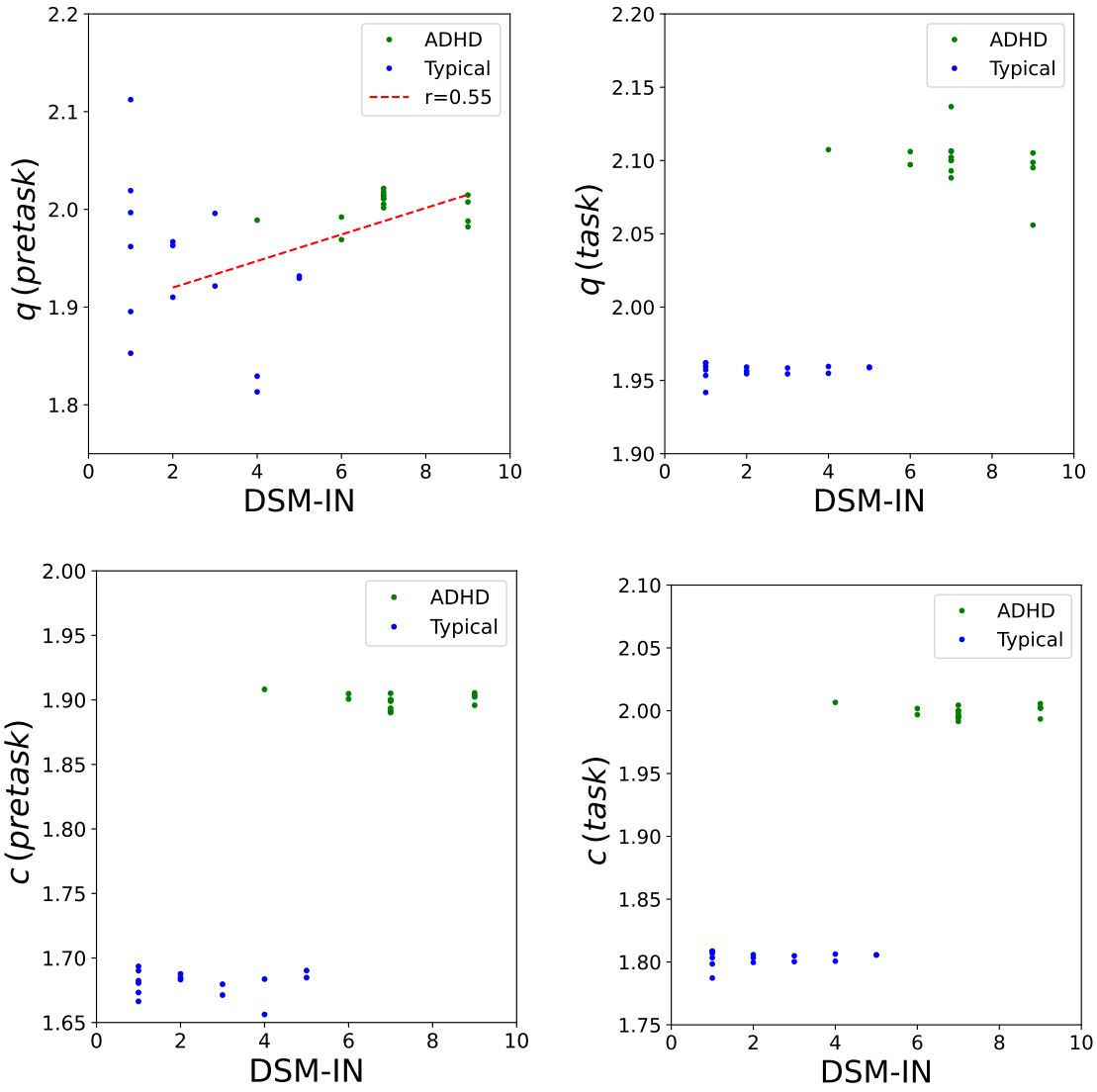


Figure 11.4: $q$ (pretask), $q$ (task), $c$ (pretask), and $c$ (task) versus DSM score (top left, top right, bottom left, and bottom right, respec.). Notice that $q$ (pretask) can be roughly fitted with an increasing straight line (dashed red) with $r$(Pearson)=0.55.

through long-range correlations, which modify the probability distribution of events as far from the Boltzmann-Gibbs model as the system is complex. EEG studies have found lower beta/alpha or beta/teta rates in ADHD subjects [203, 204, 205, 206], which could justify our findings. Whereas gamma oscillations are related to local and bottom-up processing, theta and alpha bands are related to long-range functional connectivity in the brain in top-down (or inner) processing [207, 208, 209, 210]. In Fig. 11.1, a probability peak on the alpha band shows that this rhythm (between 8-12Hz, which diffusely spreads across the EEG channels) is present in the probability distributions.

As we have shown in a previous study [43], $c > 1$ seems to be a marker feature of the frequency distributions from human EEG time regularity. Here, some distributions did not satisfy this condition, which was probably an artifact of shorter EEG signals from the pretask condition or noisy ones: as pointed out in the methodology, signals with higher thresholds due to contamination by large amplitude artifacts, resulted in distributions with larger time bins. In this context, small intervals between events were not recorded, which would form a left tail in the distribution. As a rule for our methodology, we advocate in favor of the exclusion of these cases to prevent excessive manipulation of the signal, which could generate spurious results. As we see above, $c$ parameter is crucial for the subject's classification.

The parameter $c$ was more sensitive to ADHD than $q$, as shown in Fig. 11.4. The larger the value of the parameter $c$, the more vertical the left slope of the stretched $q$-exponential function due to power law $a\,x^c$ (if $c$=0, the function recovers a pure $q$-stretched exponential curve). The left slope of the probability distribution is set by the expression of high-frequency EEG bands (beta and perhaps gamma). EEG gamma frequencies are not easily accessed in clinical examinations. However, there are some studies of the EEG gamma band in relation to psychiatric disorders [211].Gamma and beta bands are highly correlated to bottom-up cognitive processes [208, 209], and are more expressed in typical than in ADHD subjects [203, 204, 205, 190, 206]. Indeed, larger $c$ values correspond to lower probability of detecting higher frequencies in the EEG signal since their amplitude is usually below the threshold that has been used (in preliminary essays, we have observed $c = 0$ to larger thresholds by statistical formalism in light of the central limit theorem, we advocate in favor of a suitable threshold of one standard deviation). We are currently conducting another study focusing on the effect of different cognitive states in typical adult subjects upon $c$ and $q$ parameters.

As seen in Table 11.1 and Fig. 11.1, by including the data corresponding to all the subjects in the same distribution we found $q$ values above the average of the individual ones. Slight fitting errors are naturally possible by varying four instead of two parameters, and also because the straight lines for $b$ and $h$ may have an error close to 20 %.

Although we currently do not have enough information to establish a more enhanced discussion about the meaning of these complexities and the biological correlates with the

$q$ and $c$ parameters, we provide robust evidence for the applicability of $q$-statistics to measure brain complexity and accurately clusterize mental states and conditions.

# Chapter 12

# Quantum chaos from the de Broglie-Bohm theory of quantum mechanics

*To answer Rosen's objections, we need merely point out again that the usual interpretation can give no meaning to the motion of particles in a stationary state; at best, it can only predict the probability that a given result will be obtained, if the velocity is measured. As we saw in Sec. 8, however, our interpretation leads to precisely the same predictions as are obtained from the usual interpretation, for any process which could actually provide us with a measurement of the velocity of the electron. One must remember, however, that the value of the momentum "observable" as it is now "measured" is not necessarily equal to the particle momentum existing before interaction with the measuring apparatus took place.*

D. Bohm, A Suggested Interpretation of the Quantum Theory in Terms of "Hidden" Variables. II (1951)

This chapter is based on the recent article with the same name of the chapter, published in Chaos in 2024 [45].

## 12.1 Introduction

Quantum chaos [212, 213, 214] is a rich problem in the realm of quantum mechanics. Moreover, it has a wide variety of applications, e.g., quantum computing [215, 216, 217, 218], quantum dots [219, 220], nuclear physics [221, 222] and even in cosmology and black holes [223]. Our present goal for advancing the understanding of this phenomenon is to scrutinize the correspondence between quantum and classical chaotic dynamics by tuning the value of the Planck constant. Starting from classical dynamics, it is necessary to integrate all equations of motion to determine whether a system is dissipative, ordered, strongly or weakly chaotic. Conversely, in quantum mechanics, the Schrödinger equation

$\mathcal{H}\Psi = i\hbar\partial_t\Psi$ is linear and acts on probability amplitudes instead of trajectories. So, to study quantum chaotic dynamics, many authors suggest that the de Broglie-Bohm (dBB) theory [224, 225, 226] is an intriguing alternative to investigate quantum chaos [227, 228, 229, 230, 231, 232, 233, 234, 235, 236, 237, 238, 239, 240, 241, 242], as it is based on trajectories determined by heavily nonlinear terms. On classical grounds, the Liouville equation

$$\partial_t\rho = -\{\rho, \mathcal{H}\} \equiv -i\mathcal{L}\rho, \tag{12.1}$$

where $\rho$ is the probability density, $\{.\}$ is the Poisson bracket and $\mathcal{L}$ is the Liouvillian operator, governs the time evolution of the system. From Eq. (12.1) it is not possible to directly measure chaos or any consequence of it since, like the Schrödinger equation, it is linear. Quantum observables operate in the Hilbert space in such a way that the corresponding distributions are typically well-behaved, thus apparently suggesting that there is no chaos in quantum mechanics. This is obviously inadmissible since, according to the correspondence principle, quantum mechanics recovers classical mechanics [243], widely known to exhibit chaotic behavior; examples of classical chaos are found in [244, 245, 246, 247]. Although Eq. (12.1) is linear, a classical system with more than three equations of motion and nonlinearities is likely to exhibit sensitivity to initial conditions, hence some type of chaos. Therefore, at least in classical mechanics, the feasible way to analyze the collective behavior of particles is via equations of motion.

In this sense, in the Bohmian interpretation of quantum mechanics, nonlinear effects naturally arise from the equations of motion [248, 249] due the additional presence of the quantum potential $Q \equiv -\frac{\hbar^2}{2m}\frac{\nabla^2|\Psi|}{|\Psi|}$, which can exhibit the equivalence between quantum and classical trajectories in the limit $\hbar \to 0$. It is worth to emphasize that this issue is not trivial, and some authors claim that it is not always possible to study this quantum-to-classical transition by just setting $\hbar \to 0$ or taking the limit of large quantum numbers [250]. Accordingly, a simple limit in Bohmian mechanics is to consider $Q \to 0$. Nevertheless, the crossover between quantum and classical systems can be unveiled by considering $\hbar \to 0$, even with some remnants of possible quantum effects. As an example we can cite its physical importance in the study of quantum scars [251]. For instance, a constant quantum potential in the limit of null $\hbar$ provides classical equations of motion. Conversely, when the quantum potential diverges in two and three-dimensional systems, it can result in the emergence of vortices [252, 253, 254, 255, 256], an important component in the study of superconductors [259], Bose-Einstein condensates [260, 261], superfluid phenomena [262, 263], quantum field theory [264, 265, 266, 267], to cite but a few. The appearance of these quantum vortices is an important element in the emergence of chaos due to the presence of geometric structures called nodal point X-point complexes (NPXPCs) [258, 257, 240]. Additionally, chaotic dynamics constitutes a crucial factor in validating Born's rule for systems that do not satisfy the quantum equilibrium hypoth-

esis [268, 269, 270, 271], i.e., for initial conditions that are not distributed according to $|\Psi|^2$.

Here, we conduct a full numerical study of a generic two-dimensional quantum anharmonic oscillator, with high accuracy and precision, considering cubic and quartic interactions. We consider the unstable cubic potential in order to have an instability region, allowing the quantum particles to escape from the barrier repressively (negative values) and progressively (positive values) in space. The quartic potential is introduced exactly to stabilize this effect when it predominates in regards to the cubic interaction. In addition, we also consider a off-diagonal term given by $-\kappa xy$, providing a kind of entanglement between the spatial coordinates. All potentials plays an important role in our system, which will be discussed later in this article.

The main objective of this work is to show that the classical and quantum chaos can be studied along similar lines, namely, from the deviation of the trajectories. Along the article we present several evidences of chaotic tendency. We intend to show that this system exhibits quantum-classical invariant chaotic behavior in the vicinity of vortices. For this, we vary the value of $\hbar$ and subsequently analyze the separation between the quantum trajectories.

## 12.2 de Broglie-Bohm theory

The de Broglie-Bohm view of quantum mechanics is a non-local interpretation based on a classical analogy of Schrödinger equation, where the particle dynamics is driven by the guidance equations

$$m\frac{d\mathbf{x}}{dt} = \hbar\,\mathrm{Im}\left\{\frac{\nabla\Psi}{\Psi}\right\}. \tag{12.2}$$

In this perspective, the wave function guides the quantum particles in the configuration space. Assuming a polar form for the wave function $\Psi(\mathbf{x},t) = R(\mathbf{x},t)e^{iS(\mathbf{x},t)/\hbar}$ and substituting into Schrödinger equation, we obtain two real relations, together with $\mathbf{p} = \nabla S$ (which is equivalent to Eq. (12.2)), namely

$$\partial_t S + \frac{(\nabla S)^2}{2m} + V + Q = 0, \tag{12.3}$$

$$\partial_t R^2 + \nabla\cdot\left(R^2\frac{\nabla S}{m}\right) = 0, \tag{12.4}$$

with the quantum potential $Q(\mathbf{x},t)$ defined as

$$Q \equiv -\frac{\hbar^2}{2m}\frac{\nabla^2 R}{R}. \tag{12.5}$$

Eq. (12.3) is a Hamilton-Jacobi equation with an effective potential given by the sum of the classical and quantum potentials. Moreover, Eq. (12.4) is a continuity equation that reveals $|\Psi|^2 = R^2$ as a probability density. Thus, given an initial distribution $|\Psi(\mathbf{x}, 0)|^2$, the trajectories probability density at any instant will be $|\Psi(\mathbf{x}, t)|^2$. From Eqs. (12.2) and (12.3), we obtain a quantum analogue of Newton's second law with an extra quantum force $-\nabla Q$, such that

$$m\frac{d^2\mathbf{x}}{dt^2} = -\nabla V - \nabla Q. \tag{12.6}$$

The relation in(12.6) is straightforwardly obtained by assuming an effective Hamiltonian as follows:

$$\mathcal{H}_{eff} = \frac{\mathbf{p}^2}{2m} + V_{eff} \tag{12.7}$$

where $V_{eff} = V + Q$. In this form, Eq. (12.6) is very analogous to the classical equations of motion, suggesting the possibility of chaos. The main difference here is the presence of the quantum potential, which is, in general, nonlinear. Interestingly, some classical systems that do not exhibit chaotic behavior may present quantum chaos [240]. This happens because the trajectories obtained via guidance equations (12.2) undergo the influence of NPXPCs throughout their evolution [240, 257, 258]. The NPXPCs are formed by two main elements: the nodal points, defined as regions where $\mathrm{Re}(\Psi) = \mathrm{Im}(\Psi) = 0$, and the X-points, which are unstable hyperbolic points defined in the reference frame of the nodal points that accompany its evolution. The complex geometry created by this pair generates quantum vortices, which are responsible for the scattering of neighboring trajectories. So, if a particular system has a considerable number of such vortices, the nearby trajectories can experience significant deviation. Hence, it is natural to expect that such systems will exhibit chaotic behavior.

## 12.3 Model

Let us consider a generic two-dimensional anharmonic oscillator whose Hamiltonian is given as follows

$$\begin{aligned}\mathcal{H} =& \frac{p_x^2}{2m} + \frac{p_y^2}{2m} + \frac{1}{2}(\omega_x^2 x^2 + \omega_y^2 y^2) \\ &- \kappa xy + \frac{\alpha}{3}(x^3 + y^3) + \frac{\beta}{4}(x^4 + y^4),\end{aligned} \tag{12.8}$$

where $\alpha$ and $\beta > 0$ are constants of the cubic and quartic interactions, respectively. Without loss of generality, we set the mass $m$ and frequencies as unity. The coupling constant $\kappa$ connects the two spatial coordinates. Setting $\kappa$ to zero results in two independent oscil-

lators, while $\kappa \neq 0$ results in a *nonlinear membrane* . The Eq. (12.8) under the condition $\alpha \gg \beta$ is highly unstable. To avoid this problem, we set $\alpha/3$ and $\beta/4$ to be small values, with $\alpha$ slightly greater than $\beta$. Here, the nonlinear interactions may be treated as small perturbations.

## 12.4 Methods

We numerically solve the time-dependent Schrödinger equation, with the Hamiltonian given by Eq. (12.8), considering different values of $\kappa$ and $\hbar$. We employ the finite element method (FEM) [272, 273, 274] in a square domain $\mathcal{D} \equiv [-L, L] \times [-L, L]$, where $L$ is the linear size of this domain, and we integrate the temporal part with high accuracy and precision, using adaptive time-steps $dt$ requiring a significant computational effort. For each value of $\hbar$ we set $L$ in a region that the entire wave packet is included, but ensuring that this wave packet is far from the boundaries. The domain is discretized using uniform spacing square mesh elements, and Dirichlet boundary conditions are applied to prevent undesirable effects in the numerical solutions. As a consequence, the integral of the square modulus of the wave function is preserved within an error of $10^{-3}$. For numerical purposes, we consider as initial conditions a properly normalized superposition of eigenfunctions of the two-dimensional harmonic oscillator as follows:

$$\Psi(\mathbf{x}, 0) = \frac{1}{2}\left(\psi_{00}(\mathbf{x}) + \psi_{01}(\mathbf{x}) + \psi_{10}(\mathbf{x}) + \psi_{11}(\mathbf{x})\right), \tag{12.9}$$

where the eigenvectors are given by the relation

$$\psi_{nm}(\mathbf{x}) = \frac{e^{-\frac{1}{2\hbar}(x^2+y^2)}}{\sqrt{2^{n+m} n! m! \pi \hbar}} H_n\left(\frac{x}{\sqrt{\hbar}}\right) H_m\left(\frac{y}{\sqrt{\hbar}}\right), \tag{12.10}$$

with $H_n(x)$ the Hermite polynomials of order $n$. This choice of initial condition is interesting because it shares the same symmetry of the Hamiltonian (12.8), which is invariant by changing $x$ and $y$ variables. In other words, the line $y = x$ is an axis of symmetry of the system. By Curie's causality [275] we expect the manifestation of such symmetry within the calculation of the Bohmian trajectories. In our simulation, we choose $\alpha/3 = 0.05$ and $\beta/4 = 0.04$, ranging $\kappa$ from 0 to 1 and $\hbar$ from 0.05 to 1 at arbitrary steps. Eq. (12.2) is integrated using 8th order Runge-Kutta method [276, 277, 278] with time-steps of $dt = 10^{-5}$. In order to analyze the divergence of initially nearby trajectories, we compute their deviations $(\delta x, \delta y, \delta p_x, \delta p_y)$ in the fourth-dimensional phase space $(x, y, p_x, p_y)$, where $p_x$ and $p_y$ are simply the momentum components. Considering 60 different initial conditions, we perform the mean of $\ln \xi(t)$, in which $\xi(t)$ are the normalized phase space distance of each pair of neighboring trajectories, defined as $\xi(t) = \tilde{\xi}(t)/\tilde{\xi}(0)$, where $\tilde{\xi}(t) = \sqrt{\delta x(t)^2 + \delta y(t)^2 + \delta p_x(t)^2 + \delta p_y(t)^2}$. For each pair we set initial space components

equally distant by an amount of $\epsilon = 10^{-4}$. Please note that the graph of $\ln \xi(t)$ versus $t$ provides us information about the value of the Lyapunov exponent $\lambda$ formally defined as $\lambda = \lim_{t\to\infty} (\ln \xi(t)/t)$. Despite we need to consider a relatively long period of time to determine the precise value of $\lambda$, it is possible to infer its signal through the slope of the associated curve, positive slopes indicating a strongly chaotic tendency.

## 12.5 Results

Let us present now the results of our simulations. We notice that the wave packet spreads during its evolution, as shown in Fig. 12.1. This spreading is due to the $-\kappa xy$ interaction and the unstable cubic potential, which assumes both positive and negative values. When $|x|, |y| > 1$, the cubic potential becomes very unstable, leading the system to slightly escape from the potential well. However, the quartic interaction in Eq. (12.8) is responsible for stabilizing the oscillations in such a way that neither $-\kappa xy$ nor the cubic term cause an exaggerated stretching of the wave function. Analyzing the solutions of Eq. (12.2), we illustrate the velocity field in the case $\kappa = 0.1$ (see Fig. 12.2). Within a short period of time, we observe the presence of four dynamic vortices, where two distinct events can be highlighted: Firstly, we notice the formation of the upper vortex pair at $t = 2.8$, while the vortices of the lower pair coming from outside the represented region approach and eventually collide at $t = 3.2$, resulting in their disappearance. Furthermore, dynamic vortices continue to emerge in the same area and undergo similar collision phenomena. This is a direct effect of the previously mentioned symmetry. Since the Hamiltonian (12.8) and the initial condition (12.9) are invariant under the exchange of the $x$ and $y$ variables, the equations of motion should be invariant under the reflection in relation to the line $y = x$. Hence, the vortices are created and annihilated in pairs equally distant of this axis of symmetry, having the same absolute value of vorticity ($\nabla \times \mathbf{v}$), but with opposite signs. As a result, the pairs have the same diameter but spinning in opposite directions. It is worth to emphasize that the production of vortices is directly related to the increase of the coupling constant $\kappa$.

In Fig. 12.3 we show the parametric plot of the guidance equations solution until time $t = 215$, for different initial conditions. It is possible to observe that all four trajectories present very distinct and seemingly unpredictable behaviors when $\kappa = 1.0$. In contrast, the trajectories of the $\kappa = 0$ case are clearly ordered. This indicates that $\kappa \neq 0$ is crucial for inducing chaotic behavior. It is noteworthy that despite the inherent nonlinearity caused by the quantum potential, it alone is not sufficient for chaos to emerge. Without any constraint or coupling to bound the spatial coordinates, the emergence of unpredictability and sensitivity to initial conditions are nearly null, because there are no sufficient vortices to induce chaotic behavior and the dynamics are not conducive to chaos as well. Additionally, we notice that the same symmetry regarding the exchange of

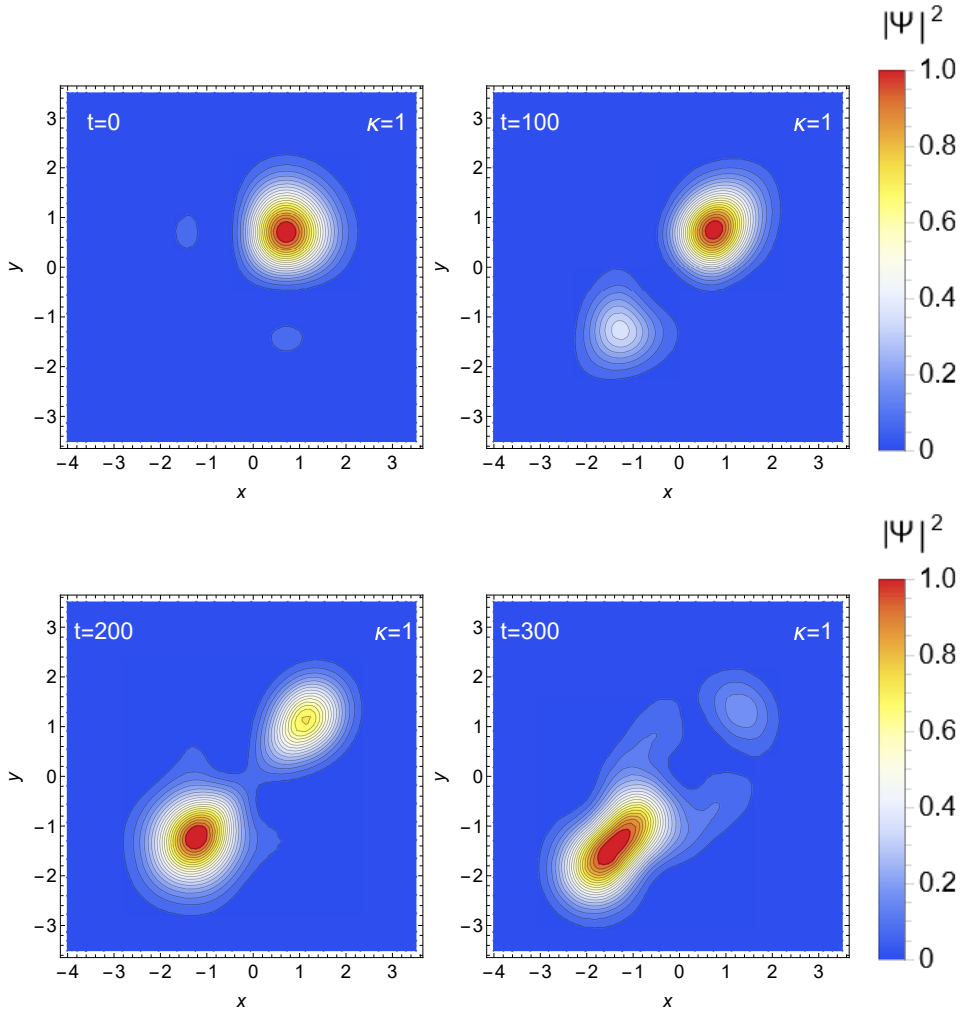


Figure 12.1: Evolution of the probability density $|\Psi(x, y, t)|^2$ of the generic anharmonic oscillator, for $\kappa = 1$, at (top left) $t = 0$, (top right) $t = 100$, (bottom left) $t = 200$ and (bottom right) $t = 300$.

the spatial variables also occurs in the level of the quantum trajectories, supporting the effectiveness of our numerical results.

Another characteristic of chaos is the sensitivity to initial conditions, where small perturbations in the system can result in significantly different outcomes. In Fig. 12.4 we illustrate such effect for $\kappa = 1.0$. We examine three trajectories with very close initial conditions, namely $(x_0, y_0) = (0.6, -0.5)$, $(x_0, y_0) = (0.6001, -0.5)$, and $(x_0, y_0) = (0.6, -0.5001)$. Initially they evolve practically together, but, as times increases, they exhibit significantly different behaviors as a consequence of the dynamical nonlinearity. Due to the nonvanishing value of the constant $\kappa$, which connects both spatial coordinates, such sensitivity is observed for both the $x$ and $y$ components, even considering an initial difference in only one of them. In Fig. 12.5, we notice that $\langle \ln \xi(t) \rangle$ is a nearly monotonically increasing function of time, when $\kappa > 0$, indicating an exponential deviation of the trajectories. Conversely, when $\kappa = 0$, no evidence exists of an exponential deviation, indicating a regular behavior.

Also analysing the results from Fig. 12.5, $\hbar$ has almost no influence in the deviation of the trajectories. Indeed, the same angular coefficient is found varying $\hbar$ from 0.05 to 1. In other words, the system studied here presents chaotic behavior in both classical and quantum regimes. Therefore, through the Bohmian approach of quantum systems, it is possible to study the quantum chaotic dynamics employing the same techniques used to study classical chaos, resulting in robust chaos in both limits ($\hbar = 1$ and $\hbar \to 0$).

Summarizing, we simulate, within the Bohmian quantum mechanical approach, a two-dimensional anharmonic oscillator under the influence of a coupling potential and of a tunnable Planck constant. The generic requirements for chaos (unpredictability and sensitivity to small perturbations of the initial conditions) are satisfied by this system. In the absence of coupling (i.e., $\kappa \to 0$), chaos disappears. Despite the fact that initial state might provide an entanglement between the spatial components, we do not observe chaos in this situation; notice that the commensurable ratio between the frequencies $\omega_x$ and $\omega_y$ [240], has been set as unity in our simulations. In remarkable contrast, for $\kappa \neq 0$ chaos emerges even considering the same frequencies. Additionally, no important influence is observed along the quantum-to-classical crossover ($\hbar \to 0$), thus validating the conjecture that no strong difference exists between quantum and classical chaos. Couplings as in Eq. (12.8) are good candidates for inducing quantum chaos (both strong and weak [46]) and possibly enlighten the study of emergence of vortices in quantum systems.

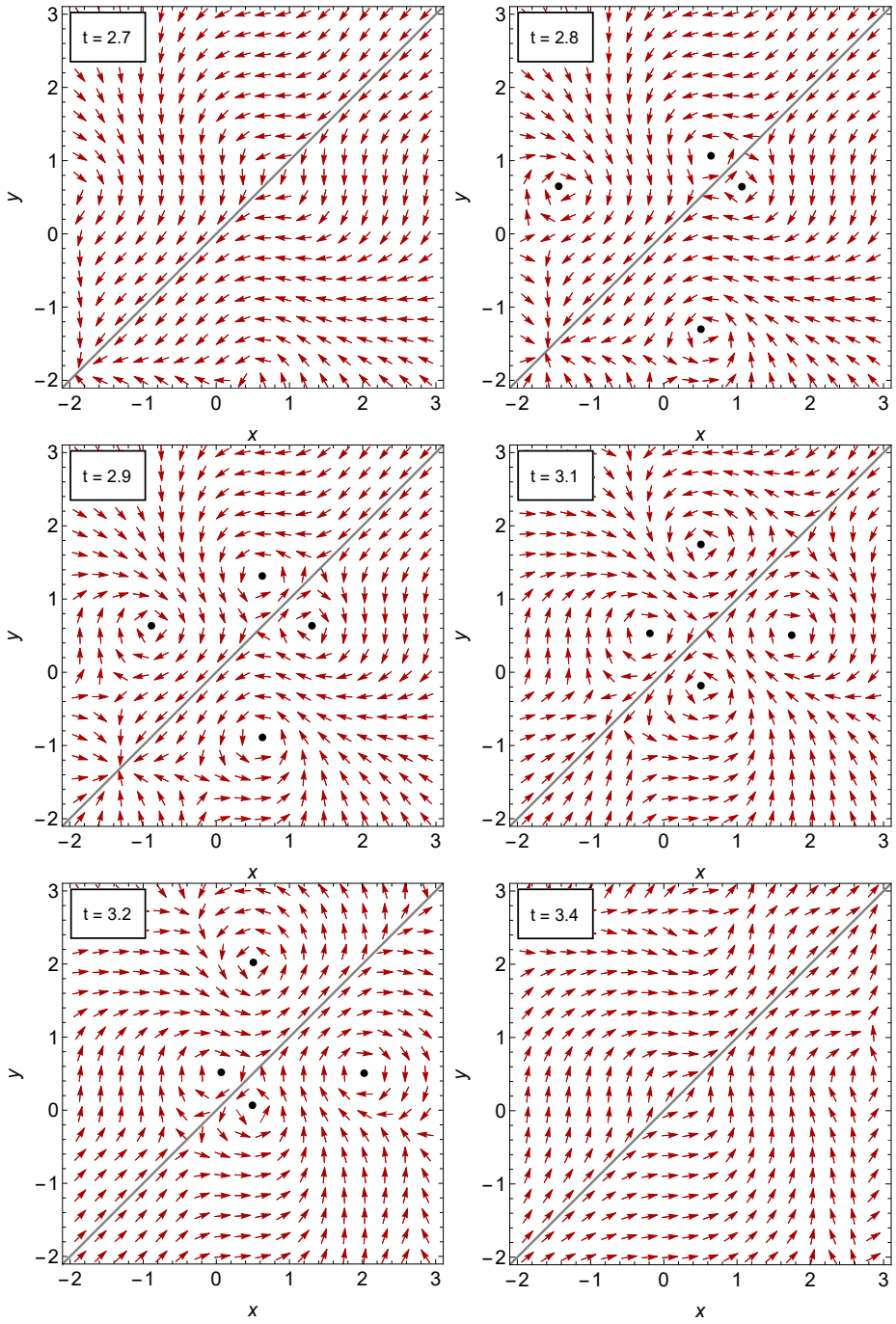


Figure 12.2: Ilustration of the emergence of four dynamical vortices in a square region $\mathbf{x} \in [-2, 3] \times [-2, 3]$ at $t = 2.7, 2.8, 2.9, 3.1, 3.2$ and $t = 3.4$ for $\kappa = 0.1$. We choose $\kappa = 0.1$ for didactic purposes (number of vortices increase as $\kappa$ also increases).

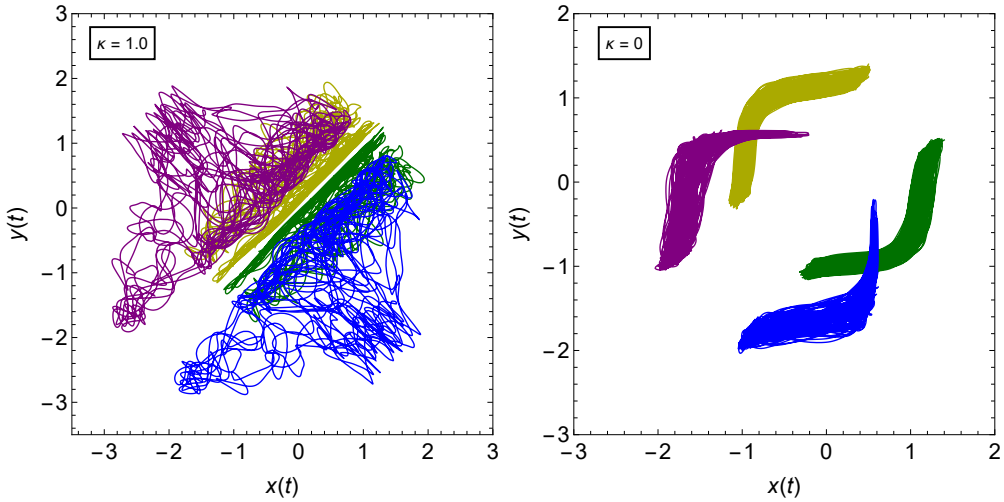


Figure 12.3: Parametric plot of the quantum trajectories $(x(t), y(t))$ until $t = 215$, considering initial conditions near vortices collision and repulsion. *Left:* $(x_0, y_0) = \{(1.4, 0.5), (0.5, 1.4), (0.6, -0.5), (-0.5, 0.6)\}$ with $\kappa = 1$. *Right:* with $\kappa = 0$ and the same previous initial conditions. Note the reflection symmetry with respect to the line $y = x$.

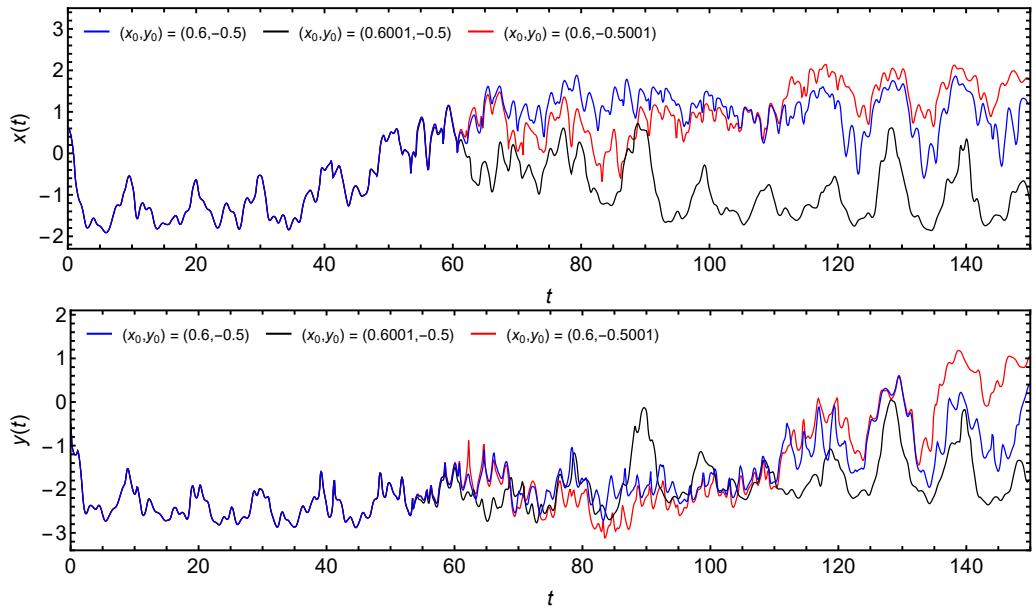


Figure 12.4: Plot of $x$ and $y$ as functions of time for $\kappa = 1.0$, considering three different initial conditions: $(x_0, y_0) = \{(0.6, -0.5), (0.6001, -0.5), (0.6, -0.5001)\}$. Even with a difference of $10^{-4}$ in just one spatial coordinate, the quantum trajectories behave very differently, highlighting the sensitivity to the initial conditions.

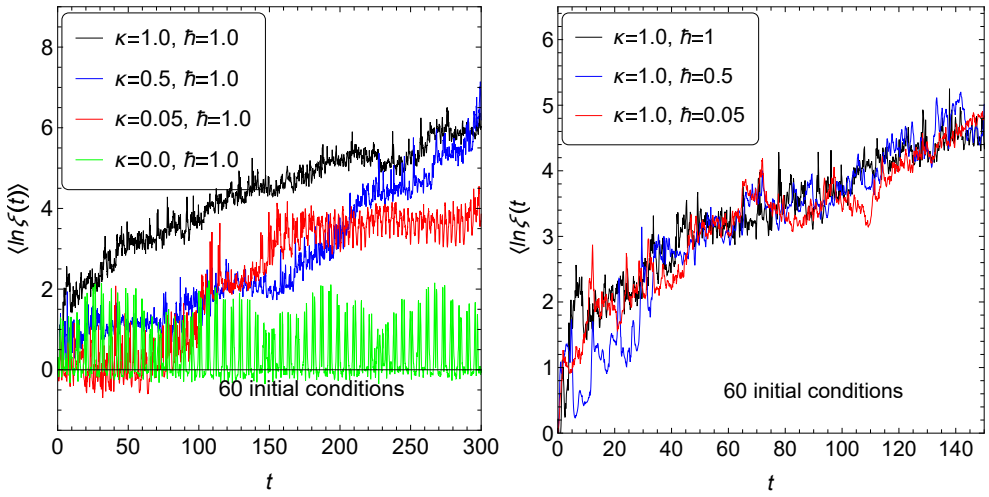


Figure 12.5: *Left:* $\langle \ln \xi(t) \rangle$ versus $t$ for $\hbar = 1$ and $\kappa = 0, 0.05, 0.5, 1$ with 60 pairs of initial conditions regularly spaced in the interval of $(x_0, y_0) \in [-1.5, -1.1] \cup [1.1, 1.5]$. *Right:* $\langle \ln \xi(t) \rangle$ versus $t$ for $\kappa = 1$ and $\hbar = 0.05, 0.5, 1$ with 60 pairs of initial conditions regularly spaced in the interval of $(x_0, y_0) \in [-0.5, -0.1] \cup [0.1, 0.5]$. We observe a growing tendency in the curves in the black, blue and red curves, thus indicating a positive Lyapunov number. While the increase in the value of $\kappa$ affects the value of the Lyapunov exponent, the change in the value of $\hbar$ does not appear to affect the chaotic behavior in the observed time window. In the limit of $\hbar \to 0$ it exactly reproduces the classical mechanical behavior.

# Chapter 13

# Final Remarks

The statistical mechanics describing a physical many-body system depends on various factors, such as interaction range and boundary conditions. For short-range interactions, the system is typically treated with the Boltzmann-Gibbs (BG) theory at thermal equilibrium ($q = 1$). However, non-equilibrium phenomena, as evidenced in our numerical results, suggest a departure from $q = 1$, emphasizing the need for nonadditive entropies.

In the $L \to \infty$ limit, our numerical results reveal a remarkable agreement with the centennial Fourier macroscopic law for thermal transport at all dimensions. Specifically, a numerical 'conspiracy' in the values of $(q, \eta, \gamma, \delta)$ implies the validity of Fourier's law, even hinting at $\delta = d - 1$ for all dimensions $d$.

Our collapsed results, expressed as $L^{d-1}\sigma(T, L) \propto e_{q(d)}^{-B(d)[L^{\gamma(d)}T]^{\eta(d)}}$, show a transition from $q$-Gaussians to $q$-stretched-exponentials due to a broader range of temperature values. Future work will explore the impact of long-range interactions on this form.

It is essential to recognize that physical systems do not adhere strictly to $q = 1$ or $q \neq 1$; the appropriate statistical mechanics depends on various factors. For instance, in thermal equilibrium with periodic boundary conditions, the BG theory applies, but a system permanently forced out of equilibrium exhibits turbulent-like fluctuations, leading to $q$-statistics.

In our studies of the classical inertial ferromagnetic $n$-vector models, we find validation of Fourier's law from first principles, with temperature-dependent thermal conductivity exhibiting independence of system size in the high-temperature regime. The thermal conductivity conforms to $q$-statistics, collapsing into a shrunken $q$-exponential form. A universal condition, $\frac{\eta(n,d)\gamma(n,d)}{q(n,d)-1} = 1$, validates Fourier's law for $n$-vector models, indicating potential universality across different values of $(n, d)$. As future perspective, we intend to investigate other linear transport relations through nonequilibrium molecular dynamics (direct method), such as Fick's law, Newton's law, and Ohm's law.

In summary, our findings provide insights into the thermal transport properties of classical rotators, confirming Fourier's law and suggesting a universal form for $q$-statistics across various dimensions and spin components.

About the human electroencephalograms, our findings suggest that the $q$-statistic offers valuable insights into brain complexity, particularly in distinguishing between ADHD and typical subjects. However, interpreting the clinical significance of $q$ values remains premature. Further studies, currently underway, are needed to elucidate the observed complexities in ADHD and typical subjects. Our research underscores the importance of considering long-range correlations in understanding brain function, as evidenced by EEG studies and the sensitivity of the parameter $c$ in ADHD detection. While our methodology presents robust evidence for utilizing $q$-statistics in assessing brain complexity and classifying mental states, further investigation is warranted to elucidate the biological correlates of $q$ and $c$ parameters. In conclusion, $q$-statistics can be useful for the diagnosis of ADHD and potentially other atypical conditions.

About the evidence of strong chaos in quantum systems with the Bohmian approach, that analysis can be a starting point for further investigations of the same model with different initial conditions. For instance, we can verify whether the increase of initial states implies the increase or decrease of the Lyapunov number. Moreover, with the development of more computational capacity, it will be possible to evaluate the precise value of the Lyapunov exponent, instead of only its tendency. Also, with this same numerical procedures we can explore other models with are not analytically tractable, not only assuming potentials as small perturbations. For instance, it is possible to conduct the analysis of systems in other coordinates as well, as in the interaction between topological insulators and superconductors, where it is suitable to use cylindrical coordinates with some symmetries [279]. It is important to note that exploring the compatibility between classical and quantum chaos derived from averaging the coordinates of a specific system is a significant aspect deserving attention. Another interesting possibility is the study of the equivalence between this Bohmian approach of the quantum chaos and other usual manners to characterize chaos at quantum level, such as the random matrix theory and the periodic orbit expansions, where the focus is on properties like spectral fluctuations and statistical properties regarding the energy eigenvalues. Also, as a final perspective, the numerical procedures implemented here in simulating a tunable Planck's constant can pave the way for the search of quantum scars [280], and also can be useful for the study of weak chaotic systems.

# Bibliography


[1] J. B. J. Fourier, *Équations du Mouvement de la Chaleur. Théorie Analytique de La Chaleur*, Paris, F. Didot, 99–158 (1822).

[2] R. W. Flumerfelt and J. C. Slattery, *An experimental study of the validity of Fourier's law*, *AIChE Journal*, **15**, 291-292 (1969).

[3] X. Xu, J. Chen, and B. Li, *Phonon thermal conduction in novel 2D materials*, *Journal of Physics: Condensed Matter*, **28**(48), 483001 (2016).

[4] X. Wu, V. Varshney, J. Lee, Y. Pang, A. K. Roy, and T. Luo, *How to characterize thermal transport capability of 2D materials fairly? – Sheet thermal conductance and the choice of thickness*, *Chemical Physics Letters*, **669**, 233–237 (2017).

[5] H. Büttner and F. Mokross, *Fourier's law and thermal conduction*, *Nature*, **311**(5983), 217–218 (1984).

[6] P. Laurençot, *Weak Solutions to a Penrose-Fife Model with Fourier Law for the Temperature*, *Journal of Mathematical Analysis and Applications*, **219**(2), 331–343 (1998).

[7] K. Aoki and D. Kusnezov, *Bulk properties of anharmonic chains in strong thermal gradients: non-equilibrium $\phi^4$ theory*, *Physics Letters A*, **265**(4), 250–256 (2000).

[8] C. Gruber and A. Lesne, *Hamiltonian model of heat conductivity and Fourier law*, *Physica A: Statistical Mechanics and Its Applications*, **351**(2-4), 358–372 (2005).

[9] C. Bernardin and S. Olla, *Fourier's Law for a Microscopic Model of Heat Conduction*, *Journal of Statistical Physics*, **121**(3-4), 271-289 (2005).

[10] J. Bricmont and A. Kupiainen, *Towards a Derivation of Fourier's Law for Coupled Anharmonic Oscillators*, *Communications in Mathematical Physics*, **274**(3), 555–626 (2007).

[11] J. Bricmont and A. Kupiainen, *Fourier's Law from Closure Equations*, *Physical Review Letters*, **98**(21) (2007).

[12] L.A. Wu and D. Segal, *Fourier's law of heat conduction: Quantum mechanical master equation analysis*, Phys. Rev. E, **77**(6) (2008).

[13] P. Gaspard and T. Gilbert, *Heat Conduction and Fourier's Law by Consecutive Local Mixing and Thermalization*, Phys. Rev. Lett., **101**(2) (2008).

[14] J. L. Lebowitz and H. Spohn, *Transport properties of the Lorentz gas: Fourier's law*, J. Stat. Phys., **19**(6), 633–654 (1978).

[15] M. Michel, M. Hartmann, J. Gemmer, and G. Mahler, *Fourier's Law confirmed for a class of small quantum systems*, Eur. Phys. J. B, **34**(3), 325–330 (2003).

[16] G. T. Landi and M.J. de Oliveira, *Fourier's law from a chain of coupled planar harmonic oscillators under energy-conserving noise*, Phys. Rev. E, **89**(2) (2014).

[17] Y. Dubi and M. Di Ventra, *Fourier's law: Insight from a simple derivation*, Phys. Rev. E, **79**(4) (2009).

[18] Y. Dubi and M. Di Ventra, *Reconstructing Fourier's law from disorder in quantum wires*, Phys. Rev. B, **79**(11) (2009).

[19] A. Gerschenfeld, B. Derrida, J.L. Lebowitz, *Anomalous Fourier's Law and Long Range Correlations in a 1D Non-momentum Conserving Mechanical Model*, J. Stat. Phys., **141**(5), 757–766 (2010).

[20] A. Dhar, K. Venkateshan, and J. L. Lebowitz, *Heat conduction in disordered harmonic lattices with energy-conserving noise*, Phys. Rev. E, **83**(2) (2011).

[21] S. Liu, X.F. Xu, R.G. Xie, G. Zhang, and B. W. Li, *Anomalous heat conduction and anomalous diffusion in low dimensional nanoscale systems*, Eur. Phys. J. B, **85**(10) (2012).

[22] N. Yang, G. Zhang, B. Li. *Violation of Fourier's law and anomalous heat diffusion in silicon nanowires*, Nano Today, **5**(2), 85–90 (2010).

[23] Z. Han, A. Fina, *Thermal conductivity of carbon nanotubes and their polymer nanocomposites: A review*, Prog. Polym. Sci., **36**(7), 914-944 (2011).

[24] H. E. Stanley, *Dependence of Critical Properties upon Dimensionality of Spins*, Phys. Rev. Lett. **20** (12): 589–592 (1968).

[25] A. V. Savin, G. P. Tsironis, and X. Zotos, *Thermal conductivity of a classical one-dimensional Heisenberg spin model*, Phys. Rev. B **72**, 140402 (2005).

[26] K. Louis, P. Prelovsêk, and X. Zotos, *Thermal conductivity of one-dimensional spin-1/2 systems coupled to phonons*, Phys. Rev. B **74**, 235118 (2006).

[27] Y. Li, N. Li, and B. Li, *Temperature dependence of thermal conductivities of coupled rotator lattice and the momentum diffusion in standard map*, Eur. Phys. J. B **88**, 182 (2015).

[28] C. Olivares and C. Anteneodo, *Role of the range of the interactions in thermal conduction*, Phys. Rev. E **94**(4) (2016).

[29] Y. Li, N. Li, U. Tirnakli, B. Li, and C. Tsallis, *Thermal conductance of the coupled-rotator chain: Influence of temperature and size*, EPL **117**, 60004 (2017).

[30] F. Azizi, H. Rezania, *Thermal transport properties of Heisenberg antiferromagnet on honeycomb lattice: The effects of anisotropy*, Physica E: Low-dimensional Systems and Nanostructures **135** (2022).

[31] R. Harris and Martin Grant, *Thermal conductivity of a kinetic Ising model*, Phys. Rev. B **38**, 9323(R) (1988).

[32] M. Mena, N. Hänni, S. Ward, E. Hirtenlechner, R. Bewley, C. Hubig, U. Schollwöck, B. Normand, K.W. Krämer, D. F. McMorrow, and Ch. Röegg, *Thermal Control of Spin Excitations in the Coupled Ising-Chain Material* $RbCoCl_3$, Phys. Rev. Lett. **124**, 257201 (2020).

[33] Y. Kojima, N. Kurita, H. Tanaka, and K. Nakajima, *Magnons and spinons in* $Ba_2CoTeO_6$*: A composite system of isolated spin-*$\frac{1}{2}$ *triangular Heisenberg-like and frustrated honeycomb Ising-like antiferromagnets*, Phys. Rev. B **105**, L020408 (2022).

[34] H. C. Chauhan, B. Kumar, A. Tiwari, J. K.Tiwari, and S. Ghosh, *Different Critical Exponents on Two Sides of a Transition: Observation of Crossover from Ising to Heisenberg Exchange in Skyrmion Host* $Cu_2OSeO_3$, Phys. Rev. Lett. **128**, 015703 (2022).

[35] C. Tsallis, *Introduction to Nonextensive Statistical Mechanics: Approaching a Complex World*, 2nd Edition (Springer: New York, NY, USA, 2023).

[36] C. Tsallis, *Possible generalization of Boltzmann-Gibbs statistics*, J. Stat. Phys. **52**, 479-487 (1988).

[37] H. S. Lima, and C. Tsallis, *Exploring the Neighborhood of q-Exponentials*, Entropy **22**, no. 12: 1402 (2020).

[38] M. A. F. dos Santos, F. D. Nobre, and E. M. F. Curado, *Entropic form emergent from superstatistics*, Phys. Rev. E **107**, 014132 (2023).

[39] C. Tsallis, H.S. Lima, U. Tirnakli, and D. Eroglu, *First-principle validation of Fourier's law in d = 1, 2, 3 classical systems*, Physica D: Nonlinear Phenomena **446**, 133681 (2023).

[40] H. S. Lima, C. Tsallis, *Ising chain: Thermal conductivity and first-principle validation of Fourier's law*, Phys. A: Stat. Mech. Appl. **628**, 129161 (2023).

[41] H. S. Lima, C. Tsallis, and F. D. Nobre, *First-Principle Validation of Fourier's Law: One-Dimensional Classical Inertial Heisenberg Model*, Entropy **26**, 1-25 (2023).

[42] H. S. Lima and C. Tsallis, *Fourier's law breakdown for the planar-rotator chain with generic-range coupling*, in progress (2024).

[43] D.M. Abramov, C. Tsallis, H.S. Lima, *Neural complexity through a nonextensive statistical-mechanical approach of human electroencephalograms.* Sci Rep. **13**(1):10318 (2023).

[44] D. M. Abramov, H. S. Lima, V. Lazarev, P. R. Galhanone, and C. Tsallis, *Identifying Attention-Deficit/Hyperactivity Disorder through the electroencephalogram complexity*, in progress (2024).

[45] H. S. Lima, M.M.A. Paixão, and C. Tsallis, *de Broglie-Bohm analysis of a nonlinear membrane: From quantum to classical chaos*, Chaos **34**(2), 023125 (2024).

[46] Y.S. Weinstein, S. Lloyd and C. Tsallis, *Border between regular and chaotic quantum dynamics*, Phys. Rev. Lett. **89**, 214101 (2002).

[47] C. Tsallis, E. P. Borges , and A. R. Plastino, *Entropy evolution at generic power-law edge of chaos*, Chaos, Solitons And Fractals **74**, 113855 (2023).

[48] H. B. Callen, *Thermodynamics and an Introduction to Thermostatistics*, 2nd ed., John Wiley & Sons (1991).

[49] R. H. Swendsen, *An Introduction to Statistical Mechanics and Thermodynamics*, 2nd edn (Oxford, 2019; online edn, Oxford Academic, 20 Feb. 2020).

[50] D. Jiulin, *Nonextensivity and the power-law distributions for the systems with self-gravitating long-range interactions*, Astrophys Space Sci **312**, 47–55 (2007).

[51] Ch. Binek, S. Polisetty, Xi He, T. Mukherjee, R. Rajesh, and J. Redepenning, *Nonextensivity in magnetic nanoparticle ensembles*, Phys. Rev. B **74**, 054432 (2006).

[52] T. Dauxois, S. Ruffo, E. Arimondo, M. Wilkens, *Dynamics and Thermodynamics of Systems with Long-Range Interactions: An Introduction*, In: T. Dauxois, S. Ruffo, E.

Arimondo, M. Wilkens, (eds) Dynamics and Thermodynamics of Systems with Long-Range Interactions. Lecture Notes in Physics, vol 602. Springer, Berlin, Heidelberg (2002).

[53] R. S. Ellis, H. Touchette, B. Turkington, *Thermodynamic versus statistical nonequivalence of ensembles for the mean-field Blume–Emery–Griffiths model*, Physica A **335**, 518-538 (2004).

[54] I. Latella, A. Pérez-Madrid, A. Campa, L. Casetti, and S. Ruffo, *Thermodynamics of Nonadditive Systems*, Phys. Rev. Lett. **114**, 230601 (2015).

[55] A. Campa et al., *Physics of Long-Range Interacting Systems* (Oxford, 2014; online edn, Oxford Academic, 23 Oct. 2014).

[56] C. Tsallis and L.J.L. Cirto, *Black hole thermodynamical entropy*, Eur. Phys. J. C, **73**, 2487 (2013).

[57] J. W. Gibbs, *On the Equilibrium of Heterogeneous Substances*, Transactions of the Connecticut Academy of Arts and Sciences. **3**, 343–524 (1874-1878).

[58] J.W. Gibbs, *Elementary Principles in Statistical Mechanics-Developed with Especial Reference to the Rational Foundation of Thermodynamics* (C. Scribner's Sons, New York, 1902).

[59] A. Einstein, *Theorie der Opaleszenz von homogenen Flüssigkeiten und Flussigkeitsgemischen in der Nähe des kritischen Zustandes*, Annalen der Physik **33**, 1275 (1910).

[60] E. Fermi, *Thermodynamics*, (Dover, New York, 1936), p. 53.

[61] E. Majorana, *The value of statistical laws in physics and social sciences*, in G. Gentile Jr. in Scientia **36**, 58 (1942), in Italian. Translated into English by R.N. Mantegna, Quantitative Finance **5**, 133–140 (2005).

[62] C.E. Shannon, *Bell Syst. Tech. J.* **27**, 379 and 623 (1948); A mathematical theory of communication. Bell Syst. Tech. J. **27**, 379–423 and 623–656 (1948); and *The Mathematical Theory of Communication* (University of Illinois Press, Urbana, 1949).

[63] L. Tisza, *Generalized Thermodynamics*, (MIT Press, Cambridge, Massachusetts, 1961), p. 123.

[64] P.T. Landsberg, *Thermodynamics and Statistical Mechanics* (Oxford University Press, New York, 1978) and (Dover, New York, 1990).

[65] P.T. Landsberg, *Is equilibrium always an entropy maximum?* J. Stat. Phys. **35**, 159 (1984).

[66] L.G. Taff, *Celestial Mechanics* (Wiley, New York, 1985).

[67] N.G. van Kampen, *Stochastic Processes in Physics and Chemistry* (North-Holland, Amsterdam, 1981).

[68] W.C. Saslaw, *Gravitation Physics of Stellar and Galactic Systems* (Cambridge University Press, Cambridge, 1985).

[69] R. Balescu, *Equilibrium and Nonequilibrium Statistical Mechanics* (Wiley, 1975, New York).

[70] R.K. Saxena, A.M. Mathai, H.J. Haubold, *Astrophysical thermonuclear functions for Boltzmann— Gibbs statistics and Tsallis statistics*. Phys. A **344**, 649–656 (2004).

[71] A.R. Plastino, A. Plastino, *Stellar polytropes and Tsallis' entropy*. Phys. Lett. A **174**, 384–386 (1992).

[72] M. Ausloos, F. Petroni, *Tsallis non-extensive statistical mechanics of El Niño southern oscillation index*. Phys. A **373**, 721–736 (2006).

[73] M.I. Bogachev, A.R. Kayumov, A. Bunde, *Universal internucleotide statistics in full genomes: A footprint of the DNA structure and packaging?* PLoS ONE **9**, e112534 (2014).

[74] L. Borland, *Closed form option pricing formulas based on a non-Gaussian stock price model with statistical feedback*. Phys. Rev. Lett. **89**, 098701 (2002).

[75] A. Deppman, E. Megias, D.P. Menezes, *Fractals, non-extensive statistics, and QCD*. Phys. Rev. D **101**, 034019 (2020).

[76] G. Combe, V. Richefeu, M. Stasiak, and A.P.F. Atman, Experimental validation of nonextensive scaling law in confined granular media, Phys. Rev. Lett. **115**, 238301 (2015).

[77] E. Lutz and F. Renzoni, Beyond Boltzmann-Gibbs statistical mechanics in optical lattices, Nature Physics **9**, 615-619 (2013).

[78] C. Tsallis, *Introduction to Nonextensive Statistical Mechanics–Approaching a Complex World*; Springer: New York, NY, USA, 2009.

[79] A Regularly Updated Bibliography. Available online: `http://tsallis.cat.cbpf.br/biblio.htm` (accessed on September 14th, 2020).

[80] C. Tsallis, G. Bemski, R.S. Mendes, *Is re-association in folded proteins a case of nonextensivity?* Phys. Lett. A **257**, 93–98 (1999).

[81] U. Tirnakli, E.P. Borges, *The standard map: From Boltzmann-Gibbs statistics to Tsallis statistics*. Sci. Rep. **6**, 23644 (2016).

[82] E.P. Borges, I. Roditi, *A family of non-extensive entropies*, Phys. Lett. A **246**, 399 (1998).

[83] V. Schwammle, C. Tsallis, *Two-parameter generalization of the logarithm and exponential functions and Boltzmann-Gibbs-Shannon entropy*. J. Math. Phys. **48**, 113301 (2007).

[84] G.A. Tsekouras, C. Tsallis, Generalized entropy arising from a distribution of q-indices. Phys. Rev. E **71**, 046144 (2005).

[85] T. Oikonomou, A. Provata, Non-extensive trends in the size distribution of coding and non-coding DNA sequences in the human genome. Eur. Phys. J. B **50**, 259–264 (2006).

[86] B. Bakar, U. Tirnakli, Analysis of self-organized criticality in Ehrenfest's dog-flea model. Phys. Rev. E **79**, 040103(R) (2009).

[87] A. Celikoglu, U. Tirnakli, S.M.D. Queiros, Analysis of return distributions in the coherent noise model. Phys. Rev. E **82**, 021124 (2010).

[88] B. Bakar, U. Tirnakli, Return distributions in dog-flea model revisited. Phys. A **389**, 3382–3386 (2010).

[89] M. Planck, Ueber irreversible Strahlungsvorgänge. Ann. d. Phys. **1**, 69–122 (1900).

[90] M. Planck, Zur Theorie des Gesetzes der Energieverteilung im Normalspectrum. Verhandl. Dtsch. Phys. Ges. **2**, 237–245 (1900).

[91] G. Sicuro, D. Bagchi, C. Tsallis, On the connection between linear combination of entropies and linear combination of extremizing distributions. Phys. Lett. A **380**, 2025–2030 (2016).

[92] G. Ruiz, U. Tirnakli, E.P. Borges, C. Tsallis, Statistical characterization of the standard map. J. Stat. Mech. **2017**, 063403 (2017).

[93] J. S. Andrade, Jr., G.F.T. da Silva, A.A. Moreira, F.D. Nobre, E.M.F. Curado, Thermostatistics of overdamped motion of interacting particles. Phys. Rev. Lett. **105**, 260601 (2010).

[94] C. Tsallis, R.S. Mendes, A.R. Plastino, The role of constraints within generalized nonextensive statistics. Phys. A **261**, 534–554 (1998).

[95] G.L. Ferri, S. Martinez, A. Plastino, Equivalence of the four versions of Tsallis' statistics. J. Stat. Mech. Theory Exp. **2005**, P04009 (2005).

[96] F. Shafee, Lambert function and a new non-extensive form of entropy. IMA J. Appl. Math. **72**, 785–800 (2007).

[97] G. Kaniadakis, Statistical mechanics in the context of special relativity. Phys. Rev. E **66**, 056125 (2002).

[98] S. Asgarani, B. Mirza, Probability distribution of (Schwammle and Tsallis) two-parameter entropies and the Lambert W-function. Phys. A **387**, 6277–6283 (2008).

[99] C.B. Corcino, R.B. Corcino, Logarithmic generalization of the Lambert W function and its applications to adiabatic thermostatics of the three-parameter entropy. arXiv:2011.04283 (2020).

[100] D. Ruelle, *Statistical Mechanics: Rigorous Results*, 4th ed, Mathematical Physics Monogram Series, 1-2 (1983).

[101] P. B. M. Vranas, *Epsilon-Ergodicity and the Success of Equilibrium Statistical Mechanics*, Philosophy of Science **65**(4):688-708 (1998).

[102] R. Kubo, M. Toda, and N. Hashitsume, Statistical Physics II: Nonequilibrium statistical mechanics, Springer Series in Solid-State Sciences. Berlin, Heidelberg: Springer (1985).

[103] C. Beck and E. G. D. Cohen, Superstatistics, Physica A **322**, 267-275 (2003).

[104] T. Tomé and M. J. de Oliveira, Stochastic Dynamics and Irreversibility, Graduate Texts in Physics, Springer (2023).

[105] A. Fick, On liquid diffusion, Philos. Mag. J. Sci **10**, 31–39 (1855).

[106] A. Paul, T. Laurila, V. Vuorinen, S. V. Divinski, *Fick's Laws of Diffusion. In: Thermodynamics, Diffusion and the Kirkendall Effect in Solids*, Springer, Cham (2014).

[107] M. G. Levitsky, *Chapter 6: Diffusion of Gases and Interpretation of Pulmonary Function Tests. In Pulmonary Physiology*, 9th ed. New York: McGraw Hill Education (2018).

[108] I. Newton, Philosophiae Naturalis Principia Mathematica, London (1687).

[109] P.G. Lemarie-Rieusset, *The Navier-Stokes Problem in the 21st Century*, 2nd ed., Chapman and Hall/CRC (2023).

[110] G. S. Ohm, *Die galvanische Kette, mathematisch bearbeitet*, Berlin: T. H. Riemann (1827).

[111] K. Yang and J. O. Hirschfelder, Generalizations of classical Poisson brackets to include spin, Phys. Rev. A **22**, 1814 (1980).

[112] H. Goldstein , *Classical Mechanics*, 2nd ed., Addison-Wesley (1980).

[113] K. Binder, and D. Landau, *Critical properties of the two-dimensional anisotropic Heisenberg model*, Phys. Rev. B **13**,1140-1155(1976).

[114] L. E. Reichl, *A Modern Course in Statistical Physics* (New York: Physics Books Co., **2005**), 197-231.

[115] Y. Shang and K. Yao, *Influence of uniaxial anisotropy on a quantum XY spin-glass model with ferromagnetic coupling*, Phys. Rev. B **68**(5), (2003).

[116] S. Jaiswal, K. Litzius, I. Lemesh, F. Büttner, S. Finizio, J. Raabe, M. Weigand, K. Lee, J. Langer, B. Ocker, G. Jakob, G. S. D. Beach, M. Kläui; Investigation of the Dzyaloshinskii-Moriya interaction and room temperature skyrmions in W/-CoFeB/MgO thin films and microwires. Appl. Phys. Lett. **111** (2): 022409 (2017).

[117] S. Dong, H. Xiang, E. Dagotto, *Magnetoelectricity in multiferroics: a theoretical perspective*, National Science Review **6**(4), 629–641 (2019).

[118] I. F. Sharafullin, M. Kh. Kharrasov, and H. T. Diep, *Dzyaloshinskii-Moriya interaction in magnetoferroelectric superlattices: Spin waves and skyrmions*, Phys. Rev. B **99**, 214420 (2019).

[119] P. Jund, S. G. Kim, and C. Tsallis, Crossover from extensive to nonextensive behavior driven by long-range interactions, Phys. Rev. B **52**, 50 (1995).

[120] C. Anteneodo and C. Tsallis, Breakdown of the exponential sensitivity to the initial conditions: Role of the range of the interaction, Phys. Rev. Lett. **80**, 5313-5316 (1998).

[121] R. Pakter and Y. Levin, *Non-equilibrium Dynamics of an Infinite Range XY Model in an External Field*, J Stat Phys **150**, 531–539 (2013).

[122] L. J. L. Cirto, L. S. Lima, and F. D. Nobre, Controlling the range of interactions in the classical inertial ferromagnetic Heisenberg model: analysis of metastable states, J. Stat. Mech. P04012 (2015).

[123] H. C. Andersen, *Molecular dynamics simulations at constant pressure and/or temperature*, J. Chem. Phys. **72** (4), 2384–2393 (1980).

[124] H. J. C. Berendsen, J. P. M. Postma, W. F. van Gunsteren, A. DiNola, J. R. Haak, *Molecular dynamics with coupling to an external bath*, J. Chem. Phys. **81**(8), 3684–3690 (1984).

[125] S. Nosé, *A unified formulation of the constant temperature molecular-dynamics methods*, J. Chem. Phys.**81** (1), 511–519 (1984).

[126] W. G. Hoover, *Canonical dynamics: Equilibrium phase-space distributions*, Phys. Rev. A. **31** (3): 1695–1697 (1985).

[127] G. Bussi, D. Donadio, M. Parrinello, *Canonical sampling through velocity rescaling*, J. Chem. Phys. **126** (1), 014101 (2007).

[128] C. Mejía-Monasterio, A. Politi, L. Rondoni, Heat flux in one-dimensional systems. Phys. Rev. E **100**, 032139 (2019).

[129] T. Prosen and D. K. Campbell, *Normal and anomalous heat transport in one-dimensional classical lattices*, Chaos **15** (1): 015117 (2005).

[130] M. S. Green, *Markoff Random Processes and the Statistical Mechanics of Time-Dependent Phenomena. II. Irreversible Processes in Fluids*, The Journal of Chemical Physics. **22** (3): 398–413 (1954).

[131] R. Kubo, *Statistical-Mechanical Theory of Irreversible Processes. I. General Theory and Simple Applications to Magnetic and Conduction Problems*, Journal of the Physical Society of Japan **12** (6): 570–586 (1957).

[132] L. Verlet, Computer "Experiments" on Classical Fluids. I. Thermodynamical Properties of Lennard-Jones Molecules. Phys. Rev. **159**, 98–103 (1967).

[133] M.G. Paterlini and D.M. Ferguson, Constant temperature simulations using the Langevin equation with velocity Verlet integration, Chemical Physics **236**, 243–252 (1998).

[134] C. Tsallis, Entropy, Encyclopedia **2**, 264-300 (2022).

[135] O. Penrose, Foundations of Statistical Mechanics: A Deductive Treatment, Pergamon, Oxford, page 167 (1970).

[136] R.M. Pickup, R. Cywinski, C. Pappas, B. Farago, P. Fouquet, Generalized Spin-Glass Relaxation, Phys. Rev. Lett **102**, 097202 (2009).

[137] E.P. Borges, C. Tsallis, A. Giansanti and D. Moroni, Dinamica de um sistema nao extensivo de rotores classicos anisotropicos acoplados, in Tendencias da Fisica Estatistica no Brasil, ed. T. Tome, volume honoring S.R.A. Salinas (Editora Livraria da Fisica, Sao Paulo, 2003), page 84.

[138] M. Blume, Theory of the First-Order Magnetic Phase Change in U$O_2$, Phys. Rev. **141**, 517 (1996).

[139] H. W. Capel, On the possibility of first-order phase transitions in Ising systems of triplet ions with zero-field splitting, Physica **32**, 5, 966-988 (1966).

[140] D. C. Rapaport and D. P. Landau, Critical dynamics of a dynamical version of the classical Heisenberg model, Phys. Rev. E **53**, 4696-4702 (1996).

[141] A. Rodríguez, F. D. Nobre, C. Tsallis, d-Dimensional Classical Heisenberg Model with Arbitrarily-Ranged Interactions: Lyapunov Exponents and Distributions of Momenta and Energies, Entropy **21**, 31 (2019).

[142] D. J. Evans, On the Representation of Orientation Space, Mol. Phys. **34**, 317-325 (1977).

[143] D. J. Evans, S. Murad, Singularity free algorithm for molecular dynamics simulation of rigid polyatomics, Mol. Phys. **34**, 327-331 (1977).

[144] A. V. Savin, G. P. Tsironis, and X. Zotos, Thermal conductivity of a classical one-dimensional spin-phonon system, Phys. Rev. B **75**, 214305 (2007).

[145] C. Giardiná, R. Livi, A. Politi, and M. Vassalli, Finite Thermal Conductivity in 1D Lattices, Phys. Rev. Lett. **84**, 2144 (2000).

[146] N. Hlubek, X. Zotos, S. Singh, R. Saint-Martin, A. Revcolevschi, B. Büchner, and C. Hess, Spinon heat transport and spin-phonon interaction in the spin-1/2 Heisenberg chain cuprates $Sr_2CuO_3$ and $SrCuO_2$, J. Stat. Mech, P03006 (2012).

[147] C. Beck, G. S. Lewis, and H. L. Swinney, Measuring nonextensitivity parameters in a turbulent Couette-Taylor flow, Phys. Rev. E **63**, 035303 (2001).

[148] A. H. Darooneh and A. Mehri, A nonextensive modification of the Gutenberg-Richter law: $q$-stretched exponential form, Phys. A **389**, 509 (2009).

[149] C. Hicke,M. I. Dykman, *Classical dynamics of resonantly modulated large-spin systems*, Phys. Rev. B **78**(2), 024401 (2008).

[150] Z. Rieder, J. L. Lebowitz, E. Lieb, *Properties of a Harmonic Crystal in a Stationary Nonequilibrium State*, J. Math. Phys. **8**, 1073 (1967).

[151] D.S. Bassett and M.S. Gazzaniga, *Understanding complexity in the human brain*, Trends Cogn. Sci. **15**(5), 200-9 (2011).

[152] J.T. Braslow, J.S. Brekke, and J. Levenson, *Psychiatry's Myopia-Reclaiming the Social, Cultural, and Psychological in the Psychiatric Gaze*, JAMA Psychiatry. **78**(4): 349-350 (2021).

[153] G. Canguilhem, *The Normal and the Pathological*, trans. Carolyn R. Fawcett and Robert S. Cohen, New York: Zone Books (1991).

[154] Z.J. Lau, T. Pham, S.H.A. Chen, and D. Makowski, *Brain entropy, fractal dimensions and predictability: A review of complexity measures for EEG in healthy and neuropsychiatric populations*, Eur J Neurosci, **56**(7):5047-5069 (2022).

[155] Erwin-Josef Speckmann, Christian E. Elger, and Ali Gorji, *Neurophysiologic Basis of EEG and DC Potentials, in Niedermeyer's Electroencephalography: Basic Principles, Clinical Applications, and Related Fields*, eds. Schomer, D. L.; da Silva, F. H. L., Lippincott Williams & Wilkins, 17-31 (2011).

[156] L. Boltzmann, Weitere Studien über das Wärmegleichgewicht unter Gasmolekülen [Further Studies on Thermal Equilibrium Between Gas Molecules], Wien, Ber. **66**, 275 (1872).

[157] J.W. Gibbs, Elementary Principles in Statistical Mechanics – Developed with Especial Reference to the Rational Foundation of Thermodynamics, C. Scribner's Sons, New York (1902); Yale University Press, New Haven (1948); OX Bow Press, Woodbridge, Connecticut (1981).

[158] M. Gell-Mann and C. Tsallis, eds., Nonextensive Entropy - Interdisciplinary Applications, Oxford University Press, New York (2004).

[159] L. Montangie, F. Montani, Quantifying higher-order correlations in a neuronal pool, Physica A: Statistical Mechanics and its Applications, **421**, 388-400 (2015).

[160] L. Montangie, F. Montani, Higher-order correlations in common input shapes the output spiking activity of a neural population, Physica A: Statistical Mechanics and its Applications, **471**, 845-861 (2017).

[161] L. Montangie, F. Montani, Common inputs in subthreshold membrane potential: The role of quiescent states in neuronal activity, Phys. Rev. E, **97**(6), 060302(R) (2018).

[162] N. Guisante, M. Pallares di Nunzio, N. Martinez, O. A. Rosso, and F. Montani, Chaotic dynamics of the Henon map and neuronal inputoutput: a comparison with neurological data, Chaos **33**, 043111 (2023).

[163] H. Yang, J. Li, and X. Zheng, Different Influences of Negative and Neutral Emotional Interference on Working Memory in Trait Anxiety, Front Psychol. **12**, 570552 (2021).

[164] J. Polich and J.R. Criado, Neuropsychology and neuropharmacology of P3a and P3b, Int J Psychophysiol. **60**(2), 172-85 (2006).

[165] M.J.D. Powell, A new algorithm for unconstrained optimization, Nonlinear Programming. New York: Academic Press. pp. 31–66 (1970).

[166] T.F. Coleman and Y. Li, An interior trust region approach for nonlinear minimization subject to bounds, SIAM J. Optim. **6**, 418-445 (1996).

[167] A. Askarzadeh, A novel metaheuristic method for solving constrained engineering optimization problems: Crow search algorithm, Computers & Structures **169**, 1-12 (2016).

[168] J. Ludescher, C. Tsallis, and A. Bunde, Universal behaviour of interoccurrence times between losses in financial markets: An analytical description, Europhys. Lett. **95**, 68002 (2011).

[169] A. Greco, C. Tsallis, A. Rapisarda, A. Pluchino, G. Fichera, and L. Contrafatto, Acoustic emissions in compression of building materials: q-statistics enables the anticipation of the breakdown point, European Physical Journal Special Topics **229**(5), 841-849 (2020).

[170] G. Tononi, O. Sporns, and G. M. Edelman, A measure for brain complexity: Relating functional segregation and integration in the nervous system, PNAS, **91**(11) (1994).

[171] F. Rosas, P. A. M. Mediano, M. Gastpar, and H. J. Jensen, Quantifying High-order Interdependencies via Multivariate Extensions of the Mutual Information, Phys. Rev. E, **100**(3) (2019).

[172] T. F. Varley, M. Pope, J. Faskowitz, and O. Sporns, Multivariate information theory uncovers synergistic subsystems of the human cerebral cortex, Commun. Biol., **6**(1) (2023).

[173] C. Meisel, E. Olbrich, O. Shriki, and P. Achermann, Fading Signatures of Critical Brain Dynamics during Sustained Wakefulness in Humans, J. Neurosci., **33**(44) (2013).

[174] O. Shriki, J. Alstott, F. Carver, T. Holroyd, R. N. A. Henson, M. L. Smith, R. Coppola, E. Bullmore, and D. Plenz, Neuronal Avalanches in the Resting MEG of the Human Brain, J. Neurosci., **33**(16) (2013).

[175] R. Wild, M. Nötzold, M. Simpson, T.D. Tran, and R. Wester, Tunnelling measured in a very slow ion–molecule reaction, Nature (2023).

[176] C. Tsallis, C. Anteneodo, L. Borland, and R. Osorio, Nonextensive statistical mechanics and economics, Physica A: Statistical Mechanics and its Applications, **324**(1–2): 89-100 (2003).

[177] C. Tsallis and U. Tirnakli, Predicting COVID-19 Peaks Around the World, Frontiers in Physics **8**, 2020.00217 (2020).

[178] E. Mitsokapas, B. Schäfer, R.J. Harris, and C. Beck, Statistical characterization of airplane delays, Sci. Rep. **11**, 7855 (2021).

[179] P. Sauseng, B. Griesmayr, R. Freunberger, and W. Klimesch, Control mechanisms in working memory: a possible function of EEG theta oscillations, Neurosci Biobehav Rev. **34**, 1015-1022 (2010).

[180] A.L. Goldberger, *Fractal variability versus pathologic periodicity: complexity loss and stereotypy in disease*, Perspect. Biol. Med. **40**(4), 543-61 (1997).

[181] J.A.S. Kelso, *Dynamic Patterns: The Self-Organization of Brain and Behavior.* Massachusetts: MIT Press. **1995**. 334pp.

[182] G. Baffy and J. Loscalzo, *Complexity and network dynamics in physiological adaptation: an integrated view.* Physiol Behav. **131**,49-56 (2014).

[183] C. K. Peng, J. Mietus, J. M. Hausdorff, S. Havlin,H. E. Stanley, A. L. Goldberger, *Long-range anticorrelations and non-Gaussian behavior of the heartbeat*, Phys Rev Lett.,**70**(9), 1343-6 (1993).

[184] S.M. Keller, U. Gschwandtner, A. Meyer, M. Chaturvedi, V. Roth, P. Fuhr, *Cognitive decline in Parkinson's disease is associated with reduced complexity of EEG at baseline*, Brain Commun. **2**(2):fcaa207 (2020).

[185] A.C. Yang and S.J. Tsai, *Is mental illness complex? From behavior to brain.* Prog Neuropsychopharmacol Biol Psychiatry, **45** : 4253-7 (2013).

[186] S. Keshmiri, *Entropy and the Brain: An Overview.* Entropy (Basel), **22**(9):917 (2020).

[187] J. Buitelaar, S. Bölte, D. Brandeis, A. Caye, N. Christmann, S. Cortese, D. Coghill, S.V. Faraone, B. Franke, M. Gleitz, C.U. Greven, S. Kooij, D.T. Leffa, N. Rommelse, J.H. Newcorn, G.V. Polanczyk, L.A. Rohde, E. Simonoff, M. Stein, B. Vitiello, Y. Yazgan, M. Roesler, M. Doepfner, T. Banaschewski, *Toward Precision Medicine in ADHD.* Front Behav Neurosci. **16**:900981 (2022).

[188] R.M. Hernández, J.C. Ponce-Meza, M.Á. Saavedra-López, W.A. Campos Ugaz, R.M. Chanduvi, W.C. Monteza, *Brain Complexity and Psychiatric Disorders.* Iran J Psychiatry. **18**(4):493-502 (2023).

[189] D.M. Abramov, C.Q. Cunha, P.R. Galhanone, R.J. Alvim, A.M. de Oliveira, V.V. Lazarev, *Neurophysiological and behavioral correlates of alertness impairment and compensatory processes in ADHD evidenced by the Attention Network Test.* PLoS One. **14**(7):e0219472 (2019).

[190] V. V. Lazarev, M. Pontes,A. T. Pontes, J. Vieira, C. Quero-Cunha, T. Tamborino, P. R. Galhanone,L. C. De Azevedo, D. M. Abramov, *EEG and ERP characteristics of Attention Deficit Hyperactivity Disorder in children and adolescents*, Int J Psychophysiol **108**, 75 (2016).

[191] D.M. Abramov, V.V. Lazarev, S.C. Gomes Junior, C.A. Mourao-Junior, M. Castro-Pontes, C.Q. Cunha, L.C. deAzevedo, E. Vigneau, *Estimating biological accuracy of DSM for attention deficit/hyperactivity disorder based on multivariate analysis for small samples.* PeerJ. **7**:e7074 (2019).

[192] O. Kratz, P. Studer, S. Malcherek, K. Erbe, G.H. Moll, H. Heinrich, *Attentional processes in children with ADHD: An event-related potential study using the attention network test.* Int J Psychophysiol **81**: 82–90 (2011).

[193] C.B. Mello, N. Argollo, P.B.M. Shayer, N. Abreu, K. Godinho, P. Duran et al., *Abbreviated version of the WISC-III: correlation between estimated IQ and global IQ of Brazilian children.* Psic Teor e Pesq **27**: 149–155 (2011).

[194] T.W. Frazier, H.A. Demaree, E.A. Youngstrom, *Meta-analysis of intellectual and neuropsychological test performance in attention-deficit/hyperactivity disorder.* Neuropsychology. **18**(3):543-55 (2004).

[195] N.S. Thaler, D.T. Bello, L.M. Etcoff, *WISC-IV profiles are associated with differences in symptomatology and outcome in children with ADHD.* J Atten Disord. **17**(4):291-301 (2013).

[196] G.B. Mackenzie, E. Wonders, *Rethinking Intelligence Quotient Exclusion Criteria Practices in the Study of Attention Deficit Hyperactivity Disorder.* Front Psychol. **7**:794 (2016).

[197] American Psychiatric Association, *Diagnostic and Statistical Manual of Mental Disorders (4th ed., text rev.)*, 2000.

[198] American Psychiatric Association, *Diagnostic and Statistical Manual of Mental Disorders (5th ed.)*, 2013.

[199] A. Fernández, J. Quintero, R. Hornero, P. Zuluaga, M. Navas, C. Gómez, J. Escudero, N. García-Campos, J. Biederman, T. Ortiz, *Complexity analysis of spontaneous brain activity in attention-deficit/hyperactivity disorder: diagnostic implications.* Biol Psychiatry. **65**(7):571-7 (2009).

[200] M.R. Mohammadi, A. Khaleghi, A.M. Nasrabadi, S. Rafieivand, M. Begol, H. Zarafshan, *EEG classification of ADHD and normal children using non-linear features and neural network.* Biomedical Engineering Letters, **6**(2), 66–73 (2016).

[201] H. Zarafshan, A. Khaleghi, M.R. Mohammadi, M. Moeini, N. Malmir, *Electroencephalogram complexity analysis in children with attention-deficit/hyperactivity disorder during a visual cognitive task.* J Clin Exp Neuropsychol. **38**(3):361-9 (2016).

[202] H. Chen, W. Chen, Y. Song, L. Sun, X. Li, *EEG characteristics of children with attention-deficit/hyperactivity disorder.* Neuroscience. **406**:444-456 (2019).

[203] R.J. Barry, A.R. Clarke, S.J. Johnstone, *A review of electrophysiology in attention-deficit/hyperactivity disorder: I. Qualitative and quantitative electroencephalography.* Clin Neurophysiol. **114**(2):171-83 (2003).

[204] S.K. Loo, S. Makeig, *Clinical utility of EEG in attention-deficit/hyperactivity disorder: a research update.* Neurotherapeutics. **9**(3):569-87 (2012).

[205] R.J. Barry, A.R. Clarke, *Resting state brain oscillations and symptom profiles in attention deficit/hyperactivity disorder.* Suppl Clin Neurophysiol. **62**:275-87 (2013).

[206] S. Markovska-Simoska, N. Pop-Jordanova, *Quantitative EEG in Children and Adults With Attention Deficit Hyperactivity Disorder: Comparison of Absolute and Relative Power Spectra and Theta/Beta Ratio.* Clin EEG Neurosci. **48**(1):20-32 (2017).

[207] A. von Stein, J. Sarnthein, *Different frequencies for different scales of cortical integration: from local gamma to long range alpha/theta synchronization.* Int J Psychophysiol. **38**(3):301-13 (2000).

[208] J.E. Lisman, O. Jensen, *The $\theta - \gamma$ neural code*, Neuron, **77**(6):1002-16 (2013).

[209] J.M. Palva, S. Palva, *Functional integration across oscillation frequencies by cross-frequency phase synchronization.* Eur J Neurosci. **48**(7):2399-2406 (2018).

[210] J.W.Y. Kam, T. Rahnuma, Y.E. Park, C.M. Hart, *Electrophysiological markers of mind wandering: A systematic review.* Neuroimage. **258**:119372 (2022).

[211] J. J. Newson, T. C. Hiagarajan, *EEG Frequency Bands in Psychiatric Disorders: A Review of Resting State Studies*, Front. Hum. Neurosci. **12**, 521 (2019).

[212] A. Peres, *Stability of quantum motion in chaotic and regular systems*. Phys. Rev. A, 30, 1610-1615 (1984).

[213] F. M. Izrailev, *Simple models of quantum chaos: Spectrum and eigenfunctions*. Phys. Rep., 196, 299-392 (1990).

[214] M. C. Gutzwiller, *Chaos in classical and quantum mechanics*. Springer New York (1990).

[215] B. Georgeot and D. L. Shepelyansky *Quantum chaos border for quantum computing*, Phys. Rev. E, 62, 3504 (2000).

[216] D. L. Shepelyansky, Quantum chaos and quantum computers, Phys. Scr., **2001**, 112 (2001).

[217] B. Georgeot and D. L. Shepelyansky, Exponential gain in quantum computing of quantum chaos and localization, Phys. Rev. Lett. **86**, 2890–2893 (2001).

[218] T. Prosen and M. Znidaric, Can quantum chaos enhance the stability of quantum computation?, J. Phys. A Math. Gen., **34**, L681 (2001).

[219] S. Lüscher, T. Heinzel, K. Ensslin, W. Wegscheider, and M. Bichler, Signatures of spin pairing in chaotic quantum dots, Phys. Rev. Lett., **86**, 2118–2121 (2001).

[220] L. A. Ponomarenko et al., Chaotic Dirac billiard in graphene quantum dots, Science, **320**, 356-358 (2008).

[221] O. Bohigas and H. A. Weidenmuller, Aspects of chaos in nuclear physics, Annu. Rev. Nucl. Sci., **38**, 421-453 (1988).

[222] G. E. Mitchell, A. Richter, and H. A. Weidenmüller, Random matrices and chaos in nuclear physics: Nuclear reactions, Rev. Mod. Phys., **82**, 2845-2901 (2010).

[223] J. M. Magan, Black holes, complexity and quantum chaos, J. High Energy Phys., **2018**, 1-34 (2018).

[224] L. de Broglie, Interference and corpuscular light, Nature, **118**, 441–442 (1926).

[225] D. Bohm, A suggested interpretation of the quantum theory in terms of "hidden" variables. I, Phys. Rev., **85**, 166 (1952).

[226] D. Bohm, A suggested interpretation of the quantum theory in terms of "hidden" variables. II, Phys. Rev., **85**, 180 (1952).

[227] R. H. Parmenter and R. W. Valentine, Deterministic chaos and the causal interpretation of quantum mechanics, Phys. Lett. A **201**, 1 (1995).

[228] F. H. M. Faisal and U. Schwengelbeck, Unified theory of Lyapunov exponents and a positive example of deterministic quantum chaos, Phys. Lett. A **207**, 31 (1995).

[229] G. G. de Polavieja, Exponential divergence of neighboring quantal trajectories, Phys. Rev. A **53**, 2059 (1996).

[230] H. Wu and D. W. L. Sprung, Quantum chaos in terms of Bohm trajectories, Phys. Lett. A **261**, 150 (1999).

[231] J. T. Cushing and G. E. Bowman, Bohmian mechanics and chaos (Cambridge University Press, Cambridge, 1999).

[232] J. T. Cushing, Bohmian insights into quantum chaos, Philos. Sci. **67**, S430 (2000).

[233] A. Makowski, P. Pepłowski, and S. Dembiński, Chaotic causal trajectories: The role of the phase of stationary states, Phys. Lett. A (2000).

[234] A.J. Makowski and M. Frackowiak, The simplest non-trivial model of chaotic causal dynamics, Acta Phys. Pol. B (2001).

[235] C. Efthymiopoulos and G. Contopoulos, Chaos in Bohmian quantum mechanics, J. Phys. A: Math. Gen., **39**, 1819 (2006).

[236] G. Contopoulos and C. Efthymiopoulos, Ordered and chaotic Bohmian trajectories, Celest. Mech. Dyn. Astr. **102**, 219 (2008).

[237] F. Borondo, A. Luque, J. Villanueva, and D. A. Wisniacki, A dynamical systems approach to Bohmian trajectories in a 2D harmonic oscillator, J. Phys. A Math. Theor. **42**, 495103 (2009).

[238] S. Sengupta, M. Khatua, and P.K. Chattaraj, Bohmian trajectory from the "classical" Schrödinger equation, Chaos **24**, 043123 (2014).

[239] A. C. Tzemos and G. Contopoulos, Chaos and ergodicity in an entangled two-qubit Bohmian system, Phys. Scr., **95**, 065225 (2020).

[240] G. Contopoulos and A. C. Tzemos, Chaos in Bohmian quantum mechanics: A short review, Regul. Chaot. Dyn., **25**, 476–495 (2020).

[241] A. C. Tzemos and G. Contopoulos, Bohmian quantum potential and chaos, Chaos Solit. and Fractals, **160**, 112151 (2022).

[242] A. C. Tzemos, G. Contopoulos, *Bohmian chaos in multinodal bound states*, Found. Phys., 52, 85 (2022).

[243] N. Bohr, *Über die Serienspektra der Elemente*, Zeitschrift für Physik, 2 (5): 423–478, (1920).

[244] M. Lecar, F. A. Franklin, M. J. Holman, and N. W. Murray, *Chaos in the Solar System*, Annu. Rev. Astron. Astrophys, 39, 581-631 (2001).

[245] C. Ma, S. Meyers, and B. Sageman, *Theory of chaotic orbital variations confirmed by Cretaceous geological evidence*, Nature, 542, 468–470 (2017).

[246] S. Bo-Wen, et al. *Is weather chaotic?: Coexistence of chaos and order within a generalized Lorenz model*, BAMS, 102, E148-E158 (2021).

[247] D. T. Mihailovic, G. Mimic, and I. Arsenic, *The chaos and complexity in climate models*, Adv. Meteorol., 2014, 878249 (2014).

[248] M.M.A. Paixão and H.S. Lima, *Numerical validation of Ehrenfest theorem in a Bohmian perspective for non-conservative systems*, Eur. Phys. J. Plus **138**, 549 (2023).

[249] M.M.A. Paixão and H.S. Lima, *Numerical validation of Ehrenfest theorem in a Bohmian perspective for non-conservative systems*, Wolfram Community, STAFF PICKS (2023).

[250] P. Holland, *The Quantum Theory of Motion: An Account of the de Broglie-Bohm Causal Interpretation of Quantum Mechanics*, Cambridge: Cambridge University Press.

[251] E. J. Heller, *Bound-state eigenfunctions of classically chaotic Hamiltonian systems: Scars of periodic orbits*, Phys. Rev. Let. 53 (16): 1515–1518 (1984).

[252] D. H. Frisk, *Properties of the trajectories in Bohmian mechanics*, Phys. Lett. A, 227, 139-142 (1997).

[253] I. Bialynicki-Birula, Z. Bialynicki-Birula, and C. Sliwa, *Motion of vortex lines in quantum mechanics*, Phys. Rev. A, 61, 032110 (2000).

[254] D. A. Wisniacki and E. R. Pujals, *Motion of vortices implies chaos in Bohmian mechanics*, Europhys. Lett., 71, 159 (2005).

[255] D. A. Wisniacki, E. R. Pujals, and F. Borondo, *Vortex interaction, chaos and quantum probabilities*, Europhys. Lett. 73, 671 (2006).

[256] D. A. Wisniacki, E. R. Pujals, and F. Borondo, *Vortex dynamics and their interactions in quantum trajectories*, J. Phys. A: Math. Theor, 40, 14353 (2007).

[257] P. Falsaperla and G. Fonte, *On the motion of a single particle near a nodal line in the de Broglie–Bohm interpretation of quantum mechanics*, Phys. Lett. A, 316, 382-390 (2003).

[258] C. Efthymiopoulos, C. Kalapotharakos, and G. Contopoulos, *Origin of chaos near critical points of quantum flow*, Phys. Rev. E, 79, 036203 (2009).

[259] G. Blatter, M. V. Feigel'man, V. B. Geshkenbein, A. I. Larkin, and V. M. Vinokur, *Vortices in high-temperature superconductors*, Rev. Mod. Phys., 66(4), 1125-1388 (1994).

[260] A. L. Fetter, *Rotating trapped Bose-Einstein condensates*, Rev. Mod. Phys. 81, 647–691 (2009).

[261] D. D. Solnyshkov, C. Leblanc, S. V. Koniakhin, O. Bleu, and G. Malpuech, *Quantum analogue of a Kerr black hole and the Penrose effect in a Bose-Einstein condensate*, Phys. Rev. B, 99, 214511 (2019).

[262] V. Ruutu, V. Eltsov, A. Gill, et al., *Vortex formation in neutron-irradiated superfluid* $^3$He *as an analogue of cosmological defect formation*, Nature, 382, 334–336 (1996).

[263] S. Autti, V. V. Dmitriev, et al., *Observation of half-quantum vortices in topological superfluid* $^3$He, Phys. Rev. Lett., 117, 255301 (2016).

[264] R. F. Rajaraman, *Some non-perturbative semi-classical methods in quantum field theory (a pedagogical review)*, Phys. Rep., 21, 227-313 (1975).

[265] J. Fröhlich and P. A. Marchetti, *Quantum field theories of vortices and anyons*, Commun.Math. Phys., 121, 177–223 (1989).

[266] W. B. De Lima and P. De Fabritiis, *Self-dual Maxwell-Chern-Simons solitons in a parity-invariant scenario*, Phys. Lett. B, **833**, 137326 (2022).

[267] M. M. A. Paixao, O. Galkina, and N. Pinto-Neto, *Unruh effect under the de Broglie–Bohm perspective*, Phys. Rev. D, **108**, 083514 (2023).

[268] A. Valentini, *Signal-locality, uncertainty, and the subquantum H-theorem. I*, Phys. Lett. A, **156**(1–2), 5-11 (1991).

[269] A. Valentini, *Signal-locality, uncertainty, and the subquantum H-theorem. II*, Phys. Lett. A, **158**(1–2), 1-8 (1991).

[270] A. C. Tzemos and G. Contopoulos, *The role of chaotic and ordered trajectories in establishing Born's rule*, Phys. Scr., **96**, 065209 (2021).

[271] A. C. Tzemos and G. Contopoulos, *Unstable points, ergodicity and Born's rule in 2d Bohmian systems*, Entropy, (2023).

[272] K. Bathe, "Finite Element Method," in *Wiley Encyclopedia of Computer Science and Engineering*, John Wiley & Sons, Ltd, 2008, pp. 1-12.

[273] Wolfram Research, Inc., Mathematica, Version 13.2, Champaign, IL, 2022, `https://reference.wolfram.com/language/FEMDocumentation/tutorial/FiniteElementOverview.html`.

[274] Wolfram Research, Inc., Mathematica, Version 13.2, Champaign, IL, 2022, `https://reference.wolfram.com/language/FEMDocumentation/tutorial/FiniteElementBestPractice.html`.

[275] P. Curie, *Sur la symétrie dans les phénomènes physiques, symétrie d'un champ électrique et d'un champ magnétique*, J. phys. theor. appl. (in French). EDP Sciences. **3**(1): 393–415 (1894).

[276] C. Runge, *Über die numerische Auflösing von Differentiagleichungen*, Math. Ann., **46**, 167-178 (1895).

[277] W. Kutta, *Beitrag zur näherungsweisen Integration totaler Differentialgleichungen*, Z. Math. Phys., **46**, 435-453 (1901).

[278] Wolfram Research, Inc., Mathematica, Version 13.2, Champaign, IL, 2022, `https://reference.wolfram.com/language/tutorial/NDSolveExplicitRungeKutta.html`.

[279] F. S. Nogueira, Z. Nussinov, and J. van den Brink, *Fractional angular momentum at topological insulator interfaces*, Phys. Rev. Lett. **121**, 227001 (2018).

[280] M. Serbyn, D.A. Abanin, and Z. Papić, *Quantum many-body scars and weak breaking of ergodicity*, Nat. Phys. **17**, 675–685 (2021).